



UNIVERSITÀ DEGLI STUDI DI PAVIA

**DOTTORATO IN SCIENZE CHIMICHE E FARMACEUTICHE E
INNOVAZIONE INDUSTRIALE
(XXXIII Ciclo)**

Coordinatore: Chiar.mo Prof. Giorgio Colombo

**(SUPRA)MOLECULAR SYSTEMS FOR
RECOGNITION, SENSING AND EXTRACTION
PROCESSES**

Tesi di Dottorato di
Sonia La Cognata

AA 2019/2020

Tutor

Chiar.ma Prof.ssa Valeria Amendola

Index

1. Abstract.....	1
2. Development of an innovative method for the detection of a benzene biomarker in urines.....	3
2.1 Introduction	3
2.1.1 Indicator Displacement Approach (IDA).....	3
2.1.2 Smartphone sensing.....	7
2.1.3 Our study	14
2.2 Experimental	16
2.2.1 Chemicals and methods	16
2.2.2 Computational study.....	16
2.2.3 Preparation of artificial urine	16
2.2.4 Pretreatment of the real urine samples.....	17
2.3 Results and discussion	18
2.3.1 DFT calculations.....	18
2.3.2 Studies in solution	20
2.3.2.1 UV-vis. studies with tt-MA	20
2.3.2.2 Fluorimetric titrations	24
2.3.3 Development of a smart device	30
2.3.3.1 Construction of the device and calibration experiments.....	30
2.3.3.2 Test with real urine samples	33
2.4 Conclusions	34
References	36
3. A fluorimetric supramolecular sensor for the sensing of fumarate in water	42
3.1 Introduction	42
3.1.1 Anion recognition	42
3.1.2 Our study	51
3.2 Experimental	53
3.2.1 Chemicals and methods	53
3.2.2 Potentiometric and pH-spectrophotometric titrations.....	53
3.2.3 X-ray diffraction studies	53
3.2.3.1 Details on crystal structure analysis.....	54
3.2.4 Spectrophotometric titrations	59

3.2.5 Spectrofluorimetric titrations.....	60
3.3 Results and discussion	60
3.3.1 Potentiometric and pH-spectrophotometric titrations.....	60
3.3.1.1 Protonation constants of L1	60
3.3.1.2 Complexation of L1 with Cu(II)	62
3.3.1.3 pH-spectrophotometric titration of L1 with Cu(II)	63
3.3.2 X-ray diffraction studies	65
3.3.3 Spectrophotometric studies on $[\text{Cu}_2(\text{L1})]^{4+}$ with dicarboxylates.....	68
3.3.4 Spectrofluorimetric studies on $[\text{Cu}_2(\text{L1})]^{4+}$ with 5-FAM and dicarboxylates	77
3.4 Conclusions	85
References	86
4. A dicopper(II) azacryptate for the liquid-liquid extraction of dicarboxylates.....	91
4.1 Introduction	91
4.1.1 Anion extraction and transport.....	91
4.1.2 Transmembrane anion transport.....	96
4.1.3 Our study.....	98
4.2 Experimental.....	100
4.2.1 Chemicals and methods	100
4.2.2 Synthesis of L2 ligand	100
4.2.3 Potentiometric and pH-spectrophotometric titrations.....	101
4.2.4 Spectrophotometric titrations	102
4.2.5 Extraction experiments	102
4.2.5.1 HPLC-UV analyses.....	102
4.2.5.2 $^1\text{H-NMR}$ studies	103
4.3. Results and discussion	104
4.3.1 Potentiometric and pH-spectrophotometric titrations.....	104
4.3.1.1 Protonation constants of L2	104
4.3.1.2 Complexation of L2 with Cu(II)	105
4.3.1.3 pH-spectrophotometric titration of L2 with Cu(II)	107
4.3.1.4 Potentiometric titrations on H_2suc and H_2glut in dioxane/water 20% v/v	109
4.3.2 Spectrophotometric studies on $[\text{Cu}_2(\text{L2})]^{4+}$ with dicarboxylates.....	109
4.3.2.1 UV-vis. titrations of $[\text{Cu}_2(\text{L2})]^{4+}$ in dioxane/water 20% v/v at pH 7	109
4.3.2.2 UV-vis. titration of $[\text{Cu}_2(\text{L2})]^{4+}$ with succinate in dichloromethane.....	115
4.3.3 Extraction experiments	116
4.3.3.1 UV-vis. spectrum of extracting solution	116
4.3.3.2 HPLC-UV chromatographic analysis	117
4.3.3.3. $^1\text{H-NMR}$ study.....	121
4.4 Conclusions	123

Supplementary information125

Characterization of L2 125

HRMS-ESI spectra of L2 125

References129

5. New hydrophilic azacryptands as complexing agents for $^{99}\text{TcO}_4^-$ in extraction processes 132

omissis

1. Abstract

Since the dawn of supramolecular chemistry, many researchers tried to understand and to handle the principles at the base of the non-covalent interactions between molecules. For example, the host-guest recognition, *i.e.* the selective interaction of a receptor (host) with a specific substrate (guest), can be achieved only with a total geometrical and interaction complementarity between the species. An accurately design of the receptor, together with a deep knowledge of the chemical features of the guest of interest, is necessary to develop selective molecular systems.

Macrobicyclic receptors, such as *bistren* azacryptands, are highly preorganized molecules with a well-defined three-dimensional cavity, widely applied for recognition of anionic species in solution. Thanks to the easy preparation and modulation of their molecular structure, some peculiar features of azacryptands (*e.g.* size, shape and donor groups) can be finely tuned, thus obtaining a series of ligands able to perform selective recognition of substrates for a wide variety of applications.

My PhD project was focused on the development of new molecular receptors to be applied in the recognition and sensing of anionic guests in aqueous solution and in liquid-liquid extraction processes.

The first chapter of this thesis is focused on the successful combination of the Indicator Displacement Approach with the smartphone sensing for the development of a portable device for the detection of the trans-trans muconic acid (tt-MA), a urinary metabolite of benzene. The affinity of a dicopper(II) azacryptate for tt-MA was investigated through spectrophoto- and spectrofluorimetric titrations (through the Indicator Displacement Approach). The selectivity of this supramolecular system for the metabolite was tested in presence of interferents and in complex media (such as artificial urine). Then, in order to develop a smart portable device, the chemosensing ensemble was absorbed on silica gel using ELISA-like plastic wells as the support. By exposing the microplate to a UV-lamp and recording RGB values with a smartphone, the indicator displacement could be detected, permitting to quantify the concentration of tt-MA. The new device was also successfully applied to real urine.

The second chapter describes the development of a fluorimetric supramolecular sensor for the fumarate anion. The binding properties of a dicopper(II) azacryptate towards dicarboxylates were deeply investigated through UV-vis. and fluorimetric titrations in buffered neutral water.

The coordination geometries of the metal ions in some inclusion complexes with anions were also evaluated through X-ray diffraction analysis. Through the Indicator Displacement Approach, an outstanding affinity for fumarate was confirmed, thus opening the possibility to apply this complex:indicator chemosensing ensemble as a fluorimetric sensor for the selective recognition of fumarate in water.

In the third chapter, the synthesis of a new lipophilic cryptand, realised by appending alkyl chains on the spacers of a *bistren* cage, is reported. Spectrophotometric titrations of the dicopper(II) complex were then performed to evaluate the effect of the ligand functionalization on binding properties towards dicarboxylates in aqueous mixture. The enhanced hydrophobicity makes the dicopper(II) complex completely soluble in organic solvent, thus allowing to test its properties as extractant of target anions. Liquid-liquid extraction experiments were performed, using succinate as a model anion: to evaluate the efficiency of the process, the concentration of the anion into the aqueous phase was monitored before and after extraction through HPLC-UV and ¹H-NMR analyses.

The last chapter of this PhD thesis is based on the design and development of new molecular systems to be applied in spent nuclear fuel separation processes. This part of my research project was realised in collaboration with the CEA (Commissariat à l'Énergie Atomique et aux Énergies Alternatives, France). The whole chapter is omitted for a secrecy agreement with CEA.

The results described in the first three chapters of this PhD thesis have been published in two scientific journals (Merli, D.; La Cognata, S.; Balduzzi, F.; Miljkovic, A.; Toma, L.; Amendola, V. A smart supramolecular device for the detection of t,t-muconic acid in urine, *New J. Chem.*, **2018**, 42 (18), 15460-15465; DOI:[10.1039/c8nj02156b](https://doi.org/10.1039/c8nj02156b); La Cognata, S.; Mobili, R.; Merlo, F.; Speltini, A.; Boiocchi, M.; Recca, T.; Maher III, L. J.; Amendola, V. Sensing and Liquid–Liquid Extraction of Dicarboxylates Using Dicopper Cryptates, *ACS Omega*, **2020**, 5 (41), 26573-26582; DOI:[10.1021/acsomega.0c03337](https://doi.org/10.1021/acsomega.0c03337)).

During the lockdown period, imposed by the Italian Government because of the Coronavirus emergency, I collaborated on the writing of a review published in ChemPlusChem (Wiley Online Library, DOI:[10.1002/cplu.202000274](https://doi.org/10.1002/cplu.202000274)).

2. Development of an innovative method for the detection of a benzene biomarker in urines

2.1 Introduction

The work reported in this section focuses on the successful combination of the high sensitivity of the Indicator Displacement Approach and the great capabilities of the smartphone sensing in the development of an easy-to-handle device for the detection of a urinary benzene biomarker. Before the discussion of the experimental results, an overview of the Indicator Displacement Approach and the smartphone sensing is reported in two dedicated subchapters.

2.1.1 Indicator Displacement Approach (IDA)

First reported in the early 2000s, this well-known technique represents a powerful tool in (supra)molecular chemistry for the sensing and recognition of a wide range of charged and neutral guests.^{1,2} The principle is very simple: if a receptor can establish strong non-covalent interactions with a fluorescent/coloured indicator, a labile “chemosensing-ensemble” can be formed. When a specific analyte interacts with the receptor more strongly than the indicator, the latter is displaced from the receptor’s cavity, thus causing significant optical changes in solution correlated to the amount of the analyte. A schematic representation is reported in Figure 1.

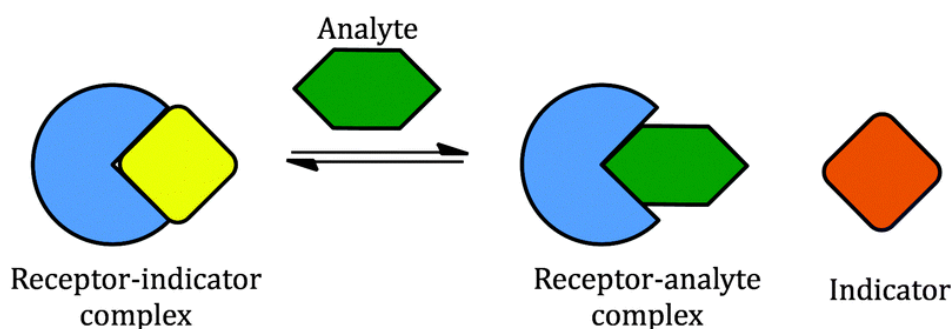


Figure 1. Scheme of the Indicator Displacement Approach.

If the indicator is fluorescent and the emission changes are collected through a spectrofluorimeter, the sensitivity of this method can be very high, with very low detection

limits.² Starting from this simple approach and tuning the single elements of the ensemble, several variations were investigated, thus resulting in a huge number of works on the topic.³⁻⁵ To cite some examples, Joliffe and colleagues investigated a series of cyclic peptide receptors, functionalized with two Zn(II)-dipicolylamine arms, for the selective recognition of phosphate anions through colorimetric Indicator Displacement. Combinations of three different indicators allowed the sensing of pyrophosphate ions (visible naked-eye) in aqueous solution, even in presence of 100-fold excess of ATP.⁶

The Indicator Displacement Approach was also applied for the real-time monitoring of biomembrane transport. In particular, the no-fluorescent chemosensing ensemble formed by p-sulfonatocalix[4]arene and lucigenin (CX4-LCG) was encapsulated in liposomes, with a channel protein on the membrane (see Fig. 2a-b). Protamine, the target analyte, was translocated in the liposome through the channel: by interaction with the receptor, the indicator was released, with an increase of its fluorescence emission. Real-time transport kinetic measurements were performed through stopped-flow experiments because of the very fast translocation process.⁷

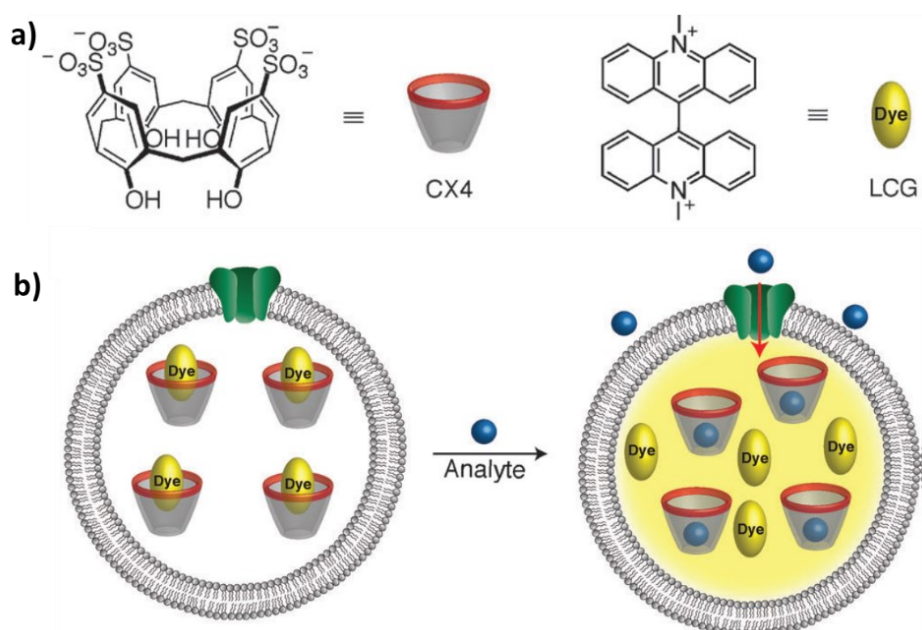


Figure 2. a) Sketches of the calix[4]arene receptor (CX4) and the lucigenin indicator (LCG); b) Scheme of the Indicator Displacement occurring across the membrane. From ref [7].

Some recent works showed unlimited ways to apply the great potentialities of this technique.⁸⁻
¹¹ For example, chiral Cu(II)-based receptors and coumarin-343 were applied in the development of a chemosensing assay for chiral carboxylates, based on the enantioselective Indicator Displacement Approach. This method also allowed the determination of the

enantiomeric composition of the chiral analyte. Different chiral drugs were tested, obtaining a very good discrimination between the enantiomers of atorvastatin (*i.e.* a anti-cholesterol medicine), ibuprofen and naproxen (*i.e.* two anti-inflammatory drugs).¹²

In another interesting article, the authors fine-tuned the synthesis of functionalized Zr-MOFs, containing cationic electron-deficient bipyridinium sites (MQ²⁺ and DQ²⁺) in the framework and anionic indicator 8-anilino-naphthalenesulfonate (ANS⁻) in the pores (see Fig. 3b).¹³ The formation of charge-transfer (CT) ANS-bipyridinium complexes quenched the indicator fluorescence (off-state of the MOFs): in presence of alkylamines (BA = butylamine), ANS⁻ molecules were displaced from the CT complexes, thus turning on the ANS⁻ emission. It was confirmed that, even after the displacement, the indicator molecules stayed in the MOFs pores, without any dispersion in solution (see Fig. 3a).

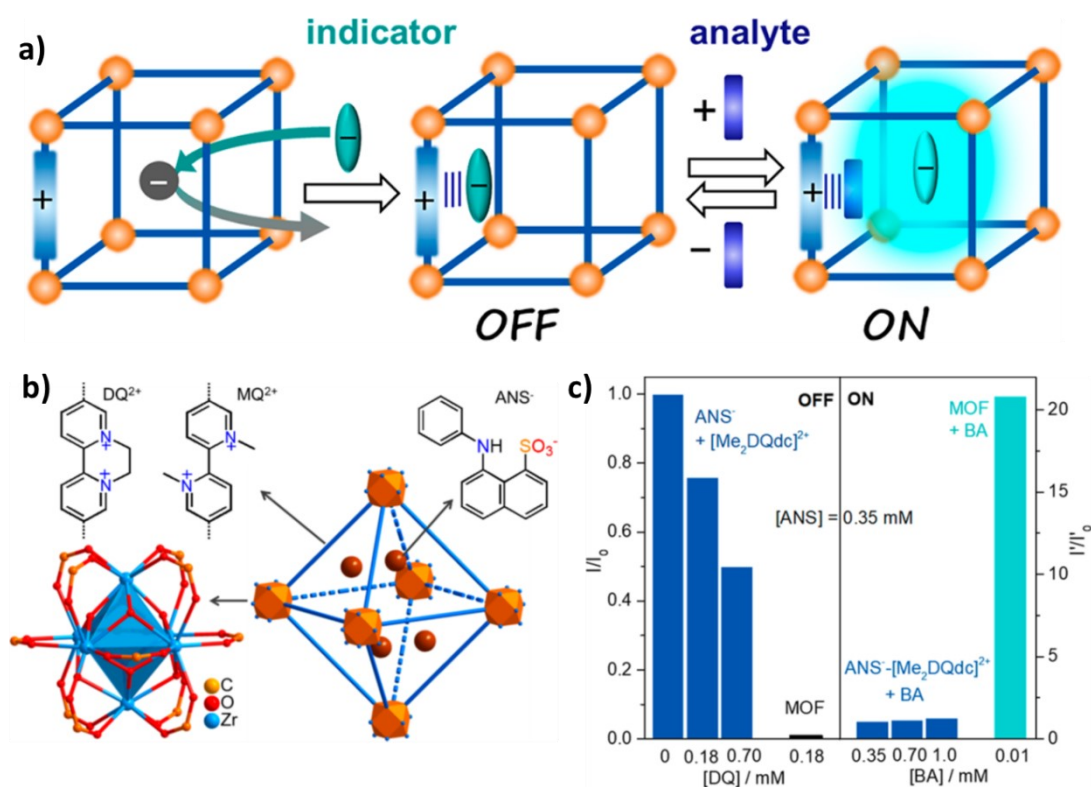


Figure 3. a) Scheme of the confined Indicator Displacement Assay; b) 3D-structure of the Zr-ANS MOF; c) **Left:** decrease of I/I_0 ($I_0 = I_{\max}$ ANS) for the unconfined system $[\text{Me}_2\text{DQdc}]^{2+}$ compared with the MOF; **Right:** Increase of I_0'/I' upon addition of BA, for $[\text{Me}_2\text{DQdc}]^{2+}$ compared with the MOF ($I_0 = I_{\max}$ ANS; I_0' and I' : intensity before and after addition of BA, respectively). From ref. [13].

This confinement enhanced the CT complexation, thus increasing both the quenching efficiency in the OFF-state of the MOFs and the turn-ON process. In order to study the confinement effects on process efficiency, IDA experiments were carried out on the unconfined homogeneous solution using $[\text{Me}_2\text{DQdc}]^{2+}$ (*i.e.* dimethyl ester of the DQ-containing dicarboxylate linker for

Zr-DQ). As shown in Figure 3c, the quenching efficiency of the unconfined system is 50% and the fluorescence restoration in presence of BA reaches ~25% only. On the other hand, an almost complete ANS quenching (~99%) and a very efficient emission enhancement is observed for the MOFs. The confined Indicator Displacement Assay, obtained using Zr-ANS-based MOFs, allowed the selective detection of alkylamines at subnanomolar concentrations. The successful application in the solid state and the reusability of the material were also confirmed.

Among the last published works on the topic, ruthenium vinyl complexes (sketch in Fig. 4) of the 5-(3-thienyl)-2,1,3-benzothiadiazole (TBTD) ligand (blue moiety in Fig. 4), were applied in the chromo-fluorogenic sensing of carbon monoxide in several media (air, aqueous solution and cells).¹⁴

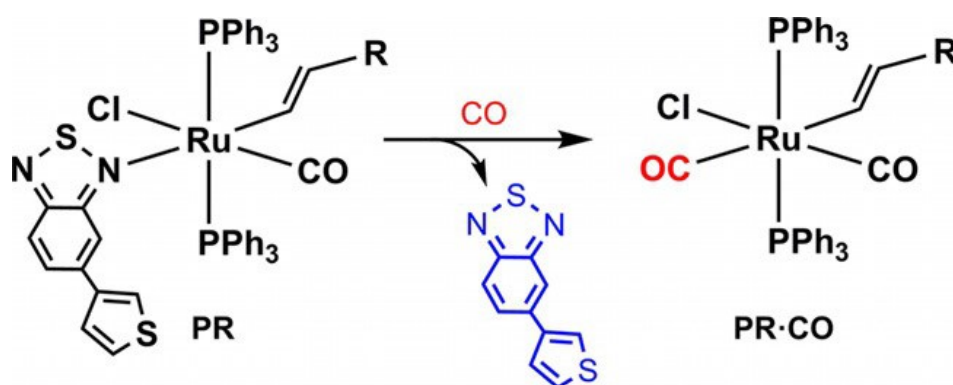


Figure 4. Reaction of the tested probes with carbon dioxide, R = phenyl. From ref. [14].

In particular, the emission of TBTD is typically quenched by coordination to Ru(II), as found in the case of the complex PR shown in Figure 4. However, in presence of CO, TBTD is released in solution and a consequent restoration of the emission is observed. The immobilization of the complex on silica and studies with gaseous CO showed a naked-eye progressive colour change of the solid from red to light, which can be very useful for the detection of air CO under the toxicity level (see Fig. 5). Diffuse reflectance spectra on the solid permitted the determination of the detection limit (*i.e.* LOD), which resulted to be 1.4 ppm and confirmed the selectivity of the system for CO compared with other gases (*e.g.* N₂, O₂, CO₂, Ar, NO_x).

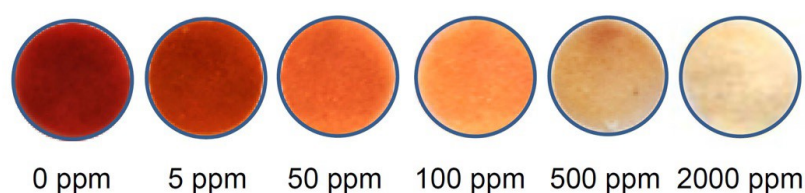


Figure 5. Naked-eye colour change of the immobilized Ru(II)-complex in presence of increasing CO concentrations. From ref. [14].

The functionalization on the R- substituent with a polyethylene glycol chain (see Fig. 6a) enhanced the solubility of the Ru(II)-complex in water. The new molecular system, which was demonstrated to be non cytotoxic through MTT assays on HeLa cells, was successfully applied in the detection of CO in cells, in particular after release by CORM-3 (*i.e.* a well-known CO-release molecule). CO-levels are determined by following the increase of the blue emission of TBTD, displaced by CO in the Ru(II) complex. A confocal microscope can be used for these measurements (see Fig. 6b).

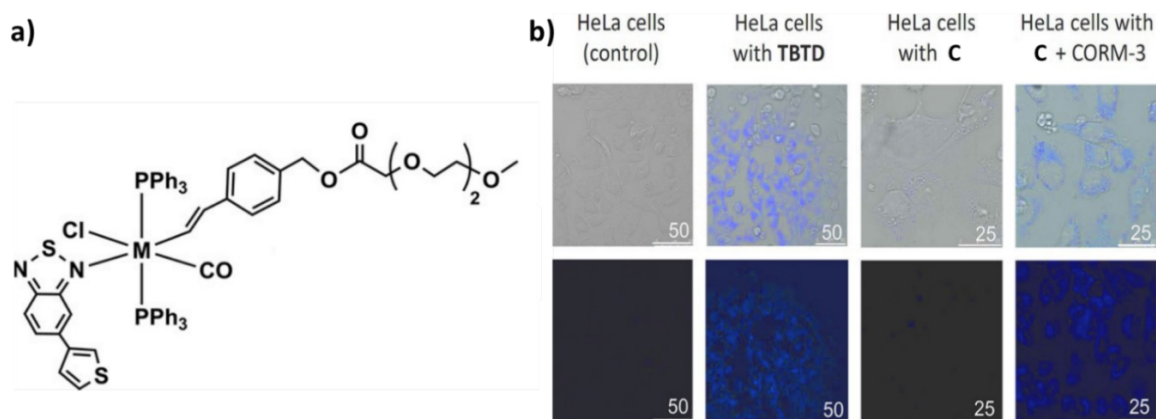


Figure 6. **a)** Molecular structure of the PEG-functionalized complex ($M = Ru^{II}$); **b)** Microscopy images showing HeLa cells in transmitted light (above) and confocal modes (below). **C** = functionalized Ru(II)-complex. Scales are in μM . From ref. [14].

The Indicator Displacement Approach can be also combined with smartphone sensing in order to obtain new portable devices for the determination of analytes in the field.

2.1.2 Smartphone sensing

Principle and first devices

The development of cheap and portable devices for “point-of-care” (POC) diagnostics, able to perform tests in the field without advanced laboratory instruments, has found a great and increasing interest in the last decade. Thanks to their simple design and intuitive use, lots of tests can be performed when and where necessary, without traditional expensive analyses, obtaining immediate and reliable results. For this reason, several researchers have been focusing on the development on new devices for POC diagnostics to be applied in many fields, from the environment to the healthcare. The great attention towards this innovative technology is driven by both economic and social reasons: in developing countries, where expensive medical tests are not available for the entire population, the discover of new cheap and simple

diagnostic methods plays a key role in the well-being of the community. Moreover, the availability of portable, cost-effective, and fast diagnostic devices could help patients and consumers in the prevention and monitoring of specific upsets or diseases, also giving an important support to the healthcare professionals.^{15,16}

Among the available technologies, smartphones surely represent an important resource. In recent years, the worldwide distribution of this device is exponentially grown, accompanied by the creation of more and more sophisticated and high-performance models. Among its peculiar features, high storage capacity, high-resolution cameras, Wi-fi connectivity and a wide selection of applications make the smartphone a promising all-in-one tool suitable for POC diagnostics.¹⁷⁻²⁰

One of the first examples of smartphone-integrated technology was reported by Ozcan and co-workers in 2013. Their study focused on a smartphone based digital sensing platform, termed as *Albumin Tester*, able to detect and quantify albumin in urine samples through a sensitive and specific fluorescent assay.²¹ A schematic illustration of the platform is reported in Figure 7. The platform was first designed ad-hoc with a dedicated software and then realised through a 3D printer: it contained a compact laser diode, two AA batteries, a plastic lens, and an emission interference filter and it can be installed on the existing camera unit of the smartphone.

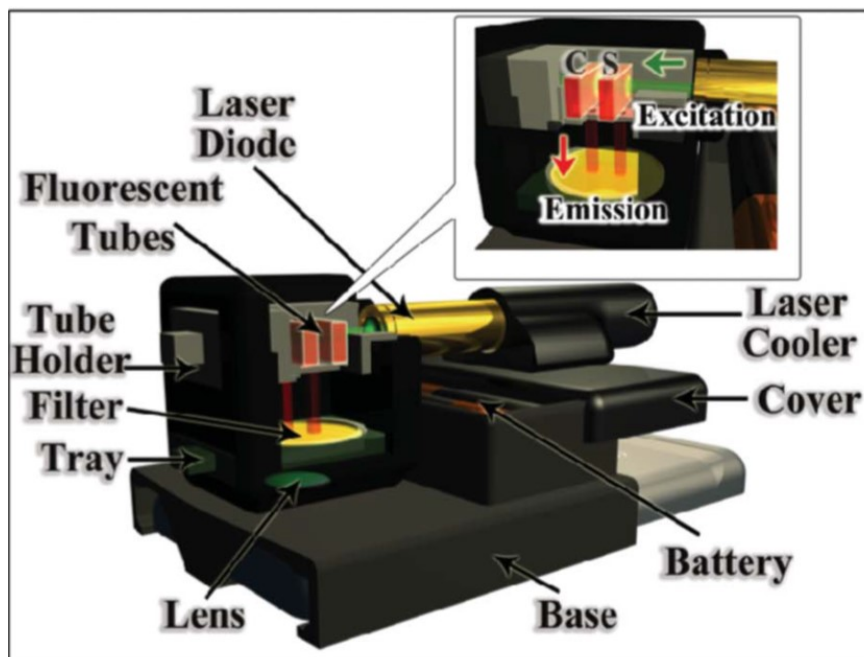


Figure 7. Scheme of the *Albumin Tester* platform for smartphone. From ref. [21].

The specific quantification of albumin in real urine samples was obtained through the following procedure: the control tube and the test tube (C and S red sections in Fig. 7, respectively) were partially filled with a solution of a specific dye for albumin and 25 μL of the sample were then injected in the test tube. A single laser beam ($\lambda_{\text{exc}} = 532 \text{ nm}$) excited the solutions in control and test tubes, and the image of the consequent fluorescent emission (perpendicular to the direction of excitation) was captured by the smartphone camera. A custom-developed application processed the image for the automated determination of the albumin concentration in the tested sample, with a LOD value of 5-10 $\mu\text{g mL}^{-1}$. Several tests on random urine samples demonstrated the successful application of *Albumin Tester* for a fast and simple detection of the albumin level in urine (pathological if higher than 30 $\mu\text{g mL}^{-1}$), useful for monitoring high-risk patients afflicted by hypertension, diabetes and/or cardiovascular diseases and for early diagnosis of kidney disease.

A similar approach was adopted by Roda and colleagues in the creation of specific smartphone assays for the quantification of cholesterol and bile acids in biological fluids (see Fig. 8).²² In this case, the detection of the analytes is based on bioluminescence coupled to biospecific enzymatic reactions, using the smartphone as detector. In specific minicartridges (see Fig. 8d), a little volume of sample was placed in the back opening and it was directed towards the reaction chamber. The enzymatic reagent was driven in the chamber from the reservoir and the reaction took place. The minicartridge was then placed in a dark box of the smartphone accessory and the light signal of the taken image was automatically processed by a specific software obtaining the concentration of the analyte.

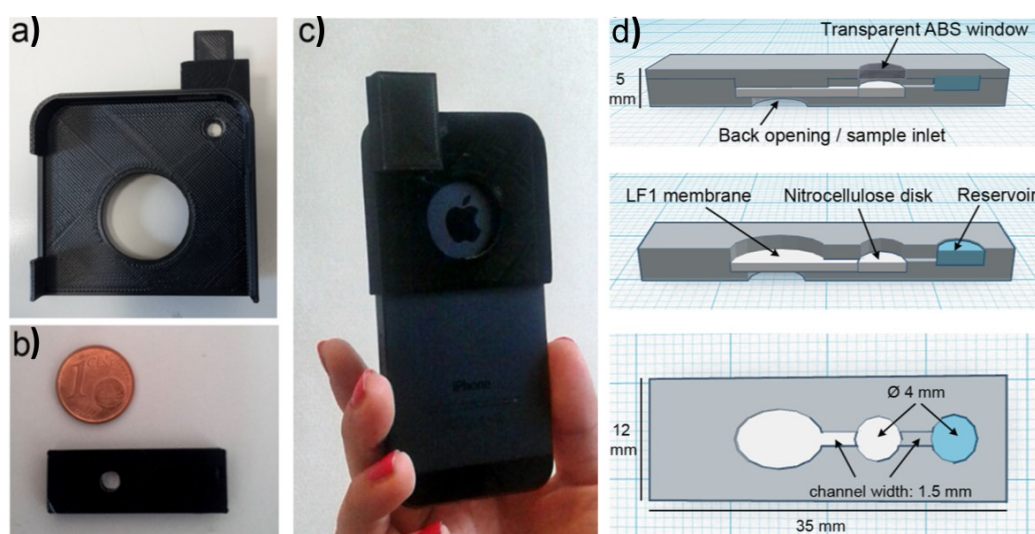


Figure 8. **a)** Picture of the accessory, **b)** picture of the minicartridge, and **c)** picture of the accessory snapped into the smartphone; **d)** Schematic cutaway drawings of the minicartridge. From ref. [22].

The versatility of this portable device allowed to obtain two assays for two different analytes only by changing the specific reagents charged in the reservoir. The cholesterol assay (*i.e.* SmartChol), based on cholesterol esterase/cholesterol oxidase (detection of the produced H_2O_2 through the luminol– H_2O_2 –HRP system), could perform the quantification of the analyte in serum ($\text{LOD} = 20 \text{ mg dL}^{-1}$). Regarding the bile acids assay (*i.e.* SmartBA), 3α -hydroxyl steroid dehydrogenase co-immobilized with bacterial luciferase system allowed to quantify bile acids concentrations in serum and in saliva ($\text{LOD} = 0.5 \text{ } \mu\text{mol L}^{-1}$). Through the same strategy, Roda research group also created a smartphone-based biosensor for lactate in saliva and sweat.²³

This innovative diagnostic technique was successfully applied in the environmental field for the detection of contaminants in water.^{24,25} For example, McCracken and co-workers designed a device for the detection of Bisphenol-A (BPA) in contaminated water samples.²⁶ In this study, the authors firstly confirmed the high specificity of 8-hydroxypyrene-1,3,6-trisulfonic acid (HPTS), as fluorescent probe for BPA, through fluorimetric spectroscopy. An increasing dynamic quenching of HPTS fluorescence was observed in presence of an increasing amount of BPA ($\text{LOD} = 4.4 \text{ mM}$). For smartphone detection, the role of smartphone flash as light source for excitation and the hardware camera as detector was separately evaluated, before to build a single smartphone sensing device integrated with a single cuvette holder platform (see Fig. 9).

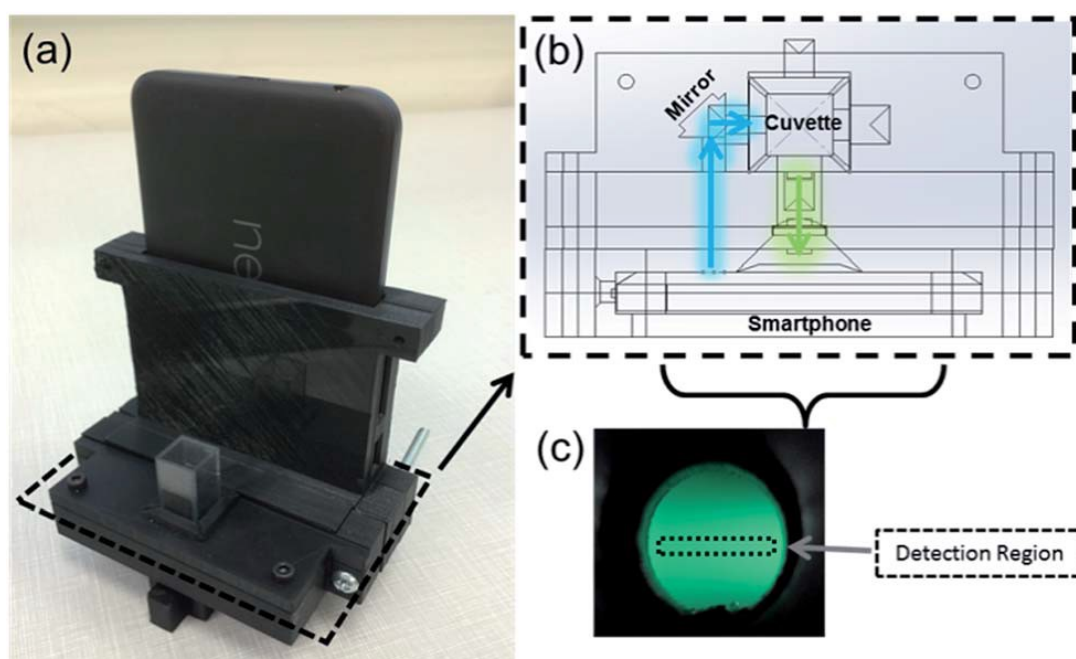


Figure 9. a) Photo of the smartphone sensing platform for cuvette samples; b) Scheme of the internal area of the platform; c) Captured image of the cuvette sample; RGB data are collected in the detection region. From ref. [26].

From the taken images, a detection region of the green channel of RGB image was isolated to the collection of the average intensity. The application of this smartphone-integrated platform showed very promising performances in selectivity and LOD values for the BPA detection in water samples.

Last updates

More recently, a smartphone-based fluorescent lateral flow immunoassay (LFIA) platform was designed by Wang et al. for the highly sensitive detection of Zika virus non-structural protein 1 (ZIKV NS1) in serum, reported in Figure 10.²⁷

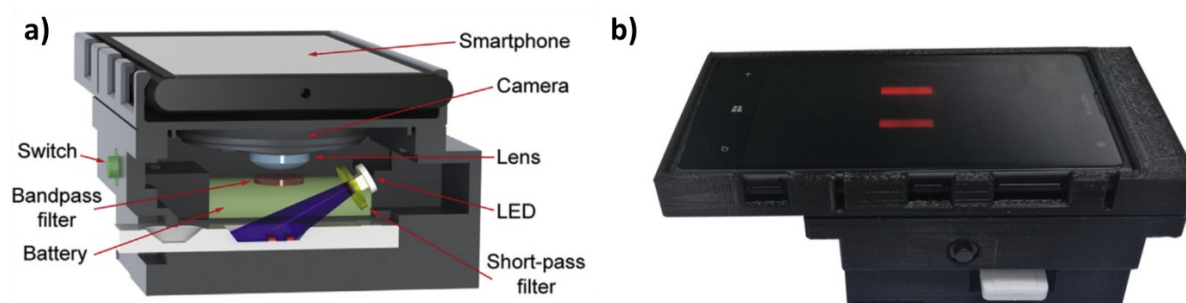


Figure 10. a) 3D scheme of the internal structure of the device; b) Photograph of the developed fluorescent LFIA reader. From ref. [27].

As fluorescent probe, highly fluorescent quantum dot (QD) microspheres were conjugated by ZIKV NS1 detection antibodies. The scheme of the strips and the detection process is reported in Figure 11. Capture ZIKV NS1 antibodies (violet Y-shape), attached to the test line, interact with the target ZIKV NS1 protein (black dot) and formed a sandwich antibody-target-antibody immune complex with the QD-antibody bioconjugates (detection antibody, light blue Y-shape in Fig. 11, left). The formation of this complex immobilizes QD microspheres (red dots) on the test line, with a proportional increase of the fluorescence. The excess QD-antibody bioconjugates is immobilized on the control line by interaction with polyclonal goat anti-mouse IgG antibodies (green Y-shape). A specific software installed on the smartphone processed the image (see Fig. 11, right) in order to determine the concentration of the protein in the tested samples. In this way a fast, high specific, and selective detection of ZIKV NS1 protein could be performed without laboratory equipment, even in complex biological samples with a very good detection limit (LODs in buffer and serum 0.045 and 0.15 ng mL⁻¹, respectively).

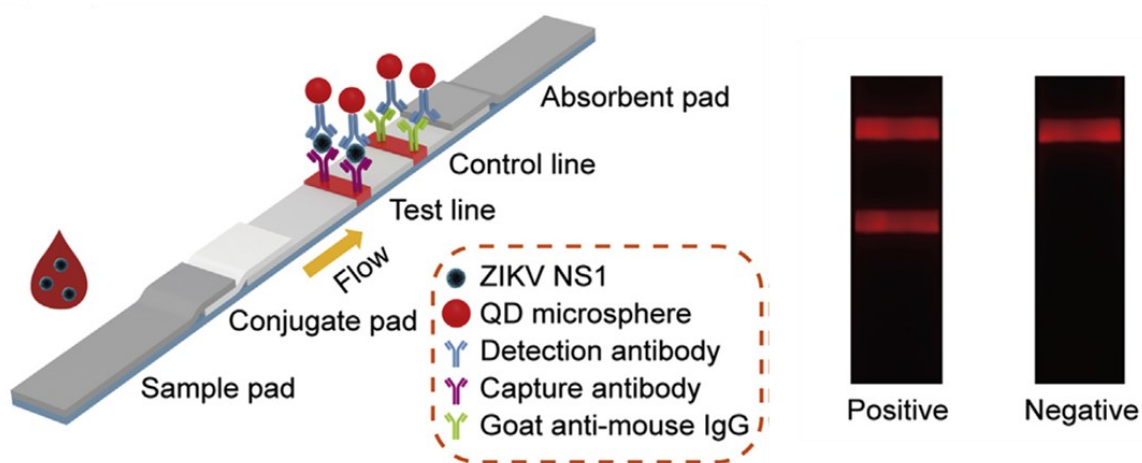


Figure 11. Left: Schematic of the fluorescent LFIA for the detection of ZIKV NS1. **Right:** Images of the test strips in the presence (left) and absence (right) of ZIKV NS1. From ref. [27].

In another recent work, Liu et al. reported a microfluidic paper-based analytical device for the colorimetric detection of dopamine (DA).²⁸ An oxidation-reduction process allowed the formation of a coloured phenanthroline complex, proportional to the amount of dopamine present in the sample. Changes in colour intensity were captured through a smartphone camera: the analysis of the image by Photoshop application yielded a LOD for DA of $0.37 \mu\text{mol L}^{-1}$ with a linear range of $0.527\text{--}4.75 \mu\text{mol L}^{-1}$. Tests on real cow serum and human blood serum and plasma samples confirmed the quantitative detection of DA through this innovative, cheap and easy-to-use method.

Blood is an incredible source of diagnostic information because of the presence of several biomarkers of interest. However, the very complex matrix makes the blood analysis very tedious and problematic: a pre-treatment of the biological sample (*e.g.* centrifugation, separation, filtration, etc.) is often necessary to exclude some potential interferents. Therefore, new smartphone-based sensors are moving from blood to other biological fluids, such as urine, saliva, and sweat: lots of biomarkers can be identified and analysed, the sample collection is easier and non-invasive and few (or none) pre-treatment techniques are required before the analysis.^{29–32} Recently, Choi group designed a fluorometric skin-interfaced microfluidic device that, if combined with a smartphone-based imaging module, allowed the quantitative analysis of several biomarkers in sweat.³³ Besides other smartphone platforms, this is a thin and flexible wearable-device composed by multi-layers stacks, able to follow the curved surfaces of the skin and to sample the sweat naturally released by skin pores (see Fig. 12).

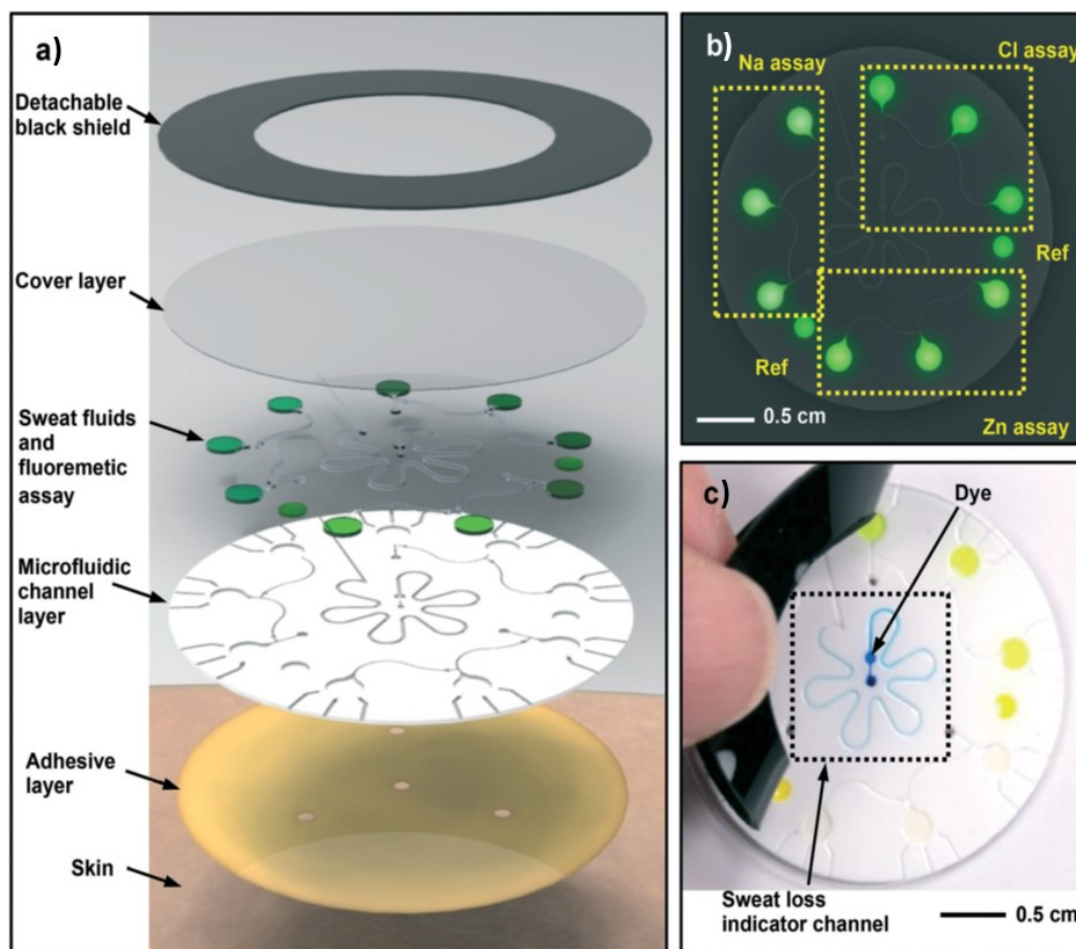


Figure 12. a) Schematic exploded view illustration of the microfluidic platform; b) Image of fluorescence signals associated with chemical probes designed to respond to chloride, sodium, and zinc. c) Image of peeling the detachable black shield away from the microfluidic device. From ref. [33].

A schematic representation of the multi-layered structure of the device is reported in Figure 12a. Fluorescent probes for chloride, sodium and zinc were placed in the microfluidic channels. Sweat flowing through the channels could reach and interact with the probes, giving detectable signals (Fig. 12b). Even the total sweat loss and rate were measured thanks to the flower-shaped microchannel in the center of the device. To prevent photobleaching of the fluorescent assays, a thin ring of black silicone is placed in the surface (see Fig. 12c). Sweat analysis was performed through a very simple process (reported in Fig. 13): after collecting the sweat in the device, the black silicone ring was removed, and photos of the fluorescent assays were captured by using the smartphone with the installed optical module. A dedicated software processed the fluorescent signals of the images of the assays, thus determining the concentration of the target analytes (*i.e.* chloride, sodium, zinc).

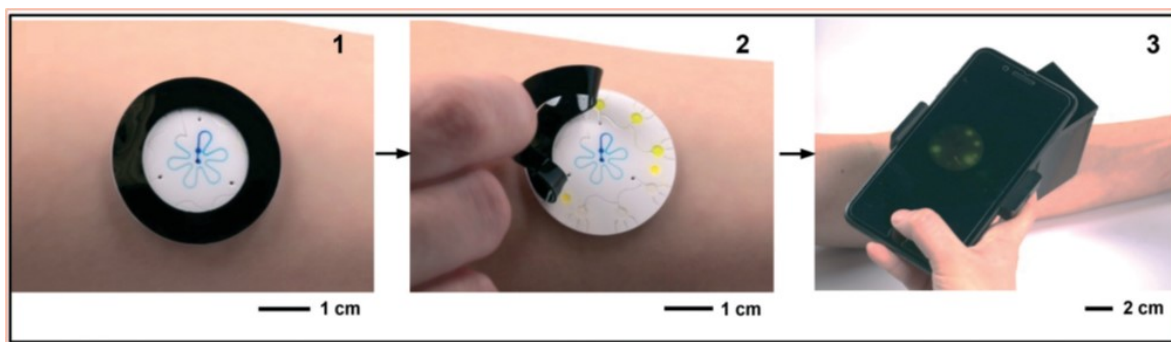


Figure 13. Procedure for performing a fluorometric assay: **1.** collecting sweat using a skin-interfaced microfluidic device; **2.** peeling away the black shield; **3.** capturing a photo of the device using a smartphone interfaced to the device with the optics module. From ref. [33].

Among the most recent published works, the Ozcan group reported a rapid and cost-effective method useful to the tear-fluid analysis.³⁴ Interestingly, tears were collected through wearing commercially available contact lens for few minutes before the analysis. The combination of a specific well-plate reader and a time-lapse imaging of the increasing fluorescent signal with the smartphone camera permitted an easy and fast detection of lysozyme concentration, indicative of several ocular diseases.

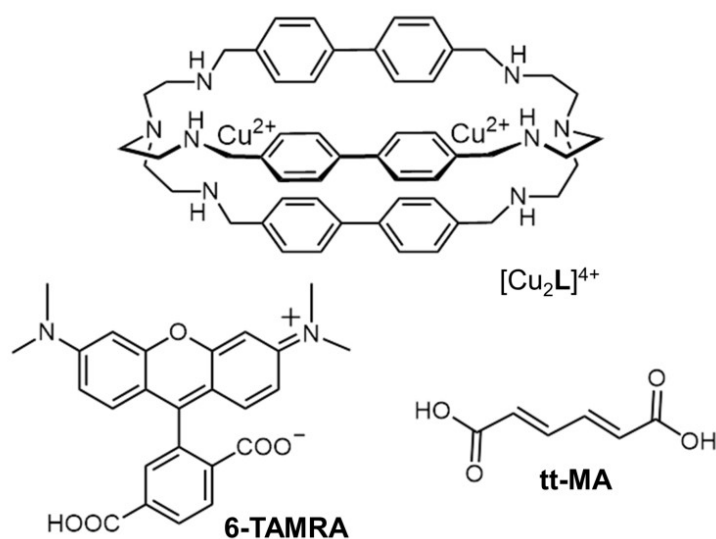
The potentiality of these smart systems is clearly demonstrated by the wide literature on the topic reported during the last years. The range of potential applications is unlimited: by changing the detection method (*e.g.* fluorescence, bio- or chemiluminescence, electrochemistry, etc.) and by modulating the design of ad-hoc smartphone-based platforms, the point-of-care identification and quantification of various analytes of interest in many fields, from environment to health-care, can be successfully achieved.

2.1.3 Our study

In this work, the combination of the high sensitivity of the Indicator Displacement Approach² and the great capabilities of the smartphone sensing allowed us to develop an easy-to-handle device for the detection of the *trans,trans*-muconic acid (*i.e.* tt-MA in the Scheme 1), a urinary benzene biomarker.^{35,36} Depending on the exposure, 2-25% of benzene is converted into tt-MA, detectable in human urines: the wide employ of this carcinogen solvent³⁷ in the chemical industry (*e.g.* for the production of detergents, dyes, drugs, plastics, pesticides and rubbers) requires the constant monitoring of the exposure for higher-risk workers.^{35,36,38,39} Despite some doubt about the specificity of tt-MA for low-level benzene exposure⁴⁰, the quantification of tt-MA results the worldwide applied method to control the benzene exposure level, in according

with both the European Union and the American Conference of Governmental Industrial Hygienists (ACGIH).⁴¹ The determination of this metabolite is generally performed through HPLC-UV or HPLC-MS analysis: the physiological limit of tt-MA, fixed by ACGIH, is 0.5 mg g⁻¹ of creatinine (corresponding to ~ 0.5 mg L⁻¹ in physiological conditions).^{42,43} It has to be noted that an 8-h time exposure to 1 mg L⁻¹ benzene averagely results in the excretion of 2.5 mg L⁻¹ tt-MA (corresponding to 1.8 x 10⁻⁵ M) in urine.^{35,38,44,45}

Azacryptates are known in the literature to bind dicarboxylate anions of appropriate bite length in a selective way.^{46,47} Considering the high affinity for terephthalate and L-glutamate⁴⁸ species in aqueous solution and knowing the similarity between terephthalic acid and tt-MA molecular structures, we decided to employ the dicopper(II) azacryptate [Cu₂L]⁴⁺ as receptor (see Scheme 1) for the recognition of tt-MA. The affinity of this dicopper(II) azacryptate for tt-MA (suggested by computational calculations) was investigated through spectrophoto- and spectrofluorimetric titrations (through the displacement of the indicator 6-carboxytetramethylrhodamine, *i.e.* 6-TAMRA, see Scheme 1). The selectivity of this supramolecular system for the metabolite was tested even in presence of interferents and in more complex media (such as artificial urine). Then, in order to develop a smart portable device, the chemosensing ensemble was absorbed on silica gel using ELISA-like plastic wells as the support. By exposing the microplate to a UV-lamp (366 nm) and recording RGB values with a smartphone, the indicator displacement could be detected, permitting to quantify the concentration of tt-MA. Experiments with real spiked urine (pre-treated) samples were also performed.



Scheme 1. Sketches of the molecular receptor [Cu₂L]⁴⁺, the indicator 6-TAMRA and the guest tt-MA.

2.2 Experimental

2.2.1 Chemicals and methods

All reagents and solvents were purchased from Alfa-Aesar, VWR and Sigma-Aldrich, and used without further purification. Synthesis and characterization of the azacryptand **L** as well as experimental procedures of UV-vis. and fluorimetric titrations are described elsewhere.^{48–50} Titration data were processed with the Hyperquad package to determine the equilibrium constants.⁵¹

For the determination of the spectrophotometric detection limit (LOD), titration experiments were repeated at least three times.⁵² In each titration, volumes of tt-MA standards were added to a freshly prepared solution of the in-situ prepared complex $[\text{Cu}_2\text{L}]^{4+}$ (20 μM in 0.05 M HEPES buffer, pH 7; T =25°C). For the determination of the spectrofluorimetric detection and quantification limits (*i.e.* LOD and LOQ), using indicator displacement assays, titration experiments were repeated at least three times.⁵³ In each titration, volumes of tt-MA standards were added to a freshly prepared solution of the chemo-sensing ensemble (1.5 μM $[\text{Cu}_2\text{L}]^{4+}$, 0.2 μM 6-TAMRA) in 0.05 M HEPES buffer, pH 7; T =25°C. Fluorescence spectra were recorded under nitrogen.

2.2.2 Computational study

All the calculations were carried out using the GAUSSIAN09 program package.⁵⁴ The structures were optimized in the triplet spin state at the UB3LYP/6-31G(d) level for all atoms, except Cu for which the effective core potential LanL2DZ was used. All the optimizations were performed in water as solvent, using the classical polarizable continuum model (PCM). Vibrational frequencies were computed at the same level of theory to define the optimized structures as minima, showing all positive frequencies.

2.2.3 Preparation of artificial urine

Artificial urine was prepared following the method described by Brooks et al.⁵⁵ Components and their concentration are reported in Table 1. The solution of tt-MA, employed in the titration of the chemosensing ensemble (0.05 M HEPES buffer, pH 7), was prepared using artificial urine A), which also contained two possible interferents, *i.e.* citric and lactic acids. The effect

of these components on the emission of the chemosensing ensemble was investigated using the artificial urines B) and C), see Table 1.

Table 1. Composition of artificial urines: sample A) contained both citric and lactic acids, while B) and C) contained either citric or lactic acid, respectively.

Component	Concentration	Type of artificial urine
Citric acid	2 mM	A) and B)
Lactic acid	1.1 mM	A) and C)
Sodium chloride	90 mM	A), B) and C)
Ammonium chloride	25 mM	A), B) and C)
L-glutamine	2 mM	A), B) and C)
Urea	170 mM	A), B) and C)
Uric acid	0.4 mM	A), B) and C)
Creatinine	7 mM	A), B) and C)
Calcium chloride.2H ₂ O	0.25 mM	A), B) and C)
Magnesium sulphate.7H ₂ O	2 mM	A), B) and C)
Sodium sulphate.10H ₂ O	10 mM	A), B) and C)
Sodium bicarbonate	25 mM	A), B) and C)
Sodium nitrate	6 mM	A), B) and C)
Iron(II) sulphate	0.005 mM	A), B) and C)
Potassium dihydrogen phosphate	1.8 mM	A), B) and C)
Di-potassium hydrogen phosphate	1.8 mM	A), B) and C)

2.2.4 Pretreatment of the real urine samples

Before analysis, urine samples were pretreated following the procedure proposed by Bahrami et al., consisting in a micro-extraction by packed sorbent (MEPS).⁵⁶ For the preparation of SAX cartridges, ~20 mg of quaternary ammonium exchange resin (SAX) were packed between two polyethylene frits inside a 1 mL plastic syringe. After sorbent conditioning (3 x 500 µl MeOH followed by 3 x 500 µl water), the urine sample (either blank or spiked with tt-MA) was passed through the sorbent (4 x 500 µl). The sorbent was then washed with water (3 x 500 µl). The

anionic components of urine were eluted with 500 μl of 10% (v/v) acetic acid. The eluate was then taken to dryness and the residue was re-dissolved in 500 μl of 0.05 M HEPES buffer, pH 7. The analyte concentration in the final solution was 4X.

2.3 Results and discussion

The azacryptand **L** was synthesized using a known procedure.⁴⁸ The affinity of the dicopper(II) complex $[\text{Cu}_2\text{L}]^{4+}$ for tt-MA (suggested by DFT calculations) was investigated through spectrophoto- and spectrofluorimetric titrations in buffered solution at pH 7 (0.05 M 4-(2-hydroxyethyl)-1-piperazineethanesulfonic acid, *i.e.* HEPES buffer). In particular, the displacement of the indicator 6-TAMRA from the $[\text{Cu}_2\text{L}]^{4+}$ complex, in presence of the tt-MA, was followed fluorimetrically, permitting the determination of $\text{Log}K_{11}$ binding constant. Analogue experiments with possible interferents (normally found in urine) and in artificial urine were also performed in order to confirm the selectivity. A smart portable device for the detection of tt-MA was then obtained through the absorption of the chemosensing ensemble solution on silica gel using ELISA-like plastic wells as support. After the addition of an increasing amount of the analyte, and exposing the wells to a UV-lamp, the indicator displacement was detected by recording RGB values with a smartphone. Experiments with real spiked (pre-treated) urine samples were also performed.

2.3.1 DFT calculations

DFT calculations in water confirmed the good match between the t,t-muconate anion and the azacryptate cavity, giving interesting insights into the structure of the $[\text{Cu}_2\text{L}(\text{tt-MA})]^{2+}$ inclusion complex. When hosted inside the azacryptate, the dicarboxylate can adopt different conformations characterized by either a s-trans or s-cis arrangement of the central single bond (*i.e.* C3-C4). According to our calculations (see Table 2), the s-trans arrangement is preferred (the optimized structure was named Muconate-**A**). In fact, the s-cis arrangement led to lower stability conformations, called Muconate-**B** and Muconate-**C**.

Table 2. Relative energy and selected geometrical features of the preferred conformers of the $[\text{Cu}_2\text{L}(\text{tt-MA})]^{2+}$ complex.

	E_{rel} (kcal/mol)	copper-copper distance (\AA)	coordinated oxygen atoms distance (\AA)	C2-C3-C4-C5 torsional angle ($^\circ$)
Muconate-A	0.00	10.77	7.05	-177
Muconate-B	2.28	10.72	6.91	-19
Muconate-C	3.05	10.75	6.94	-19

The 3D-plots of the three conformers are shown in Fig. 14. The muconate complex was found to be geometrically very similar to the inclusion complex of the azacryptate with the terephthalate anion.⁴⁹ Both the complexes show only one oxygen atom of each carboxylate group coordinated to copper (*i.e.* $\eta 1$ coordination), while the other one is involved in a H-bonding with the secondary N-H groups of the ligand. Both copper centres exhibit a trigonal bipyramidal geometry, with a distortion towards a square-pyramid: the values of the corresponding index structural parameter τ (0.59 and 0.85) permit to evaluate the extent of the distortion for each metal ion (being $\tau = 0$ and 1 for C_{4v} and D_{3h} coordination polyhedrons, respectively).⁵⁷ The distortion in the coordination geometry around copper, occurring with anion binding, could depend also on a more or less pronounced elongation of one of the Cu-N_{sec} bonds of the azacryptate. The optimized structure of the inclusion complex displays the presence of π - π interactions between the sp^2 carbon atoms of tt-MA and the azacryptand's diphenyl moieties, that positively contribute to the overall stability of the $[\text{Cu}_2\text{L}(\text{tt-MA})]^{2+}$ species.

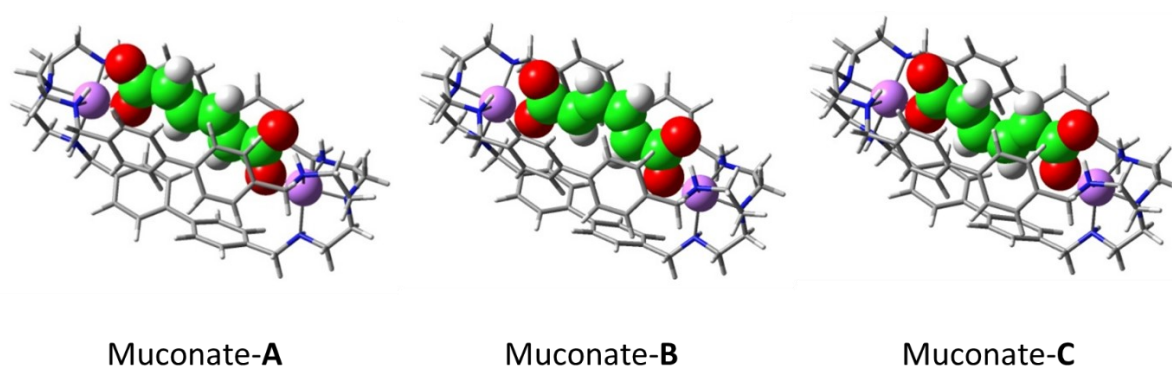


Figure 14. Three-dimensional plots of the preferred conformers of the $[\text{Cu}_2\text{L}(\text{tt-MA})]^{2+}$ complex. Cu(II) ions are represented as pink spheres. Different color codes have been applied for carbon atoms, in order to differentiate receptor and guest carbon skeletons and better visualize the conformation assumed by tt-MA inside the cavity (*e.g.* C of the guest: green; C of the receptor: grey).

2.3.2 Studies in solution

2.3.2.1 UV-vis. studies with tt-MA

Before testing the binding properties of $[\text{Cu}_2\text{L}]^{4+}$ in complex matrix, the affinity of the complex for tt-MA was investigated through UV-vis. titrations in buffered aqueous solution (0.05 M HEPES buffer, pH 7, 25°C). In these conditions, the classic d-d band of the dicopper(II) complex over 800 nm was observed (solid black line in Fig. 15): upon the addition of tt-MA, its intensity gradually decreased until one equivalent of anion, when the plateau was reached.⁴⁹ At the end of the titration, the absorption spectrum displayed two d-d bands centred at 670 and 780 nm. These spectral variations are tied to the change of the coordination geometry around the Cu(II) centres occurring with the binding of tt-MA in the complex cavity.⁴⁶ The titration profile around the equivalence point results very steep (as shown in the inset left in Fig. 15), thus indicating the formation of a very stable complex between $[\text{Cu}_2\text{L}]^{4+}$ and tt-MA. The Job plot confirmed the 1:1 stoichiometry of the adduct (see Fig. 15, inset right). Even working at lower concentration of $[\text{Cu}_2\text{L}]^{4+}$, the steepness of the curvature in the titration profiles was maintained, thus highlighting the strength of the anion:complex interaction (see Fig. 16). In these conditions, the calculation of the binding constant could not be performed.

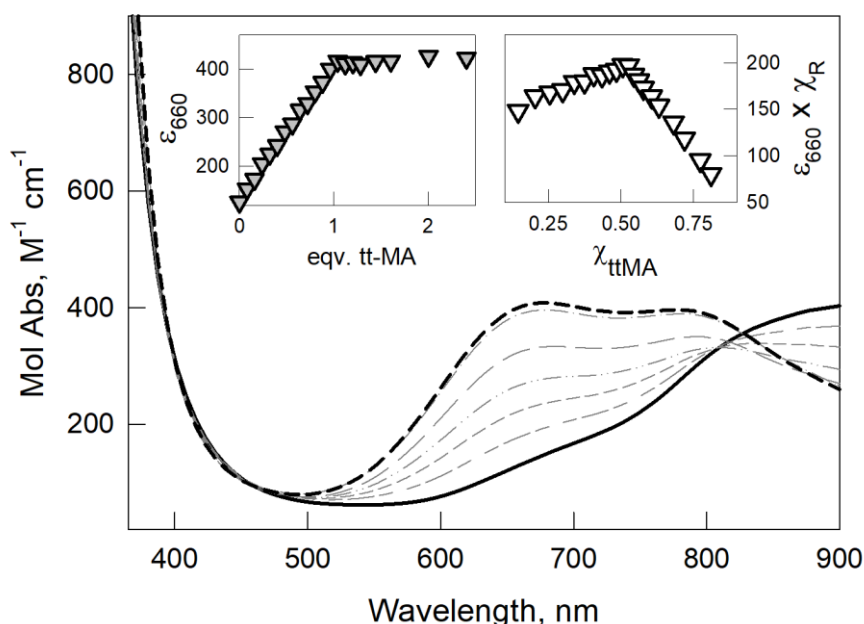


Figure 15. UV-vis. titration of a 20 μM solution of $[\text{Cu}_2\text{L}]^{4+}$ with tt-MA (0.05 M HEPES buffer, pH 7, path length=10 cm); solid black line: initial spectrum; dashed black line: final spectrum. **Inset left:** profile of ϵ (*i.e.* Mol Abs) at 660 nm vs *eqv.* of tt-MA. **Inset right:** Job Plot (χ_{R} and χ_{ttMA} : molar fractions of $[\text{Cu}_2\text{L}]^{4+}$ and tt-MA, respectively).

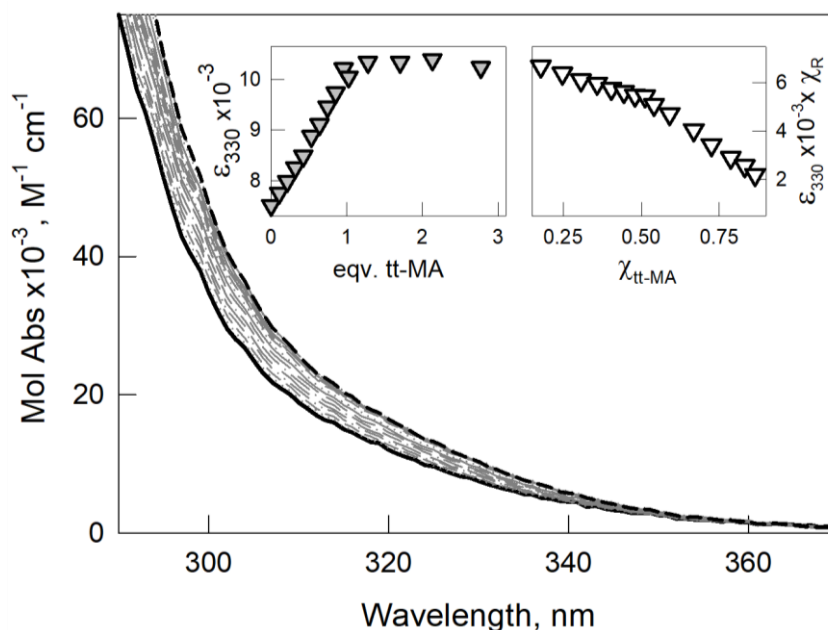


Figure 16. UV-vis. titration of a 8.7 μM solution of $[\text{Cu}_2\text{L}]^{4+}$ with tt-MA (0.05 M HEPES buffer, pH 7; path length = 1cm), family of spectra as Mol Abs $\times 10^{-3}$ vs wavelength; solid black line: initial spectrum; dashed black line: final spectrum. **Inset left:** profile of ϵ (*i.e.* Mol Abs) $\times 10^{-3}$ at 330 nm vs *eqv.* of tt-MA. **Inset right:** Job Plot (χ_R and $\chi_{\text{tt-MA}}$: molar fractions of $[\text{Cu}_2\text{L}]^{4+}$ and tt-MA, respectively).

On the other hand, we could estimate the detection limit by linear regression, through the IUPAC method ($\text{LOD} = 3\sigma/s$; σ = standard deviation of the blank; s = slope of the calibration curve).⁵² Interestingly, the obtained LOD of 8×10^{-7} M (*i.e.* 0.1 mg L^{-1}) permits to detect tt-MA, through UV-vis. spectroscopy, at micromolar concentrations (see the calibration curve in Fig. 17).

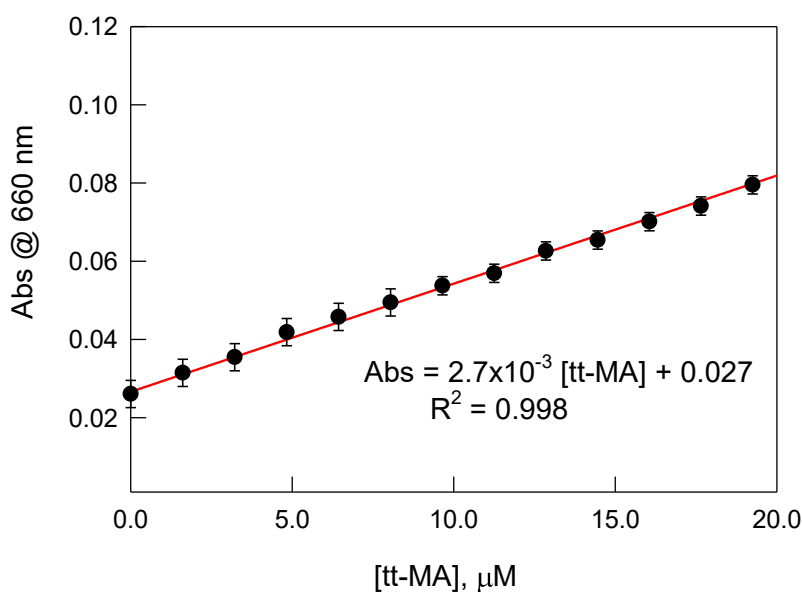


Figure 17. tt-MA calibration curve (red line: fitting curve; dots: experimental data), obtained from the UV-vis. titrations of $[\text{Cu}_2\text{L}]^{4+}$ (20 μM) with tt-MA (HEPES 0.05 M, pH 7, path length=10 cm). The plotted parameters are linearly correlated for Abs values between 0.027 and 0.080 ($R^2 = 0.998$).⁴ Data are averages of $n = 3$; error bars represent s.d.

Other aliphatic dicarboxylates were tested to confirm the selectivity of $[\text{Cu}_2\text{L}]^{4+}$ for tt-MA. With shorter or longer anions, we observed a drop of the affinity because the anion bite does not match the distance between the two copper ions in the receptor cavity. As example, UV-vis. titrations of $[\text{Cu}_2\text{L}]^{4+}$ with succinate and pimelate in buffered aqueous solution (0.05 M HEPES buffer, pH 7, 25°C) are reported in Figures 18 and 19, respectively. Different spectral changes depend on different coordination geometry of the two Cu(II) ions in presence of the anions. Assuming a 1:1 binding equilibrium, we determined the binding constants, that are 3.07(2) and 4.89(2) Log units for succinate and pimelate, respectively. For other tested dicarboxylates (*i.e.* suberic acid, sebacic acid), this calculation was not possible because of the too small spectral variations.

We also performed UV-vis. titrations on solutions of $[\text{Cu}_2\text{L}]^{4+}$ with citric and uric acids, commonly present in urine⁵⁸: even in this case, we confirmed a lower affinity of the cage for these species. In particular, significant changes in the d-d bands we only found under titration with citric acid (see Fig. 20); these changes are attributable to the coordination of the anion to the copper ions. The obtained binding constant, 4.6(1) Log units, is much lower than for tt-MA.

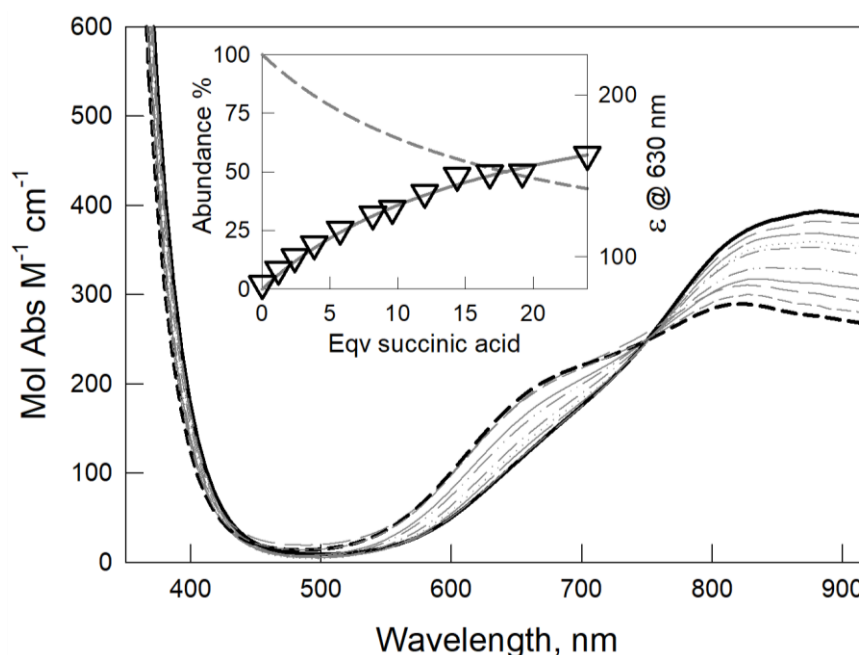


Figure 18. UV-vis. titration of a 50 μM solution of $[\text{Cu}_2\text{L}]^{4+}$ with succinic acid (0.05 M HEPES buffer, pH 7, path length=10 cm); solid black line: initial spectrum; dashed black line: final spectrum **Inset:** titration profile of ϵ (*i.e.* Mol Abs) at 630 nm (empty triangles) with superimposed distribution diagram of the species $[\text{Cu}_2\text{L}]^{4+}$ (dashed line) and $[\text{Cu}_2\text{L}(\text{succinate})]^{2+}$ (solid line) vs *eqv* of the added guest, calculated for $\text{Log}K_{11}=3.07(2)$.

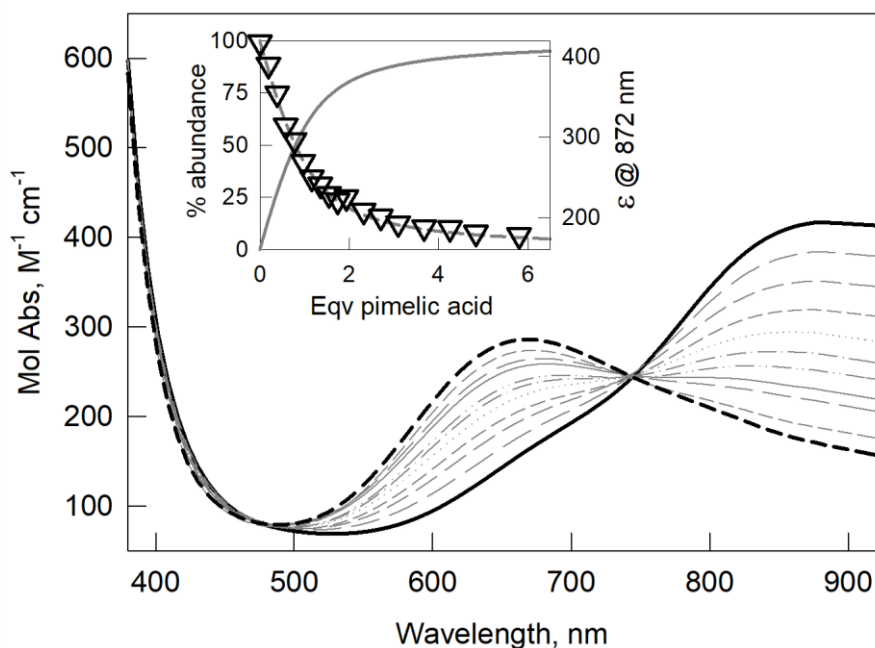


Figure 19. UV-vis. titration of a 75 μM solution of $[\text{Cu}_2\text{L}]^{4+}$ with pimelic acid (0.05 M HEPES buffer, pH 7, path length=10 cm); solid black line: initial spectrum; dashed black line: final spectrum. **Inset:** titration profile of ϵ (*i.e.* Mol Abs) at 872 nm (empty triangles) with superimposed distribution diagram of the species $[\text{Cu}_2\text{L}]^{4+}$ (dashed line) and $[\text{Cu}_2\text{L}(\text{pimelate})]^{2+}$ (solid line) vs *eqv* of the added guest, calculated for $\text{Log}K_{11}=4.89(2)$.

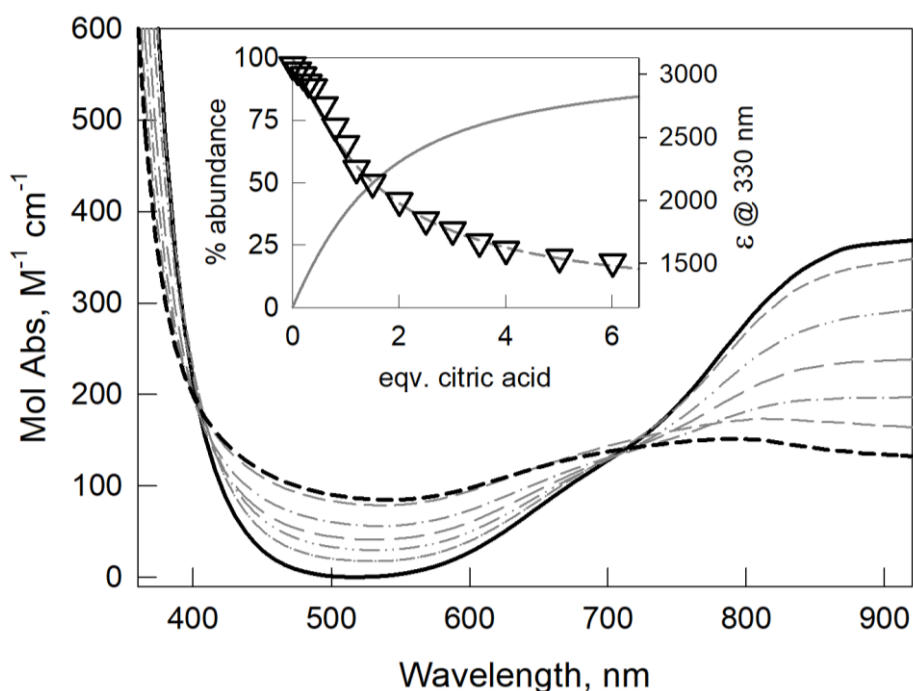


Figure 20. UV-vis. titration of a 20 μM solution of $[\text{Cu}_2\text{L}]^{4+}$ with citric acid (0.05 M HEPES buffer, pH 7, path length=10 cm); solid black line: initial spectrum; dashed black line: final spectrum. **Inset:** titration profile of ϵ (*i.e.* Mol Abs) at 330 nm (empty triangles) with superimposed distribution diagram of the species $[\text{Cu}_2\text{L}]^{4+}$ (dashed line) and $[\text{Cu}_2\text{L}(\text{citrate})]^{2+}$ (solid line) vs *eqv* of the added guest, calculated for $\text{Log}K_{11}=4.6(1)$.

2.3.2.2 Fluorimetric titrations

2.3.2.2.1 The Indicator Displacement Approach

The calculation of the 1:1 binding constant between tt-MA and $[\text{Cu}_2\text{L}]^{4+}$ was performed through fluorimetric titrations, by exploiting the Indicator Displacement Approach. We chose as indicator 6-Carboxytetramethylrhodamine (*i.e.* 6-TAMRA, see Scheme 1), because of its known affinity for the $[\text{Cu}_2\text{L}]^{4+}$ complex at pH 7 in water (0.05 M HEPES buffer): in these conditions, the formation of a stable 1:1 complex occurs, with a binding constant of 7.0(2) Log units (see the titration in Fig. 21).⁴⁸ The terephthalate moiety in the indicator scaffold matches almost perfectly the receptor's binding site, granting a strong coordinative interaction.

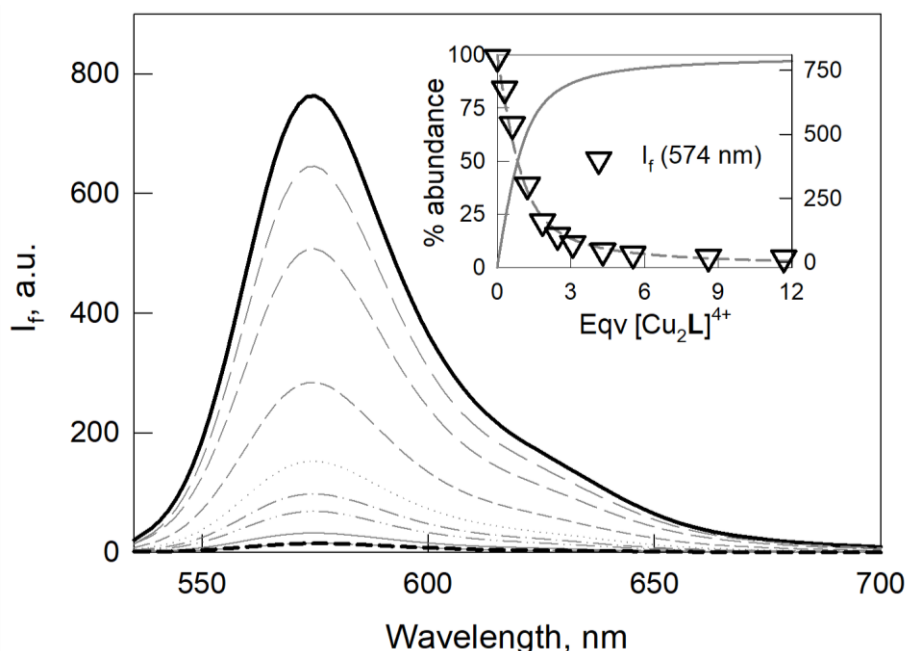


Figure 21. Fluorimetric titration of 6-TAMRA (0.3 μM , $\lambda_{\text{exc}} = 520 \text{ nm}$) with $[\text{Cu}_2\text{L}]^{4+}$ (0.05 M HEPES buffer, pH 7, path length=1 cm); solid black line: initial spectrum; dashed black line: final spectrum. **Inset:** Profile of the fluorescence intensity (I_f) at 574 nm vs *eqv* of $[\text{Cu}_2\text{L}]^{4+}$ (empty triangles), superimposed to the distribution diagram of the species $[\text{Cu}_2\text{L}(6\text{-TAMRA})]^{3+}$ (solid line) and free 6-TAMRA (dashed line), calculated for $\text{Log}K_{11}=7.0(2)$.

When 6-TAMRA is bound to $[\text{Cu}_2\text{L}]^{4+}$, its emission is quenched (see Fig. 21). If another substrate (tt-MA in our case), present in solution, is able to interact strongly with the dicopper(II) complex, the indicator is displaced from the receptor's cavity, thus restoring the fluorescence again. To study this process, we prepared solutions of the chemo-sensing ensemble (0.05 M HEPES buffer, pH 7) by mixing $[\text{Cu}_2\text{L}]^{4+}$ complex and 6-TAMRA, at 2 μM and 0.2 μM concentrations, respectively. This complex:indicator ratio was chosen to ensure the

complete quenching of the indicator's emission (see the solid black line in the family of spectra shown in Fig. 22). The incremental addition of tt-MA caused the development of the typical emission band of 6-TAMRA at 574 nm ($\lambda_{exc} = 520$ nm). The titration profile obtained by plotting the emission intensity (I_f) at 574 nm vs *eqv.* of the added tt-MA is reported in the inset in Figure 22.

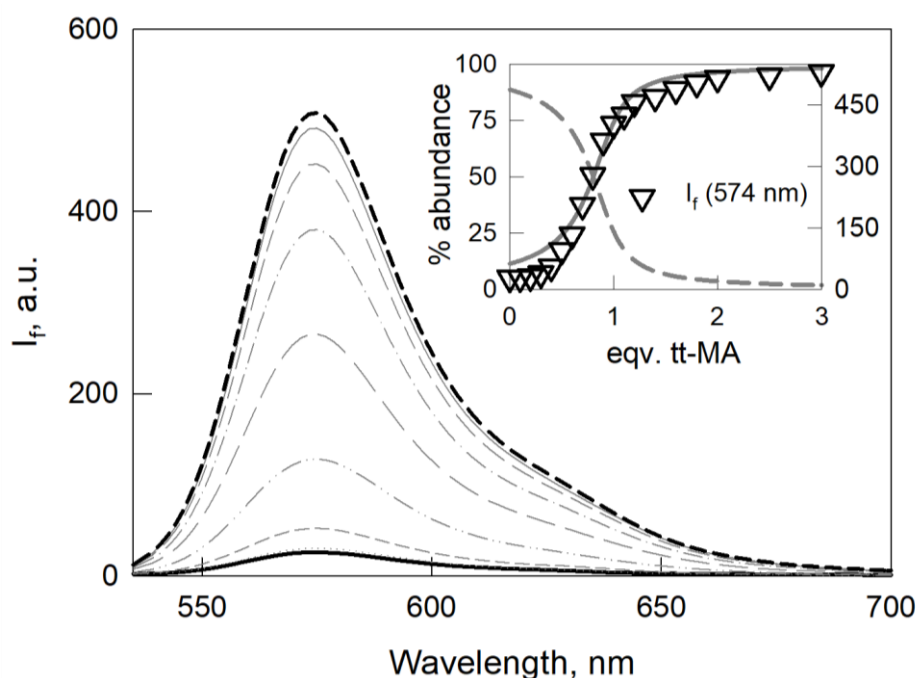
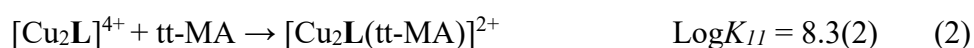


Figure 22. Fluorimetric titration of the chemosensing ensemble solution ($2 \mu\text{M} [\text{Cu}_2\text{L}]^{4+}$ and $0.2 \mu\text{M}$ 6-TAMRA, $\lambda_{exc} = 520$ nm) with tt-MA (0.05 M HEPES buffer, pH 7, path length=1 cm); solid black line: initial spectrum; dashed black line: final spectrum. **Inset:** Profile of the fluorescence intensity (I_f) at 574 nm vs *eqv.* of tt-MA (empty triangles), superimposed to the distribution diagram of the species, calculated for a 1:1 association constant with tt-MA of 8.3(2) log units ($\log K_{11}=7.0$, receptor:6-TAMRA). Solid line: % free 6-TAMRA; dashed line: % $[\text{Cu}_2\text{L}(5\text{-TAMRA})]^{3+}$.

Through the least-squares treatment on the linear section of the fluorimetric titration plot (see Fig. 23)⁵³, we could estimate both LOD ($3\sigma/s$) and LOQ ($10\sigma/s$) parameters for tt-MA, which resulted 7×10^{-8} M (*i.e.* $9.9 \mu\text{g L}^{-1}$) and 2×10^{-7} M (*i.e.* $28 \mu\text{g L}^{-1}$), respectively.

The binding constant between $[\text{Cu}_2\text{L}]^{4+}$ and tt-MA was determined by elaborating the titration data through the Hyperquad package.⁵¹ Considering the two competing equilibria in solution involving the dicopper(II) complex, the indicator and the guest (see equations (1) and (2)), the $\text{Log}K_{11}$ of tt-MA resulted 8.3(2).



The good overlay of the fluorimetric titration profile with the corresponding distribution diagram (% abundance for $[\text{Cu}_2\text{L}(6\text{-TAMRA})]^{3+}$ and free 6-TAMRA, see inset in Fig. 22) confirmed the goodness of this model.

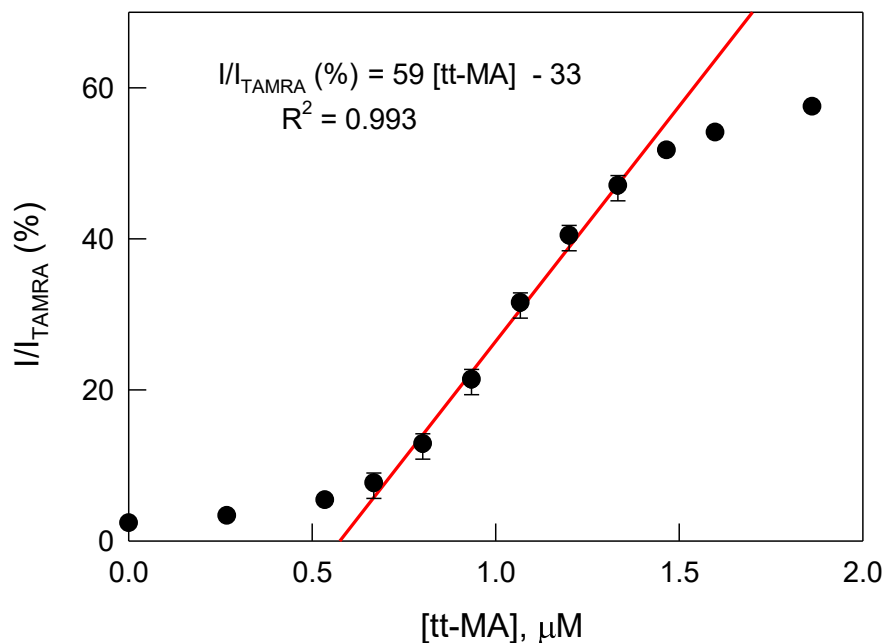


Figure 23. tt-MA calibration curve⁵ (red line: fitting curve; dots: experimental data), obtained from the fluorimetric titrations of the chemosensing ensemble solution (1.5 μM $[\text{Cu}_2\text{L}]^{4+}$ and 0.2 μM 6-TAMRA, $\lambda_{\text{exc}} = 520$ nm) with tt-MA (0.05 M HEPES buffer, pH 7, path length=1 cm). I_{TAMRA} = fluorescence intensity of a 0.2 μM 6-TAMRA solution (recorded before the addition of $[\text{Cu}_2\text{L}]^{4+}$). The plotted parameters are linearly correlated when I/I_{TAMRA} is between ~10% and 50% ($R^2 = 0.993$). Data are averages of $n = 4$; error bars represent s.d..

2.3.2.2.2 Studies with possible interferents and in a more complex medium

In order to evaluate the selectivity of our supramolecular system for tt-MA, fluorimetric titrations in buffered aqueous solution with some possible interferents were performed: in particular citric, lactic and uric acids (see Fig. 24) and dioic acids of either short or long chain (*i.e.* maleic, fumaric, succinic, adipic, sebacic and suberic acids, see Fig. 25) were tested.

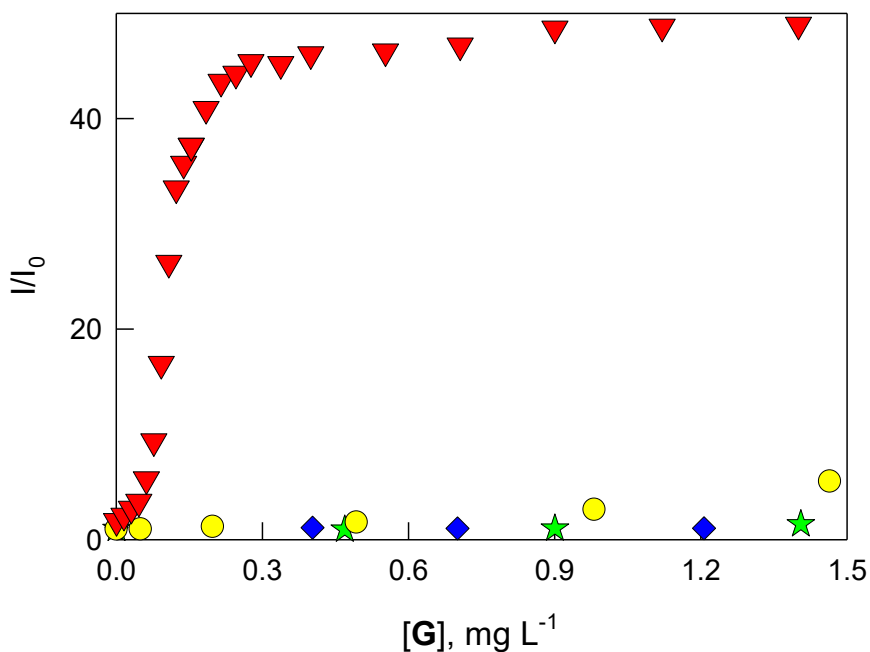


Figure 24. Plots of I/I_0 at 574 nm vs concentration of the added guest $[G]$ in mg L^{-1} ($G = \text{tt-MA}$, red triangles; citric acid, green stars; lactic acid, yellow circles; uric acid, blue diamonds). The experimental data were taken under titrations of the chemosensing ensemble ($1.5 \mu\text{M} [\text{Cu}_2\text{L}]^{4+}$ and $0.2 \mu\text{M}$ 6-TAMRA in HEPES 0.05M, pH 7) with solutions of the guests prepared in the same medium.

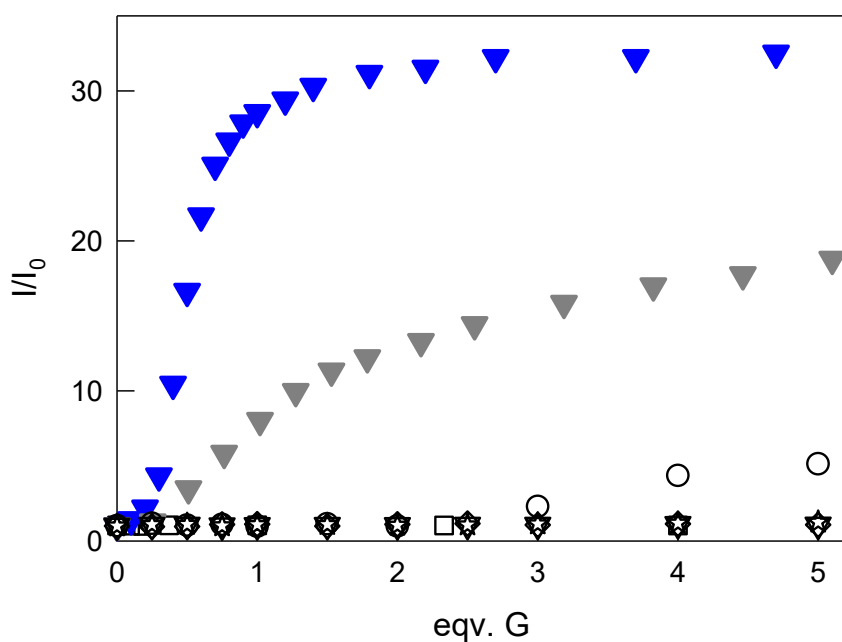


Figure 25. Plots of I/I_0 at 574 nm vs *eqv.* of the added guest (G), obtained under fluorimetric titrations of the chemosensing ensemble solution ($1.5 \mu\text{M} [\text{Cu}_2\text{L}]^{4+}$ and $0.2 \mu\text{M}$ 6-TAMRA in HEPES 0.05 M, pH 7; $\lambda_{\text{exc}} = 520 \text{ nm}$ path length=1 cm) with a series of dioic acids: t,t-MA (blue triangles), adipic acid (grey triangles), maleic acid, fumaric acid, succinic acid, suberic and sebacic acid (white circles, triangles, squares, stars and diamonds, respectively).

Notably, the much lower affinity of these potential competitors for $[\text{Cu}_2\text{L}]^{4+}$ with respect to tt-MA did not induce the displacement of 6-TAMRA from the cage cavity, that could be observed

only under addition of excess substrate ($> 2 \text{ mg L}^{-1}$), except for adipate. For this guest, titration data treatment led to a 1:1 binding constant of 6.9(2) Log units (see Fig. 26), a value similar to that found in the literature.⁴⁸ Although the similarity between adipate and tt-MA, especially in the bite length, the affinity of $[\text{Cu}_2\text{L}]^{4+}$ for these two substrates resulted markedly different, with $\text{Log}K_{11} = 6.9$ and 8.3 for adipic acid and tt-MA, respectively.

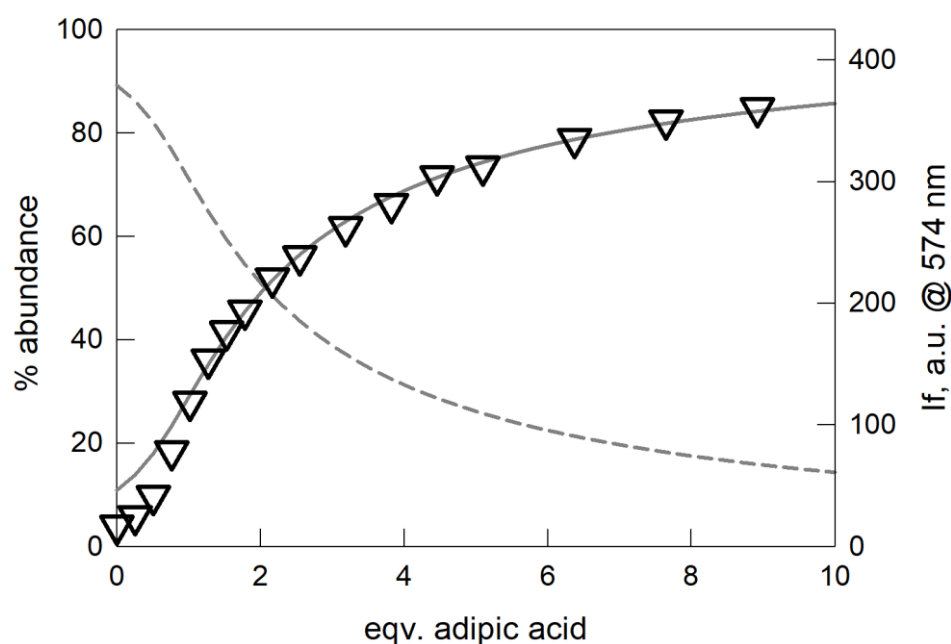


Figure 26. Fluorimetric titration of the chemosensing ensemble solution ($1.5 \mu\text{M} [\text{Cu}_2\text{L}]^{4+}$ and $0.2 \mu\text{M}$ 6-TAMRA, $\lambda_{\text{exc}} = 520 \text{ nm}$) with adipic acid (HEPES 0.05 M, pH 7, path length 1 cm). Profile of the fluorescence intensity at 574 nm vs *eqv* of the adipic acid (empty triangles) with the superimposed distribution diagram of the species $[\text{Cu}_2\text{L}(6\text{-TAMRA})]^{3+}$ (dashed line) and free 6-TAMRA (solid line), calculated for $\text{Log}K_{11}=6.9(2)$ log units.

To study the potentialities of our system in a more complex matrix, preliminary tests were carried out in artificial urines, *i.e.* a medium containing a series of possible interferents (*e.g.* Fe(II) ions, chloride, sulphate, uric acid, lactic acid) at physiological concentrations (see the Experimental section for details).⁵⁵ These experiments involved fluorimetric titrations of the chemosensing ensemble, in 0.05 M HEPES buffer at pH 7, with solutions of tt-MA, citric and lactic acids in artificial urine. The results are reported in Figure 27. Interestingly, the high affinity for tt-MA was not affected by the matrix: in fact, the obtained titration profile, reported as I/I_0 vs tt-MA concentration in mg L^{-1} (white triangles), matches almost perfectly the plot relative to the titration in HEPES medium (grey triangles).

Also in this case, the presence of lactic and citric acids did not give relevant effects (see white circles and stars, respectively, in Fig. 27). Moreover, the experiment in artificial urine pointed out the high sensitivity for tt-MA, even in this complex medium, being the plateau reached around 0.3 mg L^{-1} (*i.e.* $\sim 2 \text{ }\mu\text{M}$).

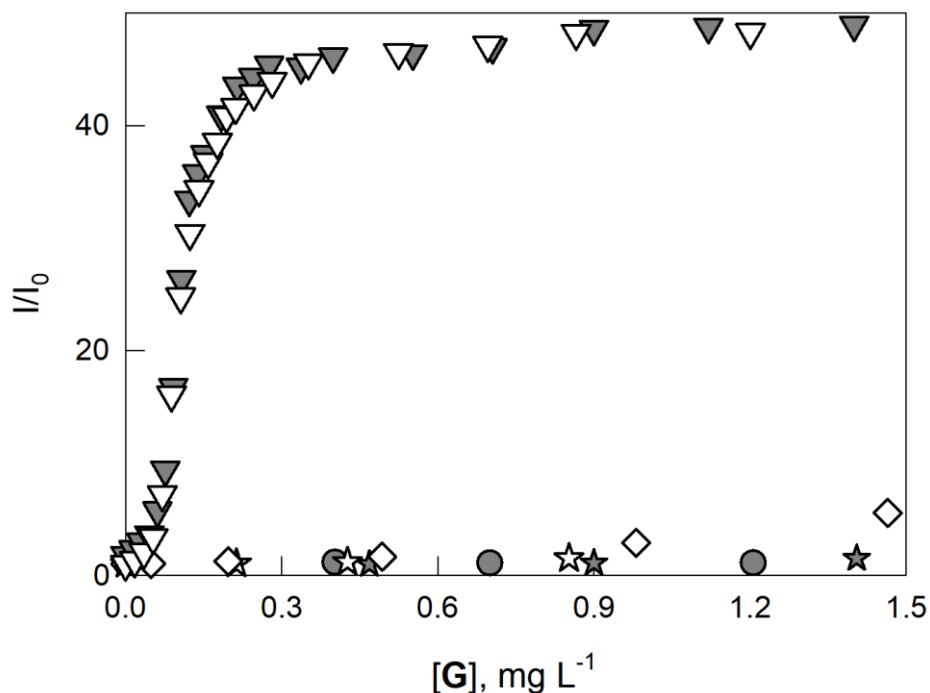


Figure 27. Plots of I/I_0 at 574 nm vs concentration of the added guest $[G]$ in mg L^{-1} ($G = \text{tt-MA}$, triangles; citric acid, stars; lactic acid, circles; uric acid, diamonds). The experimental data were taken under titrations of the chemosensing ensemble ($1.5 \text{ }\mu\text{M}$ $[\text{Cu}_2\text{L}]^{4+}$ and $0.2 \text{ }\mu\text{M}$ 6-TAMRA in HEPES 0.05 M , pH 7) with solutions of the guests prepared in either the same medium (grey symbols) or artificial urine (white symbols).

Finally, we performed the fluorimetric titration of the chemosensing ensemble solution (in HEPES buffer) with artificial urine containing human serum albumin (HSA), a macromolecule that may be present in urine in pathological conditions.⁵⁹ Very interestingly, even if a large excess of HSA was employed for this experiment (*i.e.* 150 ppm), no significant effect was detected (see Fig. 28).

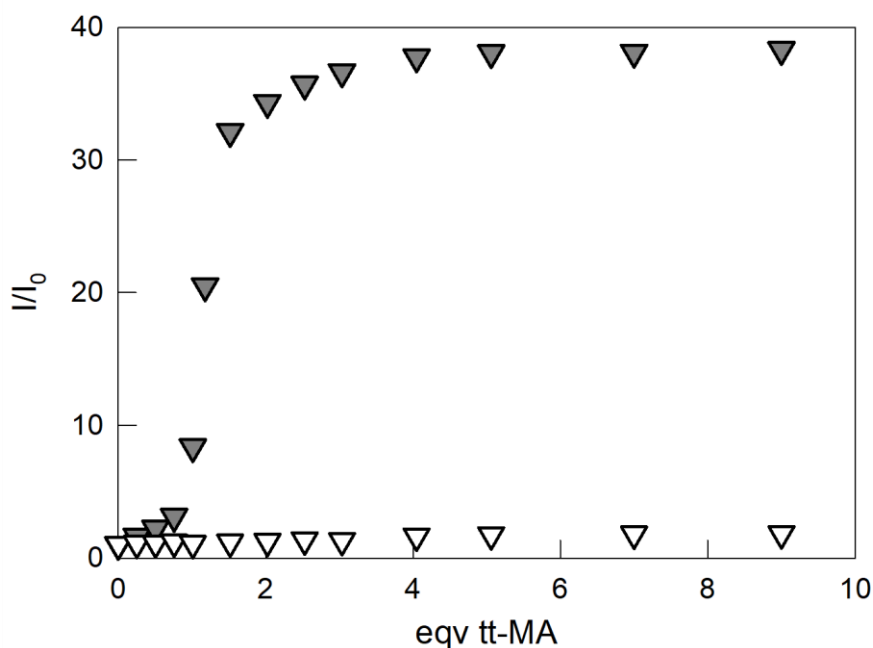


Figure 28. Grey triangles: plot of I/I_0 at 574 nm vs *eqv* of tt-MA obtained under titration of the chemosensing ensemble solution ($1.5 \mu\text{M}$ $[\text{Cu}_2\text{L}]^{4+}$ and $0.2 \mu\text{M}$ 6-TAMRA) in HEPES (0.05M, pH 7) with t,t-MA in artificial urine + 150 ppm HSA. White triangles: profile of I/I_0 at 574 nm for the blank titration (addition of same volumes of artificial urine + 150 ppm HSA, to the chemosensing ensemble solution).

2.3.3 Development of a smart device

2.3.3.1 Construction of the device and calibration experiments

The promising results obtained in solution, through UV-vis. and fluorimetric investigations on the $[\text{Cu}_2\text{L}]^{4+}$ receptor with tt-MA, prompted us to employ the chemosensing ensemble $[\text{Cu}_2\text{L}(6\text{-TAMRA})]^{3+}$ in a new smart device for the detection of urinary tt-MA. Our idea was i) to adsorb the chemosensing ensemble on silica gel (63 μm , silica for chromatography, supported on ELISA-like plastic wells), ii) add the sample containing tt-MA to the wells, iii) expose the wells to a UV-lamp, iv) and monitor the variation of the emission intensity using the camera of a smartphone as detector (see Fig. 29).

For the experiment, 200 μL of a solution containing the chemosensing ensemble (in MeOH/ H_2O 1:1 v/v, 0.05 M HEPES buffer, pH 7) were dropped on the silica gel (~ 100 mg), in order to have 2.3 nmol of $[\text{Cu}_2\text{L}]^{4+}$ and 0.23 nmol of 6-TAMRA in each well. Solutions were taken to dryness in the dark, so as to adsorb the chemosensing ensemble on silica.

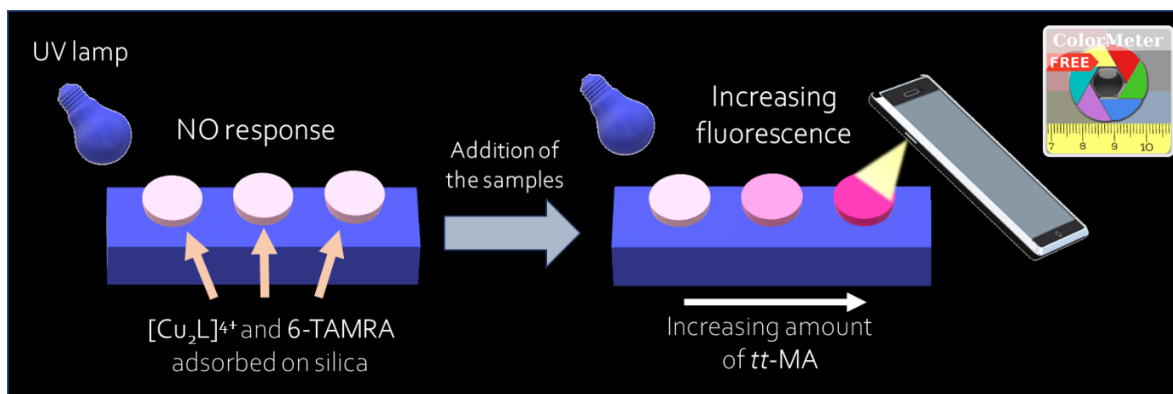


Figure 29. Scheme of the device for the detection of tt-MA.

In absence of the analyte, no emission was observed under exposure of the microplate to a UV-lamp ($\lambda = 366 \text{ nm}$, 16W) in a dark room. On the other hand, under the addition of increasing amounts of standard tt-MA to the wells (solutions prepared in 0.05 M HEPES, pH 7), a significant increase of the indicator emission was visible to the naked-eye (see Fig. 30 and inset Fig. 31). Monitoring and quantification of the fluorescence increase were achieved by recording the RGB values with a smartphone (*i.e.* Samsung S6), provided with the ColorMeter Free App. In particular, by placing the phone camera in front of the microplate (distance = 15 cm), the digital image of each well was taken under UV illumination in a dark room. Notably, only the R index showed a correlation with the increasing red emission of the displaced indicator, and thus with the concentration of tt-MA (see Fig. 31).



Figure 30. Increase of 6-TAMRA emission upon the addition of tt-MA on the adsorbed chemosensing ensemble in wells exposed to a UV lamp.

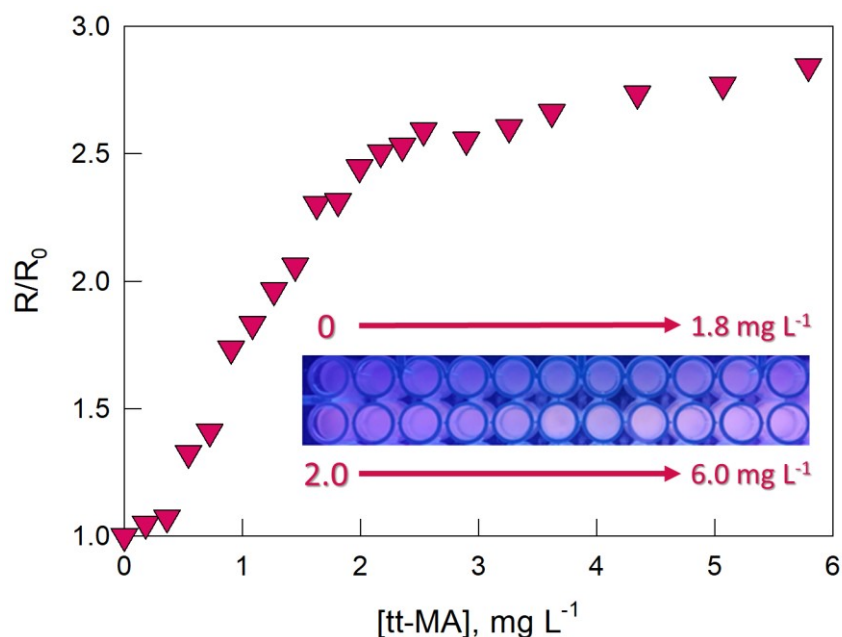


Figure 31. Plot of the normalized R index (R/R_0) vs mg L^{-1} concentration of tt-MA in the wells. **Inset:** picture of the microplate after the addition of tt-MA. The trials were performed in HEPES 0.05M pH 7.

It is important to note that the concentrations of azacryptate and 6-TAMRA into the wells were carefully chosen so as to obtain a clearly readable response of the RGB indexes with the employed cost-effective instrumentation. The addition of standard solutions of tt-MA (in 0.05 M HEPES buffer, pH 7) allowed us to build the calibration curve shown in Figure 32.

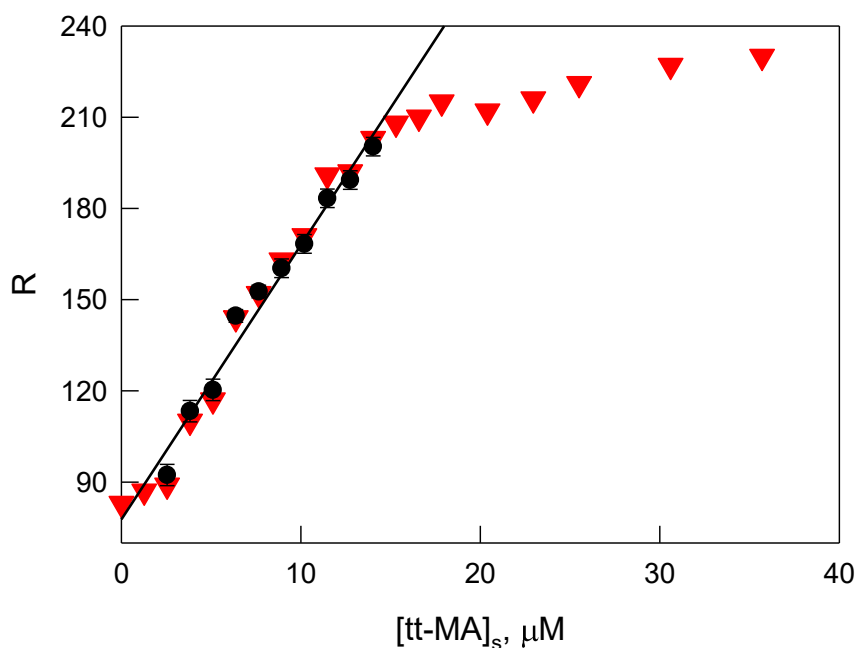


Figure 32. tt-MA calibration curve (black line: fitting curve; dots: R averaged), obtained from the RGB determination in ELISA-type wells. Red symbols correspond to experimental data obtained in one of the trials. Black dots are averages of $n = 3$ repetitions. The plotted parameters are linearly correlated for R averaged values between 90 and 200 ($R^2 = 0.983$); error bars represent s.d..

The experiment was repeated three times, with three repetitions each. Through the treatment of the data in the linear section of the curve, between 0.2 and 2 mg L⁻¹, the LOD and LOQ were determined, obtaining 0.06 and 0.2 mg L⁻¹, respectively. These values are surely higher than those obtained in the fluorimetric studies, because of the lower sensitivity of a smartphone camera compared with a spectrofluorimeter. However, this result pointed out the need to pre-concentrate the samples for the detection of tt-MA in real urines, where the concentration of the metabolite should be lower than 0.5 mg L⁻¹.

2.3.3.2 Test with real urine samples

The test with real samples was performed with urines of non-smokers, spiked with tt-MA (0.18 and 0.36 mg L⁻¹) and pre-concentrated through a known method based on the micro-extraction of urine by packed sorbent in a SAX cartridge (see Fig. 33).⁵⁶ In a plastic syringe, about 20 mg of quaternary ammonium exchange resin (*i.e.* SAX) were placed between two polyethylene frits. Then, the four phases of the process were performed in the order reported in Figure 33 (see MEPS protocol and the Experimental section for details). This fast and simple procedure allowed us to: i) extract and pre-concentrate the anionic components of each urine sample (including tt-MA) by four-times; ii) remove neutral and cationic interferents. The elution with acetic acid (10% v/v) permitted to eluate tt-MA and other anionic species from the SAX cartridge: after to take the eluate to dryness, the residue was re-dissolved in 0.05 M HEPES buffer at pH 7 and dropped into the wells for analysis.

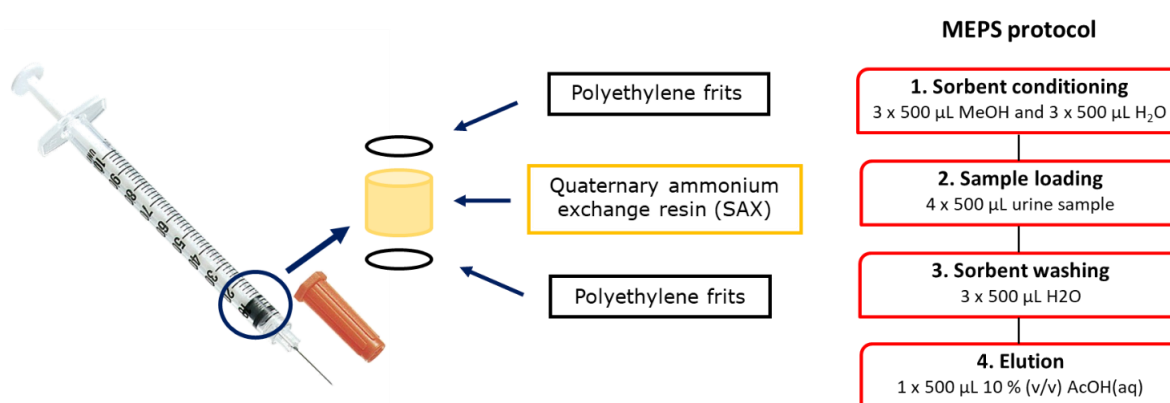


Figure 33. Scheme of the method used for the micro-extraction: preparation of the packed sorbent (left) and the four phases of the process (right).

The recorded RGB values were compared to those obtained with standard tt-MA in 0.05 M HEPES buffer: the % recovery was determined by dividing the averaged R indexes recorded

with the real samples by the indexes determined with standard solutions ($\times 100$). The obtained results are reported in Table 3. At 0.7 and 1.4 mg L⁻¹ concentrations of the pre-concentrated samples, which correspond to 0.18 and 0.36 mg L⁻¹ in real urine, a ~98% recovery of tt-MA was obtained. This test pointed out that, with our device, tt-MA in real urines can be detected at concentrations below the limits fixed by the ACGIH.^{42,43}

Table 3. For each sample [tt-MA]_s (obtained by pre-concentration of the initial urine sample, [tt-MA]₀, on SAX cartridge), the % **recovery** was calculated by dividing the averaged R indexes recorded with real samples, \bar{R} **urine**, by the indexes determined with standard solutions, \bar{R} **standard**, $\times 100$. Experiments were repeated at least three times, with three repetitions each.

[tt-MA] ₀ , M, mg L ⁻¹	[tt-MA] _s , M, mg L ⁻¹	\bar{R} urine	\bar{R} standard	% recovery
1.25×10^{-6} , 0.18	5.01×10^{-6} , 0.71	117.7	120.1	98.0
2.55×10^{-6} , 0.36	1.02×10^{-5} , 1.4	166.7	168.7	98.7

2.4 Conclusions

In this work, the combination of the Indicator Displacement Approach with the smartphone sensing allowed us to develop a smart device for the detection of the trans-trans muconic acid (tt-MA), a urinary metabolite of benzene. The high affinity of tt-MA the dicopper complex [Cu₂L]⁴⁺ was first verified by both spectrophotometric and spectrofluorimetric titrations in buffered aqueous solution at pH 7 (0.05 M HEPES buffer). As for the emission studies, the guest-induced displacement of the 6-TAMRA indicator from the azacryptate's cavity was followed. Titrations with possible competitors (*i.e.* dicarboxylates of different lengths) highlighted the strong selectivity of our system for tt-MA: even the saturated analogue anion (*i.e.* adipate) showed a much lower affinity for the azacryptate compared with tt-MA. The selectivity of [Cu₂L]⁴⁺ for the metabolite of interest was also confirmed in presence of possible interferents (*i.e.* citric, uric and lactic acids, commonly present in urine, and the HSA macromolecule) and in a more complex medium, such as artificial urines.

The development of a smart, cost-effective device for the detection of tt-MA in real urine samples was achieved through the adsorption of the chemosensing ensemble (*i.e.* a solution containing [Cu₂L]⁴⁺ and 6-TAMRA in 100:1 ratio) on silica gel, using plastic wells as support. By exposing the wells on a UV-lamp ($\lambda = 366$ nm, 16 W) in the dark, an increase of the indicator fluorescence in presence of tt-MA was visible even to the naked-eye. By recording the RGB

values with a smartphone, the emission increase could be quantified and correlated to the concentration of the metabolite.

Through this method, the detection of tt-MA in real spiked urine samples (previously pre-treated through a known method) was achieved. Even if the sensibility resulted lower compared to HPLC-UV or HPLC-MS analysis, this supramolecular approach permits to selectively detect tt-MA in urines at concentrations below the limits fixed by the ACGIH, with the minimum use of materials (*e.g.* receptor and indicator) and the possibility for immediate “point-of-care” diagnostics.

The research described in this chapter was published in *New Journal of Chemistry*, 2018, 42, 15460.

References

- [1] Wiskur, S. L.; Ait-Haddou, H.; Lavigne, J. J.; Anslyn, E. V. Teaching Old Indicators New Tricks, *Acc. Chem. Res.*, **2001**, *34* (12), 963–972. DOI:10.1021/ar9600796.
- [2] Nguyen, B. T.; Anslyn, E. V. Indicator–Displacement Assays, *Coord. Chem. Rev.*, **2006**, *10*, 3118–3127. DOI:10.1016/j.ccr.2006.04.009.
- [3] Norouzy, A.; Azizi, Z.; Nau, W. M. Indicator Displacement Assays Inside Live Cells, *Angew. Chem. Int. Ed.*, **2015**, *54* (3), 792–795. DOI:10.1002/anie.201407808.
- [4] Amendola, V.; Bergamaschi, G.; Guglielmo, L.; Izzo, L.; Mangano, C.; Mella, M.; Milanese, C.; Miljkovic, A. Dicopper(II) Mozobil™: A Dinuclear Receptor for the Pyrophosphate Anion in Aqueous Solution, *Supramolecular Chemistry*, **2017**, *29* (11), 834–845. DOI:10.1080/10610278.2017.1373194.
- [5] Liu, X.; Smith, D. G.; Jolliffe, K. A. Are Two Better than One? Comparing Intermolecular and Intramolecular Indicator Displacement Assays in Pyrophosphate Sensors, *Chem. Commun.*, **2016**, *52* (54), 8463–8466. DOI:10.1039/C6CC03680E.
- [6] Liu, X.; Ngo, H. T.; Ge, Z.; Butler, S. J.; Jolliffe, K. A. Tuning Colourimetric Indicator Displacement Assays for Naked-Eye Sensing of Pyrophosphate in Aqueous Media, *Chem. Sci.*, **2013**, *4* (4), 1680–1686. DOI:10.1039/c3sc22233k.
- [7] Ghale, G.; Lanctôt, A. G.; Kreissl, H. T.; Jacob, M. H.; Weingart, H.; Winterhalter, M.; Nau, W. M. Chemosensing Ensembles for Monitoring Biomembrane Transport in Real Time, *Angew. Chem. Int. Ed.*, **2014**, *53* (10), 2762–2765. DOI:10.1002/anie.201309583.
- [8] Zheng, Z.; Geng, W.-C.; Gao, J.; Wang, Y.-Y.; Sun, H.; Guo, D.-S. Ultrasensitive and Specific Fluorescence Detection of a Cancer Biomarker via Nanomolar Binding to a Guanidinium-Modified Calixarene, *Chem. Sci.*, **2018**, *9*, 2087–2091. DOI:10.1039/c7sc04989g.
- [9] Sasaki, Y.; Leclerc, É.; Hamedpour, V.; Kubota, R.; Takizawa, S.; Sakai, Y.; Minami, T. Simplest Chemosensor Array for Phosphorylated Saccharides, *Anal. Chem.*, **2019**, *91* (24), 15570–15576. DOI:10.1021/acs.analchem.9b03578.
- [10] Sierra, A. F.; Hernández-Alonso, D.; Romero, M. A.; González-Delgado, J. A.; Pischel, U.; Ballester, P. Optical Supramolecular Sensing of Creatinine, *J. Am. Chem. Soc.*, **2020**, *142* (9), 4276–4284. DOI:10.1021/jacs.9b12071.
- [11] Yue, Y.; Kong, Y.; Yang, F.; Zheng, Z.; Hu, X.; Guo, D. Supramolecular Tandem Assay for Pyridoxal-5'-phosphate by the Reporter Pair of Guanidinocalix[5]Arene and Fluorescein, *ChemistryOpen*, **2019**, *8* (12), 1437–1440. DOI:10.1002/open.201900316.

- [12] Sheykhi, S.; Mosca, L.; Durgala, J. M.; Anzenbacher, P. An Indicator Displacement Assay Recognizes Enantiomers of Chiral Carboxylates, *Chem. Commun.*, **2019**, 55 (50), 7183–7186. DOI:10.1039/C9CC03352A.
- [13] Yin, X.-M.; Gao, L.-L.; Li, P.; Bu, R.; Sun, W.-J.; Gao, E.-Q. Fluorescence Turn-On Response Amplified by Space Confinement in Metal–Organic Frameworks, *ACS Appl. Mater. Interfaces*, **2019**, 11, 47112–47120. DOI:10.1021/acsami.9b18307.
- [14] Toscani, A.; Marín-Hernández, C.; Robson, J. A.; Chua, E.; Dingwall, P.; White, A. J. P.; Sancenón, F.; de la Torre, C.; Martínez-Mañez, R.; Wilton-Ely, J. D. E. T. Highly Sensitive and Selective Molecular Probes for Chromo-Fluorogenic Sensing of Carbon Monoxide in Air, Aqueous Solution and Cells, *Chem. Eur. J.*, **2019**, 25 (8), 2069–2081. DOI:10.1002/chem.201805244.
- [15] Luppa, P. B.; Müller, C.; Schlichtiger, A.; Schlebusch, H. Point-of-Care Testing (POCT): Current Techniques and Future Perspectives, *Trends in Analytical Chemistry*, **2011**, 30 (6), 887–898. DOI:10.1016/j.trac.2011.01.019.
- [16] Nayak, S.; Blumenfeld, N. R.; Laksanasopin, T.; Sia, S. K. Point-of-Care Diagnostics: Recent Developments in a Connected Age, *Anal. Chem.*, **2017**, 89 (1), 102–123. DOI:10.1021/acs.analchem.6b04630.
- [17] Ozcan, A. Mobile Phones Democratize and Cultivate Next-Generation Imaging, Diagnostics and Measurement Tools, *Lab Chip*, **2014**, 14 (17), 3187–3194. DOI:10.1039/C4LC00010B.
- [18] Wood, C. S.; Thomas, M. R.; Budd, J.; Mashamba-Thompson, T. P.; Herbst, K.; Pillay, D.; Peeling, R. W.; Johnson, A. M.; McKendry, R. A.; Stevens, M. M. Taking Connected Mobile-Health Diagnostics of Infectious Diseases to the Field, *Nature*, **2019**, 566 (7745), 467–474. DOI:10.1038/s41586-019-0956-2.
- [19] Rezazadeh, M.; Seidi, S.; Lid, M.; Pedersen-Bjergaard, S.; Yamini, Y. The Modern Role of Smartphones in Analytical Chemistry, *Trends in Analytical Chemistry*, **2019**, 118, 548–555. DOI:10.1016/j.trac.2019.06.019.
- [20] Calabretta, M. M.; Zangheri, M.; Lopreside, A.; Marchegiani, E.; Montali, L.; Simoni, P.; Roda, A. Precision Medicine, Bioanalytics and Nanomaterials: Toward a New Generation of Personalized Portable Diagnostics, *Analyst*, **2020**, 145 (8), 2841–2853. DOI:10.1039/C9AN02041A.
- [21] Coskun, A. F.; Nagi, R.; Sadeghi, K.; Phillips, S.; Ozcan, A. Albumin Testing in Urine Using a Smart-Phone, *Lab Chip*, **2013**, 13 (21), 4231–4238. DOI:10.1039/c3lc50785h.
- [22] Roda, A.; Michelini, E.; Cevenini, L.; Calabria, D.; Calabretta, M. M.; Simoni, P. Integrating Biochemiluminescence Detection on Smartphones: Mobile Chemistry Platform for Point-of-Need Analysis, *Anal. Chem.*, **2014**, 86 (15), 7299–7304. DOI:10.1021/ac502137s.

- [23] Roda, A.; Guardigli, M.; Calabria, D.; Maria Maddalena Calabretta; Cevenini, L.; Michelini, E. A 3D-Printed Device for a Smartphone-Based Chemiluminescence Biosensor for Lactate in Oral Fluid and Sweat, *Analyst*, **2014**, *139*, 6494–6501. DOI:10.1039/c4an01612b.
- [24] Wei, Q.; Nagi, R.; Sadeghi, K.; Feng, S.; Yan, E.; Ki, S. J.; Caire, R.; Tseng, D.; Ozcan, A. Detection and Spatial Mapping of Mercury Contamination in Water Samples Using a Smartphone, *ACS Nano*, **2014**, *8* (2), 1121–1129. DOI:10.1021/nn406571t.
- [25] Sarwar, M.; Leichner, J.; Naja, G. M.; Li, C.-Z. Smart-Phone, Paper-Based Fluorescent Sensor for Ultra-Low Inorganic Phosphate Detection in Environmental Samples, *Microsyst Nanoeng*, **2019**, *5* (1), 56. DOI:10.1038/s41378-019-0096-8.
- [26] McCracken, K. E.; Tat, T.; Paz, V.; Yoon, J.-Y. Smartphone-Based Fluorescence Detection of Bisphenol A from Water Samples, *RSC Adv.*, **2017**, *7* (15), 9237–9243. DOI:10.1039/C6RA27726H.
- [27] Rong, Z.; Wang, Q.; Sun, N.; Jia, X.; Wang, K.; Xiao, R.; Wang, S. Smartphone-Based Fluorescent Lateral Flow Immunoassay Platform for Highly Sensitive Point-of-Care Detection of Zika Virus Nonstructural Protein 1, *Anal. Chim. Acta*, **2019**, *1055*, 140–147. DOI:10.1016/j.aca.2018.12.043.
- [28] Liu, C.; Gomez, F. A.; Miao, Y.; Cui, P.; Lee, W. A Colorimetric Assay System for Dopamine Using Microfluidic Paper-Based Analytical Devices, *Talanta*, **2019**, *194*, 171–176. DOI:10.1016/j.talanta.2018.10.039.
- [29] Shin, J.; Chakravarty, S.; Choi, W.; Lee, K.; Han, D.; Hwang, H.; Choi, J.; Jung, H.-I. Mobile Diagnostics: Next-Generation Technologies for in Vitro Diagnostics, *Analyst*, **2018**, *143* (7), 1515–1525. DOI:10.1039/C7AN01945A.
- [30] Liu, J.; Geng, Z.; Fan, Z.; Liu, J.; Chen, H. Point-of-Care Testing Based on Smartphone: The Current State-of-the-Art (2017–2018), *Biosens. Bioelectron.*, **2019**, *132*, 17–37. DOI:10.1016/j.bios.2019.01.068.
- [31] Lee, J.-R.; Choi, J.; Shultz, T. O.; Wang, S. X. Small Molecule Detection in Saliva Facilitates Portable Tests of Marijuana Abuse, *Anal. Chem.*, **2016**, *88* (15), 7457–7461. DOI:10.1021/acs.analchem.6b01688.
- [32] Potluri, V.; Kathiresan, P. S.; Kandula, H.; Thirumalaraju, P.; Kanakasabapathy, M. K.; Kota Sai Pavan, S.; Yarravarapu, D.; Soundararajan, A.; Baskar, K.; Gupta, R.; Gudipati, N.; C. Petrozza, J.; Shafiee, H. An Inexpensive Smartphone-Based Device for Point-of-Care Ovulation Testing, *Lab Chip*, **2019**, *19* (1), 59–67. DOI:10.1039/C8LC00792F.
- [33] Sekine, Y.; Kim, S. B.; Zhang, Y.; Bandodkar, A. J.; Xu, S.; Choi, J.; Irie, M.; Ray, T. R.; Kohli, P.; Kozai, N.; Sugita, T.; Wu, Y.; Lee, K.; Lee, K.-T.; Ghaffari, R.; Rogers, J. A. A Fluorometric Skin-Interfaced Microfluidic Device and Smartphone Imaging Module for in Situ

Quantitative Analysis of Sweat Chemistry, *Lab Chip*, **2018**, *18* (15), 2178–2186. DOI:10.1039/C8LC00530C.

[34] Ballard, Z.; Bazargan, S.; Jung, D.; Sathianathan, S.; Clemens, A.; Shir, D.; Al-Hashimi, S.; Ozcan, A. Contact Lens-Based Lysozyme Detection in Tear Using a Mobile Sensor, *Lab Chip*, **2020**, *20* (8), 1493–1502. DOI:10.1039/C9LC01039D.

[35] Fustinoni, S.; Buratti, M.; Campo, L.; Colombi, A.; Consonni, D.; Pesatori, A. C.; Bonzini, M.; Farmer, P.; Garte, S.; Valerio, F.; Merlo, D. F.; Bertazzi, P. A. Urinary t,t-Muconic Acid, S-Phenylmercapturic Acid and Benzene as Biomarkers of Low Benzene Exposure, *Chem. Biol. Interact.*, **2005**, *153–154*, 253–256. DOI:10.1016/j.cbi.2005.03.031.

[36] Scherer, G.; Renner, T.; Meger, M. Analysis and Evaluation of Trans,Trans-Muconic Acid as a Biomarker for Benzene Exposure, *J. Chromatogr. B*, **1998**, *717* (1–2), 179–199. DOI:10.1016/S0378-4347(98)00065-6.

[37] International Agency for Research on Cancer; IARC Working Group on the Evaluation of Carcinogenic Risks to Humans. *Benzene*; 2019.

[38] Gomes, R. de P.; Sanson, A. L.; Lobo, F. A. Method for the Determination of Benzene Metabolite t,t-Muconic Acid in Urine by HPLC-UV with an Ion Exclusion Column, *Separations*, **2016**, *3* (2), 14. DOI:10.3390/separations3020014.

[39] Pruneda-Alvarez, L. G.; Ruíz-Vera, T.; Ochoa-Martínez, A. C.; Pérez-Maldonado, I. N. Urinary Trans-Trans Muconic Acid (Exposure Biomarker to Benzene) and Hippuric Acid (Exposure Biomarker to Toluene) Concentrations in Mexican Women Living in High-Risk Scenarios of Air Pollution, *Arch. Environ. Occup. Health*, **2017**, *72* (6), 351–358. DOI:10.1080/19338244.2016.1272539.

[40] Jalai, A.; Ramezani, Z.; Ebrahim, K. Urinary Trans, Trans-Muconic Acid Is Not a Reliable Biomarker for Low-Level Environmental and Occupational Benzene Exposures, *Saf. Health Work*, **2017**, *8* (2), 220–225. DOI:http://dx.doi.org/10.1016/j.shaw.2016.09.004.

[41] ACGIH. *Threshold Limit Values for Chemical Substances and Physical Agents and Biological Exposures Indices*; 2005.

[42] Hoet, P.; Smedt, E. D.; Ferrari, M.; Imbriani, M.; Maestri, L.; Negri, S.; Wilde, P. D.; Lison, D.; Haufroid, V. Evaluation of Urinary Biomarkers of Exposure to Benzene: Correlation with Blood Benzene and Influence of Confounding Factors, *Int. Arch. Occup. Environ. Health*, **2009**, *82*, 985–995. DOI:10.1007/s00420-008-0381-6.

[43] Protano, C.; Andreoli, R.; Manini, P.; Vitali, M. Urinary Trans, Trans-Muconic Acid and S-Phenylmercapturic Acid Are Indicative of Exposure to Urban Benzene Pollution during Childhood, *Sci. Total Environ.*, **2012**, *435–436*, 115–123. DOI:10.1016/j.scitotenv.2012.07.004.

- [44] De Palma, G.; Manno, M. Metabolic Polymorphisms and Biomarkers of Effect in the Biomonitoring of Occupational Exposure to Low-Levels of Benzene: State of the Art, *Toxicol. Lett.*, **2014**, *231* (2), 194–204. DOI:10.1016/j.toxlet.2014.10.007.
- [45] Ghamari, F.; Bahrami, A.; Yamini, Y.; Shahna, F. G.; Moghimbeigi, A. Development of Hollow-Fiber Liquid-Phase Microextraction Method for Determination of Urinary Trans, Trans-Muconic Acid as a Biomarker of Benzene Exposure, *Anal. Chem. Insights*, **2016**, *11*, 65–71. DOI:10.4137/ACI.S40177.
- [46] Amendola, V.; Bergamaschi, G.; Miljkovic, A. Azacryptands as Molecular Cages for Anions and Metal Ions, *Supramol. Chem.*, **2018**, *30* (4), 236–242. DOI:10.1080/10610278.2017.1339885.
- [47] Alibrandi, G.; Amendola, V.; Bergamaschi, G.; Fabbri, L.; Licchelli, M. *Bistren* Cryptands and Cryptates: Versatile Receptors for Anion Inclusion and Recognition in Water, *Org. Biomol. Chem.*, **2015**, *13* (12), 3510–3524. DOI:10.1039/C4OB02618G.
- [48] Boiocchi, M.; Bonizzoni, M.; Fabbri, L.; Piovani, G.; Taglietti, A. A Dimetallic Cage with a Long Ellipsoidal Cavity for the Fluorescent Detection of Dicarboxylate Anions in Water, *Angew. Chem. Int. Ed.*, **2004**, *43* (29), 3847–3852. DOI:10.1002/anie.200460036.
- [49] Amendola, V.; Miljkovic, A.; Legnani, L.; Toma, L.; Dondi, D.; Lazzaroni, S. Self-Assembly of Pseudorotaxane Structures from a Dicopper(II) Molecular Cage and Dicarboxylate Axles, *Inorg. Chem.*, **2018**, *57* (7), 3540–3547. DOI:10.1021/acs.inorgchem.7b02534.
- [50] Doria, F.; Amendola, V.; Grande, V.; Bergamaschi, G.; Freccero, M. Naphthalene Diimides as Selective Naked-Eye Chemosensor for Copper(II) in Aqueous Solution, *Sens. Actuators B.*, **2015**, *212*, 137–144. DOI:10.1016/j.snb.2015.01.113.
- [51] Gans, P.; Sabatini, A.; Vacca, A. Investigation of Equilibria in Solution. Determination of Equilibrium Constants with the HYPERQUAD Suite of Programs, *Talanta*, **1996**, *43* (10), 1739–1753. DOI:10.1016/0039-9140(96)01958-3.
- [52] Rajmohan, R.; Ahmed, K. B. A.; Sangeetha, S.; Anbazhagan, V.; Vairaprakash, P. C–H Oxidation and Chelation of a Dipyrromethane Mediated Rapid Colorimetric Naked-Eye Cu(II) Chemosensor, *Analyst*, **2017**, *142*, 3346–3351. DOI:10.1039/c7an01052d.
- [53] Saleh, L.; Plieth, C. A Coelenterazine-Based Luminescence Assay to Quantify High-Molecular-Weight Superoxide Anion Scavenger Activities, *Nat. Protoc.*, **2010**, *5* (10), 1635–1641. DOI:10.1038/nprot.2010.121.
- [54] Frisch, M. J.; Trucks, J. W.; Schlegel, H. B.; Scuseria, G. E.; Robb, M. A.; Cheeseman, J. R.; Scalmani, G.; Barone, V.; Mennucci, B.; Petersson, G. A.; Nakatsuji, H.; Caricato, L.; Xie, X.; Hratchian, H. P.; Izmaylov, A. F.; Bloino, J.; Zheng, G.; Sonnenberg, J. L.; Hada, M.; Ehara, M.; Toyota, K.; Fukuda, R.; Hasegawa, J.; Ishida, M.; Nakajima, T.; Honda, Y.; Kitao, O.;

Nakai, H.; Vreven, T.; Montgomery, J. A.; Peralta, J. E.; Ogliaro, F.; Bearpark, M.; Heyd, J. J.; Brothers, E.; Kudin, K. N.; Staroverov, V. N.; Kobayashi, R.; Normand, J.; Raghavachari, K.; Rendell, A.; Burant, J. C.; Iyengar, S. S.; Tomasi, J.; Cossi, M.; Rega, N.; Millam, J. M.; Klene, M.; Knox, J. E.; Cross, J. B.; Bakken, V.; Adamo, C.; Jaramillo, J.; Gomperts, R.; Stratmann, R. E.; Yazyev, O.; Austin, A. J.; Cammi, R.; Pomelli, C.; Ochterski, J. W.; Martin, R. L.; Morokuma, K.; Zakrzewski, V. G.; Voth, G. A.; Salvador, P.; Dannenberg, J. J.; Dapprich, S.; Daniels, A. D.; Farkas, O.; Foresman, J. B.; Ortiz, J. V.; Cioslowski, J.; Fox, D. J. *Gaussian 09*; Gaussian, Inc.: Wallingford CT, USA, 2009.

[55] Brooks, T.; Keevil, C. W. A Simple Artificial Urine for the Growth of Urinary Pathogens, *Let. Appl. Microbiol.*, **1997**, *24* (3), 203–206. DOI:10.1046/j.1472-765X.1997.00378.x.

[56] Soleimani, E.; Bahrami, A.; Afkhami, A.; Shahna, F. G. Rapid Analysis of Trans,Trans-Muconic Acid in Urine Using Microextraction by Packed Sorbent, *Toxicol. Environ. Health Sci.*, **2017**, *9* (5), 317–324. DOI:10.1007/s13530-017-0337-x.

[57] Addison, A. W.; Rao, T. N.; Reedijk, J.; Rijn, J. van; Verschoor, G. C. Synthesis, Structure, and Spectroscopic Properties of Copper(II) Compounds Containing Nitrogen–Sulphur Donor Ligands; the Crystal and Molecular Structure of Aqua[1,7-Bis(N-Methylbenzimidazol-2'-Yl)-2,6-Dithiaheptane]Copper(II) Perchlorate, *J. Chem. Soc., Dalton Trans.*, **1984**, No. 7, 1349–1356. DOI:10.1039/DT9840001349.

[58] Altman, P. L. Physical Properties and Chemical Composition of Urine: Mammals. Part 1: Man. In *Blood and Other Body Fluids*; Dittmer D. L.: Washington, D.C. : Federation of American Societies for Experimental Biology, 1961; pp 363–369.

[59] Kramer, H.; Molitch, M. E. Screening for Kidney Disease in Adults with Diabetes, *Diabetes Care*, **2005**, *28* (7), 1813–1816. DOI:10.2337/diacare.28.7.1813.

3. A fluorimetric supramolecular sensor for the sensing of fumarate in water

3.1 Introduction

3.1.1 Anion recognition

Molecular recognition continues to be a challenge in supramolecular chemistry: according to the kind of the guest of interest, that could be either neutral or positively/negatively charged, an accurate design is needed to create ad-hoc receptors, able to selectively interact with a specific species even in presence of possible competitors. In particular, the receptor must have a series of functional groups in its scaffold to ensure a synergy of interactions with the guest, and the right dimensions and geometry to minimize the conformational changes necessary to the binding (*i.e.* geometrical and interaction complementarity).¹

Over the course of the last fifty years, the development of receptors for anions has proceeded slower than for cations. This is not surprising because anionic targets present a series of intrinsic properties that complicate the design of suitable receptors: these properties comprise the low charge to radius ratio, a wide variety of geometries and the acid-base behaviour. Moreover, if the process occurs in water, the hydration of the anion and the competition of the solvent molecules for the binding have to be overcome.²

Among the receptors applied in anion recognition, the systems reported by Schmidtchen et al. are of particular interest. These systems are represented by macrotricyclic ligands, containing four quaternary ammonium groups linked by aliphatic $-(CH_2)_n-$ chains.³ The tetrahedral arrangement of the positive charges in the cavity allows the inclusion of halides in water, thanks to a maximization of the attractive electrostatic interactions with the anion and the minimization of the repulsion among the ammonium groups. Moreover, by changing the length of the aliphatic chains connecting the ammonium groups, selectivity can be tuned towards a specific halide. After this work, that gave birth to the so called “anion coordination chemistry”, a wide range of receptors for anions was synthesized. Different kinds of interaction (and their possible combinations) were explored to maximize the recognition process: electrostatic (as in the case of Schmidtchen), dipole-anion, hydrogen bonding, π -anion, halogen bonding and metal coordination.⁴⁻⁶ Due to the innumerable works reported in literature, in this section I will focus on H-bonding and coordinative interactions.

H-bonding interactions

Among non-covalent interactions, the directional hydrogen bonding interaction brought about the design of specific molecular receptors for the binding of anions with well-defined geometries, *e.g.* trigonal (nitrate), tetrahedral (phosphate), and Y-shaped (carboxylates). The most applied H-bond donors undoubtedly are N-H groups, belonging to protonated amines, amides, urea/thiourea moieties, pyrrole, indole, carbazole and benzimidazole groups. These moieties have been extensively used in the synthesis of both neutral and protonated receptors.

Regarding receptors containing amide groups as H-donors, Pascal et al. first reported a tris-amide cryptand able to selectively bind fluoride through multiple H-bonding interactions, as demonstrated by ^{19}F - and ^1H -NMR studies.⁷ Over the course of the years, many scientists investigated how the functionalization of amide-based anion receptors could modulate the interaction strength and selectivity for anions. For instance, the structural modification of the polyamide **1**, first reported by Anslyn et al. as nitrate-selective receptor⁸, promoted the modulation of the receptor anion binding properties (see Figure 1). Through the insertion of pyrroles (as H-bonding donors) and imine groups (as H-bonding acceptors), the macro-bicycle **2** showed high affinities for tetrahedral anionic species - such as H_2PO_4^- , HSO_4^- , SO_4^{2-} , and $\text{HP}_2\text{O}_7^{3-}$ - and also for spherical anions (*e.g.* halides).⁹ On the other hand, Swager and colleagues recently reported the macrocyclic polyamide cage **3** containing 1,4-dithiin moieties. This system, displaying unique electrochemical properties, selectively recognises the HCO_3^- anion and can discriminate arsenate in presence of phosphate.¹⁰

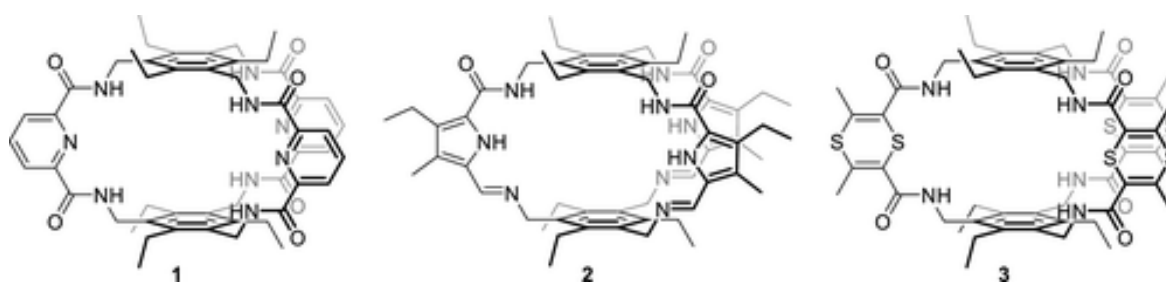


Figure 1: Similar polyamide cages **1**⁸, **2**⁹ and **3**¹⁰, with structural modification, present different binding properties. From ref. [10].

Urea/thiourea-based ligands have been widely applied in anion recognition. These bidentate H-donor groups can strongly bind both spherical and geometrically more complicated anions, through the formation of very stable six/eight-membered chelate rings. This peculiar property could be further increased in oligoureas, *i.e.* poly(thio)urea systems with multiple interaction

sites. Notably, the presence of electron-withdrawing groups (*i.e.* -CF₃, -NO₂) in the receptor scaffold increases the acidity of the -NH protons, thus enhancing the H-bonding tendencies towards anions.^{11,12} For instance, bis(thio)urea ligand **4-6** (reported in Fig. 2) were investigated as anion receptors by Wu al colleagues.¹³

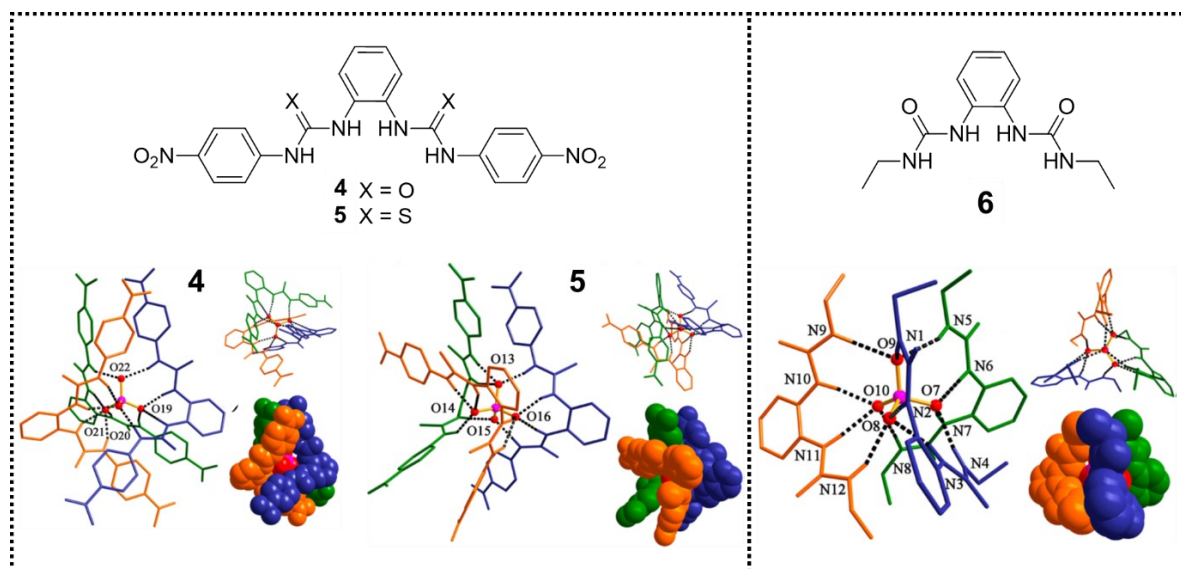


Figure 2. Crystal structures of the phosphate complexes $[\text{PO}_4(\mathbf{4-6})_3]^{3-}$, for each: side view (left), top view (right up), and space-filling representation (right down). Nonacidic hydrogen atoms and counteranions were omitted for clarity. From ref. [13].

X-ray diffraction studies revealed the formation of tris-chelates with phosphate, according to the formula $[\text{PO}_4(\text{L})_3]^{3-}$, for all the ligands: the anion is coordinated by three (thio)urea groups, through the formation of twelve H-bonds. However, studies in solution showed the formation of a 3:1 ligand:anion adduct only for **4** with phosphate, while receptors **5** and **6** either undergo deprotonation or form a 1:1 adduct with the same anion.

A very promising alternative to urea – as H-bonding donor group – is represented by the squaramide unit. As demonstrated by Amendola et al., receptors containing this subunit form higher stable complexes with halides and oxoanions, if compared to the analogue urea-based derivatives.¹⁴ In contrast with urea, the geometrical arrangement of the squaramide-based ligand allows the instauration of two additional H-bonds (through the C_α-H fragments of phenyl substituents) with the anion, thus enhancing the binding properties of the receptor. In Figure 3, the comparison between the $[\text{LH}-\text{Cl}]^-$ complexes of squaramide- (**a**) and urea-based¹⁵ (**b**) receptors is reported.

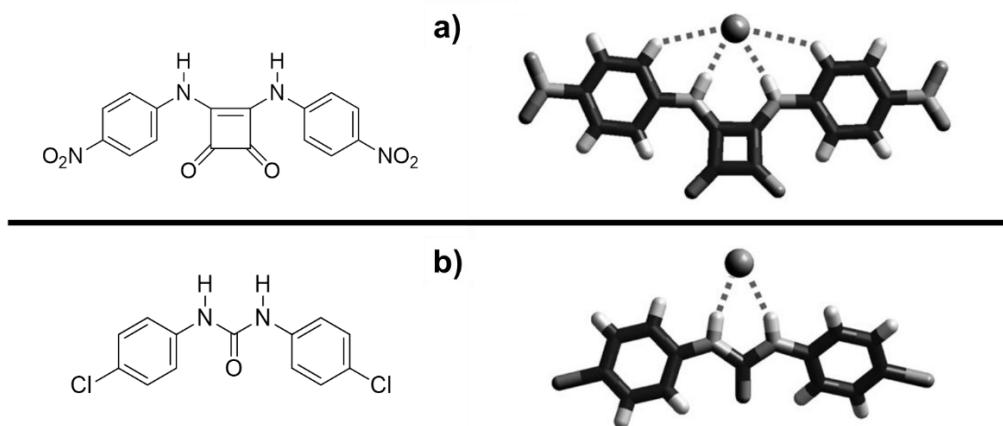


Figure 3. Structures of the $[\text{LH}-\text{Cl}]^-$ complexes with **a)** squaramide¹⁴ and **b)** urea¹⁵-based receptors. H-bonding interactions are highlighted with dashed lines. From ref. [14].

During the last years, very interesting imidazolium/benzimidazolium-based receptors were also published. For example, the bowl-shaped tripodal receptor $7(\text{PF}_6)_3$ (see Fig. 4) strongly binds halides trapping them within its cavity.¹⁶ As shown by crystal structures of the inclusion complexes with chloride (reported in Fig. 4) and bromide, anion inclusion is obtained through the cooperative H-bonding interactions of both imidazolium units and the tetrafluorobenzyl substituents, that act as more efficient H-donors compared to the simple benzyl groups (as demonstrated through ¹H-NMR titrations).

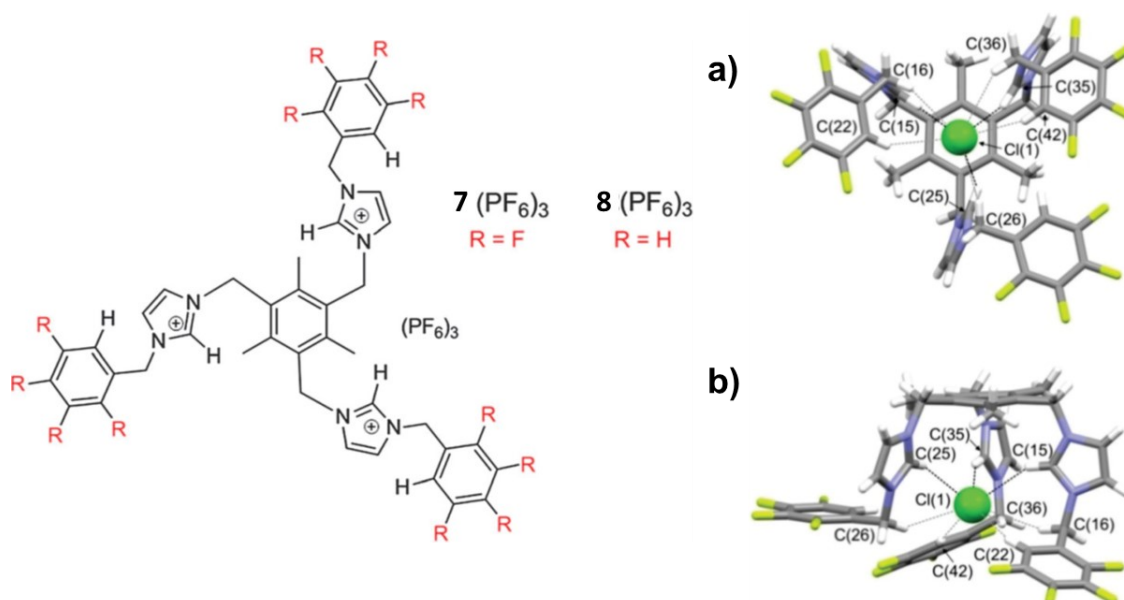


Figure 4. Left: molecular structures of the studied tripodal receptors. **Right:** Crystal structure of $[\text{7}(\text{Cl})](\text{PF}_6)_2 \cdot \text{CH}_3\text{CN}$. **a)** Top and **b)** lateral views of the molecular cation 7^{3+} interacting with chloride (PF_6^- counterions and CH_3CN have been omitted for clarity). Hydrogen bonds are drawn with black dashed lines. From ref. [16].

Last, but not least, polyamines represent a very important class of receptors for anion recognition. If protonated, amino-containing systems could bind anions through both hydrogen bonds and electrostatic interactions: this synergy enhances the binding properties of the ligand and the affinity towards the guest of interest.

Among polyamino receptors, cage-like macrobicycles (*e.g.* the so-called *bistren* cages) have been widely employed in anion recognition.^{1,17} These molecular systems actually show better binding properties, if compared with the analogue acyclic and macrocyclic compounds, thanks to the well-defined shape and higher degree of structural preorganization. The synthetic procedure is generally based on the Schiff condensation, by reaction of the *tren* polyamine (*i.e.* tris(2-aminoethyl)amine) with the chosen dialdehyde. The formation of imine bonds is reversible and allows a trial-and-error process, until the most thermodynamic stable structure is formed. The Schiff condensation is followed by reduction of the imine bonds with NaBH₄, leading to a more stable amine derivative. It has to be noticed that a simple modification of the structure (*i.e.* by changing the reagents involved in the Schiff condensation) permits to tune the cage cavity (*e.g.* size, shape, functional groups) and enhances the selectivity of the system towards specific anions.^{18–20}

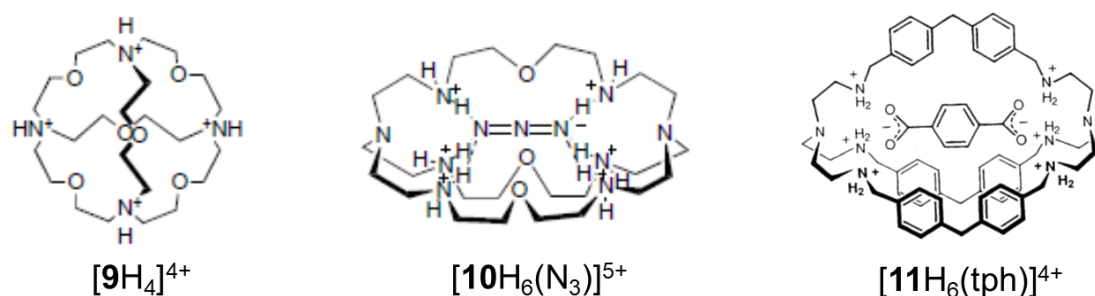


Figure 5. Three different *bistren* cages reported by Lehn and colleagues. From ref.s [22], [23] and [24], respectively.

The spherical cage **9** (in Fig. 5), reported by Lehn and Graf, was tested for halide binding, showing a selectivity for chloride in aqueous solution.^{21,22} On the other hand, the ellipsoidal protonated cryptand **10** (see Fig. 5) selectively binds linear anions that show geometrical complementarity with the cavity, such as azide N₃⁻.^{17,23} Notably, Lehn reported the first example of dicarboxylates recognition by a *bistren* cage. Through ¹H-NMR titrations, the authors demonstrated the remarkable ability of the ammonium azacryptand **11** to include linear dianions in its elongated cavity, with specific affinity preferences based on the distance between the respective binding sites of the guest and the receptor. In fact, as showed by crystal structure analysis, terephthalate anion (tph in the Figure) possesses the right geometrical features to give

a perfect complementarity with the cavity, thus revealing the highest association constant for the cryptand **11** (see Fig. 5).²⁴

More recently, the hexaprotonated cryptand **12** was demonstrated to selectively recognize and trap the radioactive pertechnetate anion ($^{99}\text{TcO}_4^-$) in water at pH 2.²⁵ Some years later, the same authors reported a fluorescent chemo-sensor for $^{99}\text{TcO}_4^-$ (**12b**), obtained by replacing one of the p-xylyl spacers of **12** with a 9,10-anthracenyl unit.²⁶ This structural modification allowed to i) preserve the selectivity of the hexaprotonated ligand for pertechnetate and ii) produce a fluorescent signal of the binding. The hexaprotonated cage **12b** actually displays the typical emission band of anthracene, centred at 425 nm; this emission is switched off by $^{99}\text{TcO}_4^-$, when the anion is trapped into the receptor cavity and forms a stable 1:1 inclusion complex (see Fig. 6).

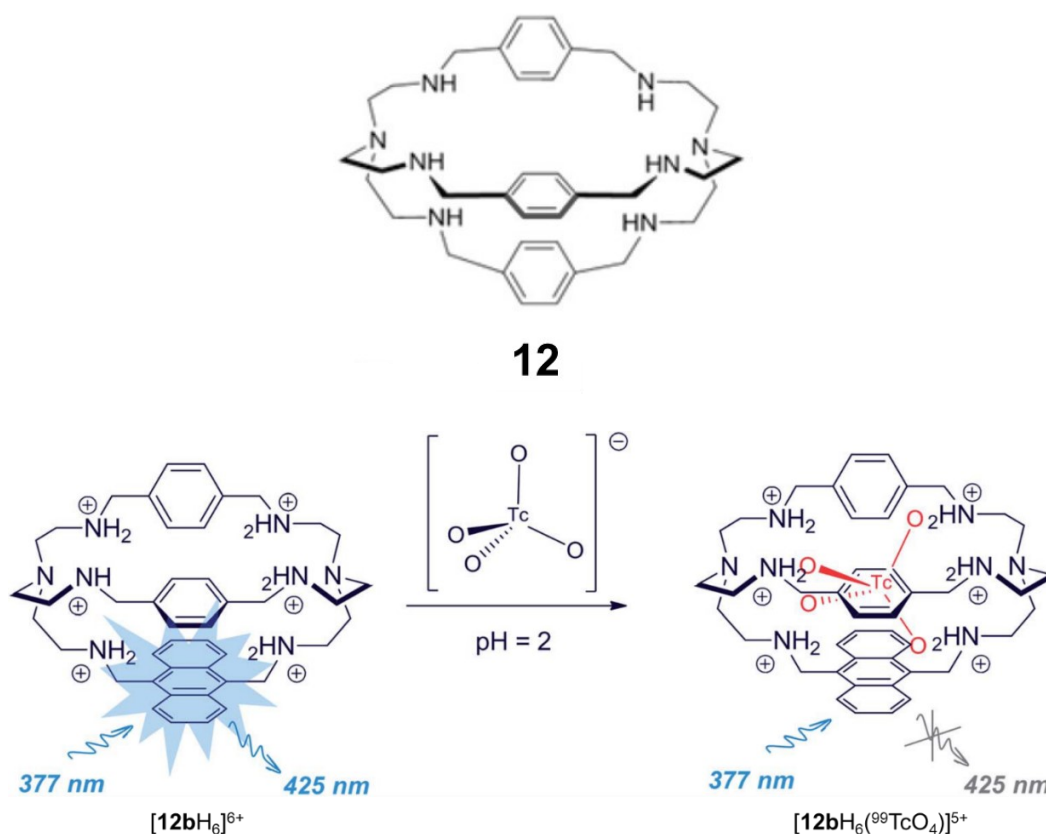


Figure 6. *Bistren* cage **12** and the mono-anthracenyl derivative **12b** in a scheme showing the binding of pertechnetate and the consequent fluorescent signal. From ref. [26].

Over the course of the last thirty years, several cage-like systems have been reported in the literature. Although their promising features, polyammonium cryptands can be generally applied as anion receptors in a restricted pH range. This of course represents an important limit

for applications, since most anions are pH-sensitive, and their protonation degree should be considered for a proper receptor design.

Coordinative interactions

The issue can be overcome by inclusion of transition metal ions in the receptor cavity. Coordinative interactions have been actually investigated by several authors, demonstrating that the metal complexes could be applied as anion receptors in neutral aqueous solution. Considering that the detection of anions of interest, from the biological to the environmental fields, is performed in neutral water, this approach could open unlimited possibilities for the anion recognition.

In the case of the *bistren* cages, each *tren* subunit can coordinate a metal ion – for instance Cu(II) – in a trigonal bipyramidal arrangement. The free apical positions on the metal ions are available for anion coordination. In this way a *bistren* cryptand, coordinating two Cu(II) ions in its cavity, can bridge a dianion through the so-called “cascade process”. This approach ensures a high selectivity, because the anion inclusion is obtained when an almost perfect match is reached between the “anion bite” (*i.e.* the distance between the donor atoms of the anion) and the separation between the free apical positions on the metal ions within the cavity.^{19,20,27,28}

To cite some examples, the dicopper(II) complex of the *bistren* cryptand **13** (see Fig. 7) showed a high affinity towards halides, with a remarkable selectivity for chloride. Besides coordinative interactions with metal ions, anions are also stabilized in the cavity by the hydrogen bonds established with the furanyl spacers.²⁹ Moreover, the presence of these heterocycles on the cryptand scaffold causes the development of a bright yellow colour in solution, corresponding to an intense charge transfer (CT) band in the UV-vis. spectrum at 412 nm, when chloride bridges the Cu(II) ions within the cavity. Very interestingly, the progressive replacement of furanyl spacers with p-xylyl groups (receptors **14-16** in Fig. 7) induces a general lost affinity for halides, with changes in the selectivity order, and the disappearance of the CT band in the visible spectrum.³⁰

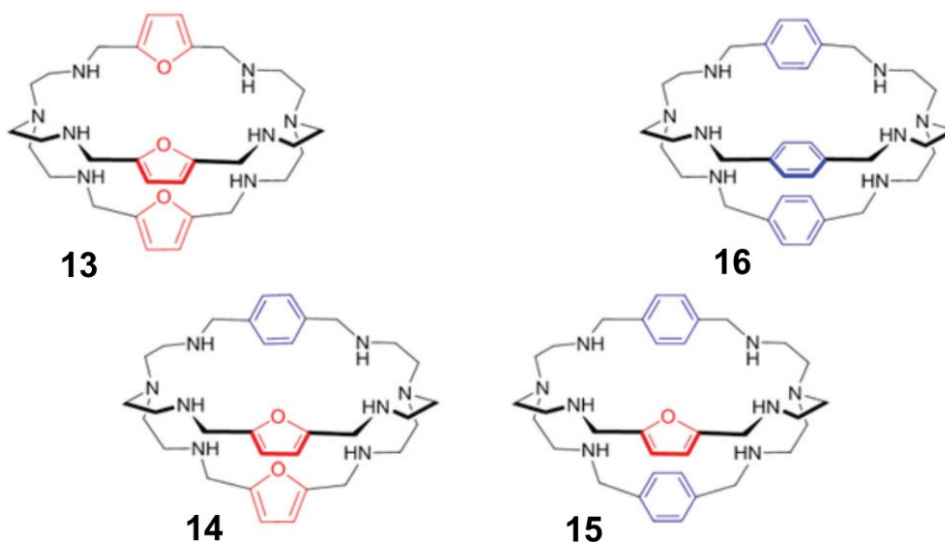


Figure 7. *Bistren* cages with different combination of furanyl and p-xylyl spacers. From ref. [30].

The *bistren* cryptand **17** with flexible biphenylmethane spacers, investigated by Delgado and colleagues, is reported in Figure 8.³¹ UV-vis. titrations in H₂O/MeOH 50:50 v/v on the dicopper(II) complex with dicarboxylates of different lengths revealed a peak of selectivity for adipate and terephthalate (*i.e.* dianions with four carbon atoms between the carboxylate groups), with remarkable binding constants of 10.01 and 9.79 Log units, respectively. A minor affinity is observed with shorter or longer anions, even if all determined Log*K* values resulted very high, in a range between 8.5 and 7.3 Log units. This probably depends on the flexibility of the cryptand, able to adapt its cavity and to ensure a strong affinity for anions with different lengths.

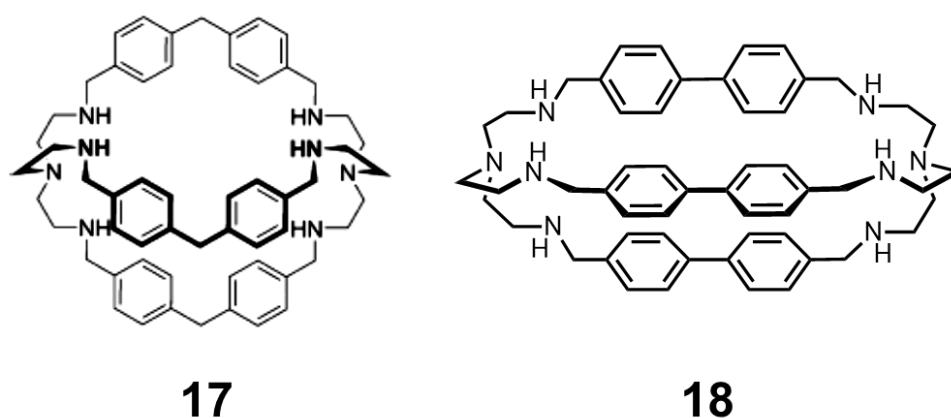


Figure 8. *Bistren* cages: **17** reported by Delgado et al. (from ref. [31]); **18** reported by Fabbrizzi et al. (from ref. [32]).

An example that clearly highlights the potentialities of *bistren* cages is illustrated by the cryptand **18** (see Fig. 8). First reported by Fabbrizzi et al., the dicopper complex [Cu₂(**18**)⁴⁺

showed a high selectivity for the terephthalate anion among the benzenedicarboxylate isomers in neutral water.³² In this work, the binding properties of the cryptate were investigated through the Indicator Displacement Approach (IDA).^{33,34} For this purpose, the fluorescent indicator 6-TAMRA (*i.e.* 6-carboxytetramethylrhodamine) was chosen by the authors because its terephthalate moiety matches almost perfectly the Cu(II)-Cu(II) distance within the cavity. The proximity with the metal centers favours quenching processes, thus turning off the indicator emission when the complex:indicator adduct is formed. The association constant of $[\text{Cu}_2(\mathbf{18})]^{4+}$ with 6-TAMRA resulted 7.0 Log unit. Studies with dicarboxylates clearly revealed the high selectivity of this system: in fact, only the anions that strongly interacts with the cryptate (with binding constants higher than the value calculated for 6-TAMRA) can significantly displace the indicator from the cavity. Notably, among aromatic dicarboxylates, fluorescence was completely restored only upon addition of terephthalate, with a $\text{Log}K > 8$; for the structural isomers, phthalate and isophthalate, a minimum increase of 6-TAMRA emission was observed, and much lower binding constants were determined ($\text{Log}K < 5$). Regarding aliphatic anions, adipate and glutarate showed the highest affinity, even if with lower binding constants compared to terephthalate ($\text{Log}K = 7$ for both anions).

Very recently, Amendola and co-workers employed the high affinity of the dicopper cryptate $[\text{Cu}_2(\mathbf{18})]^{4+}$ for terephthalate in the self-assembly of a pseudo-rotaxane structure³⁵. In particular, functionalized terephthalate derivatives (see Fig. 9), obtained by inserting alkyl or polyoxoethylene chains of different length on both sides of the benzene ring, showed a good affinity for the dicopper complex, with the formation of 1:1 receptor:anion inclusion complexes in aqueous solution (binding constants values between 5.18 and 4.98 Log units).

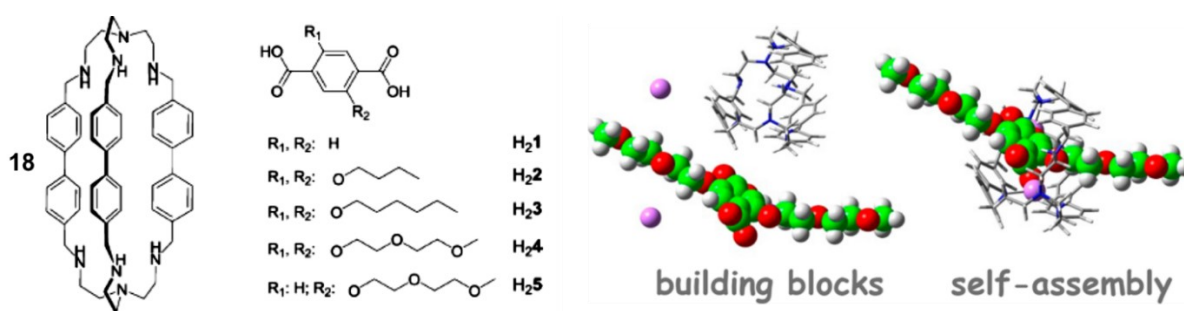


Figure 9. Left: *Bistren* cage **18**, the functionalized terephthalate derivatives **1-6** tested in this work. Right: three dimensional plots representing the self-assembly of $[\text{Cu}_2(\mathbf{18})\text{D}\mathbf{4}]^{2+}$ complex in a pseudo-rotaxane structure. Building blocks: Cu(II), purple spheres; **18** cage: sticks (C: grey; H: white; N: blue); $\mathbf{4}^{2-}$ anion: balls (C: green; H: white; O:red). From ref. [35].

This result demonstrates that the geometrical complementarity between terephthalate fragment and the dicopper cryptate $[\text{Cu}_2(\mathbf{18})]^{4+}$ ensures a strong interaction and the spontaneous self-assembly of the pseudo-rotaxane structure in aqueous solution, even in presence of long-chain substituents on the anion scaffold. As confirmation of this result, computational calculations showed the threading of the molecular axles through the cryptate cavity, with the two carboxylate groups of the terephthalate coordinated to the Cu(II) ions. A slight strain of the axle, induced by the inner chain of the thread, was observed. A three-dimensional plot of the supramolecular assembly $[\text{Cu}_2(\mathbf{18})\supset\mathbf{4}]^{2+}$ is reported in Figure 9.

In another research (see Chapter 2), the $[\text{Cu}_2(\mathbf{18})]^{4+}$ complex was employed as selective receptor for the detection of trans,trans-muconic acid (tt-MA), a benzene metabolite in urine.³⁶

3.1.2 Our study

Over many years, the development of new innovative molecular systems for the selective recognition of carboxylates continues to be an extremely important research topic because of the central role of these substrates in industrial, environmental, and biological fields. For instance, polycarboxylates are key intermediates in the Krebs cycle and their dysregulation could cause metabolic disorders and neurological diseases; moreover, aspartate and glutamate play a critical role in central nervous system as regulators of the synaptic impulse.³⁷ Furthermore, polycarboxylic species such as tartrate, adipate or citrate are used as food additives in alimentary industry and aromatic carboxylate species (*e.g.* trimesates and phthalates) are widely employed in the industry of plastics.³⁸ These few examples undoubtedly give an idea of the need of more and more efficient receptors for the selective recognition of this class of substrates.

As already described in this section, polyamino molecular receptors were widely applied in anion recognition. Macrobicyclic receptors, in particular, showed peculiar selectivity properties compared to macrocycle derivatives: the preorganization and the well-defined three-dimensional cavity impose more rigid parameters to satisfy in the interaction with the guest, thus enhancing the selectivity of the recognition process.

Bistren azacryptands gave very interesting results when applied for the recognition of bidentate anions, especially dicarboxylates. Among these molecular systems, the binding preferences of the dizinc(II) complex of the cryptand **L1** (see Fig. 10) was investigated by Lu and co-workers some years ago.³⁹ The authors demonstrated the successful discrimination of fumarate anion

(fum^{2-}) in presence of its geometrical isomer, maleate (male^{2-}) in aqueous solution at physiological pH. The binding constants, determined through fluorimetric titrations, resulted to be 4.6 and 3.4 Log units for fum^{2-} and male^{2-} , respectively. Crystal structure analysis on the adducts of the dicopper(II) complex $[\text{Cu}_2(\text{L1})]^{4+}$ with fum^{2-} and succinate (suc^{2-}) showed that the good match between the bite length of the two anions and the Cu(II)-Cu(II) distance favours the inclusion of the anions within the cavity, with the cage in a cradle-like arrangement. Moreover, π - π interactions between the double bond of fum^{2-} and the naphthyl spacers of the ligand contribute to the stabilization of the adduct. Although these interesting results, no further studies on the binding properties of the dicopper(II) complex in aqueous solution were performed.

In this work, the affinity of the $[\text{Cu}_2(\text{L1})]^{4+}$ complex towards a series of polycarboxylate anions (reported in Fig. 10) was deeply investigated through UV-vis. and fluorimetric titrations in neutral water (*i.e.* HEPES 0.05 M, pH 7). Notably, the Indicator Displacement Approach (IDA), well known in the literature, was applied for the sensing of fum^{2-} , reaching very low detection limits. For this study, the fluorescent indicator 5-carboxyfluorescein (*i.e.* 5-FAM) was employed (see Fig. 10).

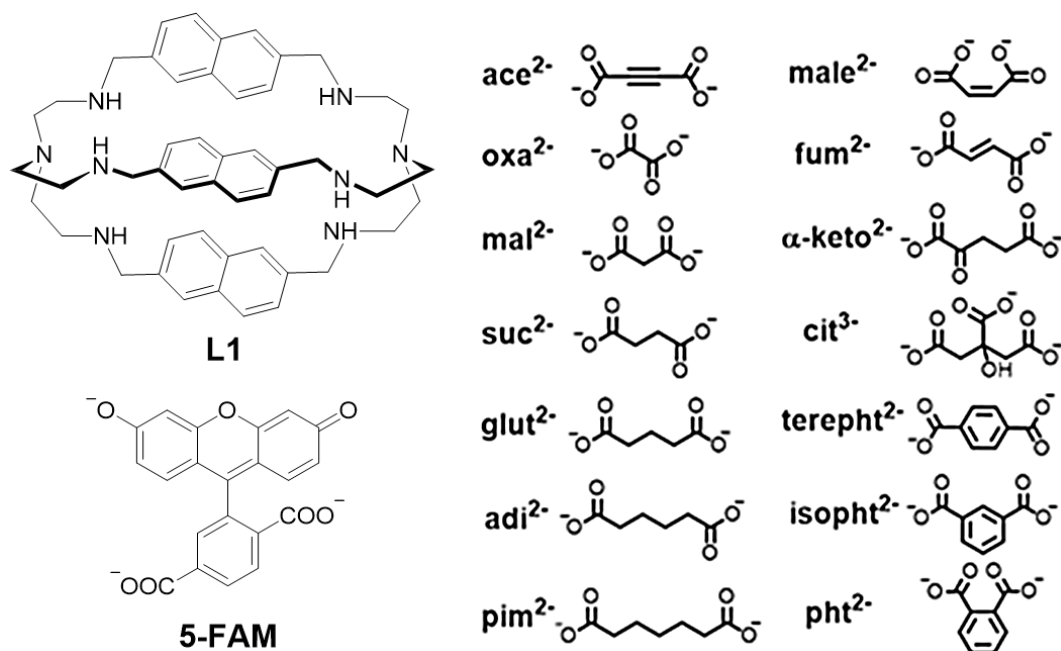


Figure 10. Sketches of the azacryptand L1, the fluorescent indicator 5-FAM and the anions involved in this work.

3.2 Experimental

3.2.1 Chemicals and methods

All reagents for syntheses were purchased from Sigma-Aldrich and used without further purification. All reactions were performed under dinitrogen. UV-vis. spectra were collected using a Varian Cary 50 SCAN spectrophotometer, with quartz cuvettes of the appropriate path length (1 or 10 cm) at $25.0 \pm 0.1^\circ\text{C}$. Emission spectra were collected using a Perkin Elmer LS50B fluorimeter, with a quartz cuvette of 1 cm path length. Cryptand **L1** was prepared following a known procedure.³⁹

3.2.2 Potentiometric and pH-spectrophotometric titrations

Protonation constants of ligand **L1** were determined in water/methanol (30% v/v) mixture, 0.05 M in NaNO_3 . In a typical experiment, a solution of **L1** (15 mL, 5×10^{-4} M) was treated with an excess of a standard solution of HNO_3 1.0 M. Titrations were performed by addition of 10 μL aliquots of carbonate-free standard 0.1 M NaOH, recording 80-100 points for each titration. Complexation constants of **L1** cage were determined by performing a potentiometric titration experiment in presence of two equivalents of $\text{Cu}(\text{CF}_3\text{SO}_3)_2$. Prior to each potentiometric titration, the standard electrochemical potential (E°) of the glass electrode was determined in the water/methanol mixture, by a titration experiment according to the Gran method.^{40,41} Protonation and complexation titration data (emf vs mL of NaOH) were processed with the HyperQuad package⁴² to determine the equilibrium constants.

pH-spectrophotometric titrations were performed on solutions of **L1** (4×10^{-4} M) in presence of two equivalents of Cu(II) (as triflate salt) in the same solvent mixture used in potentiometric titrations (*i.e.* water/methanol 30% v/v with NaNO_3 0.05 M). In a typical experiment, aliquots of carbonate-free standard 0.1 M NaOH were added to the solution of the ligand and copper, then both the electrochemical potential and the UV-vis. spectrum of the solution were recorded after each addition.

3.2.3 X-ray diffraction studies

Diffraction data of $[\text{Cu}_2(\text{L1})(\text{glut})](\text{CF}_3\text{SO}_3)_2 \cdot 4(\text{H}_2\text{O})$ (greenish azure, $0.30 \times 0.26 \times 0.04 \text{ mm}^3$), $[\text{Cu}_2(\text{L1})(\alpha\text{-keto})](\text{CF}_3\text{SO}_3)_2 \cdot 5(\text{H}_2\text{O})$ (greenish azure, $0.30 \times 0.18 \times 0.02 \text{ mm}^3$),

[Cu₂(**L1**)(isopht)]₃(CF₃SO₃)₆·6(H₂O) (greenish azure, 0.42 × 0.20 × 0.05 mm³) and [Cu₂(**L1**)(ace)](CF₃SO₃)₂·4(H₂O) (bluish azure, 0.26 × 0.22 × 0.13 mm³) were collected on a Bruker-AXS diffractometer equipped with the SMART-APEX CCD detector. Data collection was performed at room temperature with MoK α X-radiation ($\lambda=0.7107$ Å) and crystal data are reported in Table 1. CCD frames were processed with the SAINT software⁴³ and intensities were corrected for Lorentz and polarization effects; absorption effects were empirically evaluated by the SADABS software⁴⁴ and absorption correction was applied to the data. All crystal structures were solved by direct methods (SIR 97)⁴⁵ and refined by full-matrix least-squares procedures on F^2 using all reflections (SHELXL-2018).⁴⁴ Anisotropic displacement parameters were used for all non-hydrogen atoms. Hydrogens were placed at calculated positions and their positions refined according to a riding model. Positions for H atoms belonging to water solvent molecules were not determined.

The X-ray diffraction quality of the synthetic crystals of the glut²⁻, α -keto²⁻ and isopht²⁻ adducts resulted poor and the one of the [Cu₂(**L1**)(isopht)]₃(CF₃SO₃)₆·6(H₂O) crystal was particularly poor (for this crystal, diffracted intensities at θ angle greater than 22° cannot be observable). The poor diffraction quality resulted in a low accuracy for the atom positions of the triflate counterions and of the water solvent molecules, which exhibited large and elongated atom displacement parameters, probably related to some unresolved positional disorder. In general, soft geometrical restraints and restraints on the atom displacement parameters were applied for the refinement of these atom positions.

3.2.3.1 Details on crystal structure analysis

Details on the crystal structure of [Cu₂(**L1**)(ace)](CF₃SO₃)₂·4(H₂O) showed positional disorder for one of the two triflate counterions and for a water solvent molecule. Disorder resulted in two alternative positions for these molecular species. The alternative positions were mutually exclusive and occurring with the same statistical probability. Atom sites belonging to the two alternative positions of the triflate counterion were refined with soft restraints on the molecular geometry (SAME) and on the atom displacement parameters (ISOR and DELU).

The crystal structure of [Cu₂(**L1**)(glut)](CF₃SO₃)₂·4(H₂O) was also refined with soft restraints (ISOR and DELU) for the atom displacement parameters of atom sites defining the triflate counterions. One of the two independent triflate counterions resulted disordered over two alternative positions, mutually exclusive and occurring with the same statistical probability.

The final cycles of structure refinements were done using soft restraints on the molecular geometry (SAME) for atom sites defining the alternative positions of the triflate counterion.

The crystal structure of the $[\text{Cu}_2(\mathbf{L1})(\alpha\text{-keto})](\text{CF}_3\text{SO}_3)_2 \cdot 5(\text{H}_2\text{O})$ compound was isostructural to the one of the $[\text{Cu}_2(\mathbf{L1})(\text{glut})](\text{CF}_3\text{SO}_3)_2 \cdot 4(\text{H}_2\text{O})$ compound. The alpha-ketoglutarate ion was disordered over two alternative positions, mutually exclusive and with the same statistical probability. The two alternative molecular structures differ only in the position of the carbonyl oxygen of the ketone functional group, which appears as disordered between the two alpha positions of the organic backbone. Soft restraints on the atom displacement parameters (DELU) and on the molecular geometry (SAME) were applied to atom positions belonging to the triflate counterions.

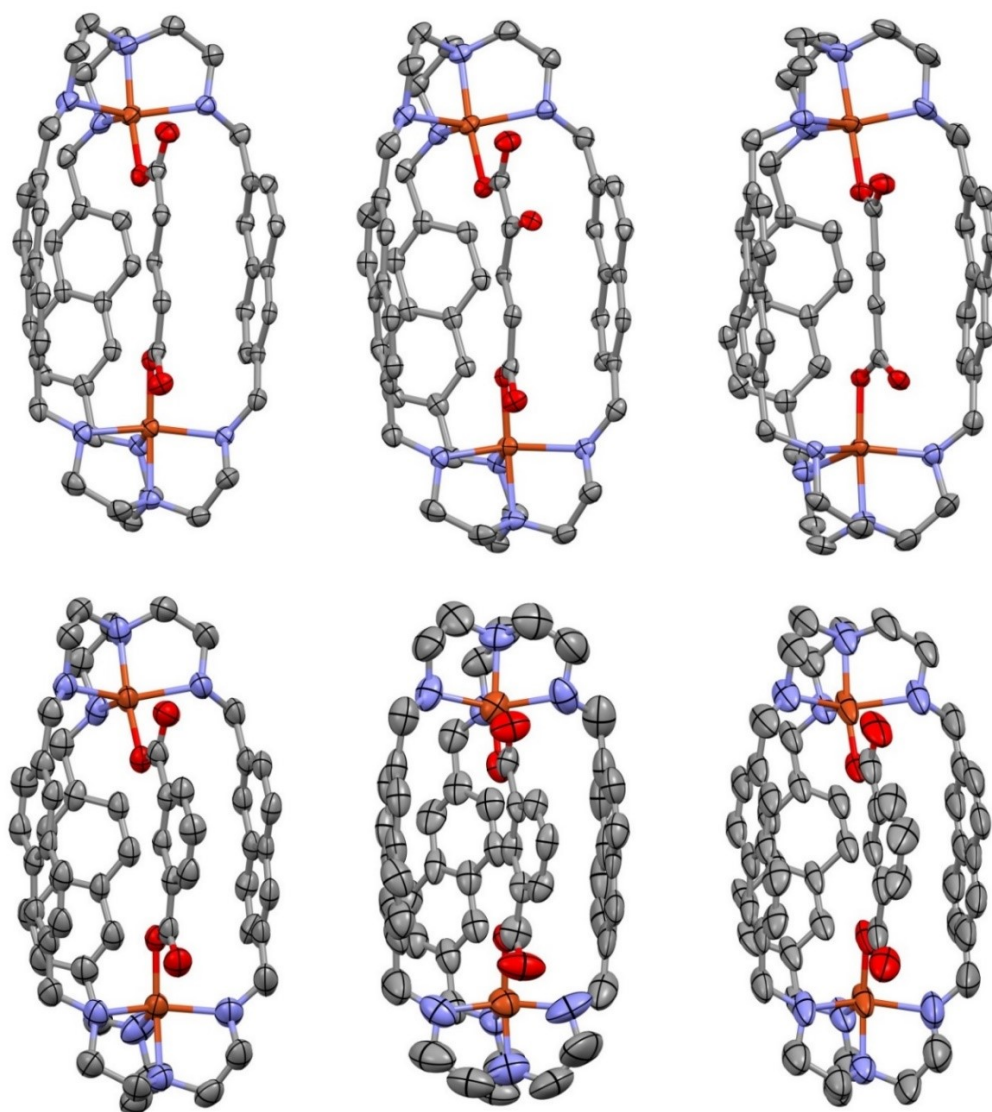


Figure 11. Plots showing thermal ellipsoids for $[\text{Cu}_2(\mathbf{L1})(\text{glut})]^{2+}$ (top left), $[\text{Cu}_2(\mathbf{L1})(\alpha\text{-keto})]^{2+}$ (top center), $[\text{Cu}_2(\mathbf{L1})(\text{ace})]^{2+}$ (top right) and for the three independent $[\text{Cu}_2(\mathbf{L1})(\text{isophth})]^{2+}$ cations (bottom). Ellipsoids are drawn at the 30% probability level.

The crystal structure of the $[\text{Cu}_2(\mathbf{L1})(\text{isopht})]_3(\text{CF}_3\text{SO}_3)_6 \cdot 6(\text{H}_2\text{O})$ compound resulted quite complicated for the presence of three similar but not symmetrically equivalent $[\text{Cu}_2(\mathbf{L1})(\text{isopht})]^{2+}$ anionic complexes. The poor X-ray diffraction quality of this synthetic crystal imposed the use of a great number of restraints during the least-square procedures. The crystal structure was refined restraining the molecular geometry of the triflate counterions to the ideal one (by using the DFIX and DANG instructions) and restraining the three arms of each $[\text{Cu}_2(\mathbf{L1})]^{4+}$ dimetallic cage to show similar geometrical features (by using the SAME instruction). Further restraints on the atom displacement parameters (DELU and ISOR) were applied for atom positions showing large and elongated thermal ellipsoids.

Table 1. Crystal data for the studied compounds.

	$[\text{Cu}_2(\mathbf{L1})(\text{glut})]$ $(\text{CF}_3\text{SO}_3)_2 \cdot 4(\text{H}_2\text{O})$	$[\text{Cu}_2(\mathbf{L1})(\alpha\text{-keto})]$ $(\text{CF}_3\text{SO}_3)_2 \cdot 5(\text{H}_2\text{O})$	$[\text{Cu}_2(\mathbf{L1})(\text{ace})]$ $(\text{CF}_3\text{SO}_3)_2 \cdot 4(\text{H}_2\text{O})$	$[\text{Cu}_2(\mathbf{L1})(\text{isopht})]_3$ $(\text{CF}_3\text{SO}_3)_6 \cdot 6(\text{H}_2\text{O})$
Formula	$\text{C}_{55}\text{H}_{74}\text{Cu}_2\text{F}_6\text{N}_8\text{O}_{14}\text{S}_2$	$\text{C}_{55}\text{H}_{74}\text{Cu}_2\text{F}_6\text{N}_8\text{O}_{16}\text{S}_2$	$\text{C}_{54}\text{H}_{67}\text{Cu}_2\text{F}_6\text{N}_8\text{O}_{14}\text{S}_2$	$\text{C}_{174}\text{H}_{204}\text{Cu}_6\text{F}_{18}\text{N}_{24}\text{O}_{36}\text{S}_6$
<i>M</i>	1376.42	1408.42	1357.35	4123.20
Crystal system	monoclinic	monoclinic	triclinic	triclinic
Space group	<i>P</i> 2 ₁ / <i>c</i> (no. 14)	<i>P</i> 2 ₁ / <i>c</i> (no. 14)	<i>P</i> -1 (no. 2)	<i>P</i> -1 (no. 2)
<i>a</i> (Å)	18.611(2)	18.4812(13)	10.2103(6)	18.547(3)
<i>b</i> (Å)	20.114(2)	20.0663(14)	17.7980(11)	21.950(4)
<i>c</i> (Å)	16.353(2)	16.5030(12)	17.8614(11)	23.907(4)
α (°)	90	90	66.3506(12)	100.574(2)
β (°)	96.2020(10)	97.1637(10)	86.0444(13)	102.098(2)
γ (°)	90	90	80.6582(13)	96.155(2)
<i>V</i> (Å ³)	6085.6(10)	6072.4(10)	2933.8(3)	9247(3)
<i>Z</i>	4	4	2	2
ρ_{calcd} (g·cm ⁻³)	1.502	1.541	1.537	1.481
θ_{max} (°)	25	25	25	22
Measured reflections	42829	57977	28102	47534
Unique reflections	10700	10737	10357	22705
<i>R</i> _{int}	0.047	0.077	0.041	0.045
Strong data [<i>I</i> _o >2σ(<i>I</i> _o)]	7164	6570	7609	10718
<i>R</i> ₁ , <i>wR</i> ₂ strong data	0.0792, 0.2270	0.072, 0.1855	0.0653, 0.2010	0.1454, 0.3889

<i>R</i> 1, <i>wR</i> 2 all data	0.1155, 0.2597	0.1245, 0.2203	0.0808, 0.2169	0.2256, 0.4473
GoF	1.057	1.026	1.061	1.396
max/min residuals (eÅ ⁻³)	1.14/-0.66	1.18/-0.62	1.04/-0.50	1.28/-0.92

Table 2. Cu(II)···Cu(II) intermetallic distance (Å), bond distances (Å) and bond angles (°) for the metal centers in [Cu₂(L1)(glut)]²⁺, [Cu₂(L1)(α-keto)]²⁺ and [Cu₂(L1)(ace)]²⁺ molecular cations.

	[Cu ₂ (L1)(glut)] ²⁺	[Cu ₂ (L1)(α-keto)] ²⁺	[Cu ₂ (L1)(ace)] ²⁺
Cu(II)···Cu(II)	8.952(1)	8.983(1)	8.884(1)
Cu(1)-O(1)	1.935(4)	1.944(4)	1.911(2)
Cu(1)-N(1)	2.031(5)	2.047(5)	2.009(3)
Cu(1)-N(2)	2.380(5)	2.339(5)	2.393(4)
Cu(1)-N(3)	2.148(5)	2.143(5)	2.131(3)
Cu(1)-N(4)	2.128(5)	2.142(5)	2.139(4)
Cu(2)-O(3)	1.923(4)	1.933(8)	1.908(3)
Cu(2)-N(5)	2.035(6)	2.038(5)	2.012(4)
Cu(2)-N(6)	2.402(6)	2.371(5)	2.440(4)
Cu(2)-N(7)	2.128(6)	2.135(5)	2.066(4)
Cu(2)-N(8)	2.147(5)	2.159(5)	2.105(4)
O(1)-Cu(1)- N(1)	168.6(2)	169.1(2)	173.57(14)
O(1)-Cu(1)- N(2)	109.6(2)	108.8(2)	105.11(12)
O(1)-Cu(1)- N(3)	91.1(2)	91.9(2)	93.44(11)
O(1)-Cu(1)- N(4)	95.2(2)	93.9(2)	94.28(13)
N(1)-Cu(1)- N(2)	81.7(2)	82.1(2)	81.24(15)
N(1)-Cu(1)- N(3)	84.4(2)	84.4(2)	83.87(14)
N(1)-Cu(1)- N(4)	83.4(2)	83.6(2)	84.50(15)
N(2)-Cu(1)- N(3)	107.2(2)	109.1(2)	103.94(13)
N(2)-Cu(1)- N(4)	100.0(2)	100.7(2)	108.68(15)

N(3)-Cu(1)- N(4)	148.1(2)	145.9(2)	143.11(15)
O(3)-Cu(2)- N(5)	167.4(2)	167.3(2)	178.27(15)
O(3)-Cu(2)- N(6)	111.9(2)	111.6(2)	100.44(12)
O(3)-Cu(2)- N(7)	94.1(2)	93.7(2)	92.18(13)
O(3)-Cu(2)- N(8)	91.2(2)	90.7(2)	94.43(14)
N(5)-Cu(2)- N(6)	80.7(2)	81.1(2)	80.91(15)
N(5)-Cu(2)- N(7)	83.6(2)	84.1(2)	86.32(17)
N(5)-Cu(2)- N(8)	84.7(2)	84.6(2)	86.10(17)
N(6)-Cu(2)- N(7)	100.7(2)	101.7(2)	110.88(14)
N(6)-Cu(2)- N(8)	105.4(2)	106.3(2)	109.68(15)
N(7)-Cu(2)- N(8)	149.2(2)	147.7(2)	136.87(16)

Table 3. Cu(II)···Cu(II) intermetallic distance (Å), bond distances (Å) and bond angles (°) for the metal centers in the three not symmetrically equivalent [Cu₂(**L1**)(isopht)]²⁺ molecular cations.

	[Cu ₂ (L1)(isopht)] ²⁺		
	mol A	mol B	mol C
Cu(II)···Cu(II)	8.923(3)	8.808(4)	8.887(4)
Cu(1)-O(1)	1.957(9)	1.977(10)	1.947(12)
Cu(1)-N(1)	2.061(12)	1.98(2)	2.06(2)
Cu(1)-N(2)	2.371(14)	2.349(14)	2.37(2)
Cu(1)-N(3)	2.105(11)	2.16(2)	2.154(14)
Cu(1)-N(4)	2.097(13)	1.93(2)	2.12(2)
Cu(2)-O(3)	1.933(8)	1.952(10)	1.96(2)
Cu(2)-N(5)	2.035(12)	2.11(2)	2.12(2)
Cu(2)-N(6)	2.445(11)	2.377(13)	2.361(14)
Cu(2)-N(7)	2.101(10)	2.074(14)	2.117(13)
Cu(2)-N(8)	2.156(10)	2.09(2)	2.172(13)
O(1)-Cu(1)- N(1)	168.1(5)	166.5(7)	168.3(8)

O(1)-Cu(1)- N(2)	110.5(4)	115.3(5)	112.2(7)
O(1)-Cu(1)- N(3)	92.2(4)	92.1(5)	92.8(5)
O(1)-Cu(1)- N(4)	95.3(4)	92.0(6)	95.7(6)
N(1)-Cu(1)- N(2)	81.5(5)	77.9(7)	79.5(7)
N(1)-Cu(1)- N(3)	83.5(5)	86.8(9)	83.1(6)
N(1)-Cu(1)- N(4)	83.0(5)	82.3(9)	82.0(7)
N(2)-Cu(1)- N(3)	109.0(6)	104.3(6)	106.5(6)
N(2)-Cu(1)- N(4)	96.7(6)	100.9(8)	100.3(8)
N(3)-Cu(1)- N(4)	148.7(5)	149.8(9)	146.3(9)
O(3)-Cu(2)- N(5)	170.8(4)	165.7(5)	168.1(7)
O(3)-Cu(2)- N(6)	109.2(4)	113.1(4)	111.8(6)
O(3)-Cu(2)- N(7)	96.8(4)	97.3(5)	96.9(5)
O(3)-Cu(2)- N(8)	90.9(4)	91.9(5)	90.2(6)
N(5)-Cu(2)- N(6)	79.7(4)	80.5(5)	79.7(6)
N(5)-Cu(2)- N(7)	83.4(4)	83.6(7)	83.7(5)
N(5)-Cu(2)- N(8)	84.4(4)	80.5(7)	83.4(6)
N(6)-Cu(2)- N(7)	100.4(4)	100.9(6)	100.6(6)
N(6)-Cu(2)- N(8)	104.9(4)	102.6(6)	104.8(6)
N(7)-Cu(2)- N(8)	149.5(4)	148.9(6)	148.8(6)

3.2.4 Spectrophotometric titrations

In a typical experiment, a concentrated solution of the dicopper(II) azacryptate $[\text{Cu}_2(\text{L1})]^{4+}$ in DMSO was diluted with 0.05 M HEPES (*i.e.* 4-(2-hydroxyethyl)-1-piperazineethanesulfonic acid) buffer at pH 7: the final concentration of the azacryptate ranged between 50-500 μM . The buffered solution of the cryptate was then titrated with a standard solution of either the chosen dicarboxylic acid or the corresponding disodium salt, in the case of phthalates. After each addition, the UV-vis. spectrum was recorded. It should be noted that with terephthalate and phthalate anions, the formation of a precipitate over the course of the titration prevented

accurate determination of the association constants. The concentration of the azacryptate solution was chosen on the basis of the p -parameter ($p = [\text{concentration of the azacryptate:anion adduct}]/[\text{maximum possible concentration of the azacryptate:anion adduct}]$), which should range between 0.2 and 0.8.⁴⁶ Titration data were processed with the HyperQuad package⁴² to estimate equilibrium constants. In some cases, even working with very dilute solutions of the azacryptate, the curvature of the titration profile was too sharp to allow accurate calculation of binding constants.

3.2.5 Spectrofluorimetric titrations

A solution of 5-FAM indicator (1 μM) was first titrated with a solution of the $[\text{Cu}_2(\text{L1})]^{4+}$ complex in 0.05 M HEPES buffer at pH 7. The indicator was excited at 473 nm, *i.e.* an isosbestic point of the corresponding UV-vis. titration. Titration data were processed with the HyperQuad package⁴² to estimate receptor:indicator binding constants. Titrations with anions were then performed on solutions of 5-FAM (0.1 μM) and the in-situ prepared $[\text{Cu}_2(\text{L1})]^{4+}$ complex (5 μM) in 0.05 M HEPES buffer at pH 7. Titration data were processed with the HyperQuad package⁴² to estimate equilibrium constants.

3.3 Results and discussion

3.3.1 Potentiometric and pH-spectrophotometric titrations

3.3.1.1 Protonation constants of L1

The determination of the protonation constants (reported in Table 4) was achieved through potentiometric titrations on **L1** in MeOH/H₂O 30% v/v, with NaNO₃ 0.05 M as supporting electrolyte. The presence of methanol in the aqueous mixture allowed me to overcome the low solubility of the free cage in water at high pH values. The emf vs volume of NaOH curve was fitted using a non-linear least squares procedure through the HyperQuad package.⁴² From the calculated protonation constants, the distribution diagram of the species (as % abundance with respect to **L1** vs pH) over the pH range 2-11 was determined (see Fig. 12).

Table 4. Protonation equilibria and the corresponding constants for **L1** in water/methanol 30% v/v (T=25 °C). Standard deviation in parentheses.

Equilibria	Log β
$\mathbf{L1} + \mathbf{H}^+ \rightleftharpoons \mathbf{L1H}^+$	9.31(4)
$\mathbf{L1} + 2\mathbf{H}^+ \rightleftharpoons \mathbf{L1H}_2^{2+}$	17.75(5)
$\mathbf{L1} + 3\mathbf{H}^+ \rightleftharpoons \mathbf{L1H}_3^{3+}$	26.13(4)
$\mathbf{L1} + 4\mathbf{H}^+ \rightleftharpoons \mathbf{L1H}_4^{4+}$	33.74(4)
$\mathbf{L1} + 5\mathbf{H}^+ \rightleftharpoons \mathbf{L1H}_5^{5+}$	38.53(8)
$\mathbf{L1} + 6\mathbf{H}^+ \rightleftharpoons \mathbf{L1H}_6^{6+}$	43.44(4)

Around pH 2, only the species $\mathbf{L1H}_6^{6+}$ (with all the secondary amine protonated) is present in solution. As pH rises, the deprotonation of the naphthyl cage occurs leading to the formation of $\mathbf{L1H}_4^{4+}$ species, as a major species between pH 5.5 and 7.0. Different protonated forms of **L1**, *i.e.* $\mathbf{L1H}_3^{3+}$, $\mathbf{L1H}_2^{2+}$, $\mathbf{L1H}^+$, coexist in solution until pH 9, where the formation of the neutral species **L1** begins: after pH 10, it is the only species in solution.

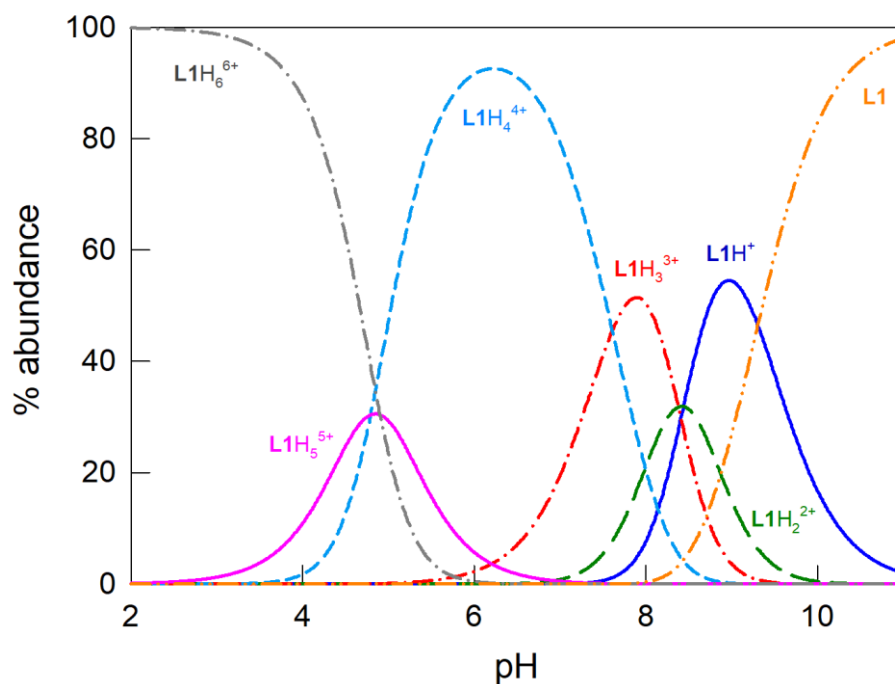


Figure 12. Distribution diagram of the species present at equilibrium over the course of the potentiometric titration of **L1** (5×10^{-4} M) with standard NaOH in water/methanol 30% v/v (T=25 °C).

3.3.1.2 Complexation of L1 with Cu(II)

The complexation constants of the ligand with copper(II) were obtained by potentiometric titrations on the cage in presence of two equivalents of $\text{Cu}(\text{CF}_3\text{SO}_3)_2$ (MeOH/H₂O 30% v/v, NaNO₃ 0.05 M). The experimental curve (emf vs volume of NaOH) was fitted using the HyperQuad package.⁴² Best fitting was obtained by assuming the development of the following complexes over the course of the titration: $[\text{Cu}(\text{L1H}_3)]^{5+}$, $[\text{Cu}_2(\text{L1})]^{4+}$, $[\text{Cu}_2(\text{L1})(\text{OH})]^{3+}$, $[\text{Cu}_2(\text{L1})(\text{OH})_2]^{2+}$. The corresponding cumulative constants (as $\text{Log}\beta$) and the distribution diagram are shown in Table 5 and Figure 13, respectively.

In the pH range 4.0-5.5, the major species in solution is the mononuclear Cu(II) complex $[\text{Cu}(\text{L1H}_3)]^{5+}$, with the metal coordinated to one of the *tren* subunits. The pH increase leads to the deprotonation of the ligand and, consequently, to the formation of the dicopper(II) complex $[\text{Cu}_2(\text{L1})]^{4+}$, with one metal center for each *tren* subunit. Every copper(II) ion is penta-coordinated, with a water molecule in the apical position left free by the polyamino ligand. The dinuclear complexed species is dominant until pH 8: over this pH value, the deprotonation of the coordinated water molecules occurs, with formation of the mono- and dihydroxide complexes $[\text{Cu}_2(\text{L1})(\text{OH})]^{3+}$ and $[\text{Cu}_2(\text{L1})(\text{OH})_2]^{2+}$. The constants relative to these equilibria are reported in Table 6.

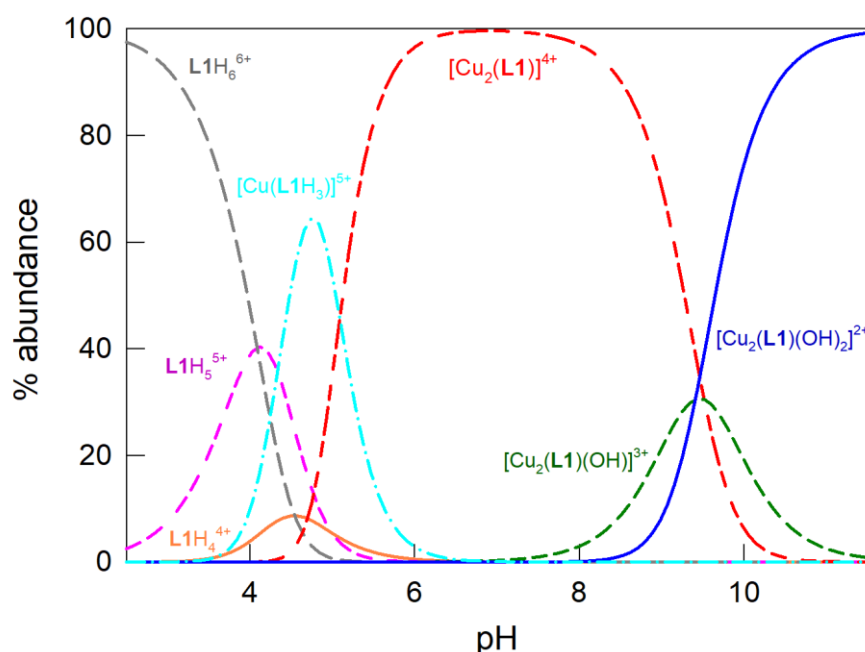


Figure 13. Distribution diagram showing the species present at the equilibrium over the course of the potentiometric titration of **L1** (0.4 mM) in presence of 2 *eqv.* $\text{Cu}(\text{CF}_3\text{SO}_3)_2$, with standard NaOH in water/methanol (30% v/v) ($T=25\text{ }^\circ\text{C}$).

Table 5. Complexation constants for **L1** with Cu(II) in water/methanol 30% v/v (T=25 °C). Standard deviations are shown in parentheses.

Equilibria	Log β
$\text{L1} + \text{Cu}^{2+} + 3\text{H}^+ \rightleftharpoons [\text{Cu}(\text{L1H}_3)]^{5+}$	33.90(4)
$\text{L1} + 2\text{Cu}^{2+} \rightleftharpoons [\text{Cu}_2(\text{L1})]^{4+}$	22.28(4)
$\text{L1} + 2\text{Cu}^{2+} + \text{H}_2\text{O} \rightleftharpoons [\text{Cu}_2(\text{L1})(\text{OH})]^{3+} + \text{H}^+$	12.83(9)
$\text{L1} + 2\text{Cu}^{2+} + 2\text{H}_2\text{O} \rightleftharpoons [\text{Cu}_2(\text{L1})(\text{OH})_2]^{2+} + 2\text{H}^+$	3.41(8)

Table 6. Equilibria obtained from the data reported in Tables 4 and 5. Standard deviations are shown in parentheses.

Equilibria	Log K
$\text{L1H}_3^{3+} + \text{Cu}^{2+} \rightleftharpoons [\text{Cu}(\text{L1H}_3)]^{5+}$	7.77(8)
$[\text{Cu}_2(\text{L1})]^{4+} + \text{H}_2\text{O} \rightleftharpoons [\text{Cu}_2(\text{L1})\text{OH}]^{3+} + \text{H}^+$	-9.5(1)
$[\text{Cu}_2(\text{L1})\text{OH}]^{3+} + \text{H}_2\text{O} \rightleftharpoons [\text{Cu}_2(\text{L1})(\text{OH})_2]^{2+} + \text{H}^+$	-9.4(1)

3.3.1.3 pH-spectrophotometric titration of **L1** with Cu(II)

pH-spectrophotometric titrations were performed on solutions of **L1** in water/MeOH 30% v/v (NaNO₃ 0.05 M; T 25°C), in presence of two equivalents of Cu(CF₃SO₃)₂. The UV-vis. spectra taken over the course of the titration are reported in Figure 14.

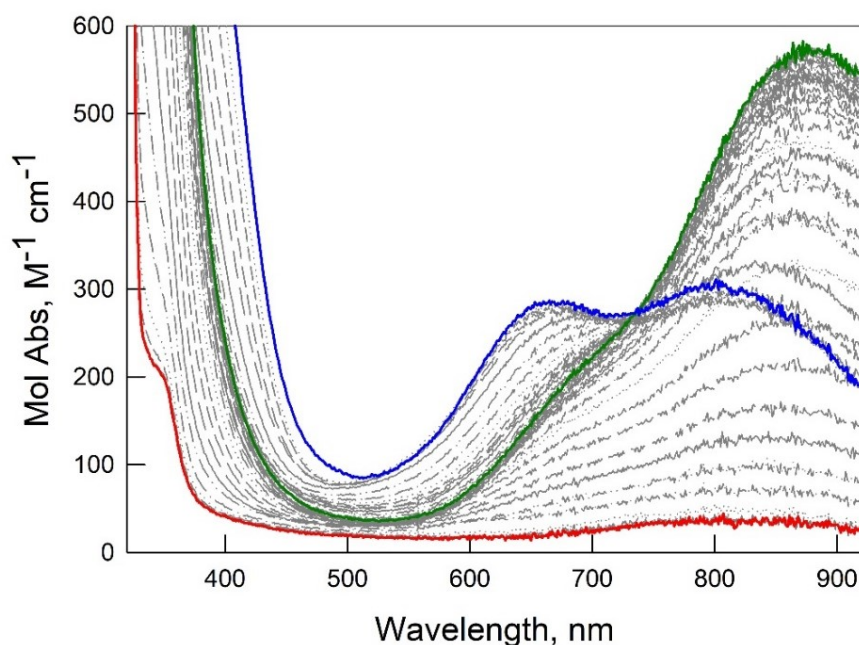


Figure 14. Spectra taken over the course of the pH-spectrophotometric titration of a solution of 4×10^{-4} M in **L1** and 8×10^{-4} M in Cu(II). The red line highlights the initial spectrum (at about pH 3), while the green and blue lines correspond to the spectra recorded at pH 7 and 11, respectively.

The solid red line corresponds to the UV-vis. spectrum of the polyprotonated cage at pH 3. The pH increase leads to the formation of adsorption bands relative to the copper(II)-containing species, accompanied by the development of a green colour in solution. The d-d band around 880 nm, with a shoulder at 670 nm, was attributed to the dinuclear complex with the copper ions displaying a trigonal bipyramid geometry: each Cu(II) ion is bound to a *tren* subunit, with a H₂O molecule coordinated to the apical position left free by the ligand. The formation of the dinuclear species is also accompanied by the development of N_{sec} → Cu(II) (LMCT) bands near 400 nm. Around pH 7 (solid green line), the d-d band at 880 nm reaches its maximum intensity. Over pH 7, the change in the intensity ratio between the bands at 880 nm and 670 nm points out the formation of hydroxide complexes [Cu₂(L1)(OH)]³⁺ and [Cu₂(L1)(OH)₂]²⁺. The hydroxide anions promote a distortion of the coordination geometry, around the copper ions, from trigonal bipyramid to square pyramid. This distortion is accompanied by a change of colour in solution from green to light blue. The blue line in Figure 14 highlights the spectrum at pH 11.

The molar absorbance at 667 and 877 nm were plotted against pH, and the resulting profiles were superimposed to the distribution diagram in Figure 15.

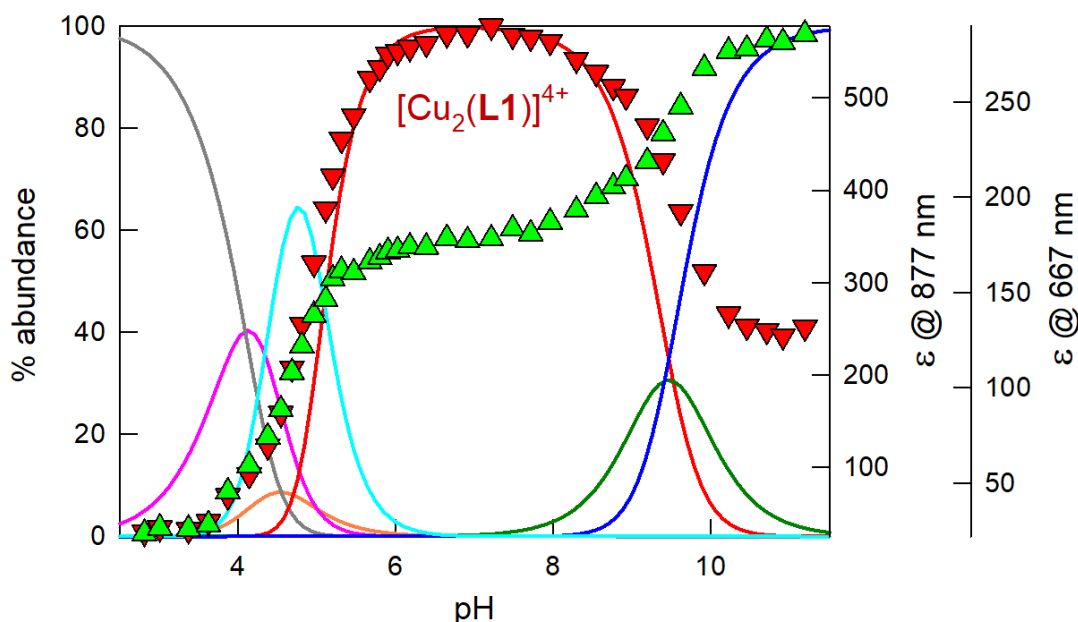


Figure 15. Distribution diagram showing species present at the equilibrium over the course of the potentiometric titration of L1 (0.4 mM) in presence of 2 *eqv.* Cu(CF₃SO₃)₂; the pH-spectrophotometric profiles of ϵ (*i.e.* Mol Abs) at 877 and 667 nm (red and green triangles, respectively) vs pH are superimposed (MeOH/water 30% v/v, 0.05 M NaNO₃; T = 25 °C). The lines in the diagram correspond to the species: H₆L1⁶⁺, grey; H₅L1⁵⁺, purple; H₄L1⁴⁺, orange; [Cu(L1H₃)]⁵⁺, cyan; [Cu₂(L1)]⁴⁺, red; [Cu₂(L1)(OH)]³⁺, green; [Cu₂(L1)(OH)₂]²⁺, blue.

Notably, the direct correlation between the abundance of the $[\text{Cu}_2(\mathbf{L1})]^{4+}$ species and the absorption band at 880 nm is clearly shown by the good superimposition of the titration profile (ϵ vs pH, see red triangles) and the curve relative to the dicopper(II) complex (% abundance vs pH, see the red solid line). Moreover, the titration profile at 677 nm (green triangles), superimposed to the diagram, shows that the change in intensity of the corresponding absorption band is strictly correlated to deprotonation processes involving the coordinated water molecules.

3.3.2 X-ray diffraction studies

The slow evaporation of aqueous solutions containing the in-situ prepared $[\text{Cu}_2(\mathbf{L1})](\text{CF}_3\text{SO}_3)_4$ complex and different dicarboxylates anions (as sodium salts) – mixed in a 1:1 molar ratio – allowed me to isolate single crystals of the inclusion complexes with glutarate (glut^{2-}), α -ketoglutarate ($\alpha\text{-keto}^{2-}$), acetylendicarboxylate (ace^{2-}) and isophthalate (isopht^{2-}). These single crystals resulted to be suitable for X-ray diffraction studies and the simplified sketches of the obtained molecular structures are shown in Figures 16 and 17.

The hydrated crystals of $[\text{Cu}_2(\mathbf{L1})(\alpha\text{-keto})](\text{CF}_3\text{SO}_3)_2 \cdot 4(\text{H}_2\text{O})$ and $[\text{Cu}_2(\mathbf{L1})(\text{glut})](\text{CF}_3\text{SO}_3)_2 \cdot 5(\text{H}_2\text{O})$ (see Fig. 16) displayed isostructural monoclinic structures, while for $[\text{Cu}_2(\mathbf{L1})(\text{isopht})]_3(\text{CF}_3\text{SO}_3)_6 \cdot 6(\text{H}_2\text{O})$ a triclinic crystal structure was found, composed by three similar but not symmetrically equivalent $[\text{Cu}_2(\mathbf{L1})(\text{isopht})]^{2+}$ complexes (named A, B, and C, see Fig. 17). Even if the quality of these single crystals was quite poor, in particular the one of the triclinic phase, the X-ray diffraction analysis allowed us to determine the chemically significant moieties of the structures, revealing a very similar molecular geometry for the $[\text{Cu}_2(\mathbf{L1})]^{4+}$ cryptate in all the investigated inclusion complexes. The obtained results showed that, in the case of dicarboxylates with a five C-atoms backbone, the anion skeleton is placed in a very similar position, so as to bridge the copper(II) ions within the cage cavity.

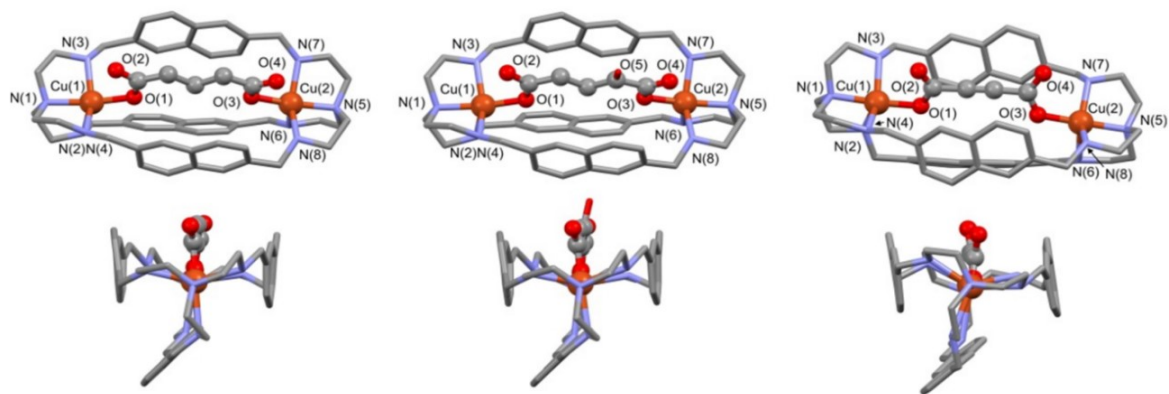


Figure 16. From the left, pairs of simplified sketches of $[\text{Cu}_2(\text{L1})(\text{glut})]^{2+}$, $[\text{Cu}_2(\text{L1})(\alpha\text{-keto})]^{2+}$ and $[\text{Cu}_2(\text{L1})(\text{ace})]^{2+}$ species. The bridging portion of each dicarboxylate anion is drawn as large spheres, in order to emphasize similarities and differences among the guests. Hydrogen atoms are omitted for clarity and atom names are reported only for Cu, N, and O.

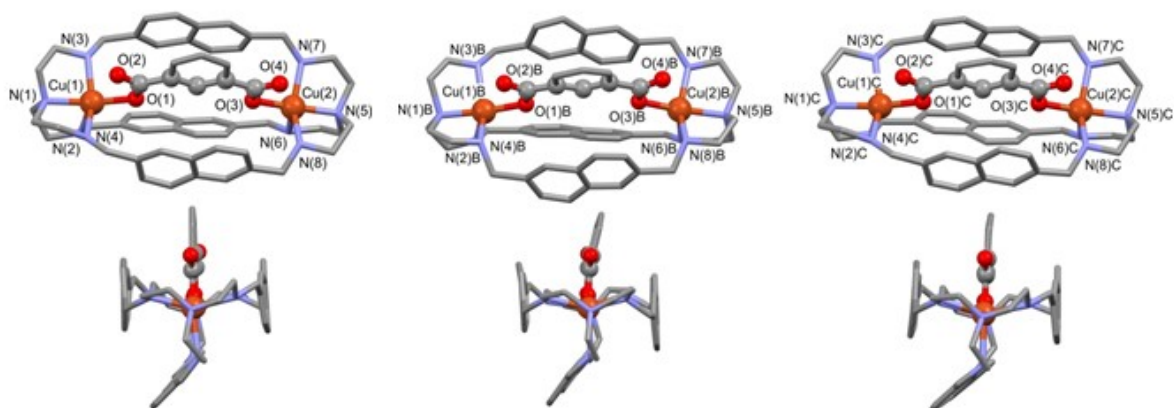


Figure 17. Simplified sketches of the A- $[\text{Cu}_2(\text{L1})(\text{isophth})]^{2+}$ (left) B- $[\text{Cu}_2(\text{L1})(\text{isophth})]^{2+}$ (middle) and of the C- $[\text{Cu}_2(\text{L1})(\text{isophth})]^{2+}$ (right) molecular cations (hydrogen atom were omitted for clarity). Atom names are reported only for Cu, N, and O atom sites.

As already reported by Lu and colleagues for fumarate (fum^{2-}) and succinate (suc^{2-})³⁹, the anionic guest is placed in the cryptate cavity, which displays a cradle-like arrangement in all the obtained crystals structures. The two Cu(II) cations show a penta-coordination geometry: four donor atoms are nitrogens belonging to the *tren* subunit, while the fifth donor is an O-atom of the dicarboxylate guest. The Cu(II)⋯Cu(II) separation found in the crystals of $[\text{Cu}_2(\text{L1})(\text{glut})]^{2+}$, $[\text{Cu}_2(\text{L1})(\alpha\text{-keto})]^{2+}$ and $[\text{Cu}_2(\text{L1})(\text{ace})]^{2+}$ (*i.e.* 8.95(1), 8.98(1) and 8.88(1) Å, respectively) is higher compared to that observed in the complexes by Lu (*i.e.* 8.77(1) Å in both $[\text{Cu}_2(\text{L1})(\text{fum})]^{2+}$ and $[\text{Cu}_2(\text{L1})(\text{suc})]^{2+}$). As a matter of fact, the 5-C dicarboxylates glut^{2-} and $\alpha\text{-keto}^{2-}$, as well as the linear ace^{2-} , cannot perfectly match the cage cavity, hence the anion inclusion induces an increase of the Cu(II)⋯Cu(II) separation in the cryptate. A similar situation was found in the three $[\text{Cu}_2(\text{L1})(\text{isophth})]^{2+}$ complexes, with Cu(II)⋯Cu(II) separations

of 8.92(1), 8.81(1), and 8.89(1) Å for the A, B, and C, respectively. Complete geometrical features of the metal center coordination are available in the Experimental Section.

Further information on the coordination geometry of the Cu(II) ions was gained by determining the structural parameter τ from the crystallographic data. The τ parameter can be obtained from the formula $\tau = \frac{(\beta - \alpha)}{60^\circ}$ (where β and α are the two greatest bond angles of the metal center, with $\beta > \alpha$): τ is close to 0 in complexes with a square pyramidal (SP) coordination geometry, while it is close to 1 for the trigonal bipyramid one (TB) (see Fig. 18).⁴⁷

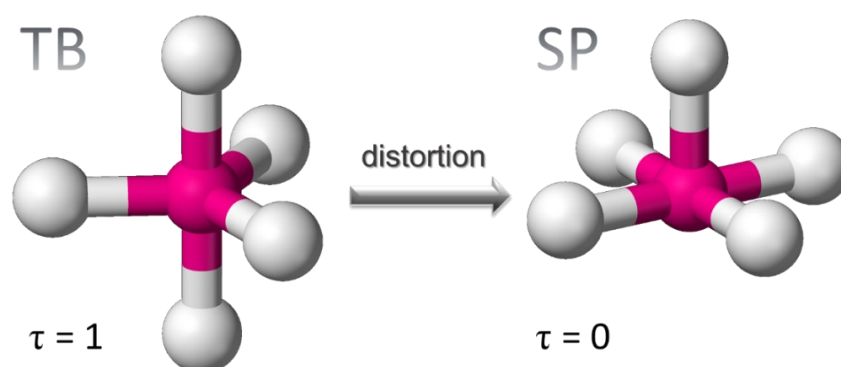


Figure 18. 3D-Ball and stick representation of trigonal bipyramidal (TB) \rightarrow square pyramidal (SP) distortion of a penta-coordinated metal center. Fucsia = metal; white = ligands.

In the $[\text{Cu}_2(\mathbf{L1})]^{4+}$ complex, two τ values (one for each copper ion, τ_1 and τ_2), can be calculated. In the inclusion complexes with fum^{2-} and suc^{2-} , the τ values are: $\tau_1, \tau_2 = 0.64, 0.89$ and $\tau_1, \tau_2 = 0.60, 0.89$, respectively. Both adducts show a Cu(II) ion in an almost ideal TB geometry, while the other one is intermediate between TB and SP. For the $[\text{Cu}_2(\mathbf{L1})(\text{ace})]^{2+}$ complex, an intermediate geometry is observed for both metals ($\tau_1, \tau_2 = 0.51, 0.69$), while in the complexes with glut^{2-} , $\alpha\text{-keto}^{2-}$ and isopht^{2-} anions, both Cu(II) ions present a significant distortion towards SP: $\tau_1, \tau_2 = 0.30, 0.34$ in $[\text{Cu}_2(\mathbf{L1})(\text{glut})]^{2+}$; $\tau_1, \tau_2 = 0.33, 0.39$ in $[\text{Cu}_2(\mathbf{L1})(\alpha\text{-keto})]^{2+}$; $\tau_1, \tau_2 = 0.32, 0.36$ in A- $[\text{Cu}_2(\mathbf{L1})(\text{isopht})]^{2+}$, $\tau_1 = \tau_2 = 0.28$ in B- $[\text{Cu}_2(\mathbf{L1})(\text{isopht})]^{2+}$ and $\tau_1, \tau_2 = 0.32, 0.37$ in C- $[\text{Cu}_2(\mathbf{L1})(\text{isopht})]^{2+}$.

Interestingly, the bond angle $\text{N}_{\text{ter}}\text{-Cu-O}_{\text{car}}$, involving the two axial atom positions of the trigonal bipyramid, also correlates with the TB \rightarrow SP distortion. In presence of fum^{2-} and suc^{2-} ions, the $\text{N}_{\text{ter}}\text{-Cu-O}_{\text{car}}$ angle results almost flat (*i.e.* in the range $175.4(2)^\circ$ - $178.8(2)^\circ$). A similar situation is found with the linear ace^{2-} anion ($173.57(14)^\circ$ and $178.27(15)$ for the two Cu(II) ions, respectively). On the other hand, a significant decrease of the $\text{N}_{\text{ter}}\text{-Cu-O}_{\text{car}}$ angle is found with

C5-dicarboxylates, such as glut²⁻, α -keto²⁻ and isoph²⁻, for which the N_{ter}-Cu-O_{car} angle is in the range 165.7(5)°-170.8(4)°.

In general, for all the anions, the best plane of the dicarboxylate groups is placed almost parallel to the best plane of naphthalene moieties of the two lateral arms, with the dihedral angle values in the range 0.8-14.1°. However, longer dicarboxylates place the C-chain outside the cage cavity, thus increasing the separations between the centroids of the naphthalenes and the centroids of the dicarboxylate groups with respect to the separation found in the inclusion complex with fum²⁻. In particular, the centroid-centroid separations are 3.42 and 3.45 Å in [Cu₂(L1)(glut)]²⁺; 3.57 and 3.60 Å in [Cu₂(L1)(α -keto)]²⁺, whereas the values reported for [Cu₂(L1)(fum)]²⁺ are 3.33 and 3.37 Å. This result suggests that the face-to-face π -stacking interactions involving C5-dicarboxylates and the cage skeleton are significantly weaker than those found with fum²⁻ or ace²⁻.

3.3.3 Spectrophotometric studies on [Cu₂(L1)]⁴⁺ with dicarboxylates

In order to thoroughly investigate the anion binding properties of [Cu₂(L1)]⁴⁺, spectrophotometric titrations were performed with a series of polycarboxylates in buffer aqueous solution at pH 7 (HEPES buffer 0.05 M). In particular, we tested polycarboxylates of different length, with either aromatic or aliphatic skeleton, and with various substituents and unsaturation degree (see Fig. 10 and Table 7). The formation of 1:1 adducts with the dinuclear cryptate was found with most of the studied anions, except for malonate and oxalate. For these latter species, the progressive addition to aqueous solutions of [Cu₂(L1)]⁴⁺ caused the disappearance of the d-d bands in the UV-vis. spectrum, suggesting an anion-induced demetallation of the dicopper(II) complex.

Table 7. Binding constants (as LogK₁₁ values) obtained by UV-vis. titrations on [Cu₂(L1)]⁴⁺ in water with 0.05 M HEPES buffer at pH 7 (T=25 °C). (a) Anion-promoted demetallation of the dicopper complex. Standard deviations are shown in parentheses.

anionic guest	abbreviations	LogK ₁₁ [Cu ₂ (L1)] ⁴⁺
oxalate	ox ²⁻	(a)
malonate	mal ²⁻	(a)
succinate	suc ²⁻	> 6
glutarate	glut ²⁻	5.39(1)
adipate	adi ²⁻	2.58(1)

pimelate	pim ²⁻	2.64(8)
maleate	male ²⁻	2.78(1)
fumarate	fum ²⁻	> 6
acetylendicarboxylate	ace ²⁻	5.90(2)
α -ketoglutarate	α -keto ²⁻	6.00(1)
citrate	cit ³⁻	5.70(1)
phthalate	pht ²⁻	2.54(1)
terephthalate	tereph ²⁻	3.54(1)
isophthalate	isoph ²⁻	> 6

The $\text{Log}K_{11}$ values, determined through a least-squares treatment of the titration data⁴², are reported in Table 7. In general, C4 and C5-dicarboxylates, especially those with a rigid skeleton, show stronger interactions with the cryptate. As observed by Lu and co-workers for the dizinc(II) analogue complex³⁹, $[\text{Cu}_2(\mathbf{L1})]^{4+}$ can successfully discriminate fum²⁻ and male²⁻ isomers, with a difference in the $\text{Log}K_{11}$ values of more than three magnitude orders for the two anions. For longer dicarboxylates, such as C6-adipate (adi²⁻) and C7-pimelate (pim²⁻) (see Figs 25-26), a drop of the affinity was found ($\text{Log}K_{11}$ are 2.58 and 2.64, respectively).

Among the tested anions, the highest affinity was found for fum²⁻, suc²⁻ and isoph²⁻ whose bite length matches the Cu(II)···Cu(II) separation within the cavity. Interestingly, the affinity for these dicarboxylates is even greater than that found for the tricarboxylate citrate (cit³⁻) anion (see Fig. 29). For fum²⁻, suc²⁻ and isoph²⁻, an accurate determination of the binding constants was unfortunately not feasible because of the steepness of the UV-vis. titration profiles.

The position of the d-d bands in the absorption spectrum of $[\text{Cu}_2(\mathbf{L1})]^{4+}$ in aqueous solution at pH 7 (see Fig. 20, back solid line) suggests a TB coordination geometry for both Cu(II) ions, with water molecules occupying the free positions left by the *tren* subunits. Notably complexes of the $[\text{Cu}(\textit{tren})(\text{X})]^{2+}$ type, with a perfect TB geometry, typically show a principal d-d band at 877 nm, with a shoulder around 660 nm (see curve **(1)** Fig. 19).⁴⁸

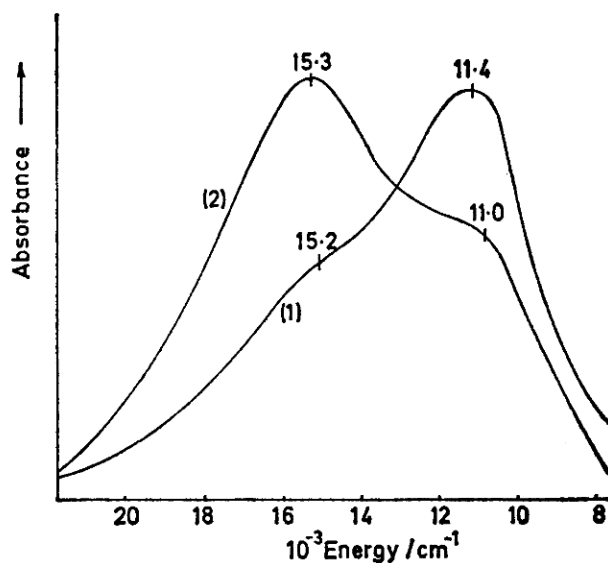


Figure 19. Electronic spectra of TB $[\text{Cu}(\text{tren})(\text{X})]^{2+}$ (1) and SP $[\text{Cu}(\text{tren})(\text{X})]^{2+}$ (2) (from ref. [48]).

UV-vis. titrations of $[\text{Cu}_2(\text{L1})]^{4+}$ with fum^{2-} and suc^{2-} (reported in Figs 20-21) point out a significant blue shift of the band at 877 nm, accompanied by an increase of the intensity of the shoulder band. This *trend* agrees with the anion-induced distortion of the coordination geometry of the metal ions observed in the solid state. In fact, one of the two Cu(II) centers is more distorted towards SP, while the other one maintains the TB geometry. On the other hand, a more significant TB→SP distortion of both Cu(II) ions would cause an exchange of the intensity ratio between the d-d bands at 877 and 660 nm (see curve (2) in Fig. 19).⁴⁸ This optical change was detected upon UV-vis. titrations of $[\text{Cu}_2(\text{L1})]^{4+}$ with glut^{2-} , $\alpha\text{-keto}^{2-}$ and isopht^{2-} anions (reported in Figs 22-24), thus confirming the relevant TB→SP distortion of both metal centers, observed in the crystals of the inclusion complexes of $[\text{Cu}_2(\text{L1})]^{4+}$ with these dicarboxylates. The comparison among C5-dicarboxylates pointed out that the preorganization of the guest and the instauration of $\pi\text{-}\pi$ interactions with the naphthyl spacers of the cage strongly contribute to the binding. A higher affinity was actually found for $\alpha\text{-keto}^{2-}$, compared to glut^{2-} , and the ace^{2-} anion (see Fig. 28) was found to strongly binds to the cryptate despite the long bite length,. Among the tested aromatic anions, the best affinity was found for isopht^{2-} . On the other hand, phthalate and terephthalate anions (UV-vis. titrations in Figs 30-31) showed a low affinity for the cage, with $\text{Log}K_{11}$ values of ~ 2.5 and 3.5 , respectively.

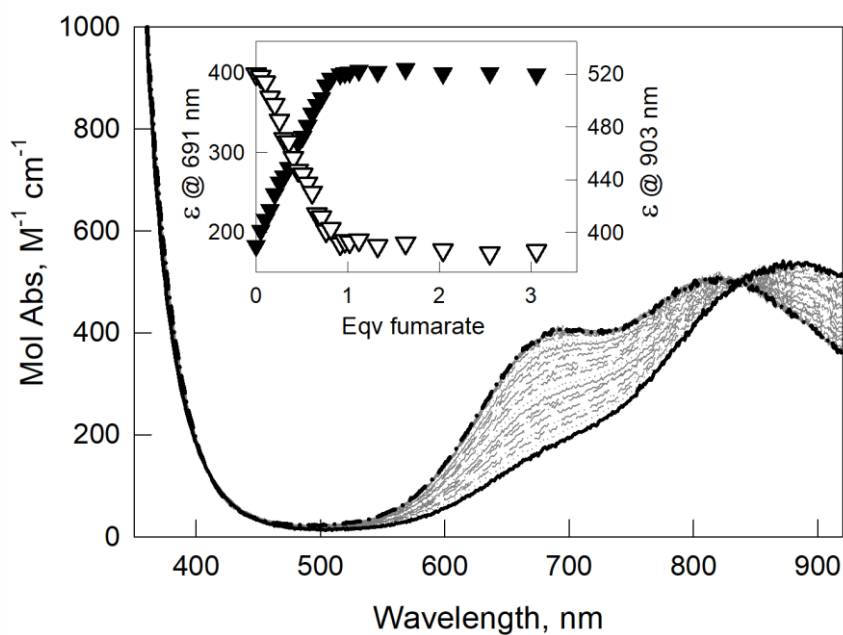


Figure 20. UV-vis. spectra taken upon the titration of $[\text{Cu}_2(\text{L1})]^{4+}$ (0.50 mM) with fumaric acid (50 mM) in water at pH 7 (0.05 M HEPES buffer, path length 1 cm). The solid and dashed black lines represent the spectra at 0 and 3 *eqv.* of the added anion, respectively. **Inset:** titration profiles of ϵ (*i.e.* Mol Abs) at 691 nm (filled triangles) and 903 nm (empty triangles) vs *eqv.* of the added anion.

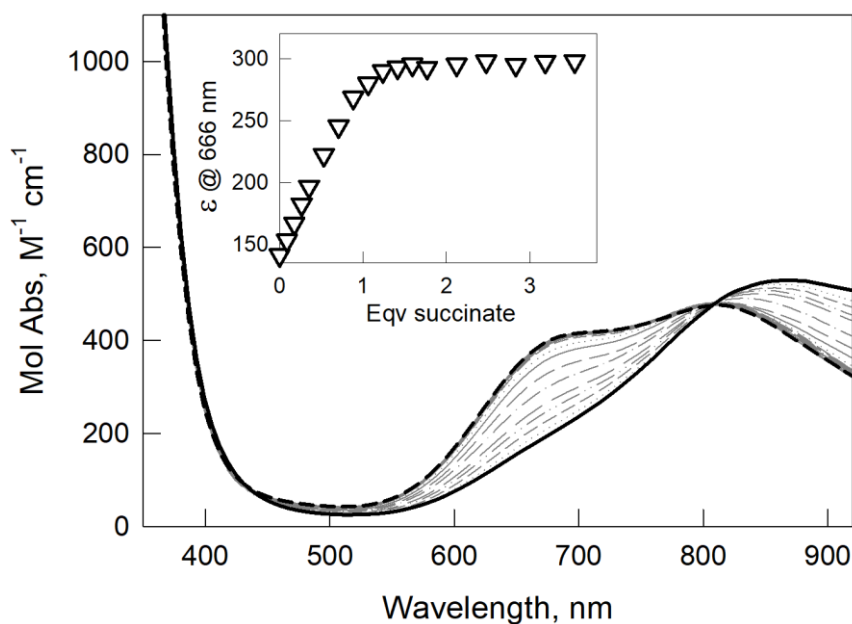


Figure 21. UV-vis. spectra taken upon the titration of $[\text{Cu}_2(\text{L1})]^{4+}$ (50 μM) with succinic acid (5 mM) in water at pH 7 (0.05 M HEPES buffer, path length 10 cm). The solid and dashed black lines represent the spectra at 0 and 4 *eqv.* of the added anion, respectively. **Inset:** titration profile of ϵ (*i.e.* Mol Abs) at 666 nm (empty triangles) vs *eqv.* of the added anion.

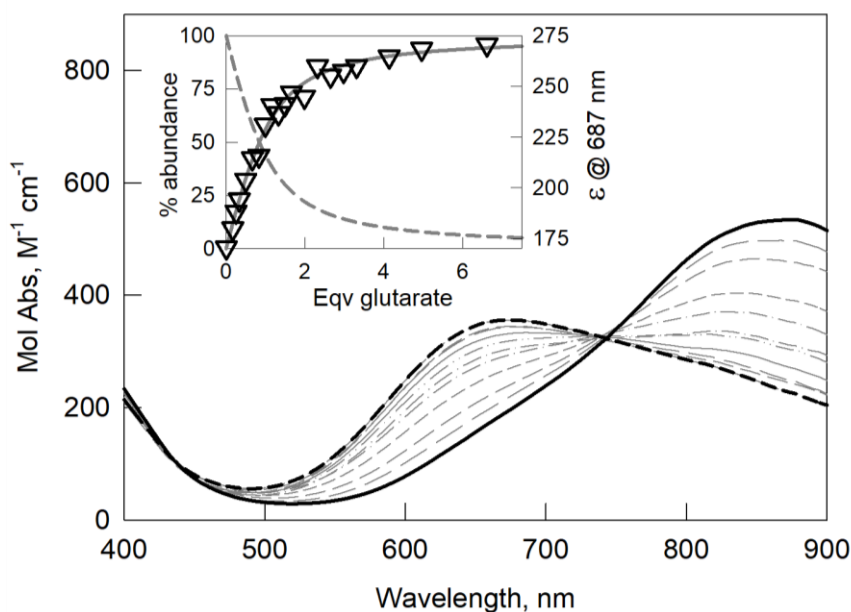


Figure 22. UV-vis. spectra taken upon the titration of $[\text{Cu}_2(\text{L1})]^{4+}$ ($50 \mu\text{M}$) with glutaric acid (5 mM) in water at pH 7 (0.05 M HEPES buffer, path length 10 cm). The solid and dashed black lines represent the spectra at 0 and 7 *eqv.* of the added anion, respectively. **Inset:** titration profile of ϵ (*i.e.* Mol Abs) at 687 nm (empty triangles) with superimposed distribution diagram of the species $[\text{Cu}_2(\text{L1})]^{4+}$ (dashed line) and $[\text{Cu}_2(\text{L1})(\text{glut})]^{2+}$ (solid line) *vs eqv.* of the added guest, calculated for $\text{Log}K_{11}=5.39(1)$.

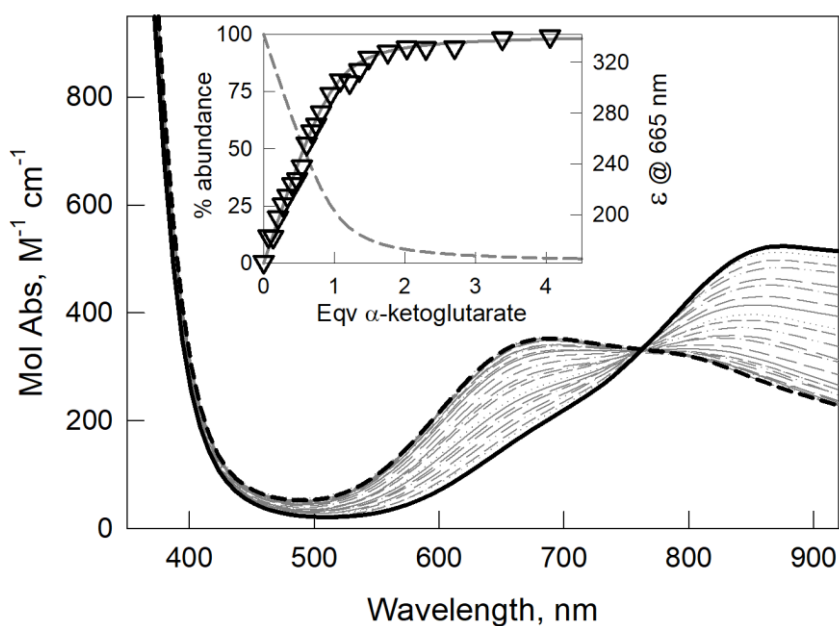


Figure 23. UV-vis. spectra taken upon the titration of $[\text{Cu}_2(\text{L1})]^{4+}$ ($20 \mu\text{M}$) with α -ketoglutaric acid (5 mM) in water at pH 7 (0.05 M HEPES buffer, path length 10 cm). The solid and dashed black lines represent the spectra at 0 and 4 *eqv.* of the added anion, respectively. **Inset:** titration profile of ϵ (*i.e.* Mol Abs) at 665 nm (empty triangles) with superimposed distribution diagram of the species $[\text{Cu}_2(\text{L1})]^{4+}$ (dashed line) and $[\text{Cu}_2(\text{L1})(\alpha\text{-keto})]^{2+}$ (solid line) *vs eqv.* of the added guest, calculated for $\text{Log}K_{11}=6.00(1)$.

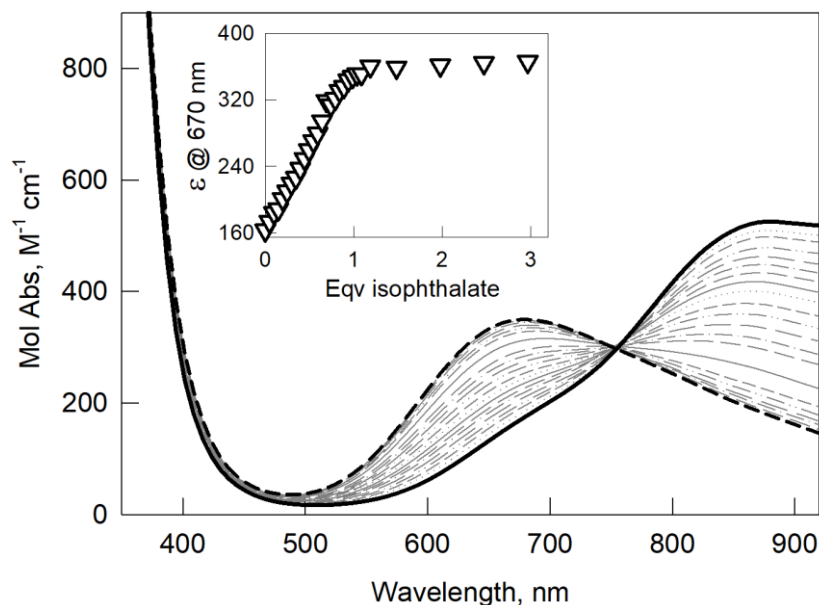


Figure 24. UV-vis. spectra taken upon the titration of $[\text{Cu}_2(\text{L1})]^{4+}$ (0.50 mM) with isophthalate (as Na^+ salt, 50 mM) in water at pH 7 (0.05 M HEPES buffer, path length 1 cm). The solid and dashed black lines represent the spectra at 0 and 3 *eqv.* of the added anion, respectively. **Inset:** titration profile of ϵ (*i.e.* Mol Abs) at 670 nm (empty triangles) vs *eqv.* of the added anion.

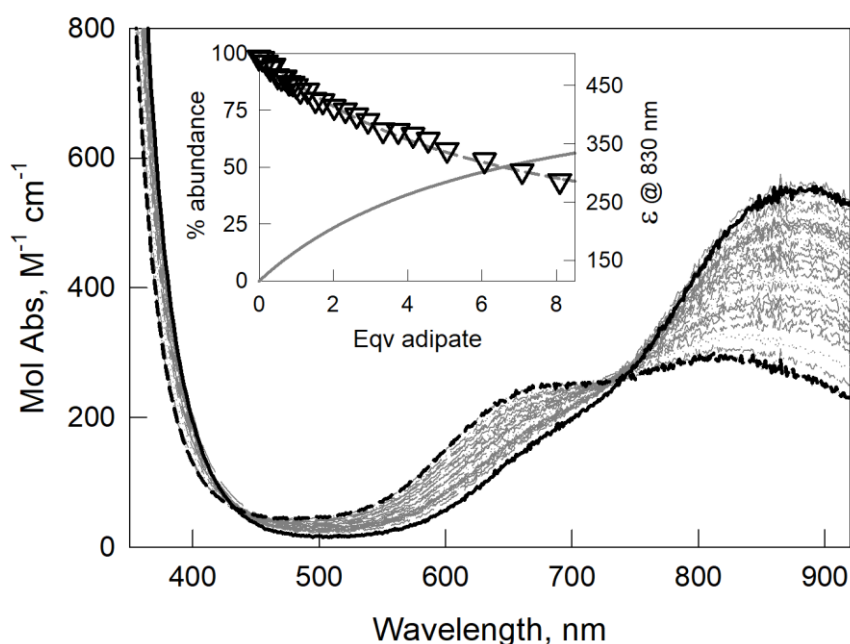


Figure 25. UV-vis. spectra taken upon the titration of $[\text{Cu}_2(\text{L1})]^{4+}$ (0.55 mM) with adipic acid (50 mM) in water at pH 7 (0.05 M HEPES buffer, path length 1 cm). The solid and dashed black lines represent the spectra at 0 and 8 *eqv.* of the added anion, respectively. **Inset:** titration profile of ϵ (*i.e.* Mol Abs) at 830 nm (empty triangles) with superimposed distribution diagram of the species $[\text{Cu}_2(\text{L1})]^{4+}$ (dashed line) and $[\text{Cu}_2(\text{L1})(\text{adi})]^{2+}$ (solid line) vs *eqv.* of the added guest, calculated for $\text{Log}K_{11}=2.58(1)$.

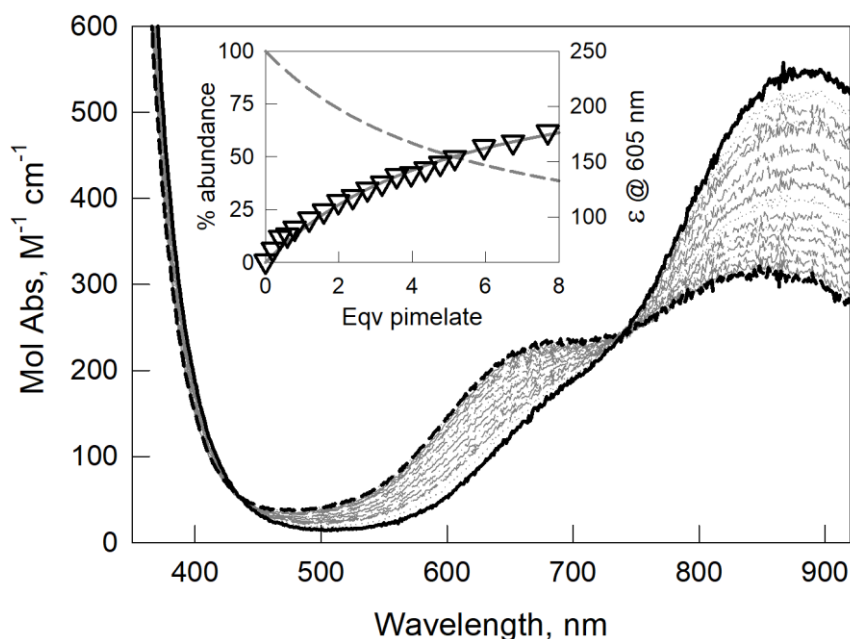


Figure 26. UV-vis. spectra taken upon the titration of $[\text{Cu}_2(\text{L1})]^{4+}$ (0.50 mM) with pimelic acid (0.20 M) in water at pH 7 (0.05 M HEPES buffer, path length 1 cm). The solid and dashed black lines represent the spectra at 0 and 8 *eqv.* of the added anion, respectively. **Inset:** titration profile of ϵ (*i.e.* Mol Abs) at 605 nm (empty triangles) with superimposed distribution diagram of the species $[\text{Cu}_2(\text{L1})]^{4+}$ (dashed line) and $[\text{Cu}_2(\text{L1})(\text{pim})]^{2+}$ (solid line) vs *eqv.* of the added guest, calculated for $\text{Log}K_{11}=2.64(8)$.

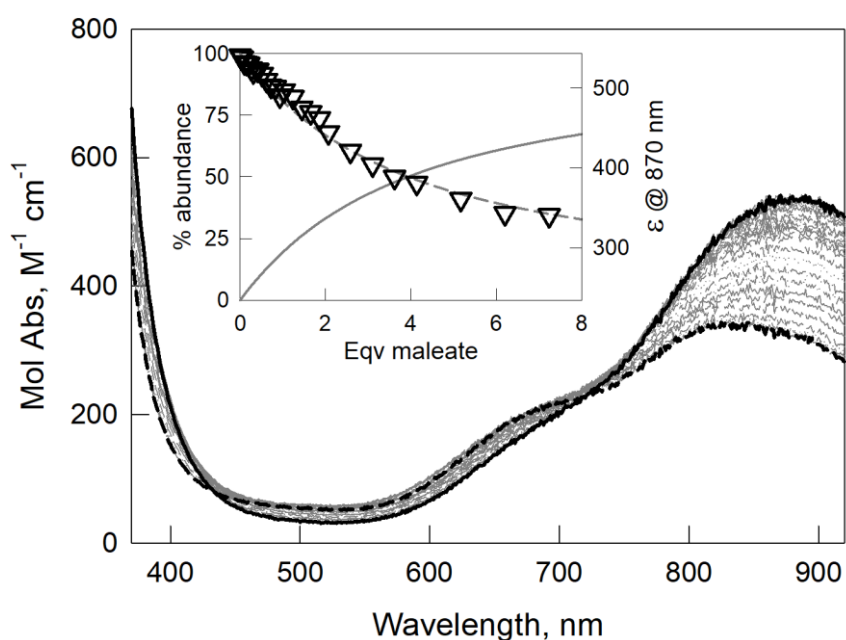


Figure 27. UV-vis. spectra taken upon the titration of $[\text{Cu}_2(\text{L1})]^{4+}$ (0.50 mM) with maleic acid (50 mM) in water at pH 7 (0.05 M HEPES buffer, path length 1 cm). The solid and dashed black lines represent the spectra at 0 and 8 *eqv.* of the added anion, respectively. **Inset:** titration profile of ϵ (*i.e.* Mol Abs) at 870 nm (empty triangles) with superimposed distribution diagram of the species $[\text{Cu}_2(\text{L1})]^{4+}$ (dashed line) and $[\text{Cu}_2(\text{L1})(\text{male})]^{2+}$ (solid line) vs *eqv.* of the added guest, calculated for $\text{Log}K_{11}=2.78(1)$.

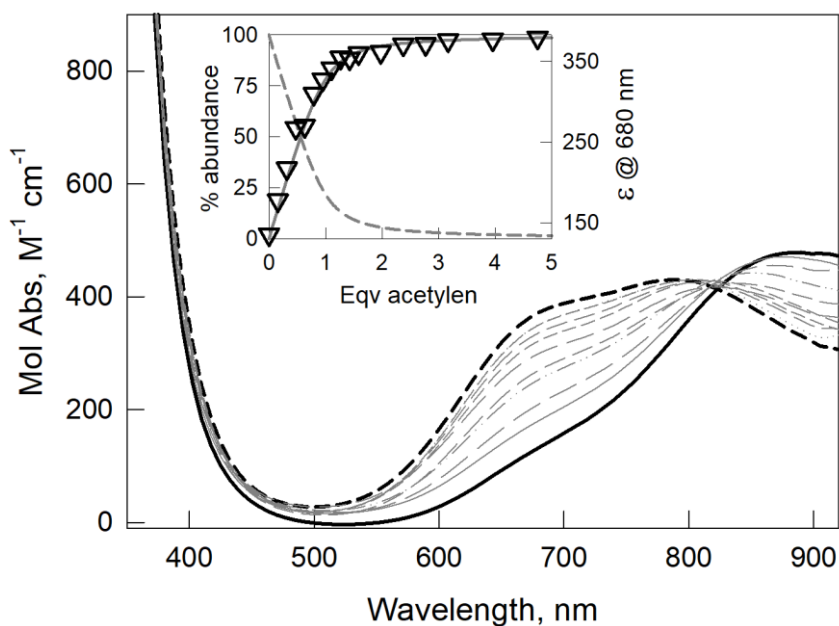


Figure 28. UV-vis. spectra taken upon the titration of $[\text{Cu}_2(\text{L1})]^{4+}$ ($20 \mu\text{M}$) with acetylenedicarboxylic acid (5 mM) in water at pH 7 (0.05 M HEPES buffer, path length 10 cm). The solid and dashed black lines represent the spectra at 0 and 5 *eqv.* of the added anion, respectively. **Inset:** titration profile of ϵ (*i.e.* Mol Abs) at 680 nm (empty triangles) with superimposed distribution diagram of the species $[\text{Cu}_2(\text{L1})]^{4+}$ (dashed line) and $[\text{Cu}_2(\text{L1})(\text{ace})]^{2+}$ (solid line) vs *eqv.* of the added guest, calculated for $\text{Log}K_{11}=5.90(2)$.

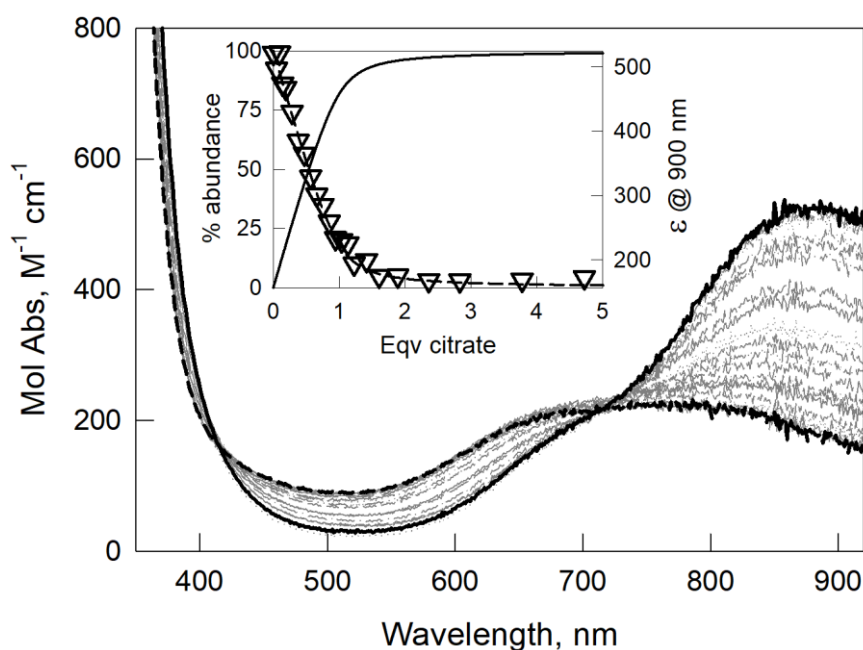


Figure 29. UV-vis. spectra taken upon the titration of $[\text{Cu}_2(\text{L1})]^{4+}$ ($50 \mu\text{M}$) with citric acid (12.5 mM) in water at pH 7 (0.05 M HEPES buffer, path length 10 cm). The solid and dashed black lines represent the spectra at 0 and 5 *eqv.* of the added anion, respectively. **Inset:** titration profile of ϵ (*i.e.* Mol Abs) at 900 nm (empty triangles) with superimposed distribution diagram of the species $[\text{Cu}_2(\text{L1})]^{4+}$ (dashed line) and $[\text{Cu}_2(\text{L1})(\text{cit})]^+$ (solid line) vs *eqv.* of the added guest, calculated for $\text{Log}K_{11}=5.70(1)$.

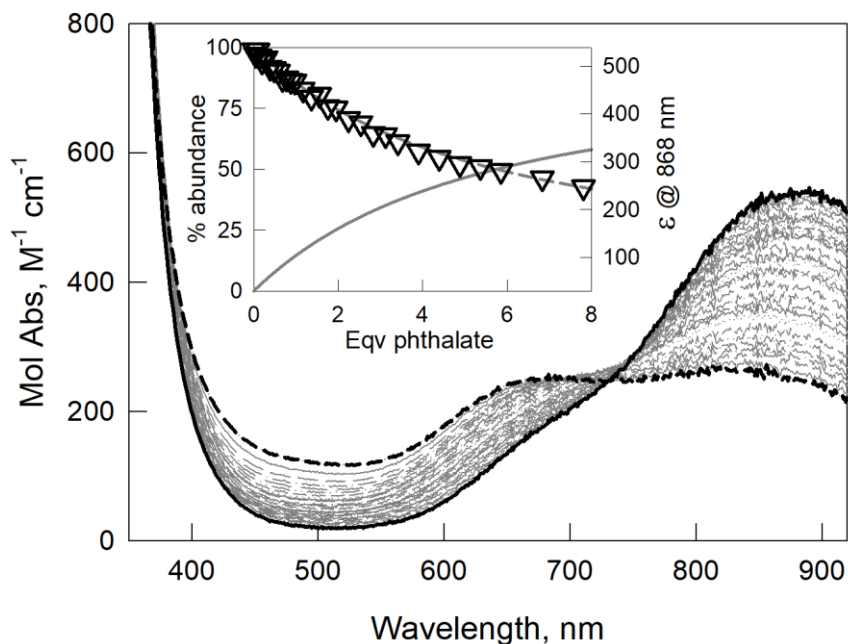


Figure 30. UV-vis. spectra taken upon the titration of $[\text{Cu}_2(\text{L1})]^{4+}$ (0.50 mM) with phthalate (as Na^+ salt, 50 mM) in water at pH 7 (0.05 M HEPES buffer, path length 1 cm). The solid and dashed black lines represent the spectra at 0 and 8 *eqv.* of the added anion, respectively. **Inset:** titration profile of ϵ (*i.e.* Mol Abs) at 868 nm (empty triangles) with superimposed distribution diagram of the species $[\text{Cu}_2(\text{L1})]^{4+}$ (dashed line) and $[\text{Cu}_2(\text{L1})(\text{pht})]^{2+}$ (solid line) *vs eqv.* of the added guest, calculated for $\text{Log}K_{11}=2.59(1)$.

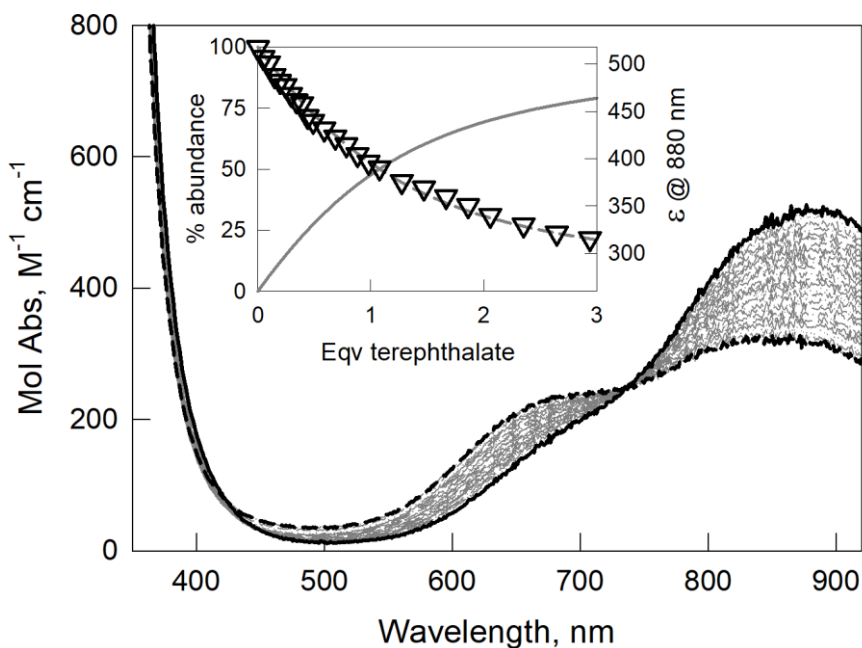
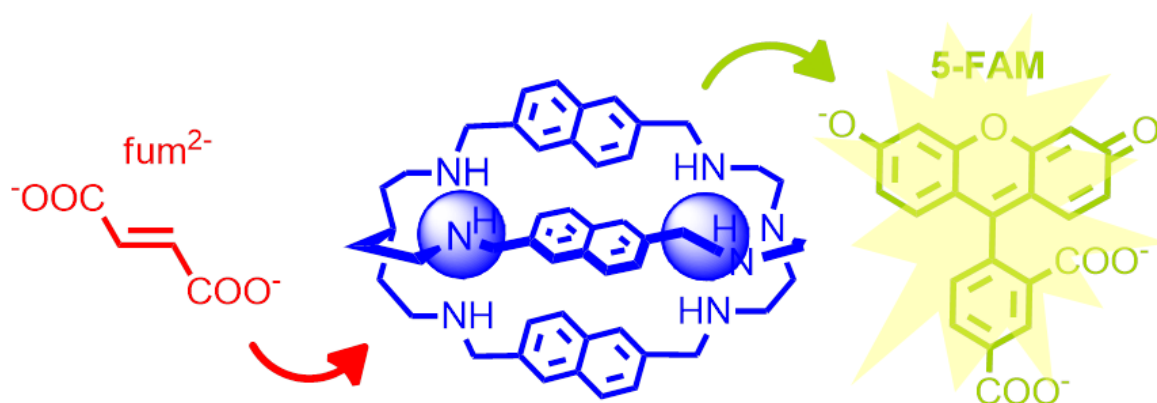


Figure 31. UV-vis. spectra taken upon the titration of $[\text{Cu}_2(\text{L1})]^{4+}$ (0.50 mM) with terephthalate (as Na^+ salt, 50 mM) in water at pH 7 (0.05 M HEPES buffer, path length 1 cm). The solid and dashed black lines represent the spectra at 0 and 3 *eqv.* of the added anion, respectively. **Inset:** titration profile of ϵ (*i.e.* Mol Abs) at 880 nm (empty triangles) with superimposed distribution diagram of the species $[\text{Cu}_2(\text{L1})]^{4+}$ (dashed line) and $[\text{Cu}_2(\text{L1})(\text{terephth})]^{2+}$ (solid line) *vs eqv.* of the added guest, calculated for $\text{Log}K_{11}=3.54(1)$.

3.3.4 Spectrofluorimetric studies on $[\text{Cu}_2(\text{L1})]^{4+}$ with 5-FAM and dicarboxylates

As reported in the previous section, spectrophotometric titrations did not allow an accurate calculation of the binding constants with a series of anions, *i.e.* fum^{2-} , suc^{2-} and isoph^{2-} . However, we could overcome this issue by applying the fluorescent Indicator Displacement Approach (IDA), which is based on the competition between a chosen fluorescent indicator and a specific guest for the binding to a selective receptor.^{33,34} In our case, the chosen indicator is an organic fluorophore, containing a dicarboxylate unit which can strongly interact with $[\text{Cu}_2(\text{L1})]^{4+}$ forming a stable 1:1 complex. In presence of a guest with a stronger affinity for the receptor cavity, the indicator is displaced from the cavity, thus causing detectable optical changes proportional to the guest concentration. 5-Carboxyfluorescein (5-FAM) was chosen as the indicator, because its isophthalate moiety can strongly bind to the azacryptate cavity, as previously confirmed by the crystal structure of the inclusion complex of $[\text{Cu}_2(\text{L1})]^{4+}$ with isoph^{2-} (see Scheme 1).



Scheme 1. Displacement of 5-FAM from $[\text{Cu}_2(\text{L1})]^{4+}$ cavity promoted by the fumarate anion.

The affinity of 5-FAM for $[\text{Cu}_2(\text{L1})]^{4+}$ was first verified in neutral aqueous solution by performing the UV-vis. titration of 5-FAM with a standard solution of $[\text{Cu}_2(\text{L1})]^{4+}$ (0.05 M HEPES buffer, pH 7). As shown in Fig. 32, over the course of the titration, the band below 300 nm relative to the dicopper(II) complex (*i.e.* $N_{\text{sec}} \rightarrow \text{Cu(II)}$ LMCT band) grows in intensity, while subtle changes in the absorption band of 5-FAM (at 490 nm) are observed.

The family of spectra displays an isosbestic point at 473 nm, that was chosen as the excitation wavelength (*i.e.* λ_{exc}) for further fluorimetric experiments.

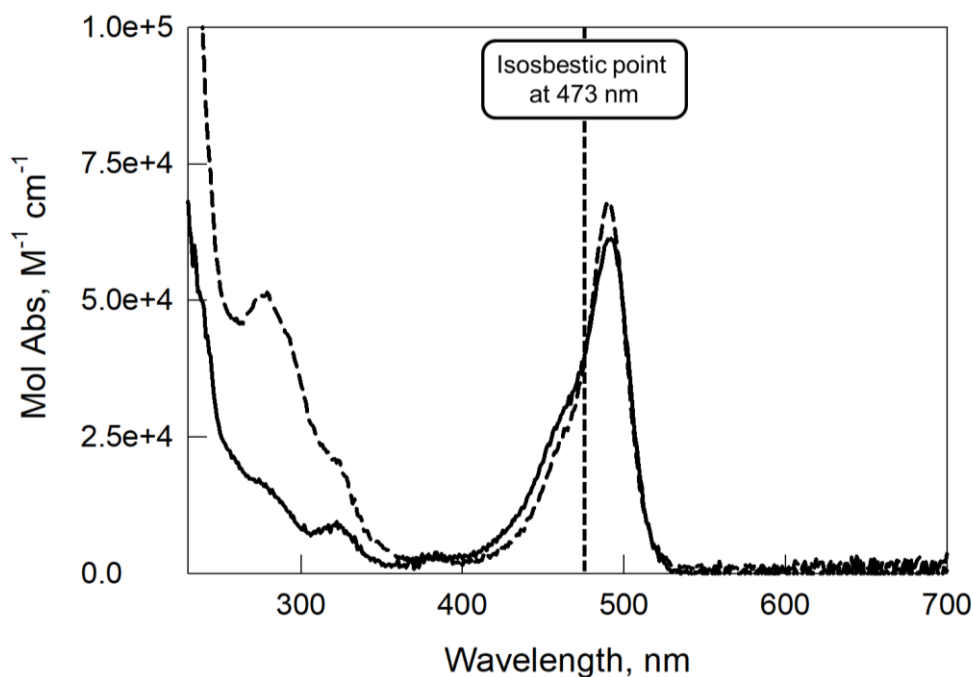


Figure 32. UV-vis. titration of 5-FAM 1 μM with a solution of the in-situ prepared $[\text{Cu}_2(\text{L1})]^{4+}$ complex. (0.05 M HEPES buffer, pH 7, path length 1 cm). Solid and dashed black lines represent the initial and final spectra of the titration, respectively.

For the determination of the association constant between $[\text{Cu}_2(\text{L1})]^{4+}$ and 5-FAM, a solution of the indicator was titrated with a solution of the dicopper(II) complex in buffered aqueous solution (0.05 M HEPES buffer, pH 7). Figure 33 shows the family of emission spectra and the corresponding titration profile at 520 nm ($\lambda_{\text{exc}} = 473$ nm) vs equivalents of the added complex. As expected, a gradual decrease of the 5-FAM emission was observed over the course of the titration: the coordination of the dicarboxylate moiety of 5-FAM to the Cu(II) ions, within the cage cavity, promotes the quenching process, as already observed in similar systems.^{32,36,49} A complete quenching is reached under addition of two equivalents of $[\text{Cu}_2(\text{L1})]^{4+}$. The best fitting of the titration profile points out the formation of a 1:1 complex $[\text{Cu}_2(\text{L1})(5\text{-FAM})]^+$, with an association constant of 7.20(2) Log units.

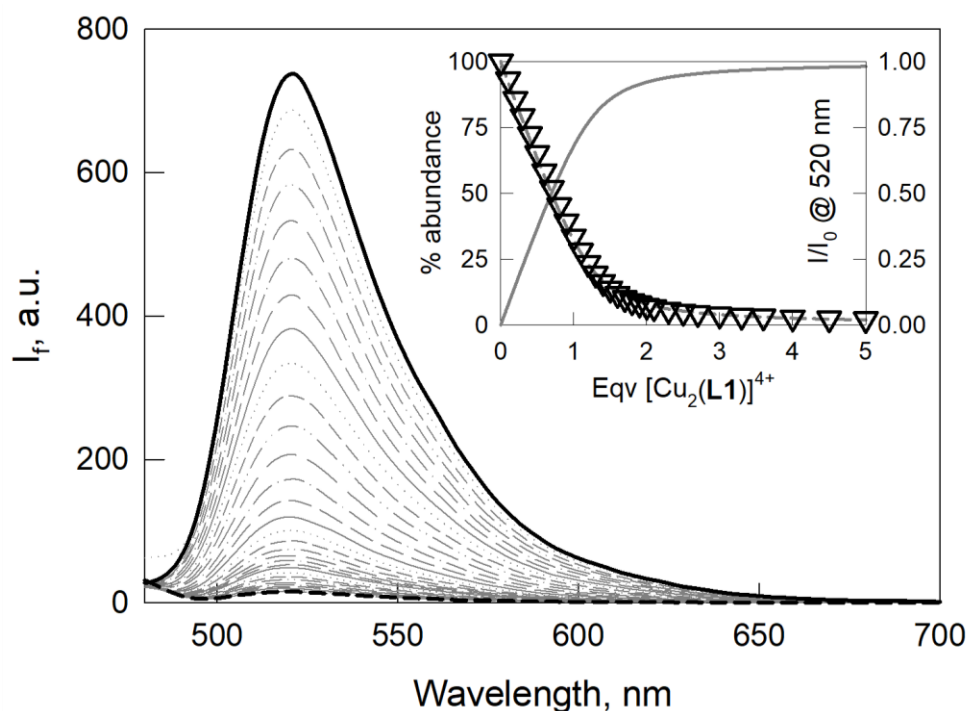


Figure 33. Family of spectra taken upon the fluorimetric titration of 5-FAM (1 μ M) with $[\text{Cu}_2(\text{L1})]^{4+}$ (0.50 mM) in 0.05 M HEPES buffer at pH 7 ($\lambda_{\text{exc}} = 473$ m; $\lambda_{\text{em}} = 520$ nm). The solid and dashed black lines represent the spectra at 0 and 5 *eqv.* of the added dicopper complex, respectively. **Inset:** Titration profile of I/I_0 at 520 nm (empty triangles) vs *eqv.* of the added dicopper complex, superimposed to the distribution diagram of the species, calculated for a 1:1 association constant of 7.20(2) Log units. Solid line: % $[\text{Cu}_2(\text{L1})(5\text{-FAM})]^{3+}$; dashed line: % free 5-FAM.

Fluorimetric titrations with dicarboxylates were then performed on a stock solution of 5-FAM (0.1 μ M) containing 50 *eqv.* of the dicopper(II) cryptate. The 1:50 indicator:complex molar ratio was chosen to ensure the complete quenching of the indicator emission. Interestingly, among the tested dicarboxylates, only fum^{2-} , suc^{2-} and isoph^{2-} caused a significant restoration of the 5-FAM fluorescence. In fact, only strongly binding anions (such as fum^{2-} , suc^{2-} and isoph^{2-}) can effectively displace the indicator from the cryptate cavity. On the other hand, under titrations with weakly binding anions (*e.g.* adi^{2-} , male^{2-} and cit^{3-}), a significant restoration of the fluorophore emission is only observed under addition of a large excess of the titrant solution. This *trend* is clearly represented by Figure 34, in which a comparison among all the tested dicarboxylates is reported.

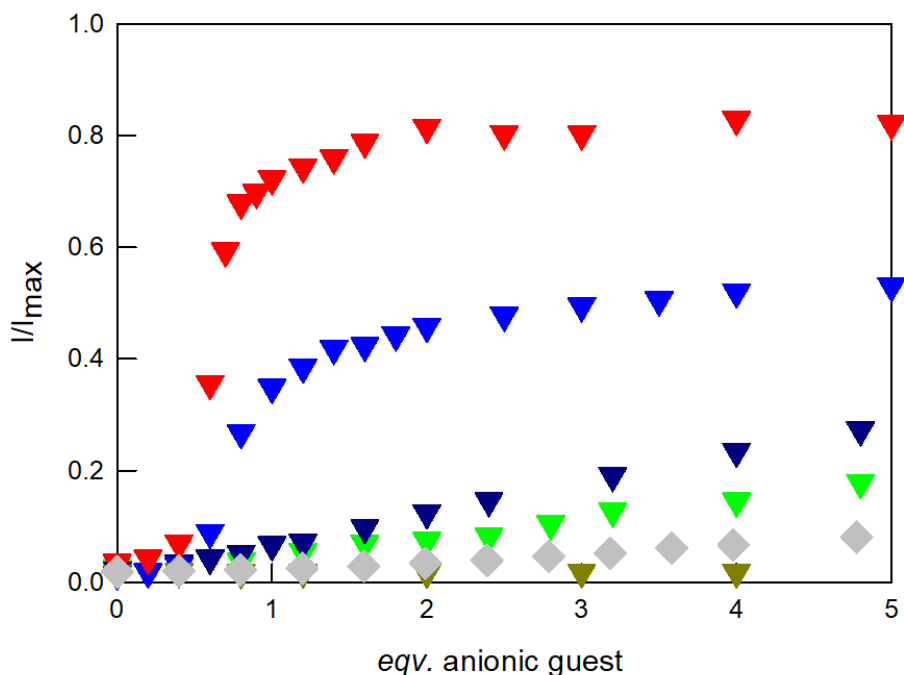
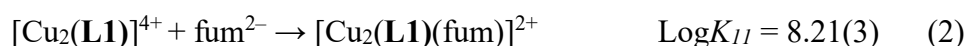
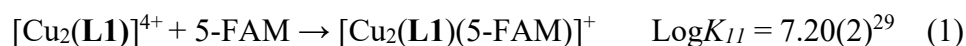


Figure 34. Profiles of the spectrofluorimetric titrations of the indicator displacement assay (0.1 μM 5-FAM, 5 μM $[\text{Cu}_2(\mathbf{L1})]^{4+}$) with solutions of the anionic guests in 0.05 M HEPES buffer at pH 7 (fum²⁻ = red triangles, suc²⁻ = blue triangles; α -keto²⁻ = dark blue triangles; glut²⁻ = green triangles; adi²⁻ = dark green triangles; cit³⁻ = grey diamonds). I = emission intensity; I_{max} = emission intensity of a solution of 5-FAM in the absence of the dicopper complex ($\lambda_{\text{exc}} = 473 \text{ nm}$; $\lambda_{\text{em}} = 520 \text{ nm}$).

An example of fluorimetric titration of the $[\text{Cu}_2(\mathbf{L1})]^{4+}$:5-FAM ensemble with dicarboxylates, in particular with fum²⁻, is reported in Figure 35 (I = point-by-point emission intensity; I_{max} = emission intensity of the indicator in the absence of the dicopper complex). Starting from the quenched 5-FAM emission (dashed black line), the fluorescence is progressively restored under anion addition (grey solid line).

The binding constant between $[\text{Cu}_2(\mathbf{L1})]^{4+}$ and fum²⁻ was determined by elaborating the titration data through the Hyperquad package.⁴² Two competing equilibria were considered for the treatment, involving the dicopper(II) complex, the indicator and the guest (see equations (1) and (2)). The $\text{Log}K_{11}$ for fum²⁻ binding resulted to be 8.21(3).



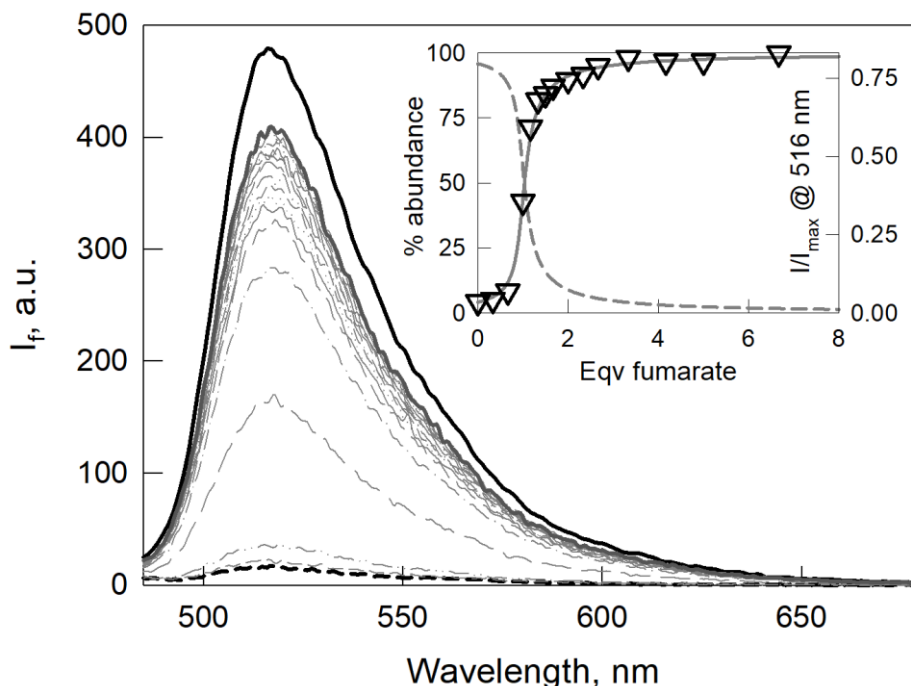


Figure 35. Family of emission spectra taken over the course of the titration of the indicator displacement assay (0.1 μM 5-FAM, 5 μM $[\text{Cu}_2(\text{L1})]^{4+}$) with fumaric acid in 0.05 M HEPES buffer at pH 7 ($\lambda_{\text{exc}} = 473 \text{ nm}$; $\lambda_{\text{em}} = 520 \text{ nm}$). Solid black line: spectrum of 5-FAM; dashed black line: initial spectrum of the chemosensing ensemble; solid dark grey line: final spectrum after addition of 8 *eqv.* of anion. **Inset:** titration profile of I/I_{max} at 516 nm *vs eqv.* of the added anion (I_{max} = maximum emission intensity of the indicator, taken in the same conditions and in the absence of the dicopper complex), superimposed to the distribution diagram of the species, calculated for a 1:1 association constant with fumarate of 8.21(3) Log units ($\text{Log}K_{11} = 7.20$, receptor:5FAM). Solid line: % free 5-FAM; dashed line: % $[\text{Cu}_2(\text{L1})(5\text{-FAM})]^+$.

By the least-squares treatment on the linear section of the fluorimetric titration plot, both limits of detection and quantification (*i.e.* LOD and LOQ, respectively) could be determined through the IUPAC method: $\text{LOD} = 3\sigma/s$ and $\text{LOQ} = 10\sigma/s$, where σ = standard deviation of the blank; s = slope of the calibration curve. The LOD and LOQ values calculated for fum^{2-} resulted to be 0.03 μM and 0.10 μM , respectively, revealing a very high sensitivity of this method for fum^{2-} detection.

The calibration curve, obtained as average of three independent experiments, is reported in Figure 36: even if standard deviation of the points on average concentrations is particularly high, a good linearity was found in the concentration range 3.3-3.8 μM .

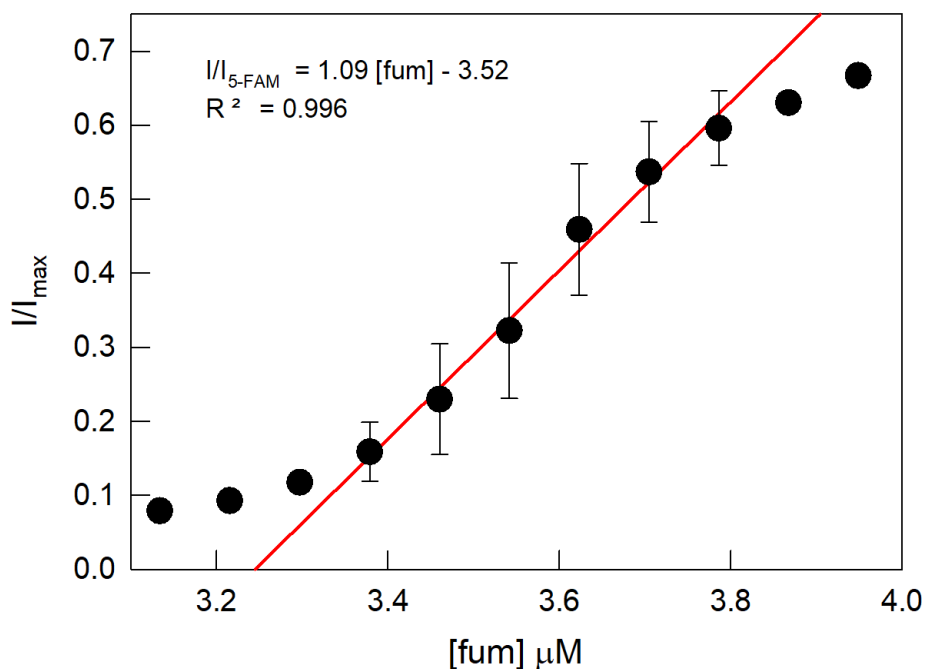


Figure 36. Fumarate calibration curve⁵ (red line: fitting curve; dots: experimental data), obtained from the fluorimetric titrations of the indicator displacement assay ($5 \mu\text{M}$ $[\text{Cu}_2\text{L}]^{4+}$ and $0.1 \mu\text{M}$ 5-FAM) with fumaric acid in 0.05 M HEPES buffer, pH 7 ($\lambda_{\text{exc}} = 473 \text{ nm}$; $\lambda_{\text{em}} = 520 \text{ nm}$). I_{MAX} = fluorescence intensity of a $0.1 \mu\text{M}$ 5-FAM solution (recorded before the addition of $[\text{Cu}_2(\text{L1})]^{4+}$). The plotted parameters are linearly correlated when I/I_{MAX} is between ~ 0.15 and 0.6 ($R^2 = 0.996$). Data are averages of $n = 3$; error bars represent s.d..

The data treatment allowed us to determine the binding constants with all the dicarboxylates reported in Table 8. The titration profiles for the fluorimetric titrations with suc^{2-} , isopht^{2-} and $\alpha\text{-keto}^{2-}$, superimposed to the relative distribution diagram of the species, are reported in Figures 37-39.

Through the Indicator Displacement Approach, the binding constants for fum^{2-} , suc^{2-} and isopht^{2-} were accurately determined. These experiments highlighted the selectivity of the dicopper(II) complex $[\text{Cu}_2(\text{L1})]^{4+}$ for the fum^{2-} anion, with a $\text{Log}K_{11}$ of $8.21(3)$, followed by suc^{2-} and isopht^{2-} (*i.e.* $\text{Log}K_{11} = 7.38(3)$ and $7.20(4)$, respectively). The binding constants calculated for $\alpha\text{-keto}^{2-}$, ace^{2-} and glut^{2-} are in accordance with the values obtained by UV-vis. titrations. On the other hand, the changes in the fluorescence emission under titrations with adi^{2-} and male^{2-} were too small to allow a safe determination of the binding constants.

Table 8. Conditional binding constants (as $\text{Log}K_{11}$ values) obtained by either UV-vis. titrations on $[\text{Cu}_2(\text{L1})]^{4+}$ with the anionic guests or fluorimetric indicator displacement titrations with selected anions; 5-FAM was used as the fluorescent indicator.

guest	$\text{Log}K_{11}$ UV-vis.	$\text{Log}K_{11}$ fluo
fum ²⁻	> 6	8.21(3)
suc ²⁻	> 6	7.38(3)
isoph ²⁻	> 6	7.20(4)
α -keto ²⁻	6.00(1)	5.95(3)
ace ²⁻	5.90(2)	5.71(3)
glut ²⁻	5.39(1)	5.40(4)
adi ²⁻	2.58(1)	n.a.
male ²⁻	2.78(1)	n.a.

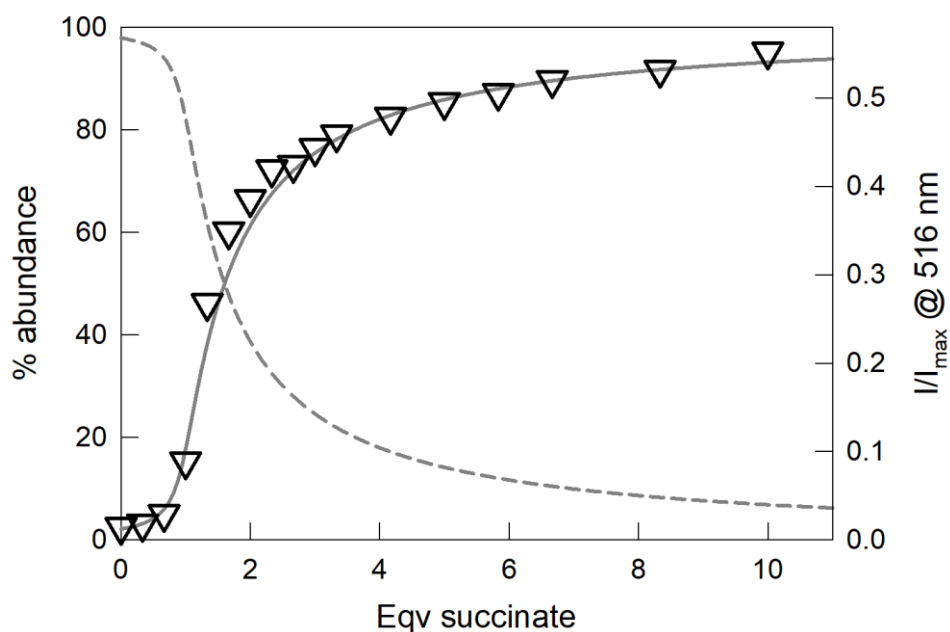


Figure 37. Titration profile of the indicator displacement assay ($0.1 \mu\text{M}$ 5-FAM, $5 \mu\text{M}$ $[\text{Cu}_2(\text{L1})]^{4+}$) with succinate in 0.05 M HEPES buffer at pH 7 ($\lambda_{\text{exc}} = 473 \text{ m}$; $\lambda_{\text{em}} = 520 \text{ nm}$), empty triangles: titration profile as I/I_{max} at 516 nm vs eqv. of the added anion (I_{max} = maximum emission intensity of the indicator, taken in the same conditions and in the absence of the dicopper complex), superimposed to the distribution diagram of the species, calculated for a 1:1 association constant with succinate of 7.38(3) Log units ($\text{Log}K_{11} = 7.2$, receptor:5FAM). Solid line: % free 5-FAM; dashed line: % $[\text{Cu}_2(\text{L1})(5\text{-FAM})]^+$.

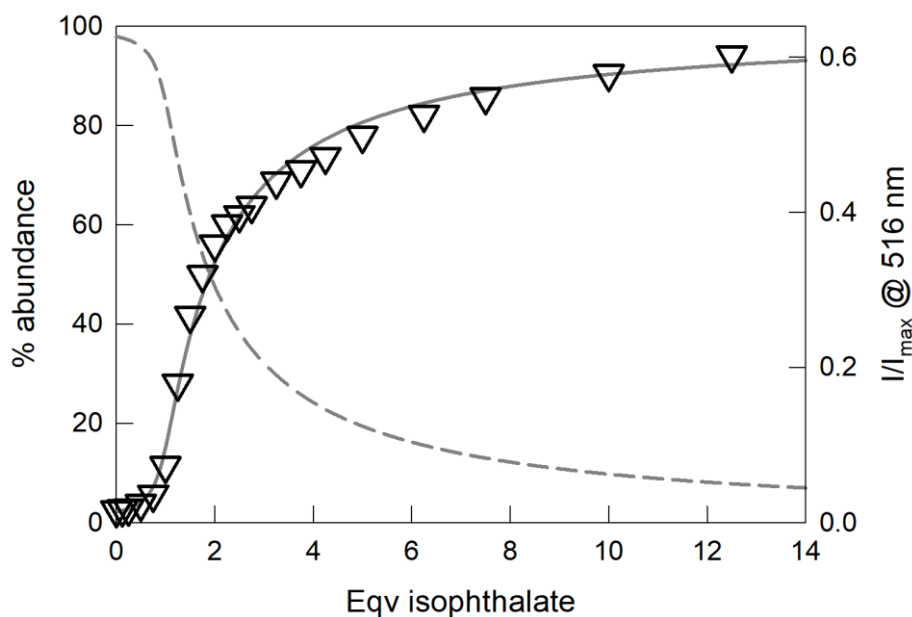


Figure 38. Titration profile of the indicator displacement assay ($0.1 \mu\text{M}$ 5-FAM, $5 \mu\text{M}$ $[\text{Cu}_2(\text{L1})]^{4+}$) with isophthalate in 0.05 M HEPES buffer at $\text{pH } 7$ ($\lambda_{\text{exc}} = 473 \text{ m}$; $\lambda_{\text{em}} = 520 \text{ nm}$), empty triangles: titration profile as I/I_{max} at 516 nm vs *eqv.* of the added anion (I_{max} = maximum emission intensity of the indicator, taken in the same conditions and in the absence of the dicopper complex), superimposed to the distribution diagram of the species, calculated for a 1:1 association constant with isophthalate of $7.20(4)$ Log units ($\text{Log}K_{11} = 7.2$, receptor:5FAM). Solid line: % free 5-FAM; dashed line: % $[\text{Cu}_2(\text{L1})(5\text{-FAM})]^+$.

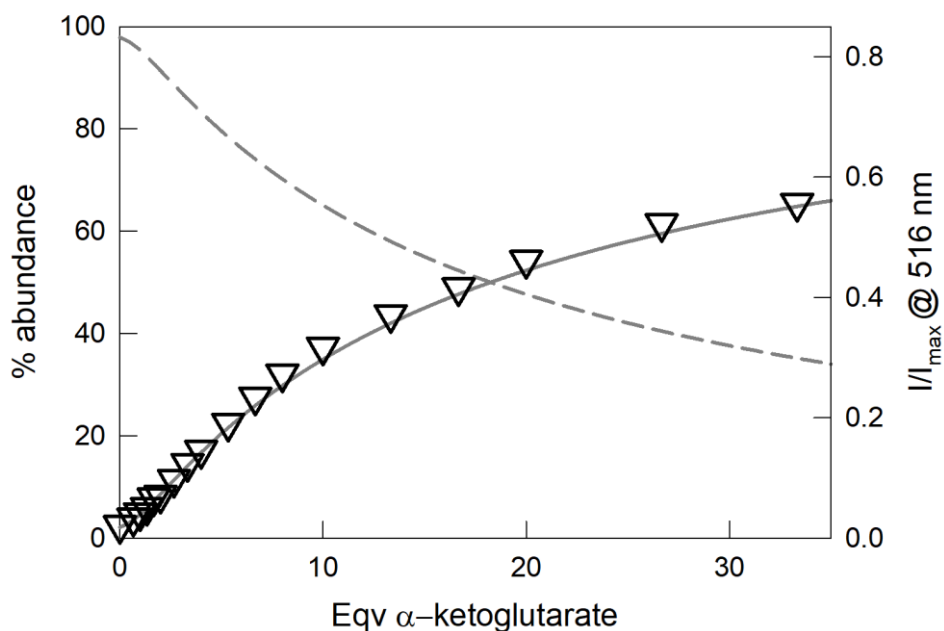


Figure 39. Titration profile of the indicator displacement assay ($0.1 \mu\text{M}$ 5-FAM, $5 \mu\text{M}$ $[\text{Cu}_2(\text{L1})]^{4+}$) with α -ketoglutarate in 0.05 M HEPES buffer at $\text{pH } 7$ ($\lambda_{\text{exc}} = 473 \text{ m}$; $\lambda_{\text{em}} = 520 \text{ nm}$), empty triangles: titration profile as I/I_{max} at 516 nm vs *eqv.* of the added anion (I_{max} = maximum emission intensity of the indicator, taken in the same conditions and in the absence of the dicopper complex), superimposed to the distribution diagram of the species, calculated for a 1:1 association constant with α -ketoglutarate of $5.95(3)$ Log units ($\text{Log}K_{11} = 7.2$, receptor:5FAM). Solid line: % free 5-FAM; dashed line: % $[\text{Cu}_2(\text{L1})(5\text{-FAM})]^+$.

3.4 Conclusions

To conclude, an accurate investigation on the binding properties of the dicopper(II) complex $[\text{Cu}_2(\text{L1})]^{4+}$ towards carboxylates was performed in neutral aqueous solution. X-ray diffraction studies on single crystals of the $[\text{Cu}_2(\text{L1})]^{4+}$:anion adducts with glut^{2-} , $\alpha\text{-keto}^{2-}$, isopht^{2-} and ace^{2-} confirmed the inclusion of the guests in the cage's cavity and gave interesting insights on the coordination geometries assumed by the two metal ions during the binding, that were confirmed also by UV-vis. studies.

Spectrophotometric titrations of the $[\text{Cu}_2(\text{L1})]^{4+}$ complex with a series of carboxylates in buffered water (*i.e.* 0.05 M HEPES buffer, pH 7) showed the formation of stable 1:1 complex:anion adducts with all the anions. Interestingly, a very high affinity was found for dicarboxylates with four and five carbon atoms in chain; in particular, for fum^{2-} , suc^{2-} and isopht^{2-} , the resulting titration profiles were too steep to allow a safe calculation of the binding constants.

In order to overcome this issue, the well-known Indicator Displacement Approach was applied. Fluorimetric titrations on the chemosensing ensemble formed by the $[\text{Cu}_2(\text{L1})]^{4+}$ complex with the fluorescent indicator 5-FAM were performed in buffered water (0.05 M HEPES buffer, pH 7). Through this method, the $\text{Log}K_{11}$ for fum^{2-} , suc^{2-} and isopht^{2-} were accurately determined and resulted to be 8.21, 7.38 and 7.20, respectively. Notably, an effective displacement of the indicator was observed only under addition of these anions. This can be attributed to the strong interaction between the dicopper(II) cryptate and 5-FAM ($\text{Log}K_{11} = 7.20$): only the anions that exhibit a greater affinity for $[\text{Cu}_2(\text{L1})]^{4+}$ are able to displace the indicator from the receptor cavity. For other dicarboxylates, the obtained binding constants are in accordance with the values calculated from UV-vis. titrations. In these cases, a significant fluorescence increase is only observed under addition of a large excess of titrant to the cage in solution.

The very high affinity of the $[\text{Cu}_2(\text{L1})]^{4+}$ complex for fum^{2-} , with a remarkable binding constant of 8.2 Log units, allows to employ the chemosensing ensemble $[\text{Cu}_2(\text{L1})]^{4+}$:5-FAM for the selective sensing of fumarate in water. Notably, through the construction of a calibration curve, a LOD value of 0.03 μM was determined, thus highlighting the promising performance of this supramolecular system for the detection of this anion in water.

The research described in this chapter was published in *ACS Omega*, 2020, 5, 41, 26573.

References

- [1] Jean-Marie Lehn. *Supramolecular Chemistry: Concepts and Perspectives*; Wiley-VCH: Weinheim, Germany, 1995.
- [2] Beer, P. D.; Gale, P. A. Anion Recognition and Sensing: The State of the Art and Future Perspectives, *Angew. Chem. Int. Ed.*, **2001**, *40*, 486–516. DOI:10.1002/1521-3773(20010202)40:3<486::AID-ANIE486>3.0.CO;2-P.
- [3] Schmidtchen, F. P. Inclusion of Anions in Macrotricyclic Quaternary Ammonium Salts, *Angew. Chem. Int. Ed. Engl.*, **1977**, *16*, 720. DOI:10.1002/anie.197707201.
- [4] Bowman-James, K.; Bianchi, A.; García-España, E. *Anion Coordination Chemistry*, John Wiley&Sons.; New York, 2012.
- [5] Langton, M. J.; Serpell, C. J.; Beer, P. D. Anion Recognition in Water: Recent Advances from a Supramolecular and Macromolecular Perspective, *Angewandte Chemie International Edition*, **2016**, *55* (6), 1974–1987. DOI:10.1002/anie.201506589.
- [6] Zhao, J.; Yang, D.; Yang, X.-J.; Wu, B. Anion Coordination Chemistry: From Recognition to Supramolecular Assembly, *Coord. Chem. Rev.*, **2019**, *378*, 415–444. DOI:10.1016/j.ccr.2018.01.002.
- [7] Pascal, R. A.; Spergel, J.; Engbersen, D. V. Synthesis and X-Ray Crystallographic Characterization of a (1,3,5)Cyclophane with Three Amide N-H Groups Surrounding a Central Cavity. A Neutral Host for Anion Complexation, *Tetrahedron Lett.*, **1986**, *27*, 4099. DOI:10.1016/S0040-4039(00)84920-5.
- [8] Bisson, A. P.; Lynch, V. M.; Monahan, M.-K. C.; Anslyn, E. V. Recognition of Anions through NH— π Hydrogen Bonds in a Bicyclic Cyclophane—Selectivity for Nitrate, *Angew. Chem. Int. Ed.*, **1997**, *36*, 2340–2343. DOI:10.1002/anie.199723401.
- [9] Oh, J. H.; Kim, J. H.; Kim, D. S.; Han, H. J.; Lynch, V. M.; Sessler, J. L.; Kim, S. K. Synthesis and Anion Recognition Features of a Molecular Cage Containing Both Hydrogen Bond Donors and Acceptors, *Org. Lett.*, **2019**, *21*, 4336–4339. DOI:10.1021/acs.orglett.9b01515.
- [10] Etkind, S. I.; Griend, D. A. V.; Swager, T. M. Electroactive Anion Receptor with High Affinity for Arsenate, *J. Org. Chem.*, **2020**, *85*, 10050–10061. DOI:10.1021/acs.joc.0c01206.
- [11] Kelly, T. R.; Kim, M. H. Relative Binding Affinity of Carboxylate and Its Isosteres: Nitro, Phosphate, Phosphonate, Sulfonate, and Δ -Lactone, *J. Am. Chem. Soc.*, **1994**, *116* (16), 7072–7080. DOI:10.1021/ja00095a009.

- [12] Amendola, V.; Fabbrizzi, L.; Mosca, L. Anion Recognition by Hydrogen Bonding: Urea-Based Receptors, *Chem. Soc. Rev.*, **2010**, *39*, 3889–3915. DOI:10.1039/b822552b.
- [13] Li, R.; Zhao, Y.; Li, S.; Yang, P.; Huang, X.; Yang, X.-J.; Wu, B. Tris Chelating Phosphate Complexes of Bis(Thio)Urea Ligands, *Inorg. Chem.*, **2013**, *52*, 5851–5860. DOI:10.1021/ic3028012.
- [14] Amendola, V.; Bergamaschi, G.; Boiocchi, M.; Fabbrizzi, L.; Milani, M. The Squaramide versus Urea Contest for Anion Recognition, *Chem. Eur. J.*, **2010**, *16*, 4368–4380. DOI:10.1002/chem.200903190.
- [15] Wamhoff, H.; Bamberg, C.; Herrmann, S.; Nieger, M. On the Synthesis of Zwitterionic Heteropolycyclic Pyrazoles by a Three-Component Reaction. Some Mechanistic Considerations, *J. Org. Chem.*, **1994**, *59*, 3985–3993. DOI:10.1021/jo00093a033.
- [16] Amendola, V.; Bergamaschi, G.; Boiocchi, M.; Legnani, L.; Presti, E. L.; Miljkovic, A.; Monzani, E.; Pancotti, F. Chloride-Binding in Organic–Water Mixtures: The Powerful Synergy of C–H Donor Groups within a Bowl-Shaped Cavity, *Chem. Commun.*, **2016**, *52*, 10910–10913. DOI:10.1039/c6cc04978h.
- [17] Lehn, J. M.; Sonveaux, E.; Willard, A. K. Molecular Recognition. Anion Cryptates of a Macrobicyclic Receptor Molecule for Linear Triatomic Species, *J. Am. Chem. Soc.*, **1978**, *100* (15), 4914–4916. DOI:10.1021/ja00483a059.
- [18] Mateus, P.; Bernier, N.; Delgado, R. Recognition of Anions by Polyammonium Macrocyclic and Cryptand Receptors: Influence of the Dimensionality on the Binding Behavior, *Coord. Chem. Rev.*, **2010**, *254* (15–16), 1726–1747. DOI:10.1016/j.ccr.2009.11.005.
- [19] Amendola, V.; Bergamaschi, G.; Miljkovic, A. Azacryptands as Molecular Cages for Anions and Metal Ions, *Supramol. Chem.*, **2018**, *30* (4), 236–242. DOI:10.1080/10610278.2017.1339885.
- [20] Fabbrizzi, L. *Cryptands and Cryptates*; World Scientific Publishing Europe Ltd.: London, 2018.
- [21] Graf, E.; Lehn, J. M. Anion Cryptates: Highly Stable and Selective Macrotricyclic Anion Inclusion Complexes, *J. Am. Chem. Soc.*, **1976**, *98* (20), 6403–6405. DOI:10.1021/ja00436a066.
- [22] Metz, B.; Rosalky, J. M.; Weiss, R. [3] Cryptates: X-Ray Crystal Structures of the Chloride and Ammonium Ion Complexes of a Spheroidal Macrotricyclic Ligand, *J. Chem. Soc., Chem. Commun.*, **1976**, *14*, 533b–5534. DOI:10.1039/C3976000533B.
- [23] Dietrich, B.; Guilhem, J.; Lehn, J. M.; Pascard, C.; Sonveaux, E. Molecular Recognition in Anion Coordination Chemistry. Structure, Binding Constants and Receptor-Substrate

Complementarity of a Series of Anion Cryptates of a Macrobicyclic Receptor Molecule, *Helv. Chim. Acta*, **1984**, *67* (1), 91-104. DOI:10.1002/hlca.19840670112.

[24] Lehn, J.-M.; Méric, R.; Vigneron, J.-P.; Bkouche-Waksman, I.; Pascard, C. Molecular Recognition of Anionic Substrates. Binding of Carboxylates by a Macrobicyclic Coreceptor and Crystal Structure of Its Supramolecular Cryptate with the Terephthalate Dianion, *J. Chem. Soc., Chem. Commun.*, **1991**, No. 2, 62–64. DOI:10.1039/C39910000062.

[25] Alberto, R.; Bergamaschi, G.; Braband, H.; Fox, T.; Amendola, V. 99TcO₄⁻: Selective Recognition and Trapping in Aqueous Solution*, *Angew. Chem.*, **2012**, *124*, 9910–9914. DOI:10.1002/ange.201205313.

[26] Amendola, V.; Bergamaschi, G.; Boiocchi, M.; Alberto, R.; Braband, H. Fluorescent Sensing of 99Tc Pertechnetate in Water, *Chem. Sci.*, **2014**, *5*, 1820–1826. DOI:10.1039/c3sc53504e.

[27] Fabbrizzi, L.; Licchelli, M.; Rabaioli, G.; Taglietti, A. The Design of Luminescent Sensors for Anions and Ionisable Analytes, *Coord. Chem. Rev.*, **2000**, *205*, 85–108. DOI:10.1016/S0010-8545(00)00239-3.

[28] Fabbrizzi, L.; Poggi, A. Anion Recognition by Coordinative Interactions: Metal–Amine Complexes as Receptors, *Chem. Soc. Rev.*, **2013**, *42* (4), 1681–1699. DOI:10.1039/C2CS35290G.

[29] Amendola, V.; Bergamaschi, G.; Boiocchi, M.; Fabbrizzi, L.; Poggi, A.; Zema, M. Halide Ion Inclusion into a Dicopper(II) *Bistren* Cryptate Containing ‘Active’ 2,5-Dimethylfuran Spacers: The Origin of the Bright Yellow Colour, *Inorganica Chimica Acta*, **2008**, *361* (14), 4038–4046. DOI:10.1016/j.ica.2008.03.049.

[30] Bergamaschi, G.; Boiocchi, M.; Perrone, M. L.; Poggi, A.; Viviani, I.; Amendola, V. Mixing the Spacers in Azacryptands: Effects on Halide Recognition, *Dalton Trans.*, **2014**, *43*, 11352–11360. DOI:10.1039/c4dt00886c.

[31] Mateus, P.; Delgado, R.; André, V.; Duarte, M. T. Dicarboxylate Recognition Properties of a Dinuclear Copper(II) Cryptate, *Inorg. Chem.*, **2015**, *54* (1), 229–240. DOI:10.1021/ic502230q.

[32] Boiocchi, M.; Bonizzoni, M.; Fabbrizzi, L.; Piovani, G.; Taglietti, A. A Dimetallic Cage with a Long Ellipsoidal Cavity for the Fluorescent Detection of Dicarboxylate Anions in Water, *Angew. Chem. Int. Ed.*, **2004**, *43* (29), 3847–3852. DOI:10.1002/anie.200460036.

[33] Wiskur, S. L.; Ait-Haddou, H.; Lavigne, J. J.; Anslyn, E. V. Teaching Old Indicators New Tricks, *Acc. Chem. Res.*, **2001**, *34* (12), 963–972. DOI:10.1021/ar9600796.

[34] Nguyen, B. T.; Anslyn, E. V. Indicator–Displacement Assays, *Coord. Chem. Rev.*, **2006**, *10*, 3118–3127. DOI:10.1016/j.ccr.2006.04.009.

- [35] Amendola, V.; Miljkovic, A.; Legnani, L.; Toma, L.; Dondi, D.; Lazzaroni, S. Self-Assembly of Pseudorotaxane Structures from a Dicopper(II) Molecular Cage and Dicarboxylate Axles, *Inorg. Chem.*, **2018**, *57* (7), 3540–3547. DOI:10.1021/acs.inorgchem.7b02534.
- [36] Merli, D.; La Cognata, S.; Balduzzi, F.; Miljkovic, A.; Toma, L.; Amendola, V. A Smart Supramolecular Device for the Detection of t,t-Muconic Acid in Urine, *New J. Chem.*, **2019**, *42* (18), 15460–15465. DOI:10.1039/c8nj02156b.
- [37] Brière, J.-J.; Favier, J.; Gimenez-Roqueplo, A.-P.; Rustin, P. Tricarboxylic Acid Cycle Dysfunction as a Cause of Human Diseases and Tumor Formation, *Am. J. Physiol. Cell Physiol.*, **2006**, *291* (6), C1114–C1120. DOI:10.1152/ajpcell.00216.2006.
- [38] Curiel, D. Complexation and Sensing of Dicarboxylate Anions and Dicarboxylic Acids, *Coord. Chem. Rev.*, **2015**, *284*, 19–66. DOI:10.1016/j.ccr.2014.09.010.
- [39] Xie, G.-Y.; Jiang, L.; Lu, T.-B. Discrimination of Cis–Trans Isomers by Dinuclear Metal Cryptates at Physiological PH: Selectivity for Fumarate vs Maleate, *Dalton Trans.*, **2013**, *42* (39), 14092–14099. DOI:10.1039/C3DT51501J.
- [40] Gans, P.; O’Sullivan, B. GLEE, a New Computer Program for Glass Electrode Calibration, *Talanta*, **2000**, *51* (1), 33–37. DOI:10.1016/S0039-9140(99)00245-3.
- [41] Gran, G. Determination of the Equivalence Point in Potentiometric Titrations. Part II, *Analyst*, **1952**, *77* (920), 661–671. DOI:10.1039/AN9527700661.
- [42] Gans, P.; Sabatini, A.; Vacca, A. Investigation of Equilibria in Solution. Determination of Equilibrium Constants with the HYPERQUAD Suite of Programs, *Talanta*, **1996**, *43* (10), 1739–1753. DOI:10.1016/0039-9140(96)01958-3.
- [43] Bruker. *SAINTE Software Reference Manual Version 6*; Bruker AXS Inc.: Madison, Wisconsin, USA, 2003.
- [44] Krause, L.; Herbst-Irmer, R.; Sheldrick, G. M.; Stalke, D. Comparison of Silver and Molybdenum Microfocus X-Ray Sources for Single-Crystal Structure Determination, *J Appl Cryst*, **2015**, *48* (1), 3–10. DOI:10.1107/S1600576714022985.
- [45] Altomare, A.; Burla, M.; Camalli, M.; Casciarano, G. L.; Giacovazzo, G.; Guagliardi, A.; Moliterni, A. G.; Polidori, G.; Spagna, R. SIR97: A New Tool for Crystal Structure Determination and Refinement, *Journal of Applied Crystallography*, **1999**, *32* (1), 115–119. DOI:10.1107/S0021889898007717.
- [46] Thordarson, P. Determining Association Constants from Titration Experiments in Supramolecular Chemistry, *Chem. Soc. Rev.*, **2011**, *40* (3), 1305–1323. DOI:10.1039/C0CS00062K.

[47] Addison, A. W.; Rao, T. N.; Reedijk, J.; Rijn, J. van; Verschoor, G. C. Synthesis, Structure, and Spectroscopic Properties of Copper(II) Compounds Containing Nitrogen–Sulphur Donor Ligands; the Crystal and Molecular Structure of Aqua[1,7-Bis(N-Methylbenzimidazol-2'-Yl)-2,6-Dithiaheptane]Copper(II) Perchlorate, *J. Chem. Soc., Dalton Trans.*, **1984**, No. 7, 1349–1356. DOI:10.1039/DT9840001349.

[48] Duggan, M.; Ray, N.; Hathaway, B.; Tomlinson, G.; Brint, P.; Pelin, K. Crystal Structure and Electronic Properties of Ammine[Tris(2-Aminoethyl)Amine]Copper(II) Diperchlorate and Potassium Penta-Amminecopper(II) Tris(Hexafluorophosphate), *J. Chem. Soc., Dalton Trans.*, **1980**, No. 8, 1342–1348. DOI:10.1039/DT9800001342.

[49] Miljkovic, A.; Cognata, S. L.; Bergamaschi, G.; Freccero, M.; Poggi, A.; Amendola, V. Towards Building Blocks for Supramolecular Architectures Based on Azacryptates, *Molecules*, **2020**, 25, 1733. DOI:10.3390/molecules25071733.

4. A dicopper(II) azacryptate for the liquid-liquid extraction of dicarboxylates

4.1 Introduction

The great importance of anion substrates in biochemical systems, industrial processes, and environmental field led the scientific community to design and develop more and more efficient molecular systems for the selective recognition, binding and extraction of specific anions of interest. The weakness of anion binding, based principally on electrostatic and hydrogen bonding interactions, requires very selective receptors able to perform the best complementarity in term of structure (size, shape and rigidity of the framework) and the established interactions (kind and position of the functional groups in the receptor's scaffold). In this context, the raise of the so-called "anion coordination chemistry" allowed the synthesis of a wide variety of highly selective hosts for anions over the course of the years.¹⁻³ In particular, polyamino molecular receptors exhibit peculiar features that allowed their successful application in different fields, from environment to industry.^{4,5}

In this section, several examples of the successful application of polyaza molecular receptors in solid-liquid and liquid-liquid extraction processes of target anions, and transmembrane anion transport are presented.

4.1.1 Anion extraction and transport

Anion extraction, *i.e.* the transfer of an anionic species across two immiscible phases, is not easy to achieve without an effective extractant. In this context, molecular receptors can play a very important role. As a matter of fact, in a competing medium such as water, solvent molecules act as strong H-bond donors, thus stabilizing the anionic species in the medium and disfavoring extraction from the energetic point of view. The issue can be however overcome by the use of a molecular receptor, present into the organic phase and characterized by a high affinity for the anionic target. If the anion:receptor affinity is strong enough to overcome the hydration energy of the anion, an effective extraction from water can be obtained.⁶

As already mentioned, desolvation energies have an important role in the extraction process. The Hofmeister series (F^- , SO_4^{2-} , CH_3COO^- , Cl^- , Br^- , NO_3^- , ClO_3^- , I^- , ClO_4^- , SCN^-) provides indications of the solvation degree of anions and of the facility of their extraction from water.⁷

Anions on the left-side of the Hofmeister series (*e.g.* F^- , SO_4^{2-}) are highly hydrated and are called kosmotropes. By proceeding towards the right-side of the series, the solvation degree decreases until perchlorate and thiocyanate anions (called chaotropes), which can be considered as the most hydrophobic anions of the list. The selective extraction of hydrophilic anions as sulfate is very challenging and requires highly selective receptors, able to overcome the Hofmeister bias.

Sessler and colleagues reported a series of macrocyclic ammonium receptors which belong to this category.⁸ In particular, fluorinated calixpyrroles **1** and **2** and the tetraamide macrocycles **3-5** (see Figure 1) successfully extract sulfate from water into an organic phase, even in presence of a large excess of nitrate. The extraction efficiency was further enhanced by adding to these H-bonding donor receptors a certain amount of the traditional quaternary ammonium extractant Aliquat 336-nitrate in the organic phase.

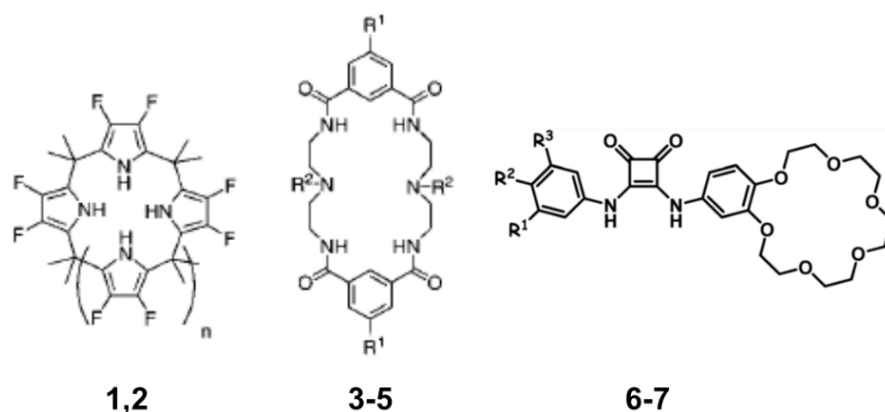


Figure 1. Left and middle: fluorinated calixpyrroles (**1**, $n = 1$; **2**, $n = 2$) and tetraamide macrocycles (**3**, $R^1 = H$, $R^2 = CH_3$; **4**, $R^1 = H$; $R^2 = \text{dansyl}$; **5**, $R^1 = t\text{-butyl}$, $R^2 = CH_3$) reported by Sessler and colleagues. Right: the squaramide-based receptors (**6**, $R^1, R^3 = CF_3$, $R^2 = H$; **7**, $R^1, R^3 = H$, $R^2 = NO_2$) reported by Romański et al. From ref.s [8-9].

An interesting paper by Romański and co-workers illustrated a lipophilic squaramide-based ion-pair receptor (**6** in Fig. 1) for the selective extraction of potassium sulfate.⁹ The presence of a crown ether site on the receptor's scaffold facilitates the formation of ion-pair complexes, thus enhancing the liquid-liquid extraction of sulfate in the form of alkali metal salt. Furthermore, the optical sensor **7** was obtained by introducing a $-NO_2$ group on the backbone of **6**. The obtained system can be employed for the "naked-eye" recognition of sulfate under both liquid-liquid and solid-liquid extraction of the anions.

In another recent work, Joliffe et al. demonstrated the efficient extraction of sulfate from an aqueous solution of Na_2SO_4 using the neutral macrocyclic squaramide **8**.¹⁰ The transport of

sulfate across a bulk chloroform layer containing the receptor was also tested in a classic U-tube (see Fig. 2). Interestingly, the receptor successfully transferred sulfate anion across the organic phase via an anion exchange mechanism with nitrate. In the experiment setup, the lipophilic tetrabutylammonium (TBA) cation (as nitrate salts) was also added to the organic phase in order to facilitate the sulfate transfer through formation of ion-pair complexes.^{4,11} Moreover, by adding BaCl₂ in the receiving phase, BaSO₄ precipitates thus increasing the rate of the sulfate transport. Further experiments confirmed the efficiency of the process even in presence of a complex mixture of anions and across a wide pH range (pH 3.2–9.4).

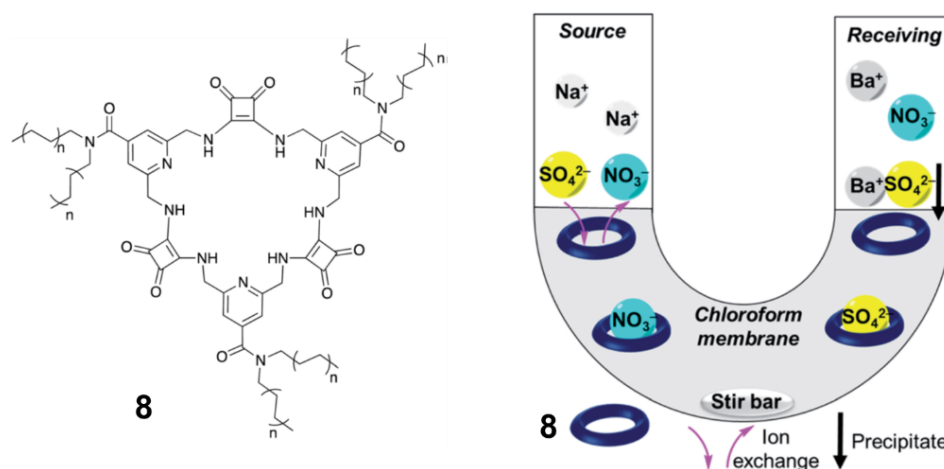


Figure 2. Left: molecular structure of the macrocyclic squaramide **8**. Right: scheme of the transport experiment mediated by receptor **8**. TBA⁺ cations are omitted for clarity. From ref. [10].

To achieve an efficient extraction of a specific anion, electroneutrality must be maintained. Depending on the host structure, charge neutralisation can be obtained in different ways: 1) the exchange of a counterion with the anion of interest, in the case of a positively charged receptor; 2) the addition of lipophilic cation for the co-transport of the anion if a neutral receptor is employed; 3) a combined system (in separated subunits or in a single molecular scaffold) able to interact with both anions and cations.⁴

Several years ago, Urban and Schmuck developed a selective transporter for N-acetylated amino acids.¹² The hydrophobic molecular receptor **9** (see Fig. 3), in the protonated form, performed the extraction of a series of N-acetylated amino acids. with best performances for aromatic guests thanks to additional cation- π interactions with the guanidinium pyrrole moiety. Transport experiments revealed the successful transfer of amino acids across an organic phase through a symport mechanism, *i.e.* simultaneous transport of the amino acid and a proton, in presence of a pH gradient between the source and receiving phase. A scheme of the transport

mechanism is reported in Figure 3. This gradient was also employed as driving force for the active transport against a concentration gradient.

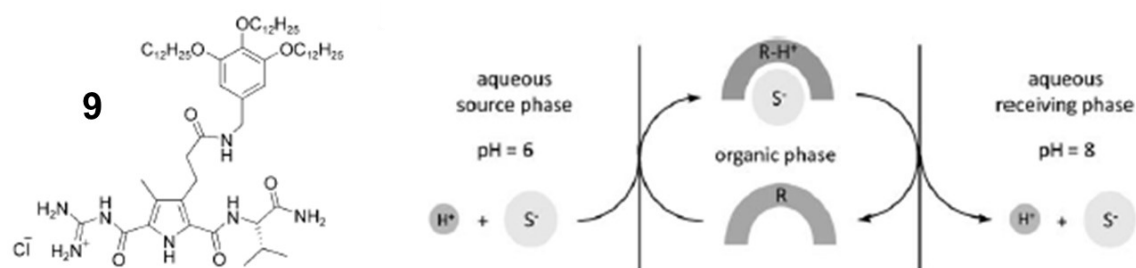


Figure 3. The N-acetylated amino acid transporter **9** and a scheme of the transport of amino acids through a symport mechanism. From ref. [12].

In a recent work, the selective extraction of lithium chloride was achieved by employing the two ditopic calix[4]pyrrole-based ion-pairs receptors **10-11** reported in Figure 4.¹³ The strong binding of LiCl was demonstrated for both the receptors through ¹H-NMR spectroscopy and crystal structure analysis. Single crystals of the adducts of the receptors with LiCl (see Fig. 4) showed that the encapsulation of the ion-pair does not affect the molecular structure of **10**, while a slight distortion is observed in the case of **11**. Both receptors were tested as extractant for LiCl. In solid-liquid extraction processes, the selective separation of LiCl was achieved even in presence of excess NaCl. In liquid-liquid extraction experiments, only receptor **11** maintained the selectivity for LiCl over NaCl and KCl while, in the case of **10**, the selectivity order turned to be KCl > NaCl > LiCl.

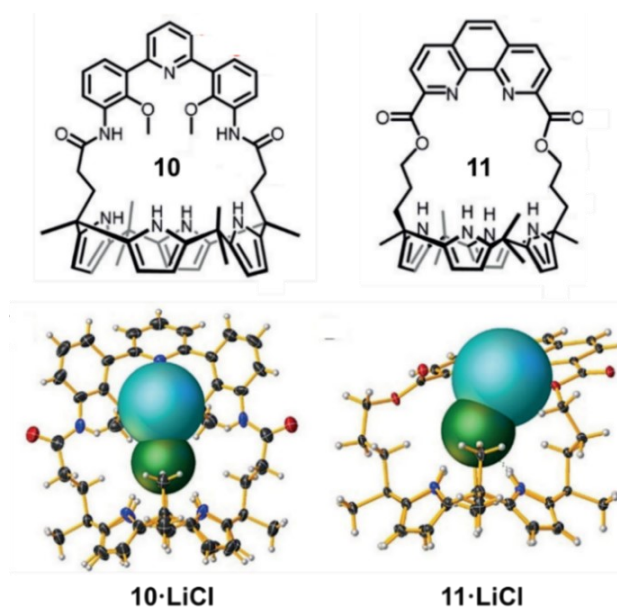


Figure 4. Molecular structure of the calix[4]pyrrole-based receptors **10-11** and the single-crystal structures of the corresponding LiCl complexes (Li⁺ and Cl⁻ ions are shown in space-filling form). From ref. [13].

Flood and colleagues recently reported a cryptand-like triazolo cage **12** able to selectively capture chloride over other halides.¹⁴ ¹H-NMR titrations in d₆-DMSO revealed the high affinity and selectivity of the cage for chloride, with a remarkably higher binding constant compared to those obtained with the macrocyclic and tripodal analogue systems, *i.e.* **13** and **14** respectively (see Fig. 5): even if the interaction sites are the same, the preorganisation and the rigidity of the cage lead to a stronger binding. This *trend* is well illustrated in the graph reported in Figure 5, where the anion affinities (in terms of LogK) of the three systems are shown and compared. Liquid-liquid extraction experiments, using dichloromethane as organic phase, revealed a higher transfer efficiency of **12** in the transfer of the Na⁺ salt compared to the other alkali salts. This result is attributed to the formation of ion-pairs between Na⁺ and the complex **12**·Cl⁻. Extraction experiments with tetraethyl- and tetrabutylammonium salts highlighted the quantitative transfer of various anions (including bromide, iodide, nitrate, and nitrite) with a 100% extraction efficiency in presence of the cage.

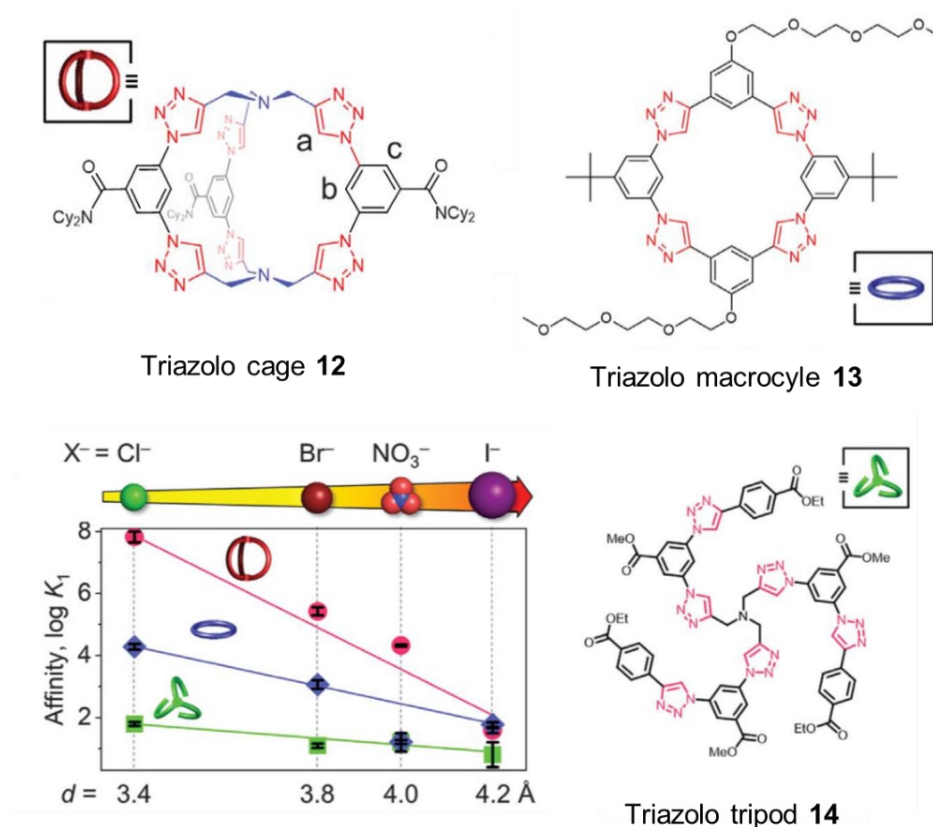


Figure 5. Molecular structures of the triazolo derivatives: cage **12**, macrocycle **13** and the tripod **14** and a graph reporting anion affinity, as LogK, of the three molecular systems for the reported anions as TBA salts: cage (red), macrocycle (blue) and tripod (green). Coloured lines highlight the *trend*. From ref. [14].

4.1.2 Transmembrane anion transport

The human body is a perfect machine, based on an incredible control of all biological processes working simultaneously every day of our lives. Sometimes, unfortunately some parts, no matter how small they could be, do not work in the right way: a disfunction of one usually causes serious damage to the whole system, with serious consequences on the health of a person.

This is the case of anions exchange across phospholipid membrane of the cell: specific channels and transporters contained in the membrane accurately regulate the enter/exit of all the molecules, to maintain the right concentration inside and outside the cell. Some genetic diseases can induce a dysregulation in anion transportation: for example, the malfunction of a protein channel for chloride, called cystic fibrosis transmembrane conductance regulator (CFTR), causes the cystic fibrosis and a consequent severe damage to the lungs, the digestive system, and other organs in the body. The great interest of the scientific community is focused on searching new treatments to resolve this kind of dysregulations thus ameliorating the conditions of patients affected by the correlated diseases.^{15,16}

Anion transport across lipid membranes can occur in two different ways: 1) mobile carriers present in the membrane bind the anion on one side and, after diffusion through the membrane as complex, they transfer the anion on the other side of the membrane; 2) channels, formed by a single molecule or by an aggregate of more units, constitute polar pathways along the membrane through which anions can diffuse from one to the other side of the membrane. Even if the transfer through the channels is faster than that performed by mobile carriers, the latter are easier to design and functionalize, and generally result in a higher degree of selectivity. In any case, electroneutrality must be maintained during the overall transfer process.⁵

To cite a couple of examples, Davis and colleagues tested a series of catechol-containing trisamides as anion transporters through lipidic membranes.¹⁷ The comparison with other derivatives confirmed that catechol moieties are essential for transport. In particular, receptor **15** (see Fig. 6) showed the best transfer performance, with a selectivity in anionic permeability across the membrane that follows the Hofmeister sequence: $\text{ClO}_4^- > \text{I}^- > \text{NO}_3^- > \text{Br}^- > \text{Cl}^-$.

In another work, Davis and co-workers reported the sphingolipid ceramide **16** (reported in Fig. 6) for the transport of chloride and bicarbonate across the phospholipidic membrane.¹⁸ The authors demonstrated that the 1,3-diol moiety and the neighbour NH amide group can act as a tridentate interaction site for binding anions, thus enhancing the transport efficiency across the EYPC liposomes bilayers (*i.e.* egg yolk phosphatidylcholine, a liposomal lipid component

frequently used for anticancer drug delivery). Interestingly, chloride transport assay performed with various anions in neutral medium highlighted that the ceramide **16** only mediates anion exchange in presence of singly charged anions in the extravesicular environment, such as NO_3^- and HCO_3^- . In presence of the more hydrophilic sulfate anion, only a slight efflux of chloride was observed.

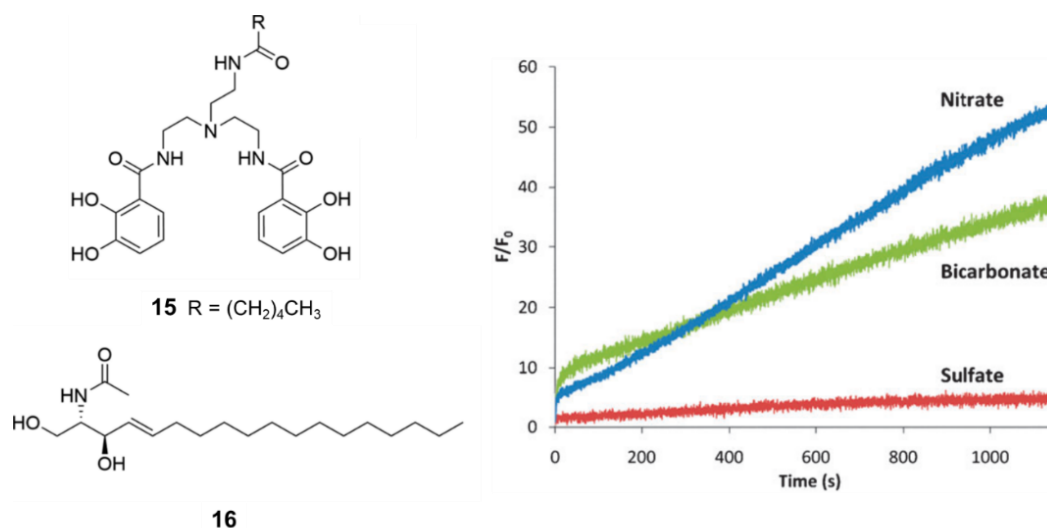


Figure 6. Left: Molecular structures of catechol-based trisamide **15** (from ref. [17]) and the ceramide **16** (from ref. [18]). Right: Chloride transport assay for **16** in EYPC liposomes with various external anions in 20 mM HEPES buffer (pH = 7.4). The Cl^- efflux from the liposomes is monitored by following the increase of fluorescence of a chloride-sensitive dye, since its emission is quenched in presence of the anion in the intra-vesicular environment.

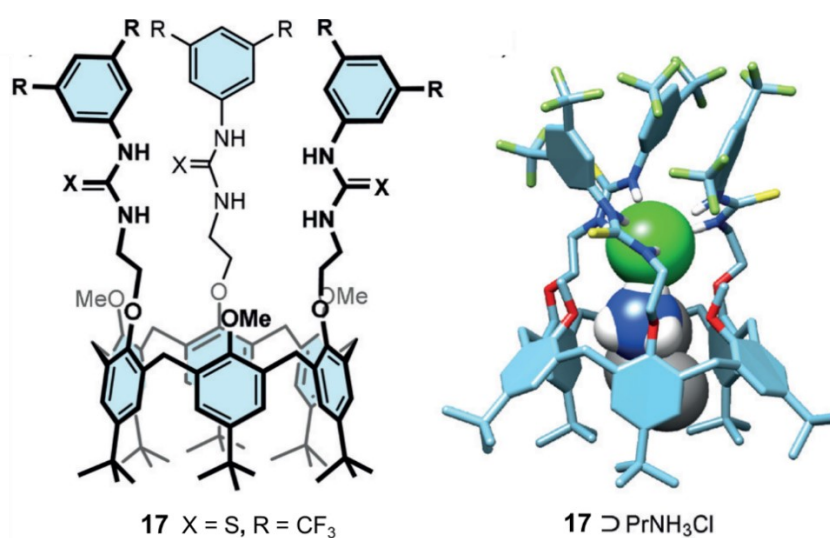


Figure 7. Left: Molecular structure of the calix[4]arene receptor **17**. Right: Molecular model of complex PrNH_3Cl , with Cl^- bound by the thioureas and PrNH_3^+ in the calixarene cavity. From ref. [19].

In a recent paper, the new calix[4]arene tris(thio)urea **17** (in Fig. 7) reported by Valkenier et al. was demonstrated to perform not only an efficient $\text{Cl}^-/\text{NO}_3^-$ antiport but also the cotransport

of organic ion-pairs such as PrNH_3Cl .¹⁹ Interestingly, upon the addition of PrNH_3Cl to vesicles containing the receptor **17**, an acceleration of the chloride transport across the membrane was detected. The cotransport of ion-pairs, more efficient compared to the $\text{Cl}^-/\text{NO}_3^-$ antiport mechanism, is favoured by the presence of a cavity in the calix[4]arene receptor, able to complex the organic cation (see Fig. 7).

Regarding anion channels, Davis and other reported a series of calix[4]arene amides tested for the transmembrane transport of chloride.²⁰ The receptor **18** (reported in Fig. 8), in particular, showed very interesting results in transport experiments performed on EYPC liposomes: **18** is able to form ion channels in bilayer membranes and to transfer chloride via a H^+/Cl^- cotransport mechanism. In fact, in presence of a Cl^- gradient, an alteration of the pH inside liposomes is observed. Moreover, a selective transport of chloride against sulfate was detected.

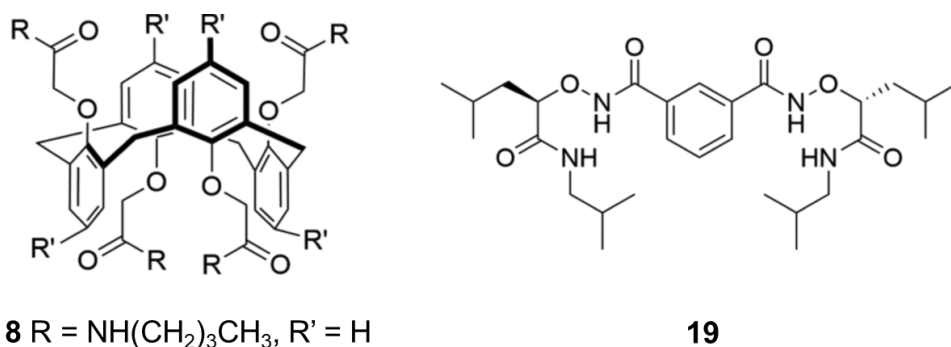


Figure 8. Molecular structures of the calix[4]arene receptor **18** and the isophthalamide **19**. From ref.s [20-21].

Another interesting article by Yang and colleagues reported the isophthalamide **19** (see Fig. 8), containing two extra amide groups derived from α -aminoxy acids, able to form an anion channel and to successfully transport chloride across lipid bilayer of model liposomes.²¹ The experimental confirmation of this transport mechanism, in spite of anion carriers, was obtained by patch clamp techniques, *i.e.* the measurement of the ionic currents in individual isolated living cells, tissue sections, or patches of cell membrane. For the compound **19**, the authors found characteristic single-channel currents in giant liposomes, thus indicating the effective formation of the functional ion channel.

4.1.3 Our study

In the previous chapters of this thesis, the peculiar properties and anion binding capability of polyamino cryptands have been extensively illustrated. As already mentioned, the effect of i) a

well-defined three-dimensional cavity, ii) preorganization and iii) presence of multiple binding sites in the receptor cavity was proven to ensure high affinity and selectivity for anionic species. In addition, the easy preparation of these cage-like systems, based on the Schiff condensation, allows a facile modulation of cavity in order to maximise the selectivity for the anion of interest. In this context, the presence of transition metal cations in the cryptand cavity allows the instauration of coordinative interactions with the included anionic guest: these interactions are stronger and more effective than the H-bonds established within the cavity of protonated azacryptands.^{22–27}

Besides the promising binding features of the dimetallic cryptates, the application of these systems in the extraction of target anions from water have not been explored. In this chapter, I will demonstrate that the proper functionalisation of an azacryptand molecule may generate new receptors, that can be exploited in the extraction of highly hydrated anions from water.

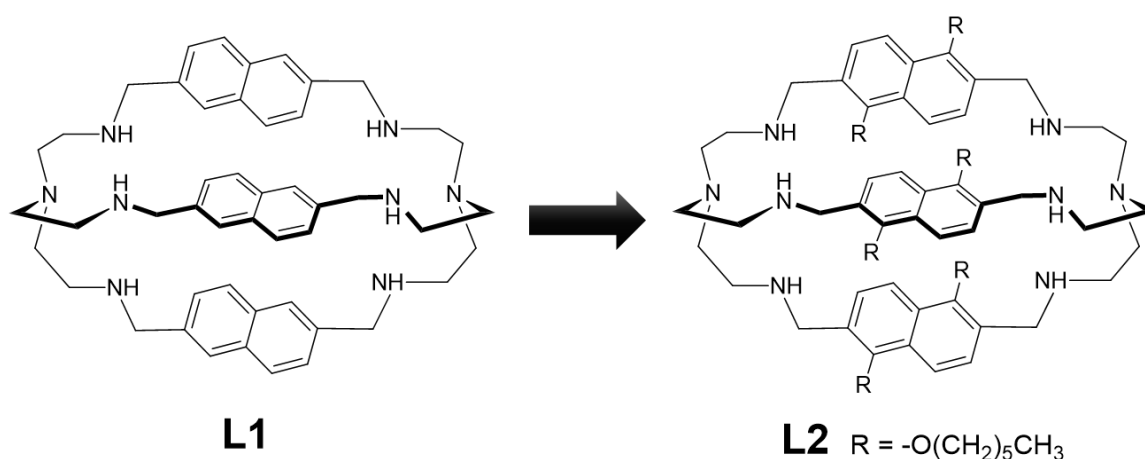


Figure 9. Molecular structures of the naphthyl cage **L1** and the new lipophilic derivatives **L2**.

In the previous chapter, the dicopper(II) complex of the naphthyl cage **L1** (see Fig. 9) was applied for the fluorescent sensing of fumarate in neutral water, using the Indicator Displacement Approach with 5-TAMRA as the fluorescent indicator. Here, I report the synthesis of a lipophilic azacryptand **L2** obtained by appending n-hexyl chains on the naphthyl spacers of **L1** (see Fig. 9). After the investigation of the anion binding properties of the dicopper(II) cryptate [Cu₂(**L2**)]⁴⁺ and once its solubility in pure dichloromethane was confirmed, the receptor was tested for the liquid-liquid extraction of dicarboxylates from neutral water. Anion extraction was quantified through HPLC-UV and quantitative ¹H-NMR analyses.

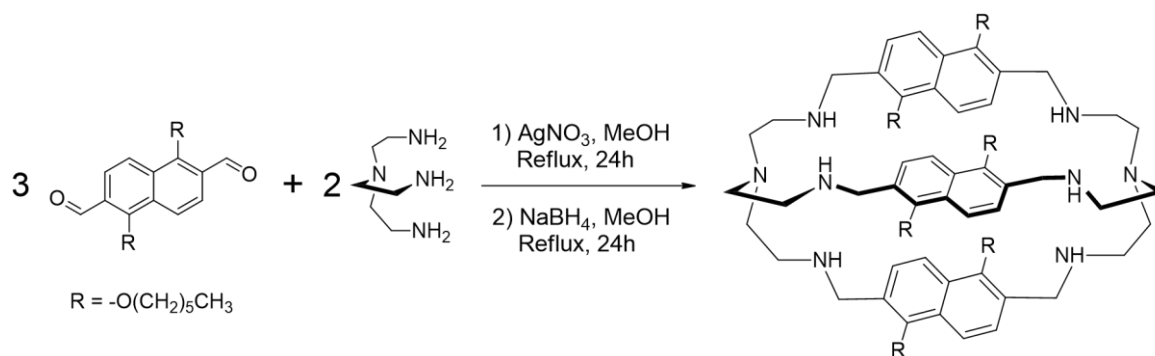
4.2 Experimental

4.2.1 Chemicals and methods

All reagents for syntheses were purchased from Sigma-Aldrich and used without further purification. All reactions were performed under dinitrogen. UV-vis. spectra were collected using a Varian Cary 50 SCAN spectrophotometer, with quartz cuvettes of the appropriate path length (1 or 10 cm) at $25.0 \pm 0.1^\circ\text{C}$. High-resolution mass spectra were recorded on a Thermo Scientific Q Exactive Plus instrument. ^1H - and ^{13}C -NMR spectra were recorded on a Bruker AVANCEIII 400 MHz (operating at 9.37 T, 400 MHz), equipped with a 5 mm BBO probe head with Z-gradient (Bruker BioSpin).

For the extraction study, ^1H -NMR analysis was performed the AVANCEIII 400 MHz. Spectra were acquired using Bruker pulse sequence noesygppr1d for water suppression, after optimisation of 90° pulse, shims and O1 parameter. Phase correction and baseline correction were applied using automatic procedure. Succinate concentration was determined using Topspin Eretic2 package. HPLC gradient grade acetonitrile and ultrapure water were purchased from VWR (Milan, Italy). The HPLC–UV apparatus consisted of a Shimadzu (Milan, Italy) LC-20AT solvent delivery module equipped with a DGU-20A3 degasser and interfaced with a SPD-20A UV detector. A Sepachrom Adamas C18-AQ (250×4.6 mm, $5 \mu\text{m}$) column coupled with a Supelco Supelguard Ascentis C18 (20×2.1 mm, $5 \mu\text{m}$) guard-column was used. 1,5-di(hexyloxy)naphthalene-2,6-dicarboxaldehyde and $[\text{TBA}]_2\text{suc}$ were synthesized following known procedures.^{28,29}

4.2.2 Synthesis of L2 ligand



A solution of 1,5-di(hexyloxy)naphthalene-2,6-dicarboxaldehyde (0.12 g; 0.31 mmol; 3.0 *equiv*) in CH_2Cl_2 (10 mL) and MeOH (70 mL) was added to a solution of AgNO_3 (0.05 g; 0.31 mmol;

3.0 *eqv*) in MeOH (70 mL). The reaction mixture was then refluxed under Ar atmosphere. A solution of tris(2-aminoethyl)amine (0.03 mL; 0.21 mmol; 2.0 *eqv*) in MeOH (50 mL) was then slowly added dropwise and the reaction was refluxed for 24 hours. The solution containing the polyimine cage compound was then transferred in a round bottom flask and the CH₂Cl₂ was evaporated under vacuum. The methanol solution was refluxed again and NaBH₄ (3.0 g) was added in small portions in order to reduce both imine bonds and Ag⁺. After 12 hours the mixture was cooled to room temperature and filtered to eliminate the Ag⁰ particles. The solvent was evaporated under vacuum to give a white solid that was dissolved with brine (200 mL) and extracted with CH₂Cl₂ (4 x 50 mL). The collected organic phase was then dried on Na₂SO₄. The solvent was evaporated under vacuum to obtain 0.13 g of the pure cage as a yellowish dense oil. Yield: 90.61%. HRMS-ESI (MeOH) *m/z*: [M-H⁺]⁺ calculated for C₈₄H₁₃₂N₈O₆, 1350.0348, found 1350.0529 (Fig. S1). ¹H-NMR (400 MHz, d₆-DMSO + HNO₃, 353 K) ppm: 7.84-7.61 (6H, naph), 4.44 (m, 12H, NH-CH₂-naph), 3.91 (m, 12H, -O-CH₂-C), 3.20-2.80 (br, m, 24H, N-CH₂-CH₂-N), 1.97 (m, 12H, -O-CH₂-CH₂-C), 1.51-1.27 (m, 36H, O(CH₂)₂-(CH₂)₃-C), 0.91 (t, 18H, -CH₃). ¹³C-NMR (100 MHz, d₆-DMSO, 298 K) ppm: 154.02, 129.16, 126.89, 122.22, 118.91, 76.32, 51.07, 45.68, 45.26, 31.78, 30.29, 25.53, 22.61, 14.40.

4.2.3 Potentiometric and pH-spectrophotometric titrations

Protonation constants of ligand **L2** were determined in dioxane/water (20% v/v) mixture, 0.05 M in [TBA]NO₃. In a typical experiment, a solution of **L2** ligand (15 mL, 4 × 10⁻⁴ M) was treated with an excess of a standard solution of 1.0 M HNO₃. Titrations were performed by addition of 10 μL aliquots of carbonate-free standard 0.1 M NaOH, recording 80-100 points for each titration. Complexation constants of **L2** cage were determined by performing a potentiometric titration experiment in presence of two equivalents of Cu(NO₃)₂. Prior to each potentiometric titration, the standard electrochemical potential (E°) of the glass electrode was determined in the dioxane/water mixture, by a titration experiment according to the Gran method.^{30,31} Protonation and complexation titration data (emf vs mL of NaOH) were processed with the HyperQuad package³² to determine the equilibrium constants.

Potentiometric titrations were also performed on H₂suc (succinic acid) and H₂glut (glutaric acid), in order to determine their p*K_a* values in dioxane/water mixture 20% v/v (0.05 M [TBA]NO₃, 25°C). In a typical experiment, 15 mL of a 1 × 10⁻³ M dicarboxylate solution were treated with an excess of a 1.0 M HNO₃ standard solution. Titrations were performed by addition of 10 μL aliquots of carbonate-free standard 0.1 M NaOH, recording 80-100 points for

each titration. Prior to each potentiometric titration, the standard electrochemical potential (E°) of the glass electrode was determined in the dioxane/water mixture, by a titration experiment according to the Gran method.^{30,31} Protonation titration data (emf vs mL of NaOH) were processed with the HyperQuad package³² to determine the pK_a of the studied acids.

pH-spectrophotometric titrations were performed on solutions of **L2** (4×10^{-4} M) in presence of two equivalents of Cu(II) (as nitrate salt) in the same solvent mixture used in potentiometric titrations, *i.e.* dioxane/water (20% v/v) with [TBA]NO₃ 0.05 M. In a typical experiment, aliquots of carbonate-free standard 0.1 M NaOH were added to the solution of the ligand and copper, both the electrochemical potential and the UV-vis. spectrum of the solution were recorded after each addition.

4.2.4 Spectrophotometric titrations

In a typical experiment, a concentrated solution of the dicopper(II) azacryptate [Cu₂(**L2**)]⁴⁺ in DMSO was diluted with 0.025 M HEPES (*i.e.* 4-(2-hydroxyethyl)-1-piperazineethanesulfonic acid) buffer in dioxane/water (20% v/v), pH 7: the final concentration of the azacryptate ranged between 50-500 μ M. The buffered solution of the cryptate was then titrated with a standard solution of either the chosen dicarboxylic acid or the corresponding disodium salt, in the case of phthalates. After each addition, the UV-vis. spectrum was recorded. It should be noted that with terephthalate and phthalate anions, the formation of a precipitate over the course of the titration prevented accurate determination of association constants. The concentration of the azacryptate solution was chosen on the basis of the p-parameter ($p = [\text{concentration of the azacryptate:anion adduct}]/[\text{maximum possible concentration of the azacryptate:anion adduct}]$), which should range between 0.2 and 0.8.³³ Titration data were processed with the HyperQuad package³² to estimate equilibrium constants. In some cases, even working with very dilute solutions of the azacryptate, the curvature of the titration profile was too sharp to allow accurate calculation of binding constants.

4.2.5 Extraction experiments

4.2.5.1 HPLC-UV analyses

For the extraction experiments, a solution of succinic acid (1.0 mM) in aqueous buffer at pH 7 (0.05 M HEPES buffer) and a 0.02 mM solution of [Cu₂(**L2**)](NO₃)₄ in CH₂Cl₂ as organic phase (obtained by dilution of a 9 mM solution in DMSO, with a final % DMSO about 2%) were

employed. In a 20 mL glass vial, the two phases were vigorously stirred for 20 minutes, then equilibrated for 10 minutes and finally separated and analysed through HPLC-UV. To evaluate the extraction efficiency, the percent decrease of the succinate concentration in the aqueous phase was quantified by the comparison of the analyte chromatographic peak after the extraction experiment with the same peak detected in the blank experiment, performed following the same procedure but in absence of $[\text{Cu}_2(\mathbf{L2})]^{4+}$ (*i.e.* using CH_2Cl_2 with 2 % v/v of DMSO as organic phase). Seven independent extraction experiments were performed, in non-consecutive days; for each repeat, the succinic acid solution was freshly prepared in order to reduce experimental errors.

To run the HPLC-UV measure, after an equilibration period of 5 min, 20 μL of each sample was injected in the HPLC system. The mobile phases were (A) 25 mM aqueous H_3PO_4 (pH 2.5) and (B) acetonitrile, working with an isocratic elution 10% B for 7 min, followed by a washing step (linear gradient to 70% B until 9 min, hold for 3 min). The flow rate was 0.8 mL min^{-1} and the detection wavelength was 214 nm.

4.2.5.2 $^1\text{H-NMR}$ studies

Succinate extraction was also monitored by $^1\text{H-NMR}$ spectroscopy. For the experiment, a solution of succinic acid (1.076 mM) was prepared in D_2O (0.05 M PBS at pH 7). As for the previous tests, the organic phase was obtained by dilution with CH_2Cl_2 of a stock solution of $[\text{Cu}_2(\mathbf{L2})(\text{CF}_3\text{SO}_3)_4]$ (5.1 mM) in $\text{d}_6\text{-DMSO}$. The final concentration of $[\text{Cu}_2(\mathbf{L2})]^{4+}$ in CH_2Cl_2 was 0.42 mM, with a % DMSO into the final solution about 6% v/v. The extraction experiment was carried out as described before: 1.5 mL of succinate solution in D_2O and 1.5 mL of $[\text{Cu}_2(\mathbf{L2})]^{4+}$ solution in CH_2Cl_2 were vigorously stirred for 20 min, allowed to equilibrate for 10 min and finally separated. A blank experiment was performed following the same procedure, but in absence of $[\text{Cu}_2(\mathbf{L2})]^{4+}$ in the organic phase (*i.e.* CH_2Cl_2 with 6% DMSO v/v). The succinate extraction from the D_2O solution into CH_2Cl_2 was quantitatively evaluated by comparing the dicarboxylate concentration in D_2O , before and after mixing with the solution of $[\text{Cu}_2(\mathbf{L2})]^{4+}$ in CH_2Cl_2 . Succinate concentration was determined using the Topspin Eretic2 package, using glycine (1.00 mM) as internal reference for the D_2O phase.

4.3. Results and discussion

4.3.1 Potentiometric and pH-spectrophotometric titrations

4.3.1.1 Protonation constants of L2

Potentiometric studies on **L2** were performed to determine the protonation constants of the ligand. Experiments were carried out in dioxane/water 20% (v/v) mixture because of the low solubility of the cage in pure water. [TBA]NO₃ 0.050 M was employed as supporting electrolyte. The emf vs volume of NaOH curve was fitted with a non-linear least squares procedure, using the HyperQuad package.³² The distribution diagram of the species (as % abundance with respect to **L2** vs pH) was determined over the pH range 2-12 (see Fig. 10), using the protonation constants reported in Table 1.

The acid-base behaviour of **L2** is similar to that reported for the **L1** azacryptand. At pH 2, **L2** is present in solution as the hexaprotonated species **L2H₆⁶⁺**, with all the secondary amine protonated. The increase of pH leads to the loss of a proton, with the formation of **L2H₅⁵⁺** species, dominant at pH 5.8. Over neutral pH, different protonated forms of **L2** (*i.e.* **L2H₄⁴⁺**, **L2H₃³⁺**, **L2H₂²⁺** and **L2H⁺**) coexist in solution until pH 8: at this pH value the free base of **L2** ligand starts to form, becoming the only species in solution over pH 10.

Table 1. Protonation equilibria and the corresponding constants for **L2** in dioxane/water 20% v/v (T=25 °C). Standard deviations are shown in parentheses.

Equilibria	Log β
L2 + H ⁺ \rightleftharpoons L2H⁺	9.03(8)
L2 + 2H ⁺ \rightleftharpoons L2H₂²⁺	17.74(4)
L2 + 3H ⁺ \rightleftharpoons L2H₃³⁺	25.72(6)
L2 + 4H ⁺ \rightleftharpoons L2H₄⁴⁺	32.66(6)
L2 + 5H ⁺ \rightleftharpoons L2H₅⁵⁺	39.25(6)
L2 + 6H ⁺ \rightleftharpoons L2H₆⁶⁺	44.50(7)

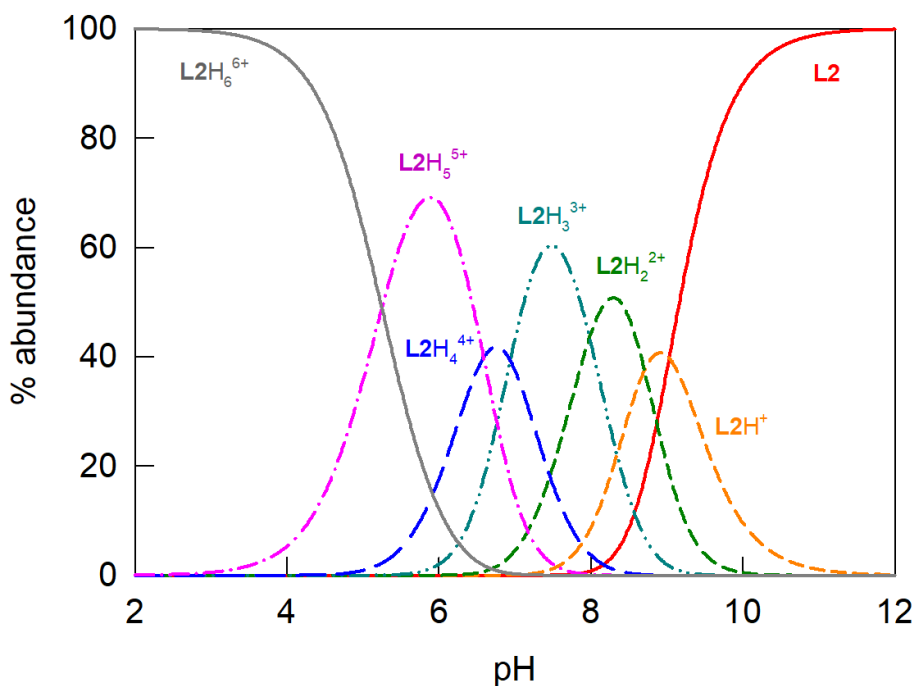


Figure 10. Distribution diagram of species present at equilibrium over the course of the potentiometric titration of **L2** (4×10^{-4} M) with standard NaOH in dioxane/water (20% v/v) ($T=25$ °C).

4.3.1.2 Complexation of **L2** with Cu(II)

Stability constants of the copper-containing species were determined through potentiometric experiments on **L2** in presence of two equivalents of $\text{Cu}(\text{NO}_3)_2$, in the same medium of the previous titrations. The experimental curve (emf vs volume of NaOH) was fitted with a non-linear least squares procedure.³² Best fitting was obtained by assuming the development of the following complexes over the course of the titration: $[\text{Cu}(\text{L2H}_3)]^{5+}$, $[\text{Cu}_2(\text{L2})]^{4+}$, $[\text{Cu}_2(\text{L2})(\text{OH})]^{3+}$, $[\text{Cu}_2(\text{L2})(\text{OH})_2]^{2+}$. The corresponding cumulative constants (as $\text{Log}\beta$) and the distribution diagram are shown in Table 2 and Figure 11, respectively.

At pH 3, L2H_6^{6+} is the only species in solution. The increase of pH leads to the formation of the mononuclear Cu(II) complex $[\text{Cu}(\text{L2H}_3)]^{5+}$, with the metal ion coordinated to one on the *tren* subunits, while the other one is triply protonated. This complexed species is relevant between pH 3.9 and 5.2 (maximum concentration at pH 4.4). Over pH 5, the full deprotonation of the ligand leads to the dimetallic complex $[\text{Cu}_2(\text{L2})]^{4+}$, which is the dominant species in solution over the wide pH range 6-10. The water molecules coordinated to the Cu(II) ions undergo deprotonation over pH 11, with the formation of the mono- and di-hydroxide complexes $[\text{Cu}_2(\text{L2})(\text{OH})]^{3+}$ and $[\text{Cu}_2(\text{L2})(\text{OH})_2]^{2+}$. The constants relative to these equilibria are reported in Table 3.

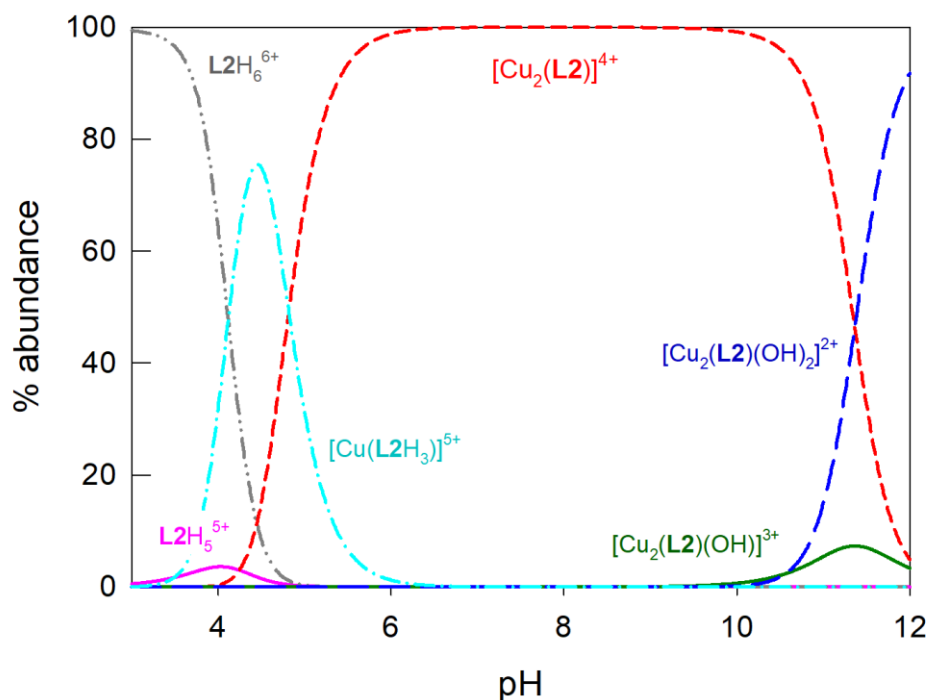


Figure 11. Distribution diagram showing species present at the equilibrium over the course of the potentiometric titration of **L2** (4×10^{-4} M) in presence of 2 *equiv.* of $\text{Cu}(\text{NO}_3)_2$, with standard NaOH in dioxane/water (20% v/v) ($T=25$ °C).

Table 2. Complexation constants for **L2** with Cu(II) in dioxane/water 20% v/v ($T=25$ °C). Standard deviations are shown in parentheses.

Equilibria	Log β
$\text{L2} + \text{Cu}^{2+} + 3\text{H}^+ \rightleftharpoons [\text{Cu}(\text{L2H}_3)]^{5+}$	35.37(3)
$\text{L2} + 2\text{Cu}^{2+} \rightleftharpoons [\text{Cu}_2(\text{L2})]^{4+}$	24.60(7)
$\text{L2} + 2\text{Cu}^{2+} + \text{H}_2\text{O} \rightleftharpoons [\text{Cu}_2(\text{L2})(\text{OH})]^{3+} + \text{H}^+$	12.4(1)
$\text{L2} + 2\text{Cu}^{2+} + 2\text{H}_2\text{O} \rightleftharpoons [\text{Cu}_2(\text{L2})(\text{OH})_2]^{2+} + 2\text{H}^+$	1.8(1)

Table 3. Equilibrium constants deriving from the overall constants shown in Tables 1 and 2. Standard deviations are shown in parentheses.

Equilibria	Log K
$\text{L2H}_3^{3+} + \text{Cu}^{2+} \rightleftharpoons [\text{Cu}(\text{L2H}_3)]^{5+}$	9.65(9)
$[\text{Cu}_2(\text{L2})]^{4+} + \text{H}_2\text{O} \rightleftharpoons [\text{Cu}_2(\text{L2})\text{OH}]^{3+} + \text{H}^+$	-12.2(1)
$[\text{Cu}_2(\text{L2})\text{OH}]^{3+} + \text{H}_2\text{O} \rightleftharpoons [\text{Cu}_2(\text{L2})(\text{OH})_2]^{2+} + \text{H}^+$	-10.6(2)

4.3.1.3 pH-spectrophotometric titration of L2 with Cu(II)

The pH-spectrophotometric titration on **L2**, in presence of two equivalents of $\text{Cu}(\text{NO}_3)_2$, was performed in dioxane/water 20% v/v (TBANO_3 0.05 M; T 25°C). The recorded family of UV-vis. spectra is reported in Figure 12.

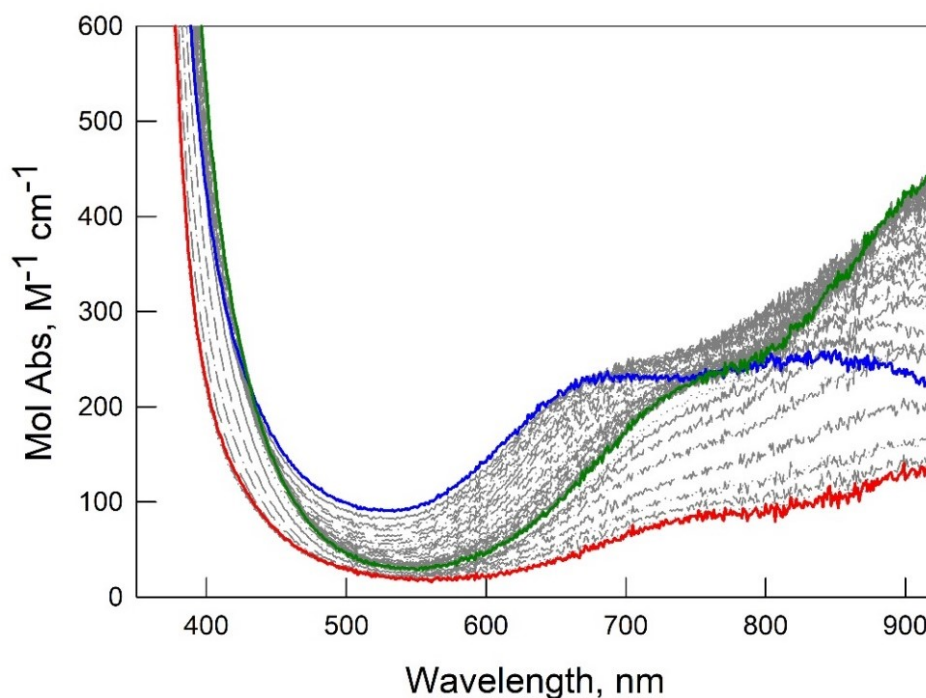


Figure 12. Spectra taken over the course of the pH-spectrophotometric titration of a solution of 4×10^{-4} M in **L2** and 8×10^{-4} M in $\text{Cu}(\text{II})$. The red line highlights the initial spectrum (at about pH 3), while the green and blue lines correspond to the spectra recorded at pH 7 and 12, respectively.

The optical changes occurring over titration are rather similar to those observed for the dicopper complex of **L1**. The initial absorption spectrum - at pH 3 - is highlighted in red (see Fig. 12). By addition of NaOH, the development of the d-d bands relative to the copper(II)-containing species can be observed between 600 and 920 nm. A significant colour change is also observed in solution, from colourless to green. In detail, the band at 900 nm and the shoulder at 730 nm are rather peculiar of a *bistren* dicopper complex, with the $\text{Cu}(\text{II})$ ions in a trigonal bipyramid geometry. The metal ions are bound to the *tren* subunits of **L2**, with water molecules in the apical positions left free by the ligand. The development of $\text{N}_{\text{sec}} \rightarrow \text{Cu}(\text{II})$ (LMCT) bands near 400 nm accompanies the formation of the complex. At neutral pH (green line), the d-d band at 900 nm reaches its maximum intensity. Over pH 7, a progressive change in the intensity ratio between the band at 900 nm and the shoulder occurs until pH 11 (blue line). In basic environment, the deprotonation of the coordinated water molecules, and the consequent

formation of the hydroxide species $[\text{Cu}_2(\text{L2})(\text{OH})]^{3+}$ and $[\text{Cu}_2(\text{L2})(\text{OH})_2]^{2+}$, are probably responsible of a slight modification of the coordination geometry around the copper centers to which are attributed the observed spectral changes. These changes in the visible region of the spectrum are accompanied by a change of the colour in solution from green to light blue.

The molar absorbance (*i.e.* ϵ in Fig. 13) at 650 and 885 nm has been plotted against pH; the resulting profiles, superimposed to the distribution diagram, are shown in Figure 13.

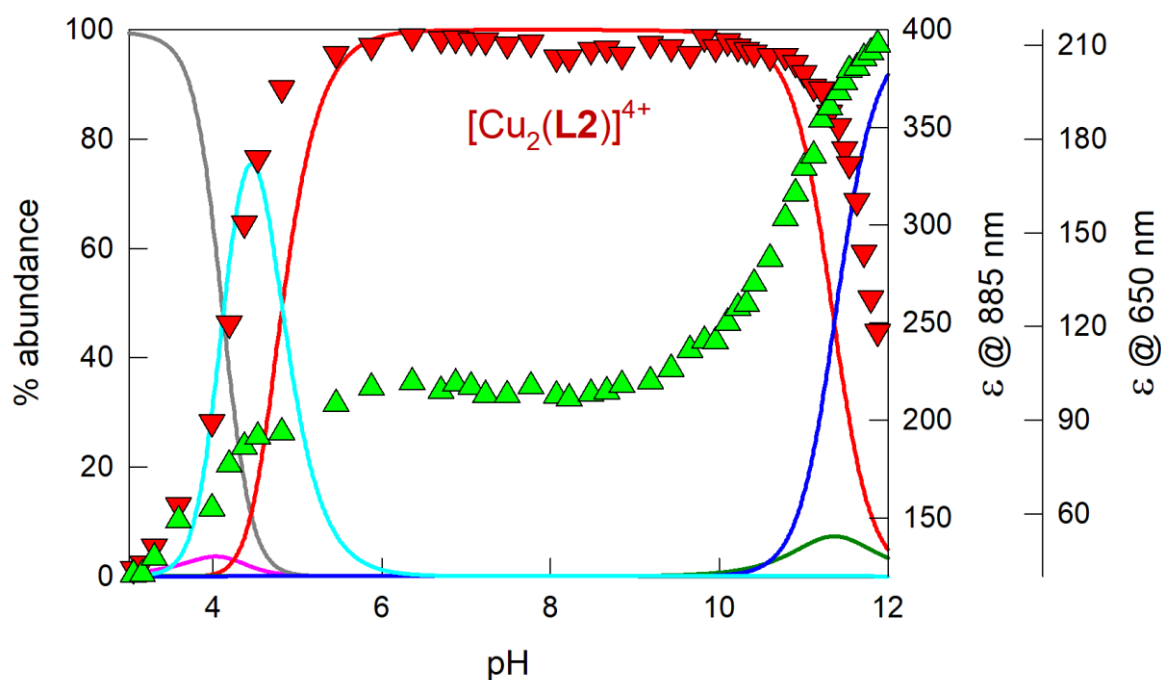


Figure 13. Distribution diagram of the species present at the equilibrium over the course of the titration with standard NaOH of a solution 4×10^{-4} M in **L2** and 8×10^{-4} M in Cu(II) with the superimposed pH-spectrophotometric profiles. Symbols: red triangles, superimposed plot of Mol Abs at 885 nm; green triangles, superimposed plot of Mol Abs at 650 nm. The lines in the diagram correspond to the species: $\text{H}_6\text{L2}^{6+}$, grey; $\text{H}_5\text{L2}^{5+}$, purple; $[\text{Cu}(\text{L2H}_3)]^{5+}$, cyan; $[\text{Cu}_2(\text{L2})]^{4+}$, red; $[\text{Cu}_2(\text{L2})(\text{OH})]^{3+}$, green; $[\text{Cu}_2(\text{L2})(\text{OH})_2]^{2+}$, blue.

Notably, the good superimposition of the titration profile at 885 nm (red triangles) vs pH to the curve relative to the $[\text{Cu}_2(\text{L2})]^{4+}$ species (red solid line) in the distribution diagram demonstrates the correlation between the d-d band at 920 nm and the abundance of the dicopper(II) complex in solution. Furthermore, the titration profile at 650 nm (green triangles), superimposed to the distribution diagram, highlights the correlation between the intensity of this absorption band and the deprotonation of the copper-coordinated water molecules.

4.3.1.4 Potentiometric titrations on H₂suc and H₂glut in dioxane/water 20% v/v

Potentiometric titrations were also performed on two representative dicarboxylic acids, H₂suc (succinic acid) and H₂glut (glutaric acid), in order to determine their pK_a values in dioxane/water mixture 20% v/v (0.05 M [TBA]NO₃, 25°C).

In pure water both acids are fully deprotonated at pH 7, being pK_{a1} and pK_{a2} values (at 25°C): 4.21 and 5.41, 4.34 and 5.22 for H₂suc and H₂glut, respectively.^{34,35} In dioxane/water mixture, the deprotonation processes are significantly shifted toward higher pH values: potentiometric titrations allowed us to determine the pK_a values in this medium, which were found to be pK_{a1} = 6.89(4), pK_{a2} = 8.74(6) for H₂suc; pK_{a1} = 7.55(5), pK_{a2} = 8.36(7) for H₂glut. The corresponding distribution diagrams are reported in Figure 14.

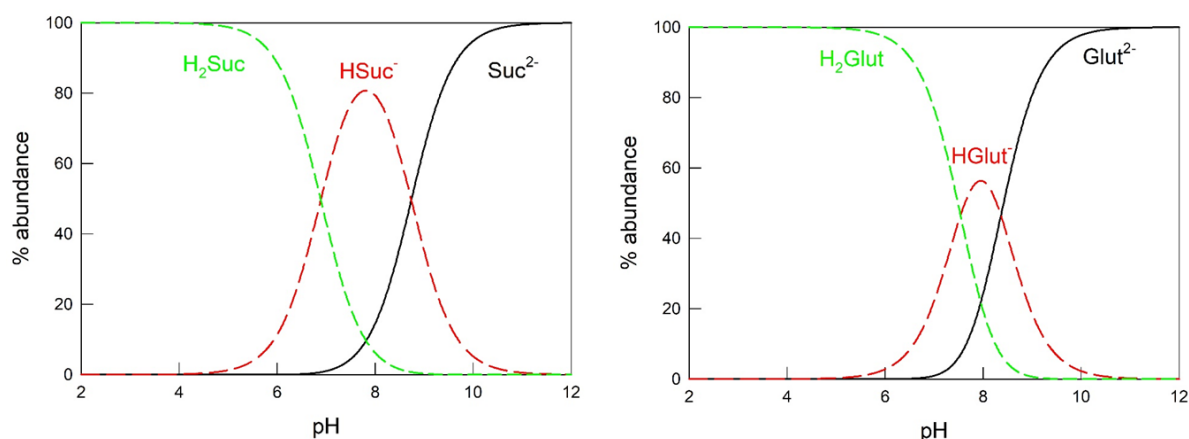


Figure 14. Distribution diagrams of the species present at the equilibrium over the course of the potentiometric titrations of H₂suc (left) and H₂glut (right) 1 × 10⁻³ M with standard NaOH in dioxane/water 20% v/v (T=25 °C).

4.3.2 Spectrophotometric studies on [Cu₂(L2)]⁴⁺ with dicarboxylates

4.3.2.1 UV-vis. titrations of [Cu₂(L2)]⁴⁺ in dioxane/water 20% v/v at pH 7

The affinity of the new receptor [Cu₂(L2)]⁴⁺ towards dicarboxylates was investigated through UV-vis. titrations. In particular, experiments on a series of anionic guests (reported in Table 4) were carried out in dioxane/water 20% v/v at pH 7 (0.025 M HEPES buffer, T = 25° C) because of the low solubility of the complex in pure water.

Although the chosen medium shifts the full deprotonation of dicarboxylic acids to pH values > 8, our titration studies (with the anions reported in Table 4) showed that the coordination of these polycarboxylates to the cage already occurs at neutral pH. In fact, the coordination of the

conjugated base to cage cavity and its interaction with the metal centers promote the complete deprotonation of the corresponding acids: stable 1:1 adducts are actually formed for most of the investigated guests (see Fig.s 16-22).

Among the studied anions, the highest affinity was found for fum^{2-} and suc^{2-} . As expected, a decrease in affinity was observed for longer anions, such as glut^{2-} (C5) and adi^{2-} (C6). The affinity *trend* of $[\text{Cu}_2(\mathbf{L2})]^{4+}$ is rather similar to that observed for $[\text{Cu}_2(\mathbf{L1})]^{4+}$. Nonetheless, the selectivity seems to be lower for $[\text{Cu}_2(\mathbf{L2})]^{4+}$; this might be attributed to an effect of the ligand functionalization or of the different solvent medium employed for the studies.

Table 4. Binding constants (as $\text{Log}K_{11}$ values) obtained by UV-vis. titrations on $[\text{Cu}_2(\mathbf{L2})]^{4+}$ in dioxane/water solution 20% v/v, 0.025 M HEPES buffer at pH 7 (T=25 °C). Standard deviations are shown in parenthesis. n.a.: not available.

Anionic guests	$\text{Log}K_{11} [\text{Cu}_2(\mathbf{L2})]^{4+}$
fum^{2-}	5.76(2)
suc^{2-}	5.60(3)
isopht^{2-}	4.98(4)
glut^{2-}	4.14(3)
male^{2-}	3.65(5)
adi^{2-}	3.47(1)
ace^{2-}	n.a.
$\alpha\text{-keto}^{2-}$	n.a.

Thanks to the similarity between the structures of **L2** and **L1** ligands, in particular in the coordination sphere around the Cu(II) ions in the complex, the spectral variations detected during the titration experiments of $[\text{Cu}_2(\mathbf{L2})]^{4+}$ are quite similar to those observed for the dicopper(II) complex of **L1**. In fact, in the absorption spectrum of $[\text{Cu}_2(\mathbf{L2})]^{4+}$, the band at 900 nm and the shoulder at 700 nm typically indicate a trigonal bipyramid geometry for the two metal ions, with water molecules in the positions left free by the *tren* subunits. The variations of these bands, occurring under anion binding, are very similar to those found for $[\text{Cu}_2(\mathbf{L1})]^{4+}$ (see Fig.s 16-22).

No single crystals of the inclusion complexes of $[\text{Cu}_2(\mathbf{L2})]^{4+}$ could be obtained, therefore we could not gain any structural information on the adducts from X-ray diffraction studies. The

formation of 1:1 adducts in solution was however confirmed in solution by HRMS-ESI analysis. In particular, the HRMS-ESI of an acetonitrile solution containing $[\text{Cu}_2(\text{L2})]^{4+}$ and 1 *eqv.* of Na_2suc showed a peak at 796.4592 m/z, attributable to the double-charged $[\text{Cu}_2(\text{L2})(\text{suc})]^{2+}$ species (see Fig. 15).

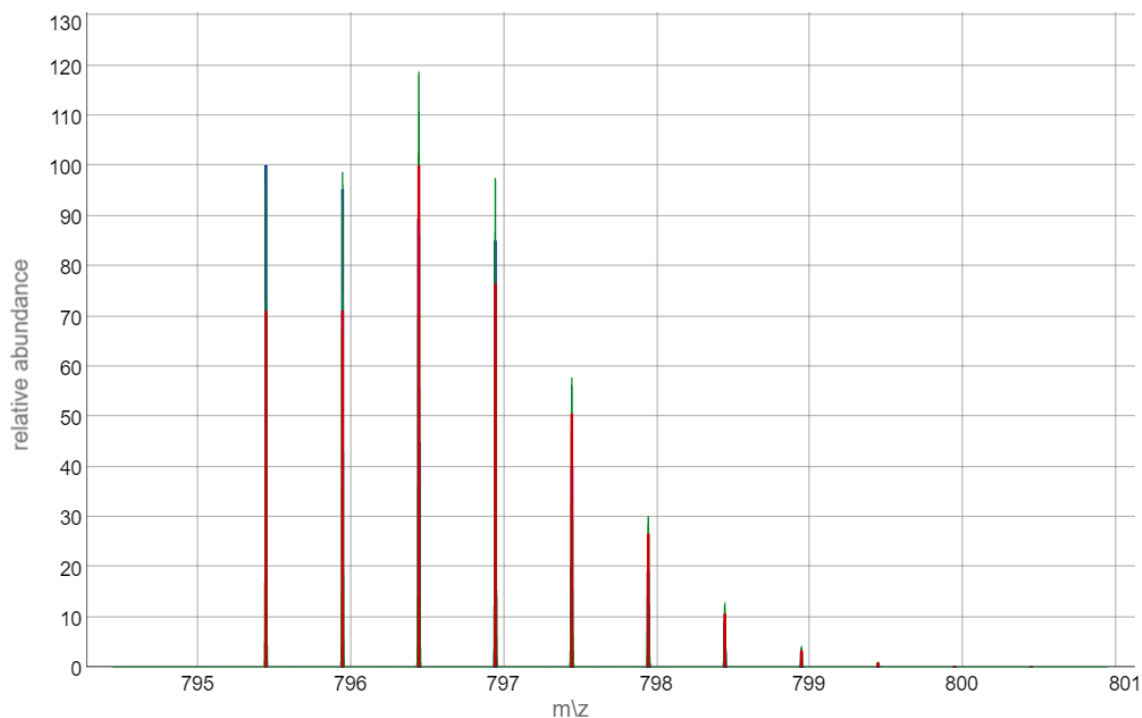
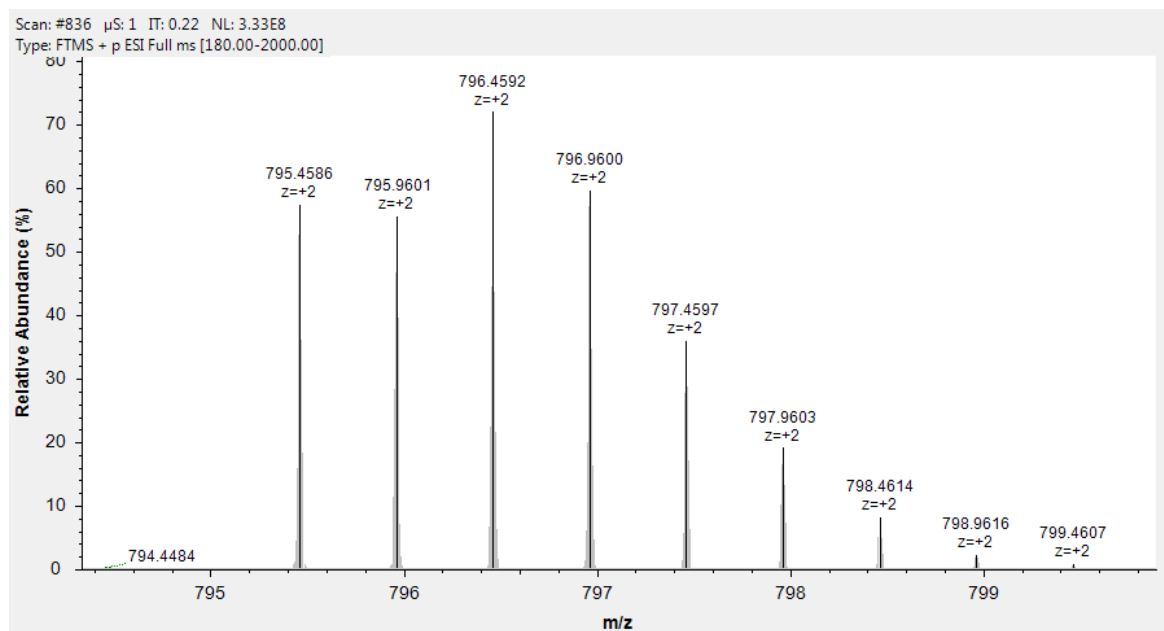


Figure 15. HRMS-ESI spectrum of a solution of $[\text{Cu}_2(\text{L2})]^{4+}$ in CH_3CN , containing 1 *eqv.* of Na_2suc . **Up:** zoom scan of the peak at 796.5492 m/z obtained from the experimental HRMS-ESI spectrum. **Bottom:** calculated spectrum of the adduct $[\text{Cu}_2(\text{L2})(\text{suc})]^{2+}$.

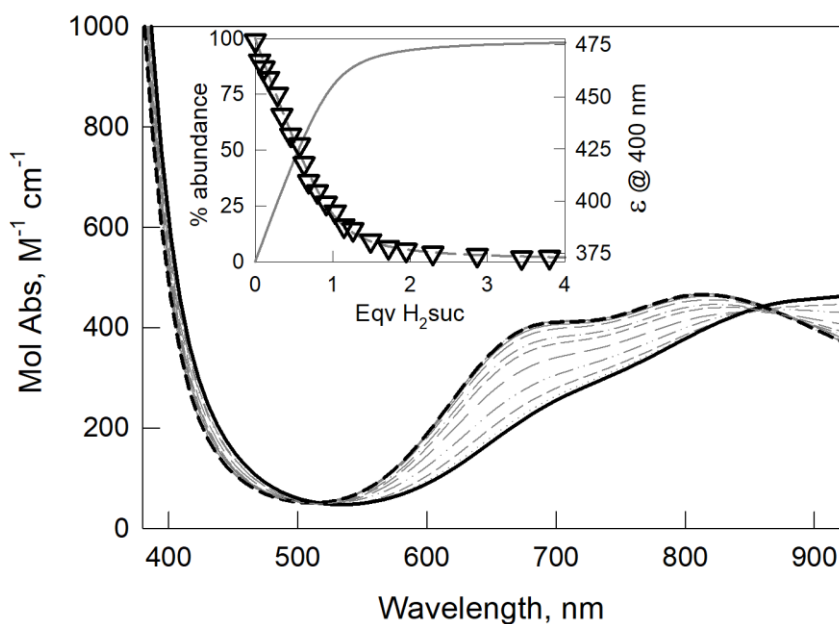


Figure 16. UV-vis. spectra taken upon titration of $[\text{Cu}_2(\text{L2})]^{4+}$ ($50 \mu\text{M}$) with a solution of H_2suc (12.5 mM) in dioxane/water 20% v/v at pH 7 (0.025 M HEPES buffer, path length: 10 cm). The solid and dashed black lines represent the spectra at 0 and 4 *eqv.* of the added anion, respectively. **Inset:** titration profile of ϵ (*i.e.* Mol Abs) at 400 nm (triangles), superimposed to the distribution diagram of the species $[\text{Cu}_2(\text{L2})]^{4+}$ (dashed line) and $[\text{Cu}_2(\text{L2})(\text{suc})]^{2+}$ (solid line) *vs eqv.* of the added guest, calculated for $\text{Log}K_{11}=5.60(3)$.

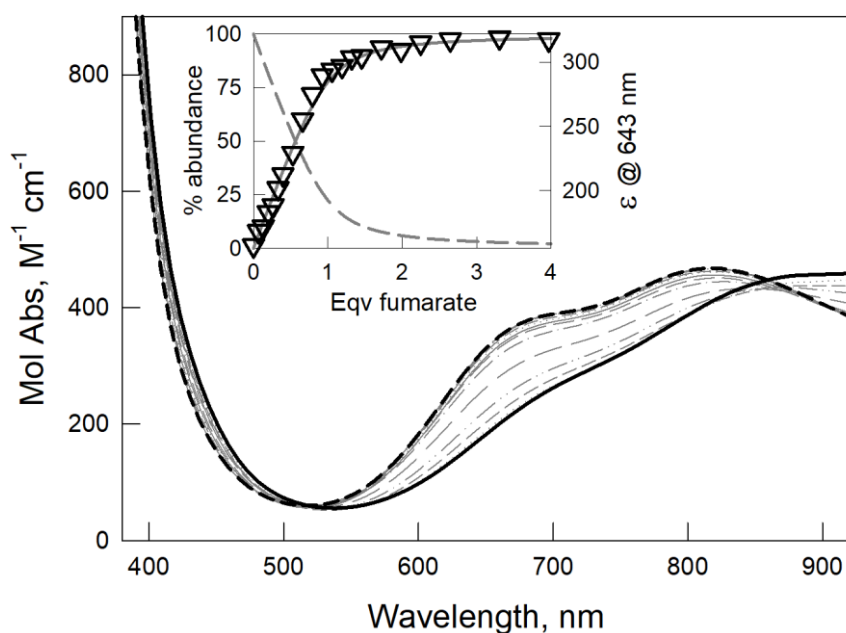


Figure 17. UV-vis. spectra taken upon titration of $[\text{Cu}_2(\text{L2})]^{4+}$ ($50 \mu\text{M}$) with fumaric acid (12.5 mM) in dioxane/water 20% v/v at pH 7 (0.025 M HEPES buffer, path length 10 cm). The solid and dashed black lines represent the spectra at 0 and 4 *eqv.* of the added anion, respectively. **Inset:** titration profile of ϵ (*i.e.* Mol Abs) at 643 nm (triangles) superimposed to the distribution diagram of the species $[\text{Cu}_2(\text{L2})]^{4+}$ (dashed line) and $[\text{Cu}_2(\text{L2})(\text{fum})]^{2+}$ (solid line) *vs eqv.* of the added guest, calculated for $\text{Log}K_{11}=5.76(2)$.

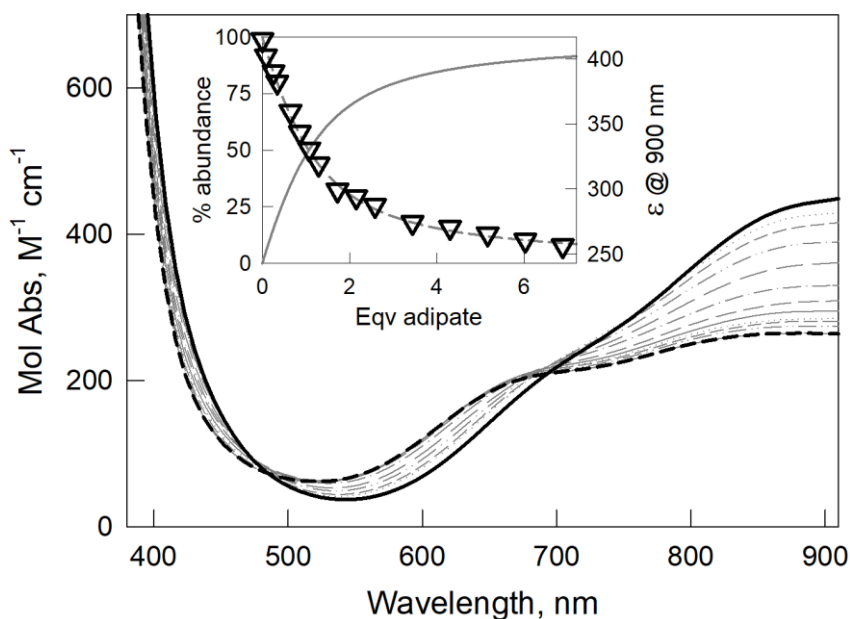


Figure 18. UV-vis. spectra taken upon titration of $[\text{Cu}_2(\text{L2})]^{4+}$ (0.55 mM) with adipic acid (0.10 M) in dioxane/water 20% v/v at pH 7 (0.025 M HEPES buffer, path length 1 cm). The solid and dashed black lines represent the spectra at 0 and 7 *eqv.* of the added anion, respectively. **Inset:** titration profile of ϵ (*i.e.* Mol Abs) at 900 nm (triangles) superimposed to the distribution diagram of the species $[\text{Cu}_2(\text{L2})]^{4+}$ (dashed line) and $[\text{Cu}_2(\text{L2})(\text{adi})]^{2+}$ (solid line) vs *eqv.* of the added guest, calculated for $\text{Log}K_{11}=3.47(1)$.

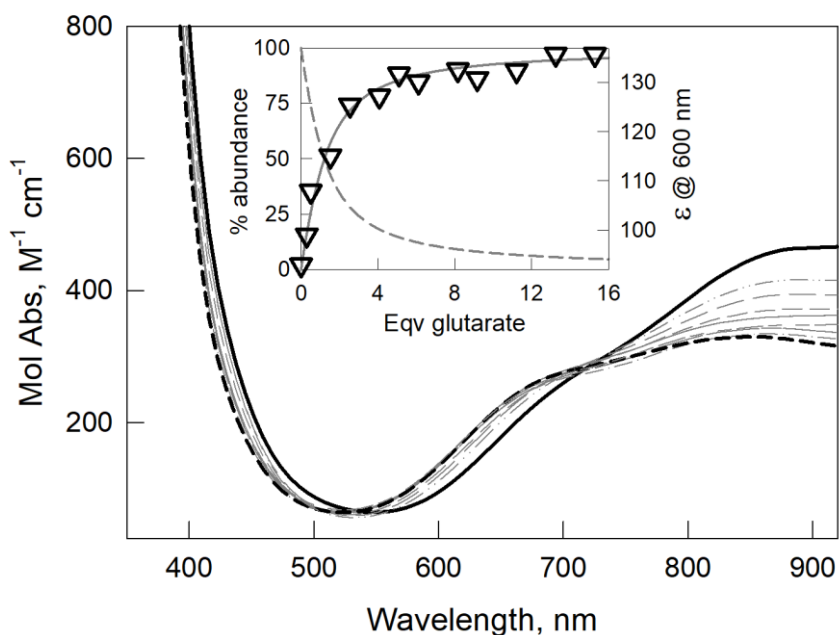


Figure 19. UV-vis. spectra taken upon titration of $[\text{Cu}_2(\text{L2})]^{4+}$ (0.20 mM) with glutaric acid (10 mM) in dioxane/water 20% v/v at pH 7 (0.025 M HEPES buffer, path length 1 cm). The solid and dashed black lines represent the spectra at 0 and 16 *eqv.* of the added anion, respectively. **Inset:** titration profile of ϵ (*i.e.* Mol Abs) at 600 nm (triangles) superimposed to the distribution diagram of the species $[\text{Cu}_2(\text{L2})]^{4+}$ (dashed line) and $[\text{Cu}_2(\text{L2})(\text{glut})]^{2+}$ (solid line) vs *eqv.* of the added guest, calculated for $\text{Log}K_{11}=4.14(3)$.

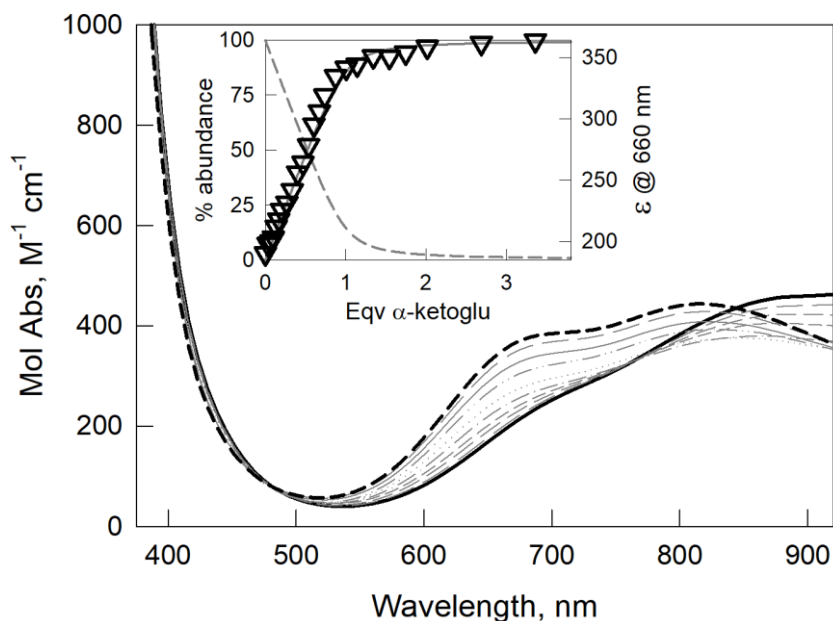


Figure 20. UV-vis. spectra taken upon titration of $[\text{Cu}_2(\text{L}2)]^{4+}$ ($50 \mu\text{M}$) with α -ketoglutaric acid (12.5 mM) in dioxane/water $20\% \text{ v/v}$ at pH 7 (0.025 M HEPES buffer, path length 10 cm). The solid and dashed black lines represent the spectra at 0 and 4 *eqv.* of the added anion, respectively. **Inset:** titration profile of ϵ (*i.e.* Mol Abs) at 660 nm (triangles) superimposed to the distribution diagram of the species $[\text{Cu}_2(\text{L}2)]^{4+}$ (dashed line) and $[\text{Cu}_2(\text{L}2)(\alpha\text{-keto})]^{2+}$ (solid line) *vs eqv.* of the added guest, calculated for $\text{Log}K_{11}=5.90(4)$.

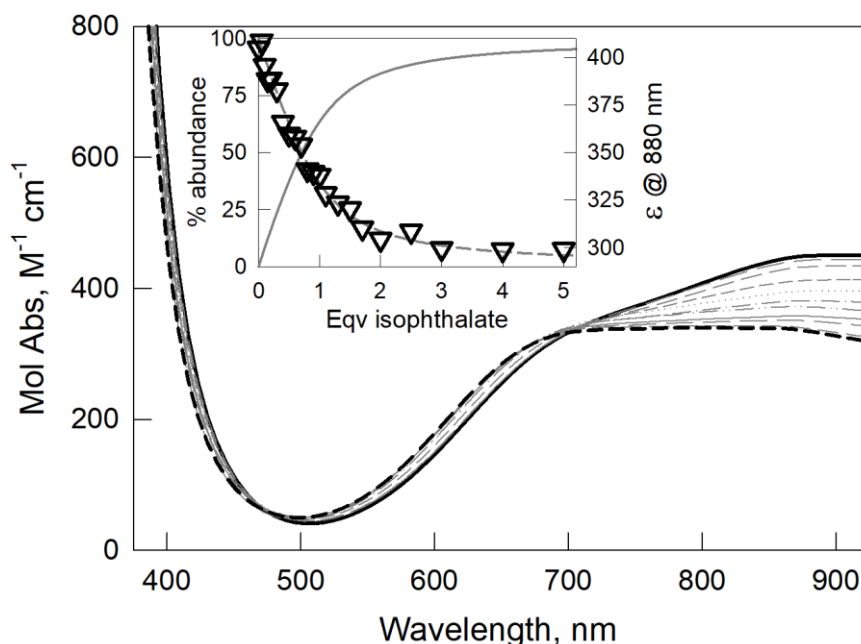


Figure 21. UV-vis. spectra taken upon titration of $[\text{Cu}_2(\text{L}2)]^{4+}$ ($50 \mu\text{M}$) with isophthalate (as Na^+ salt, 12.5 mM) in dioxane/water $20\% \text{ v/v}$ at pH 7 (0.025 M HEPES buffer, path length 10 cm). The solid and dashed black lines represent the spectra at 0 and 5 *eqv.* of the added anion, respectively. **Inset:** titration profile of ϵ (*i.e.* Mol Abs) at 880 nm (triangles) superimposed to the distribution diagram of the species $[\text{Cu}_2(\text{L}2)]^{4+}$ (dashed line) and $[\text{Cu}_2(\text{L}2)(\text{isoph})]^{2+}$ (solid line) *vs eqv.* of the added guest, calculated for $\text{Log}K_{11}=4.98(4)$.

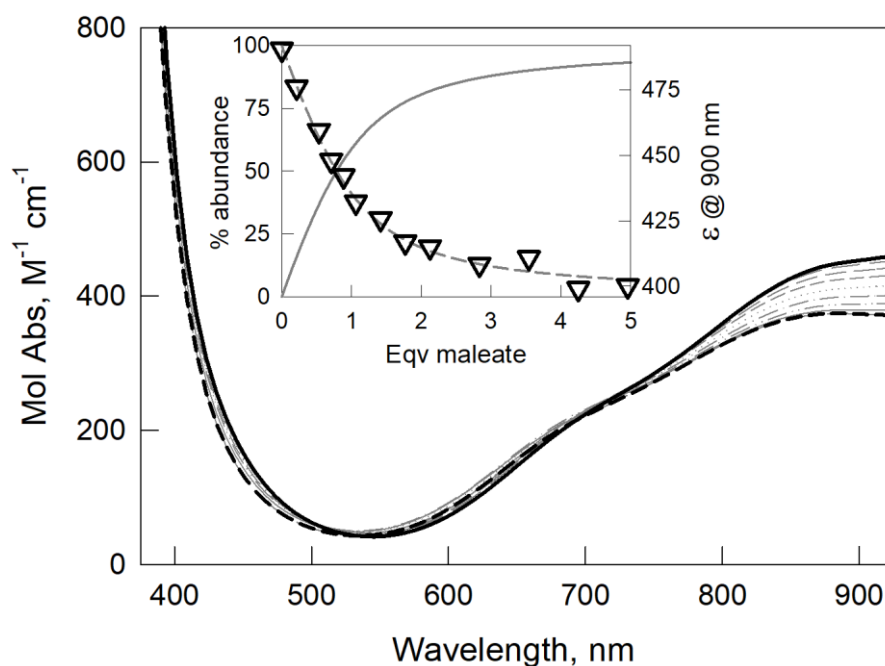


Figure 22. UV-vis. spectra taken upon titration of $[\text{Cu}_2(\text{L}2)]^{4+}$ (0.55 mM) with maleic acid (0.10 M) in dioxane/water 20% v/v at pH 7 (0.025 M HEPES buffer, path length 1 cm). The solid and dashed black lines represent the spectra at 0 and 5 *eqv.* of the added anion, respectively. **Inset:** titration profile of ϵ (*i.e.* Mol Abs) at 900 nm (triangles) superimposed to the distribution diagram of the species $[\text{Cu}_2(\text{L}2)]^{4+}$ (dashed line) and $[\text{Cu}_2(\text{L}2)(\text{mal})]^{2+}$ (solid line) vs *eqv.* of the added guest, calculated for $\text{Log}K_{11}=3.65(5)$.

4.3.2.2 UV-vis. titration of $[\text{Cu}_2(\text{L}2)]^{4+}$ with succinate in dichloromethane

In summary, the functionalization of **L1** allowed us to obtain a new lipophilic ligand, able to form stable dinuclear complex with Cu(II). Very importantly, the modification of the ligand framework on the spacers did not affect the coordination properties of the polyamine, and the obtained dicopper(II) complex $[\text{Cu}_2(\text{L}2)]^{4+}$ showed a high stability over a wide pH range and good anion binding properties towards dicarboxylates. Compared to $[\text{Cu}_2(\text{L}1)]^{4+}$, $[\text{Cu}_2(\text{L}2)]^{4+}$ is highly soluble in pure organic solvents, therefore it can be promising as an extractant for polycarboxylates. Before performing liquid-liquid extraction experiments, we tested the affinity of the dicopper cryptate for the succinate anion (chosen as a model target guest) in a water-immiscible solvent, *i.e.* dichloromethane. The experiment consisted in the UV-vis. titration of $[\text{Cu}_2(\text{L}2)]^{4+}$ with $[\text{TBA}]_2\text{suc}$ in the pure organic solvent. As shown by Figure 23, the titration experiment confirmed both the formation of a 1:1 receptor:anion adduct and the high affinity of the dicopper(II) complex for the investigated guest.

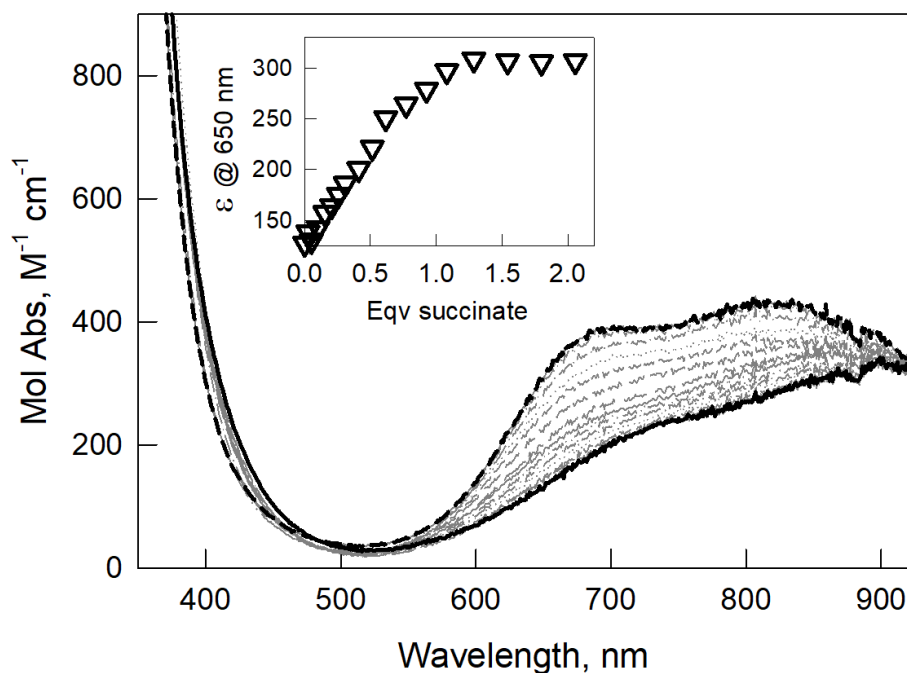


Figure 23. Family of UV-vis. spectra taken upon titration of $[\text{Cu}_2(\text{L2})]^{4+}$ ($30 \mu\text{M}$) with $[\text{TBA}]_2\text{succinate}$ (5 mM) in dichloromethane (path length 10 cm). The solid and dashed black lines represent the spectra at 0 and 2.2 eqv. of the added anion, respectively. **Inset:** titration profile of ϵ (*i.e.* Mol Abs) at 650 nm (triangles) vs *eqv.* of the added anion.

4.3.3 Extraction experiments

4.3.3.1 UV-vis. spectrum of extracting solution

Once the stability of $[\text{Cu}_2(\text{L2})]^{4+}$ and its affinity for succinate were assessed in dichloromethane, liquid-liquid extraction experiments were carried out in batch. In a typical experiment, a glass vial was filled with 5 mL of a 0.20 mM solution of $[\text{Cu}_2(\text{L2})]^{4+}$ in dichloromethane and this organic phase was kept in contact with 5 mL of a 1 mM solution of H_2suc (*i.e.* 5 eqv. vs the dicopper complex) in 0.05 M HEPES buffer, at $\text{pH } 7$. The mixture was stirred for 20 minutes . After 10 minutes equilibration, the two phases were separated and analysed. A scheme of the extraction experiment is reported in Figure 24.

The effective extraction of the succinate anion by the dicopper(II) complex was demonstrated by recording the UV-Vis. spectra of the organic phase before and after the extraction experiment. As shown in Figure 25, in the final UV-vis. spectrum of the organic phase (blue line), the d-d bands are significantly shifted towards higher energies. This shift is consisting with the complexation of the succinate anion by the dinuclear cage, the final spectrum actually

corresponds to that recorded over the course of the spectrophotometric titration of $[\text{Cu}_2(\text{L2})]^{4+}$ with $[\text{TBA}]_2\text{suc}$ in the dichloromethane (see Fig. 23).

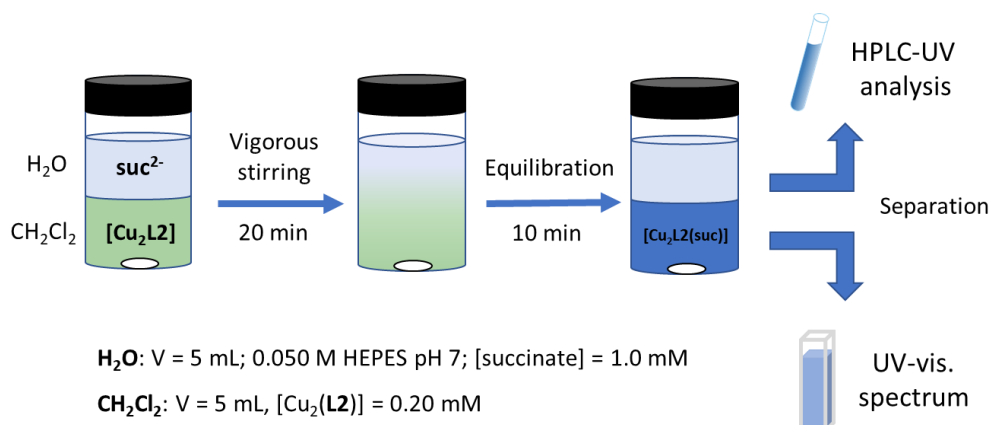


Figure 24. Scheme of the extraction experiment in batch

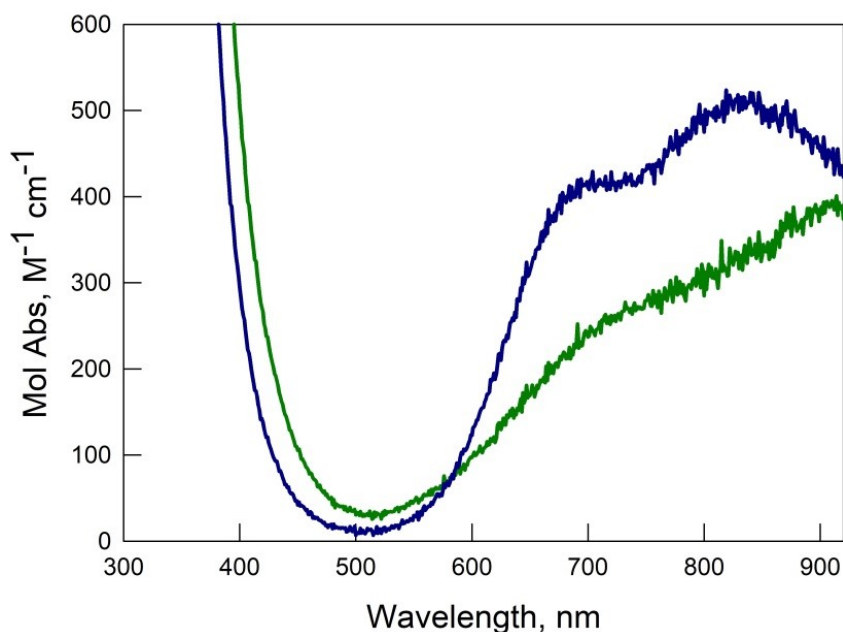


Figure 25. UV-vis. spectra of the solution of $[\text{Cu}_2(\text{L2})]^{4+}$ (0.20 mM, path length = 1 cm) in dichloromethane before (green line) and after contact (blue line) with an aqueous solution of succinate (1.0 mM).

4.3.3.2 HPLC-UV chromatographic analysis

To obtain quantitative extraction data, HPLC-UV technique was applied to monitor the suc^{2-} concentration in the aqueous phase, before and after the extraction experiments.

First of all, the best conditions to perform HPLC-UV measurements were chosen through the analysis of standard solutions of the anion in neutral water (*i.e.* 0.05 M HEPES buffer at pH 7), prepared by dilution of a 1000 mg L^{-1} stock solution. Three independent five-point calibration

curves (an example is reported in Fig. 26) confirmed a good linearity ($r^2 > 0.9982$) in the 25-200 mg L⁻¹ concentration range. The chromatographic peak relative to suc²⁻ showed a retention time of 6.1 min (see the zoom inset in Fig. 27).

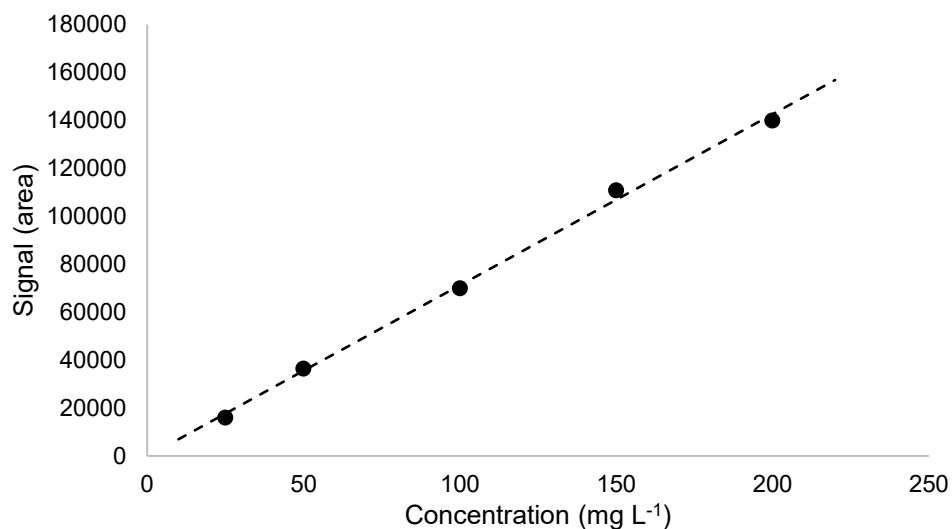


Figure 26. Calibration curve obtained by plotting the recorded area of the signal relative to succinate (retention time: 6.1 min) vs the concentrations of the standard solutions in HEPES buffer (0.05 M, pH 7).

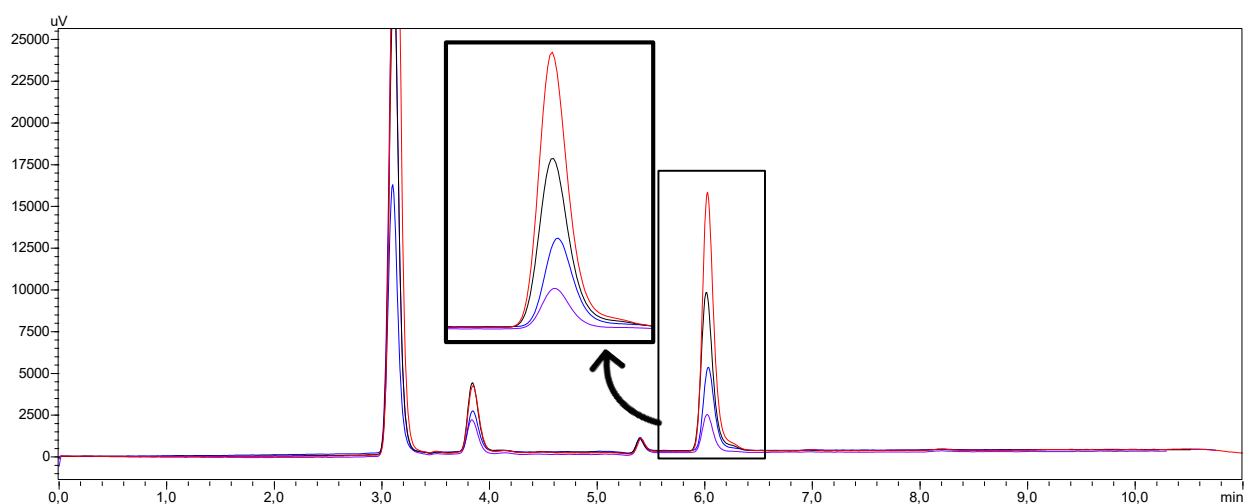


Figure 27. HPLC-UV chromatograms overlay of succinate standard solutions: 25 mg L⁻¹ (violet line), 50 mg L⁻¹ (blue line), 100 mg L⁻¹ (black line), 150 mg L⁻¹ (red line). Succinate retention time: 6.1 min (peak zoom in the inset).

After these preliminary investigations, quantitative extraction experiments were performed following the same conditions employed in the preliminary trials. In particular, a 0.20 mM solution of [Cu₂(L2)]⁴⁺ in dichloromethane was stirred in contact with a 1.0 mM solution of H₂suc in neutral water (0.05 M HEPES buffer at pH 7). After vigorously stirring for 20 minutes,

the solutions were equilibrated for 10 minutes, then were separated and the aqueous phase was analysed through HPLC-UV (see Fig. 24).

Compared to the determination of succinate in the HEPES buffer (see Fig. 27), the chromatogram of the aqueous phase showed a tailed peak eluting after 4 min (see Fig. 28) that was attributed to DMSO. For this reason, it was necessary to build a second calibration curve using standard solutions of succinate in 0.05 M HEPES buffer, previously kept in contact with dichloromethane containing 2.2% v/v DMSO. The obtained calibration curve (an example is reported in Fig. 29) showed good linearity in the working concentration range ($r^2 > 0.9944$) and allowed the quantification of the analyte in the same experimental conditions used for the extraction studies.

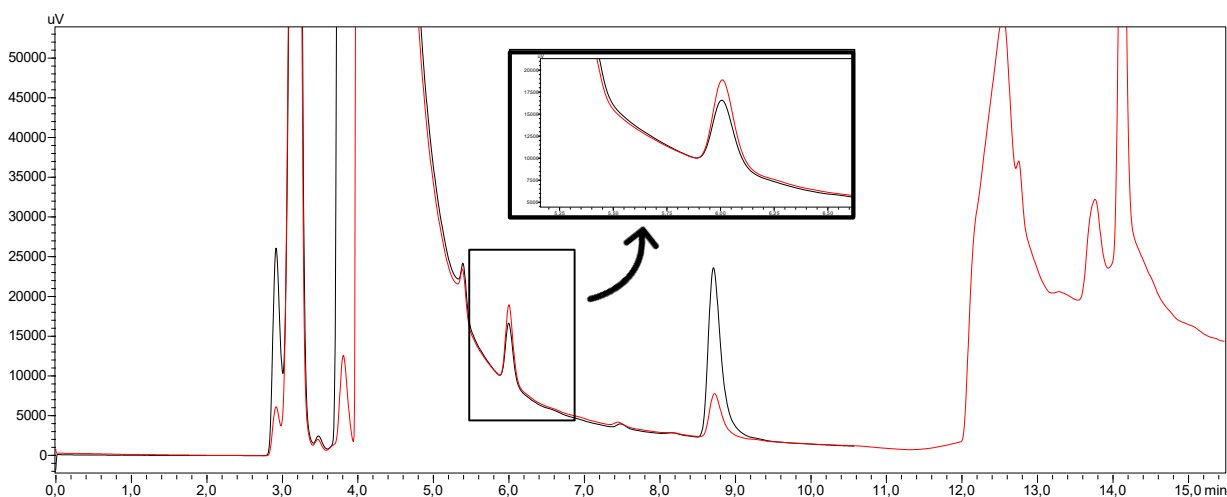


Figure 28. HPLC-UV chromatograms overlay of a succinate sample (in 0.05 M HEPES buffer) after contact with dichloromethane containing the dicopper cryptate (black line) and after contact with dichloromethane (2.2% v/v DMSO, no cage) as control sample (red line). Succinate retention time: 6.1 min (peak zoom in the inset).

To evaluate the extraction efficiency, the percentage decrease of succinate concentration was quantified in the aqueous phase by the comparing the analyte chromatographic peak after the extraction (black line in Fig. 28) with that detected in the blank experiment (*i.e.* performed in the same conditions, but without dicopper(II) complex into the organic phase, see the red line in Fig. 28).

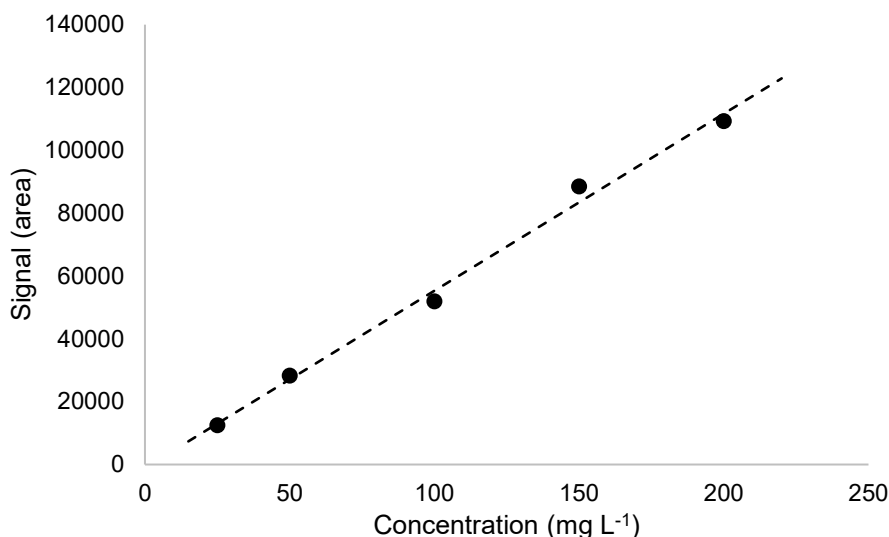


Figure 29. Calibration curve obtained by plotting the recorded area of the signal relative to succinate retention time: 6.1 min) vs the concentrations of the standard solutions in HEPES buffer (0.05 M, pH 7) kept in contact with the organic phase, following the setup of the extraction experiment.

Seven independent extraction experiments were performed over non-consecutive days. For each repetition, the % extraction yield, calculated with respect to the initial concentration of succ^{2-} in the aqueous phase, was determined. The obtained values are reported in the Table 5.

Table 5. Results from the seven independent extraction experiments. The measured average extraction yield resulted to be $20 \pm 4\%$ ($n = 7$, $\alpha 0.05$).

Succinate concentration in the aqueous phase (mg L ⁻¹)		
Without azacryptate	With azacryptate	Extraction yield (%)
142	101	28.4
161	134	17.1
143	113	20.9
152	127	16.8
119	91	24.2
163	132	18.7
154	128	16.7

The average extraction yield resulted $20 \pm 4\%$ ($n = 7$, $\alpha 0.05$). Considering that the concentration of $[\text{Cu}_2(\text{L}2)]^{4+}$ in dichloromethane is 0.20 mM and that the anion forms a 1:1

adduct with the cage, the obtained extraction yield (*i.e.* 20%, starting from a 1 mM aqueous solution of suc^{2-}) is the maximum yield that can be obtained in the employed experimental conditions. This result indicates that a hydrophilic anion such as suc^{2-} can be successfully extracted from water using the $[\text{Cu}_2(\text{L2})]^{4+}$ complex, confirming what observed by UV-vis. spectroscopy (*i.e.* from the changes in the UV-vis. spectrum of $[\text{Cu}_2(\text{L2})]^{4+}$ before and after extraction).

It is important to remark that blank extraction experiments confirmed that suc^{2-} is not significantly extracted into the organic phase without the cage. In fact, the evaporation of the organic phase, recovered from a blank experiment, and dissolution of the residue with 1 mL 0.05 M HEPES gave an undetectable concentration of the analyte.

4.3.3.3. $^1\text{H-NMR}$ study

The successful succinate extraction from water by $[\text{Cu}_2(\text{L2})]^{4+}$ was also demonstrated through $^1\text{H-NMR}$ spectroscopy. The same extraction experiment setup used for HPLC-UV analyses was followed: 1.5 mL of a 1.044 mM solution of suc^{2-} (1.57 mmol) in buffered D_2O (0.05 M PBS, pH 7) was interfaced with 1.5 mL of a 0.42 mM solution (0.63 mmol) of $[\text{Cu}_2(\text{L2})]^{4+}$ in dichloromethane. The mixture was vigorously stirred for 20 min, equilibrated for 10 min and finally separated and analysed. For the quantification of the succinate signal, glycine was employed as internal reference. Very interestingly, a 0.638 mM residual concentration of the anion in the D_2O phase was obtained: 0.61 mmol of suc^{2-} were hence extracted into the organic phase, leading to an extraction yield of 97% with respect to the complex. A blank experiment confirmed that the suc^{2-} anion is not transferred into the organic phase without the assistance of the cage. The recorded $^1\text{H-NMR}$ spectra of the D_2O phase are reported in Figures 30-32.

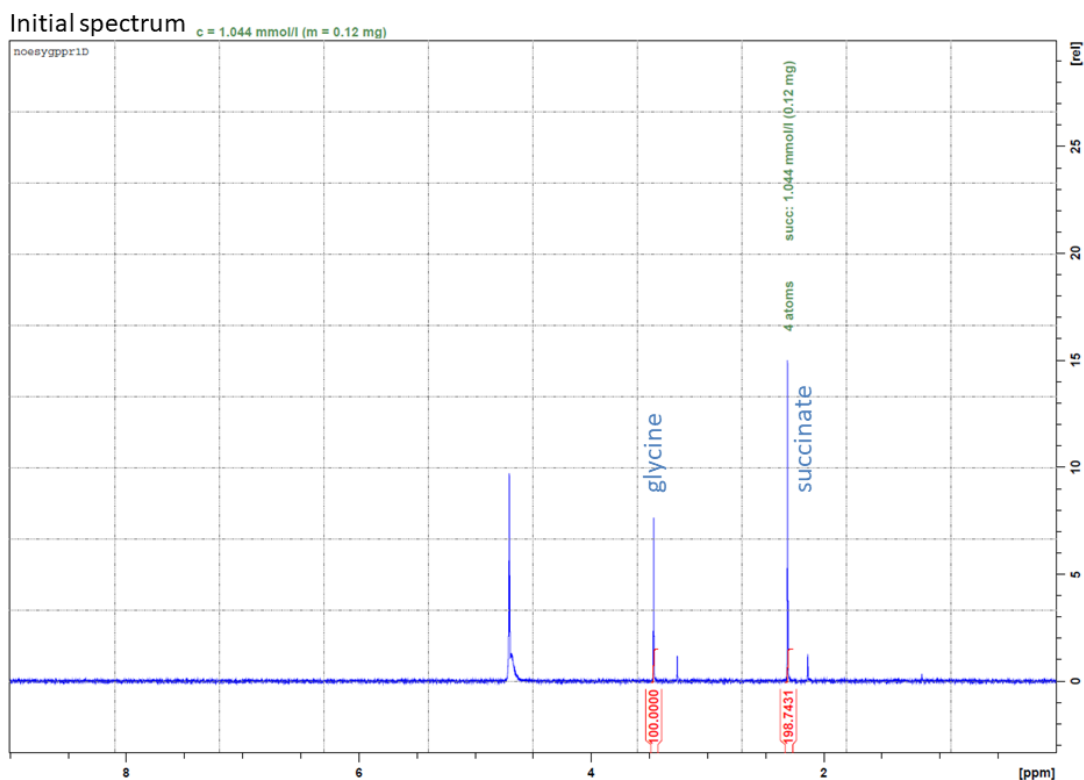


Figure 30. $^1\text{H-NMR}$ spectrum of a D_2O solution of succinate (0.05 M PBS, pH 7) in presence of glycine as internal reference. The concentration of succinate was determined using the Topspin Eretic2 package (details are reported in the Experimental section).

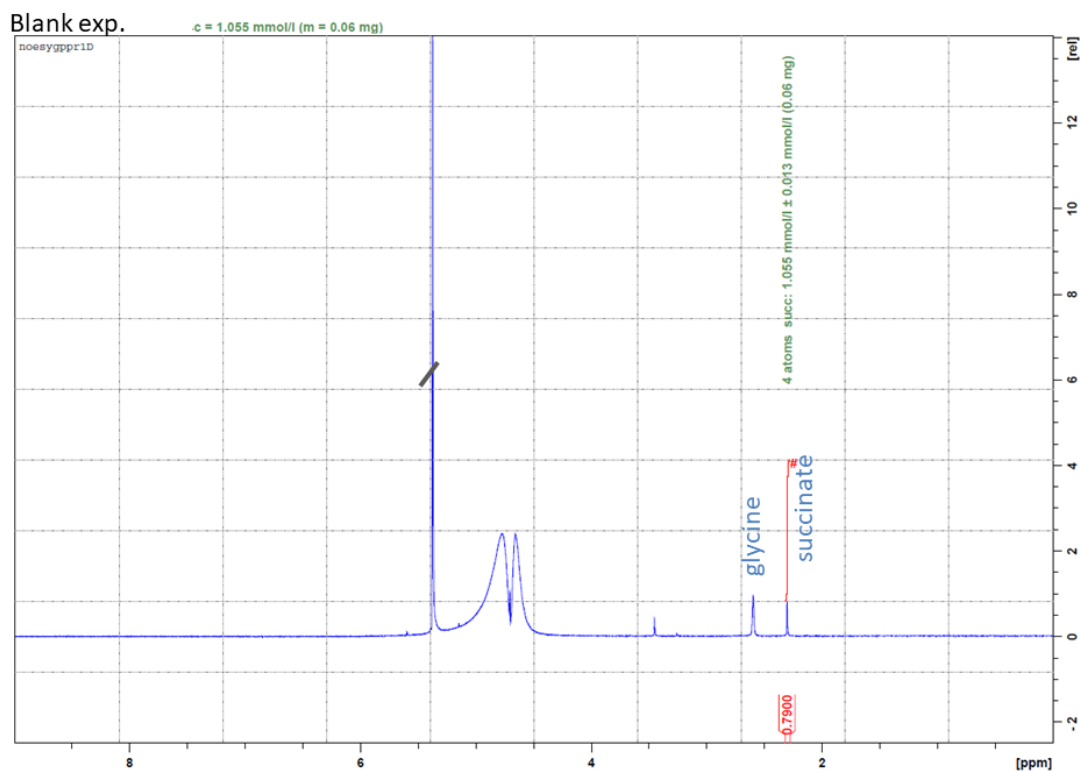


Figure 31. $^1\text{H-NMR}$ spectrum of the D_2O solution of succinate (0.05 M PBS, pH 7). The spectrum was recorded after stirring (10 min) the solution in contact with an equal volume of CH_2Cl_2 (6% DMSO). Internal reference: glycine.

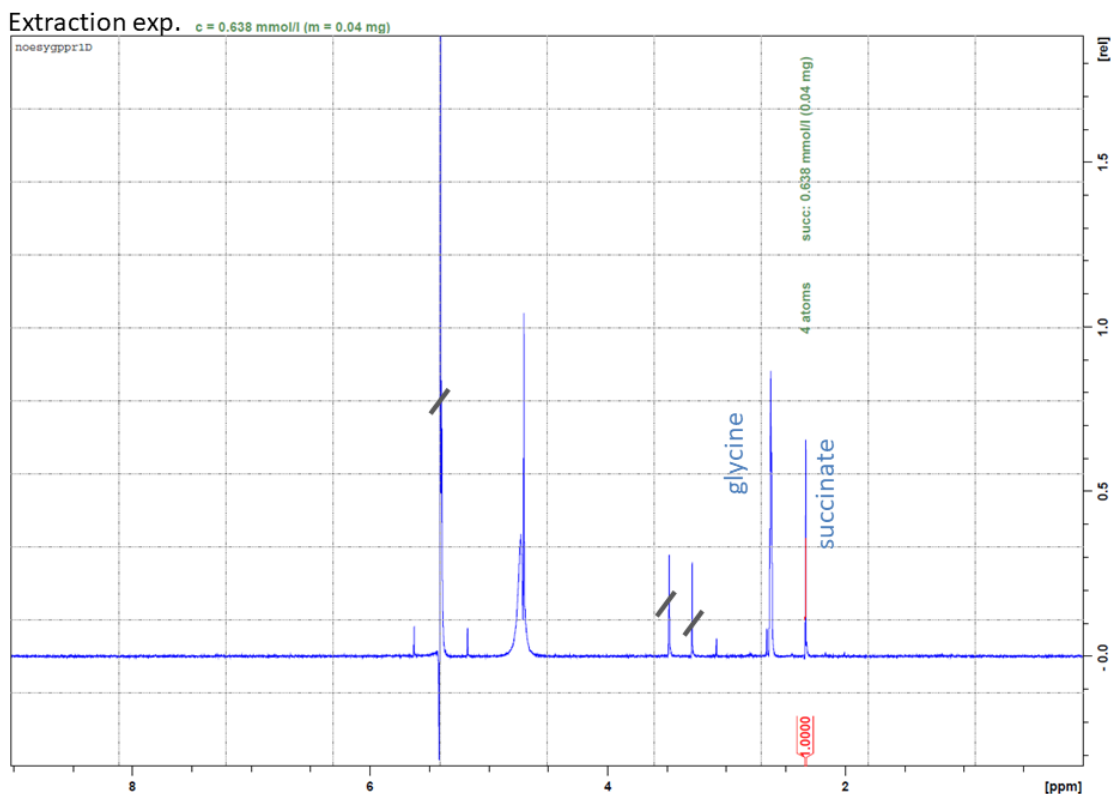


Figure 32. $^1\text{H-NMR}$ spectrum of the D_2O solution of succinate (0.05 M PBS, pH 7). The spectrum was recorded after stirring (10 min) the solution in contact with an equal volume of a solution of the dicopper complex (0.42 mM) in CH_2Cl_2 (6% DMSO). Internal reference: glycine.

4.4 Conclusions

To conclude, a new lipophilic cryptand **L2** was synthesized by appending hexyl chains on the naphthyl spacers of the cage **L1**. The dicopper(II) complex $[\text{Cu}_2(\text{L2})]^{4+}$ showed a remarkable affinity for dicarboxylates in aqueous mixture. UV-vis. titrations pointed out i) the preference of $[\text{Cu}_2(\text{L2})]^{4+}$ for succinate and fumarate anions over the investigated dicarboxylate guests, ii) a lower degree of selectivity compared to the non-functionalized analogue complex $[\text{Cu}_2(\text{L1})]^{4+}$.

Thanks to the enhanced hydrophobicity, $[\text{Cu}_2(\text{L2})]^{4+}$ resulted to be completely insoluble in pure water but soluble in dichloromethane, therefore we considered it suitable to be employed in the liquid-liquid extraction of target anions. For our extraction tests, we chose succinate as a model anion; the concentration of succinate into the aqueous phase was monitored before and after extractions through HPLC-UV and $^1\text{H-NMR}$ analyses; while the formation of the 1:1 adduct $[\text{Cu}_2(\text{L2})(\text{suc})]^{2+}$ was confirmed by recording the UV-vis. spectra of the organic phase.

Our experiments showed that $[\text{Cu}_2(\text{L2})]^{4+}$ effectively extracts suc^{2-} from neutral water, in 1:1 $[\text{Cu}_2(\text{L2})]^{4+}:\text{suc}^{2-}$ molar ratio. The successful result obtained with succinate opens perspectives

for the application of lipophilic dinuclear cryptates as selective extractants of polycharged anions from neutral water.

The research described in this chapter was published in *ACS Omega*, 2020, 5, 41, 26573.

Supplementary information

Characterization of L2

HRMS-ESI spectra of L2

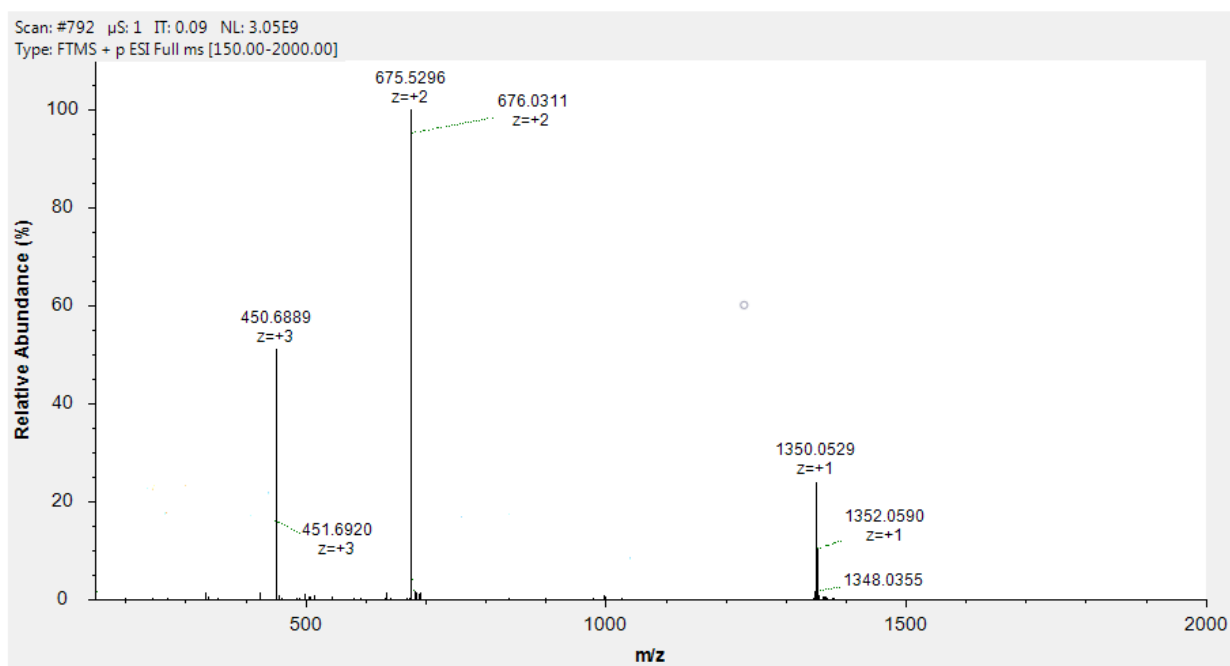


Figure S1. HRMS-ESI spectrum of L2 in methanol. Peaks found at m/z 1350.0529 (+1), 675.5296 (+2) and 450.6889 (+3) are attributable to the species $[M+H]^+$, $[M+2H]^{2+}$, $[M+3H]^{3+}$. The corresponding calculated values for the formula $C_{84}H_{132}N_8O_6$ are 1350.0348, 675.5208 and 450.6829, respectively.

NMR spectra of L2

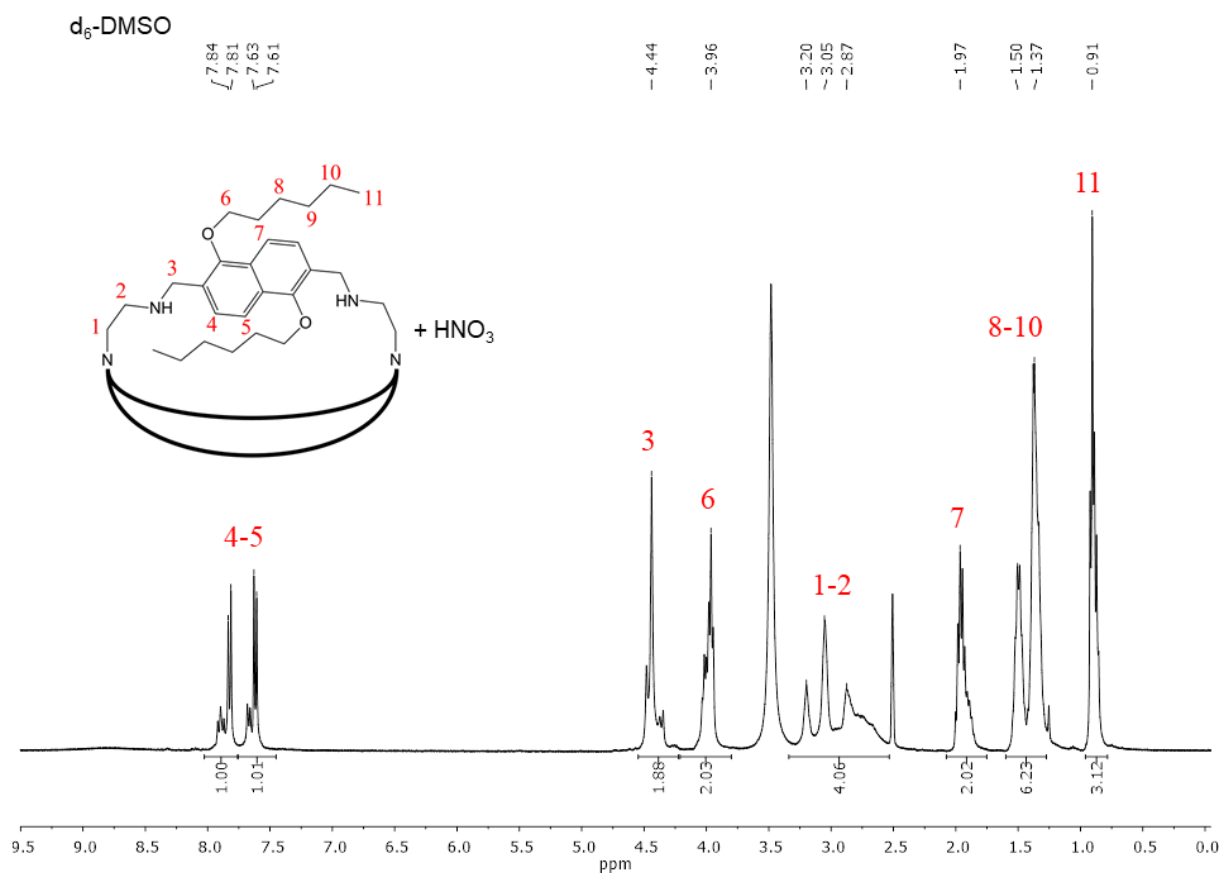


Figure S2. ¹H-NMR spectrum of L2 (10 mM) in d_6 -DMSO, recorded at 80°C and after the addition of aliquots of HNO₃ (in D₂O) to the solution. At room temperature and without acidification, the peaks were actually too large to allow a safe interpretation of the spectrum. Integrals are calculated on one portion of the molecule (see the sketch).

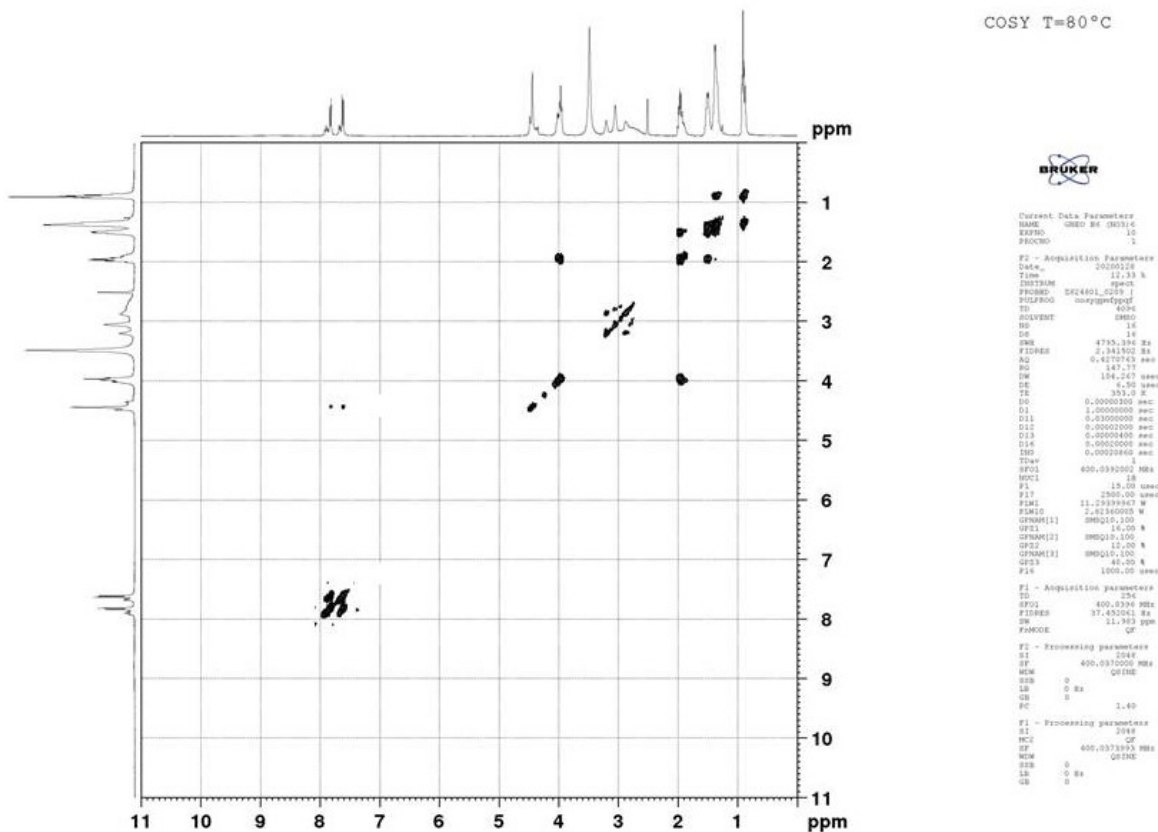


Figure S3. ¹H-¹H COSY spectrum of L2 in d₆-DMSO (+ HNO₃) recorded at 80°C.

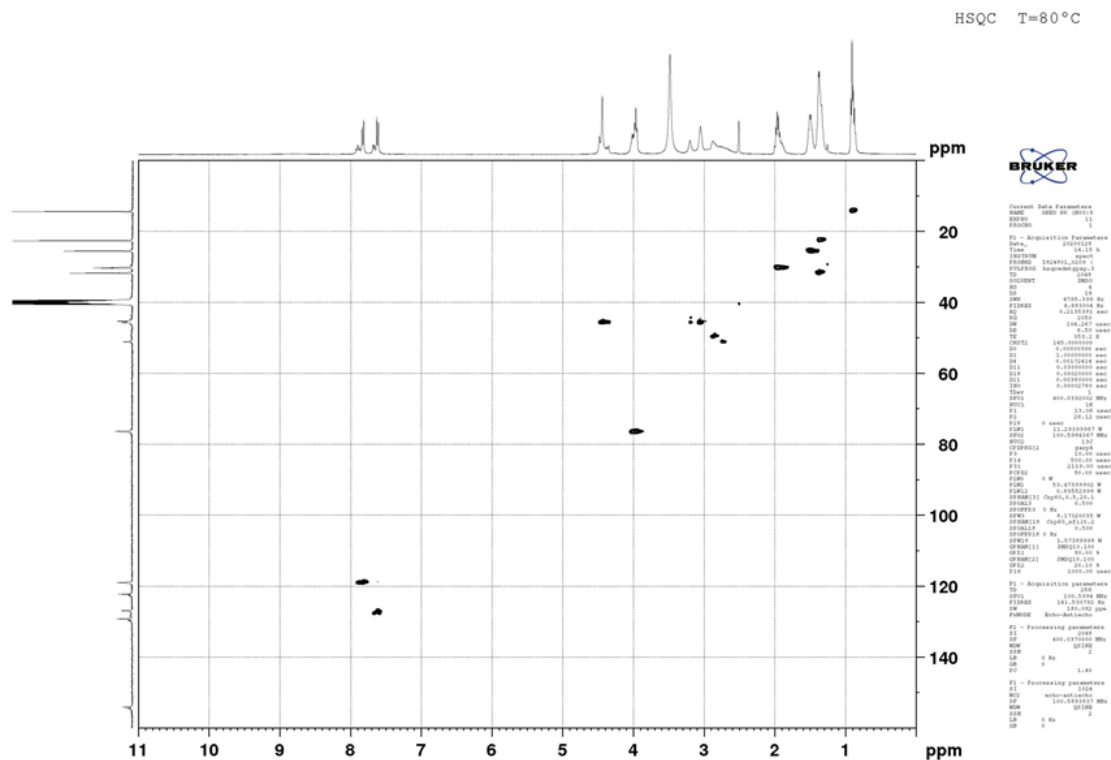


Figure S4. ¹H-¹³C HSQC spectrum of L2 in d₆-DMSO (+ HNO₃) recorded at 80°C.

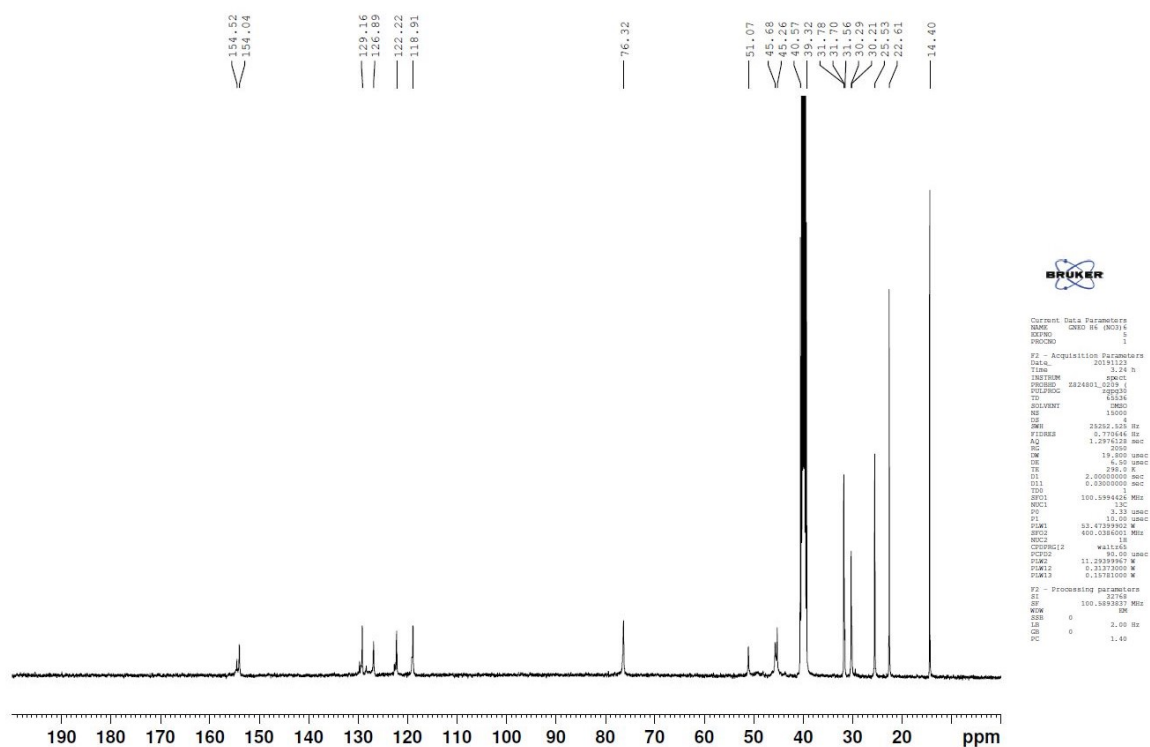


Figure S5. ^{13}C -NMR of L2 in d_6 -DMSO recorded at 25°C.

References

- [1] Bowman-James, K.; Bianchi, A.; García-España, E. Anion Coordination Chemistry, John Wiley&Sons.; New York, 2012.
- [2] Langton, M. J.; Serpell, C. J.; Beer, P. D. Anion Recognition in Water: Recent Advances from a Supramolecular and Macromolecular Perspective, *Angewandte Chemie International Edition*, **2016**, *55* (6), 1974–1987. DOI:10.1002/anie.201506589.
- [3] Zhao, J.; Yang, D.; Yang, X.-J.; Wu, B. Anion Coordination Chemistry: From Recognition to Supramolecular Assembly, *Coord. Chem. Rev.*, **2019**, *378*, 415–444. DOI:10.1016/j.ccr.2018.01.002.
- [4] Wichmann, K.; Antonioli, B.; Sohnel, T.; Wenzel, M.; Gloe, K.; Gloe, K.; Price, J. R.; Lindoy, L. F.; Blake, A. J.; Schroder, M. Polyamine-Based Anion Receptors: Extraction and Structural Studies, *Coord. Chem. Rev.*, **2006**, *250*, 2987–3003. DOI:10.1016/j.ccr.2006.07.010.
- [5] Busschaert, N.; Caltagirone, C.; Rossom, W. V.; Gale, P. A. Applications of Supramolecular Anion Recognition, *Chem. Rev.*, **2015**, *115*, 8038–8155. DOI:10.1021/acs.chemrev.5b00099.
- [6] Sommer, F.; Marcus, Y.; Kubik, S. Effects of Solvent Properties on the Anion Binding of Neutral Water-Soluble Bis(Cyclopeptides) in Water and Aqueous Solvent Mixtures, *ACS Omega*, **2017**, *2* (7), 3669–3680. DOI:10.1021/acsomega.7b00867.
- [7] Kunz, W.; Henle, J.; Ninham, B. W. ‘Zur Lehre von Der Wirkung Der Salze’ (about the Science of the Effect of Salts): Franz Hofmeister’s Historical Papers, *Curr. Opin. Colloid Interface Sci.*, **2004**, *9* (1–2), 19–37. DOI:10.1016/j.cocis.2004.05.005.
- [8] Fowler, C. J.; Haverlock, T. J.; Moyer, B. A.; Shriver, J. A.; Gross, D. E.; Marquez, M.; Sessler, J. L.; Hossain, A.; Bowman-James, K. Enhanced Anion Exchange for Selective Sulfate Extraction: Overcoming the Hofmeister Bias, *J. Am. Chem. Soc.*, **2008**, *130*, 14386–14387. DOI:10.1021/ja806511b.
- [9] Jagleniec, D.; Dobrzycki, L.; Karbarz, M.; Romanski, J. Ion-Pair Induced Supramolecular Assembly Formation for Selective Extraction and Sensing of Potassium Sulfate, *Chem. Sci.*, **2019**, *10*, 9542–9547. DOI:10.1039/c9sc02923k.
- [10] Qin, L.; Vervuurt, S. J. N.; Elmes, R. P. B.; Berry, S. N.; Proschogo, N.; Jolliffe, K. A. Extraction and Transport of Sulfate Using Macrocyclic Squaramide Receptors, *Chem. Sci.*, **2020**, *11*, 201–207. DOI:10.1039/c9sc04786g.
- [11] He, Q.; Vargas-Zúñiga, G. I.; Kim, S. H.; Kim, S. K.; Sessler, J. L. Macrocycles as Ion-pair Receptors, *Chem. Rev.*, **2019**, *119* (17), 9753–9835. DOI:10.1021/acs.chemrev.8b00734.

- [12] Urban, C.; Schmuck, C. Active Transport of Amino Acids by a Guanidiniocarbonyl–Pyrrole Receptor, *Chem. Eur. J.*, **2010**, *16* (31), 9502–9510. DOI:10.1002/chem.201000509.
- [13] He, Q.; Williams, N. J.; Oh, J. H.; Lynch, V. M.; Kim, S. K.; Moyer, B. A.; Sessler, J. L. Selective Solid-Liquid and Liquid-Liquid Extraction of Lithium Chloride Using Strapped Calix[4]Pyrroles, *Angew. Chem. Int. Ed.*, **2018**, *57* (37), 11924–11928. DOI:10.1002/anie.201805127.
- [14] Liu, Y.; Zhao, W.; Chen, C.-H.; Flood, A. H. Chloride Capture Using a C–H Hydrogen-Bonding Cage, *Science*, **2019**, *365* (6449), 159–162. DOI:10.1126/science.aaw5145.
- [15] Davis, A. P.; Sheppard, D. N.; Smith, B. D. Development of Synthetic Membrane Transporters for Anions, *Chem. Soc. Rev.*, **2007**, *36* (2), 348–357. DOI:10.1039/B512651G.
- [16] Wu, X.; Howe, E. N. W.; Gale, P. A. Supramolecular Transmembrane Anion Transport: New Assays and Insights, *Acc. Chem. Res.*, **2018**, *51* (8), 1870–1879. DOI:10.1021/acs.accounts.8b00264.
- [17] Berezin, S. K.; Davis, J. T. Catechols as Membrane Anion Transporters, *J. Am. Chem. Soc.*, **2009**, *132*, 2548–2459. DOI:10.1021/ja809733c.
- [18] Harrell, W. A.; Bergmeyer, M. L.; Zavalij, P. Y.; Davis, J. T. Ceramide-Mediated Transport of Chloride and Bicarbonate across Phospholipid Membranes, *Chem. Commun.*, **2010**, *46*, 3950–3952. DOI:10.1039/c0cc00493f.
- [19] Grauwels, G.; Valkenier, H.; Davis, A. P.; Jabin, I.; Bartik, K. Repositioning Chloride Transmembrane Transporters: Transport of Organic Ion-pairs, *Angew. Chem. Int. Ed.*, **2019**, *58* (21), 6921–6925. DOI:10.1002/anie.201900818.
- [20] Sidorov, V.; Kotch, F. W.; Abdrakhmanova, G.; Mizani, R.; Fetting, J. C.; Davis, J. T. Ion Channel Formation from a Calix[4]Arene Amide That Binds HCl, *J. Am. Chem. Soc.*, **2002**, *124* (10), 2267–2278. DOI:10.1021/ja012338e.
- [21] Li, X.; Shen, B.; Yao, X.-Q.; Yang, D. A Small Synthetic Molecule Forms Chloride Channels to Mediate Chloride Transport across Cell Membranes, *J. Am. Chem. Soc.*, **2007**, *129* (23), 7264–7265. DOI:10.1021/ja071961h.
- [22] Jean-Marie Lehn. *Supramolecular Chemistry: Concepts and Perspectives*; Wiley-VCH: Weinheim, Germany, 1995.
- [23] Mateus, P.; Bernier, N.; Delgado, R. Recognition of Anions by Polyammonium Macrocyclic and Cryptand Receptors: Influence of the Dimensionality on the Binding Behavior, *Coord. Chem. Rev.*, **2010**, *254* (15–16), 1726–1747. DOI:10.1016/j.ccr.2009.11.005.
- [24] Fabbrizzi, L.; Poggi, A. Anion Recognition by Coordinative Interactions: Metal–Amine Complexes as Receptors, *Chem. Soc. Rev.*, **2013**, *42* (4), 1681–1699. DOI:10.1039/C2CS35290G.

- [25] Alibrandi, G.; Amendola, V.; Bergamaschi, G.; Fabbrizzi, L.; Licchelli, M. *Bistren Cryptands and Cryptates: Versatile Receptors for Anion Inclusion and Recognition in Water*, *Org. Biomol. Chem.*, **2015**, *13* (12), 3510–3524. DOI:10.1039/C4OB02618G.
- [26] Amendola, V.; Bergamaschi, G.; Miljkovic, A. Azacryptands as Molecular Cages for Anions and Metal Ions, *Supramol. Chem.*, **2018**, *30* (4), 236–242. DOI:10.1080/10610278.2017.1339885.
- [27] Fabbrizzi, L. *Cryptands and Cryptates*; World Scientific Publishing Europe Ltd.: London, 2018.
- [28] Allen, C. R.; Richard, P. L.; Ward, A. J.; Masters, A. F.; Maschmeyer, T. Facile Synthesis of Ionic Liquids Possessing Chiral Carboxylates, *Tetrahedron Lett.*, **2006**, *47*, 7367–7370. DOI:0.1016/j.tetlet.2006.08.007.
- [29] Urban, M.; Durka, K.; Jankowski, P.; Serwatowski, J.; Lulins, S. Highly Fluorescent Red-Light Emitting Bis(Boranils) Based on Naphthalene Backbone, *J. Org. Chem.*, **2017**, *82*, 8234–8241. DOI:10.1021/acs.joc.7b01001.
- [30] Gans, P.; O’Sullivan, B. GLEE, a New Computer Program for Glass Electrode Calibration, *Talanta*, **2000**, *51* (1), 33–37. DOI:10.1016/S0039-9140(99)00245-3.
- [31] Gran, G. Determination of the Equivalence Point in Potentiometric Titrations. Part II, *Analyst*, **1952**, *77* (920), 661–671. DOI:10.1039/AN9527700661.
- [32] Gans, P.; Sabatini, A.; Vacca, A. Investigation of Equilibria in Solution. Determination of Equilibrium Constants with the HYPERQUAD Suite of Programs, *Talanta*, **1996**, *43* (10), 1739–1753. DOI:10.1016/0039-9140(96)01958-3.
- [33] Thordarson, P. Determining Association Constants from Titration Experiments in Supramolecular Chemistry, *Chem. Soc. Rev.*, **2011**, *40* (3), 1305–1323. DOI:10.1039/C0CS00062K.
- [34] Dawson, R. M. C.; Elliott, D. C.; Elliott, W. H.; Jones, K. M. *Data for Biochemical Research*, 3rd ed.; Oxford University Press: New York, NY, 1986.
- [35] Lide, D. R. *CRC Handbook of Chemistry and Physics*, 84th ed.; CRC Press: Boca Raton, FL, 2003.

5. New hydrophilic azacryptands as complexing agents for $^{99}\text{TcO}_4^-$ in extraction processes

omissis